Analysis of PP and PS multicomponent reflection data in the presence of seismic anisotropy

by

Lifeng Wang

Thesis submitted in fulfilment of
the requirement for the degree of
Doctor of Philosophy

School of Geosciences
University of Edinburgh
2007

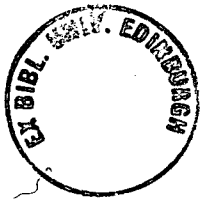

Declaration

I declare that this thesis has been composed solely by myself and that it has not been submitted, either in whole or in part, in any previous application for a degree. Except where otherwise acknowledged, the work presented is entirely my own.

Lifeng Wang

2007

Abstract

In recent years, the acquisition, processing, imaging and fracture detection capabilities using multicomponent PP- and PS-wave seismic have been improved. Unlike traditional narrow-azimuth P-wave data, multicomponent wide-azimuth data are more sensitive to the presence of seismic anisotropy. Two types of anisotropy are commonly considered within exploration seismology: vertical transverse isotropy (VTI) due to layering of sedimentary rocks, and horizontal transverse isotropy (HTI) due to vertical fracturing. Intensive efforts have been devoted to studying the effects of these types of anisotropy on both PP- and PS-waves. Nevertheless, there are still some fundamental issues which need to be investigated, and this thesis aims to address some of these issues.

First, the effect of structural variation on anisotropic parameter estimation using PS converted waves is still not fully understood. I generate and process a number of isotropic and anisotropic synthetic datasets in the presence of varying dip and VTI. I find that the errors in velocity ratio of PP- and PS-wave result in large horizontal mis-positioning and erroneous PS-wave stacking velocities make dips flip but have the same effects for both directions of offsets if the data are separated into positive and negative offsets. Errors in the velocity ratio have the same effects as errors in anisotropy measurements. These errors have different effects for positive and negative offsets.

Furthermore, for a 3D wide azimuth dataset acquired over an HTI target, the use of an optimum processing workflow is of importance since the fracture analysis is in general applied on the processed results. I suggest the use of an early rotation of the

horizontal geophones into the principal component directions instead of conventional radial and transverse directions. In order to deal with the effects of HTI, the linear transform technique, originally developed for pure shear-wave data, is extended to handle PS converted waves and is used to determine the principal S-wave directions and percentage anisotropy.

In the applications of multicomponent seismic data, recent observations and results suggest that it is worthwhile to consider frequency dependent effects in the analysis of seismic anisotropy as it has the potential to obtain fracture scale length in addition to fracture strike and density. Since the present successes are limited to several VSPs, I develop and apply various techniques to investigate whether frequency-dependent anisotropy can be detected in multicomponent reflection seismic data.

In the analysis of shear wave splitting, the time delay between the fast and slow wave is a particularly useful parameter that can often be related to fracture density. For reflection data, it is more convenient to generate attribute sections instead of discrete attribute values to aid interpretation. A robust and user-friendly tool is developed for evaluating PS converted-wave splitting in 2D data or 3D multicomponent data. This allows the generation of continuous time-delay spectra, leading to a time-delay section.

Throughout the thesis two datasets are used to validate the new findings. An integrated study of both PP- and PS-waves is applied to the ocean-bottom cable 3D/4C Emilio dataset. The inverted fracture polarization and intensity are correlated with drilled well locations. The results of the frequency dependent anisotropy analysis show that converted-wave splitting changes with frequency in some field locations. The other onshore multicomponent dataset was acquired over volcanic gas reservoirs. It is interesting that the amount of splitting determined from the data can be correlated with the known gas reservoirs in some wells, revealing a potential to use shear-wave splitting to delineate gas reservoirs in volcanic rocks.

Acknowledgements

First of all I wish to express my gratitude to my supervisor Prof. Xiang-Yang Li for his guidance throughout the research during the past several years. I thank Prof. Enru Liu and Dr. Mark Chapman for many discussions and support. They had told me a lot about the seismic method and anisotropy, and more generally how to approach scientific problems. Their extensive review and corrections help me improve this document from what was simply an amalgamation of work into this more coherent thesis. I also thank Dr. Andrew Curtis for his help and support at the University.

I hugely thank Prof. Enru Liu and Dr. Mark Chapman for their help during my job hunting. I would like to thank Hengchang Dai for many beneficial discussions and sorting out all the Cx-tools and Motif programming problems. Thank David Booth for helping me proofread and correct the thesis.

Thanks also go to BGS computing department: Brian Bainbridge, Ruth Addinall, Jane Broughton and Scott Cummings. I am grateful to B?rbel Traul, Andy Dobson, Fabio Manini, Serafeim Vlastos, Sonja Maultzsch, Jinghua Zhang, Zhongping Qian, Isabel Varela and Adam Wilson for numerous enjoyable working days in the office.

I would like to thank NERC to fund my study. I would like to thank the sponsors of the Edinburgh Anisotropy Project for supporting the research group and thank Eni-Agip and PetroChina for providing the datasets. A special thank you goes to Rodney Johnston for the part of converted wave imaging work and his help during my stay in BP.

I also thank Prof. Michael H. Worthington, my external examiner from University of Oxford, and Prof. Ian Main, my internal examiner from University of Edinburgh, for their careful review and corrections on the thesis.

Finally, I wish to express my dearest gratitude to my parents for their continuous encouraging and understanding.

To my parents

Contents

Chapter 9: Conclusions

List of Tables

List of Figures

List of abbreviations

PP-wave	P-compressional waves
PS-wave or C-wave	Converted waves with particle motion in the source receiver-conversion point plane
S-wave	Shear waves
VTI or TIV	Vertical Transverse Isotropy, Polar anisotropy
HTI or TIH	Horizontal Transverse Isotropy
NMO	Normal MoveOut
DMO	Dip MoveOut
VSP	Vertical Seismic Profile
AVO	Amplitude versus offset
TI	Transversely isotropic
4C	Four component (multicomponent), 3 geophones plus 1 hydrophone
OBC	Ocean Bottom Cable, containing the multicomponent sensors
CMP	Common Mid Point
CCP	Common Conversion Point
AGC	Automatic Gain Control
PKTM	Pre Stack Kirchhoff Time Migration
CIP	Common Image Point (CMP after PSTM)
GUI	Graphic User Interface
SWAP	Shear Wave Analysis Package
LTT	Linear Transform Technique
SU	Seismic Unix
TF	Time frequency
FT	Fourier Transform
STFT	short-time Fourier transform
CWT	Continuous wavelet transform
MEMS	Micro-Electro-Mechanical-Sysmtem

List of Symbols

Symbol	Meaning	Units
v_p	P-wave velocity	m/s
v_s	S-wave velocity	m/s
v_c	C-wave velocity	m/s
v_{pn}	NMO P-wave velocity (RMS, stacking)	m/s
v_{sn}	NMO S-wave velocity (RMS, stacking)	m/s
v_{cn}	NMO C-wave velocity (RMS, stacking)	m/s
v_{p0}	P-wave vertical velocity	m/s
v_{s0}	S-wave vertical velocity	m/s
v_{c0}	C-wave vertical velocity	m/s
x	Source-receiver offset	m
x_c	Conversion point offset	m
$t(x)$	Travel time at offset x	s
t_0	Travel time at zero-offset	s
t_{p0}	P-wave time at zero-offset	s
t_{s0}	S-wave time at zero-offset	s
t_{c0}	C-wave time at zero-offset, defined by the downgoing P-wave traveltime, t_{p0}, and the up-going S-wave traveltime, t_{s0}	s
γ	Isotropic velocity ratio, v_p/v_s	
γ_0	Vertical velocity ratio, v_{p0}/v_{s0}	
γ_n	NMO velocity ratio, v_{pn}/v_{sn}	
γ_{eff}	Effective velocity ratio, γ_{n2}/γ_0	
γ_{asy}	Depth-constant γ_{eff} used in binning C-wave data	
C_{ij}	Elastic constant	$g/(ms^2)$ (GPa)
$\delta, \varepsilon, \gamma'$	Thomsen's anisotropic parameter, combinations of elastic constants	
$\sigma, \eta, \chi, \zeta$	Different anisotropic parameters derived from Thomsen's parameters The subscript "*eff*" indicates they are "effective" parameters, the subscript "*i*") indicate interval quantity.	
ρ	Density	Kg/m^3
λ	Fluid incompressibility	N/m^2
μ	Shear modulus	N/m^2
p	Ray parameter	s/m

Chapter 1

Introduction

1.1 Multicomponent seismic

P-waves, or compressional waves, have dominated the application of seismic technology over the last seventy years of the oil and gas industry. Numerous reservoirs have been discovered, characterized and monitored through the use of P-waves. The P-wave technology has advanced from 2D and 3D to the 4D, or time-lapse seismic, methods that are available nowadays. Even though the conventional P-wave is powerful, it cannot solve every seismic imaging or reservoir-description problem. Under some conditions, S-wave, or shear wave, information is needed in addition to P-wave information to image a reservoir or describe reservoir properties adequately. S-waves were used in the past in land survey in the late 19601 s (Garotta, 2000). However, the difficulties of producing and operating a shear-wave source restricted the use of S-waves to only a few experiments.

Multicomponent seismic data allow the joint use of S-waves and P-waves. It uses a different approach from the conventional P-wave seismic since it aims to record PS converted-waves as additional components. Instead of expensive shear wave sources, current multicomponent technology records S-waves converted by P-waves at the reflector (PS-waves), as well as the traditional PP-waves. It can be applicable either

in a marine environment or in the usual onshore environment and it often allows the recording of multi-azimuthal PP- and PS-wave data.

Recent advances in multicomponent seismic are providing powerful tools in enhancing exploration results and reducing the risk in reservoir development. In an exploration setting, multicomponent seismic offers improved imaging (e.g. Thomsen *et al.*, 1997; Granli *et al.*, 1999; Pope *et al.*, 2000; Li *et al.*, 2001), direct hydrocarbon and lithology indication (MacLeod *el at.*, 1999) and multiple attenuation compared to conventional P-wave seismic. In a development setting, multicomponent seismic facilitates improved reservoir illumination and characterization (e.g. Gaiser, 2000; Horne, 2003).

Unlike traditional narrow-azimuth P-wave data, multicomponent wide-azimuth seismic data is more sensitive to the presence of seismic anisotropy. One of the common forms of anisotropy is known as Transverse Isotropy with a Vertical axis of symmetry (Vertical Transverse Isotropy), VTI or TIV. Another common form of anisotropy is known as Transverse Isotropy with a Horizontal axis of symmetry (Horizontal Transverse Isotropy), HTI or TIH.

For hydrocarbon exploration and development, the geophysical results come from a series of processing steps such as filtering, deconvolution, amplitude recovery, velocity analysis, NMO, DMO, migration and so on. Many of the conventional processing steps such as NMO, velocity analysis, DMO and migration often assume isotropy. The presence of VTI or HTI or both affects all these steps, and this thesis aims to deal with some of these issues.

The presence of VTI will introduce non-hyperbolic moveout and affect the position of geological features, such as faults and traps, causing mistie of geological horizons.

Consequently, the effects of VTI should not be ignored during the processing and interpretation of PP and PS multicomponent seismic data.

In recent years, intensive efforts have been devoted to study the effects of VTI on PP-waves. Tsvankin and Thomsen (1994) presented an analytic and numerical analysis of nonhyperbolic reflection moveout of P-waves in VTI media. Tsvankin and Thomsen (1995) examined the feasibility of inverting nonhyperbolic reflection moveouts for parameters. Alkhalifah (1997) proposed an anisotropy parameter, η, relating to P-wave anisotropy and demonstrated how to extract its values from P-wave nonhyperbolic moveout behavior. Grechka and Tsvankin (1998) recast the nonhyperbolic movout equations (Alkhalifah and Tsvankin, 1995) and improved its accuracy on intermediate spreads by introducing an additional coefficient in the denominator.

In comparison, the effect of VTI on PS wave is less well understood. Li and Yuan (2003) introduced a parameter, χ, related to PS-wave anisotropy. They presented a four-parameter equation (V_{ps2}, γ_0, γ_{eff} and χ_{eff}) for describing PS-wave travel-time in layered VTI media and a five-parameter double-square-root (DSR) equation (V_p, V_s, γ_0, η_{eff} and ζ_{eff}) for prestack time migration of PS-waves (Li *et al.*, 2001). Based on this theory, a practical workflow and a processing package, Cxtools, has been developed for processing PS converted wave data in presence of anisotropy. A number of marine and land (2D and 3D) multicomponent datasets have been successfully processed with improved images using the Cxtools (e.g. Dai *et al.*, 2004; Mancini *et al.*, 2005). Traub (2004) used horizontal-layer models to study the accuracy and sensitivity of anisotropic parameter estimation using 4C data. Dai (2006) gave a numerical analysis of the effects of migration velocity errors on traveltime accuracy in prestack Kirchhoff time migration and the image of PS converted waves.

The presence of HTI gives rise to azimuthal anisotropy, which is commonly associated with aligned vertical fractures. For PP-wave, the effect of HTI gives rise to elliptical azimuthal variations in P-wave attributes (R?ger, 1996a; Tsvankin, 1997).

For PS-wave, the effect of HTI gives rise to shear wave splitting (Li, 1997, 1998). Again, these effects of anisotropy on PP- (e.g. MacBeth *et al.*, 1999; Mallick *et al.*, 1996; Grechka and Tsvankin, 1998; Liu, 1999) and PS-waves (e.g. Li, 1997; Li, 1998; Dellinger *et al.*, 2001) have been intensively studied and widely used for fracture detection.

Conventional static equivalent medium theories can be used to recover average fracture density and strike in the long wavelength limit. Many models (e.g. Hudson *et al.*, 1981; Thosmen, 1995) have been developed for such purposes. These models predict frequency independent behaviour and there is in general an agreement between the models for dry rock, but there exist considerable differences in the case of fluid-fill and fluid flow between cracks and pores (Liu *et al.*, 2000). Scattering of seismic waves due to aligned heterogeneities has been recognised to be frequency-dependent (Werner and Shapiro, 1999). Moreover, there are observations of frequency dependent anisotropy from a range of field data (Van der Kolk *et al.*, 2001). Theoretical modelling (Chapman, 2003) predicts frequency dependent anisotropy due to squirt flow in fractured porous rock. Recent results (Maultzsch *et al.*, 2003; Liu *et al.*, 2003) presented fracture size estimates using this model from a multicomponent VSP data set. These studies indicate that there is a great potential in using frequency dependent anisotropy to estimate average fracture sizes.

1.2 Motivation and objectives

Despite the intensive efforts as stated previously and the fact that the multicomponent technique is powerful and has the potential to become one of the most useful tools in reservoir characterisation, there are still a number of fundamental issues which need to be addressed with regard to anisotropy. The objective of the thesis is to address these issues.

The first issue is the effects of structural variation on anisotropic parameter estimation using PS converted waves, which has not been fully investigated before (Rodney Johnston, BP, personal communication). Experience has shown that imaging of the earth's interior using PS converted waves is a non-trivial problem. In all but the simplest of earth structures (1D), the ability to gather the data for migration velocity analysis is complicated by the asymmetric propagation path, reflector dip, source-receiver azimuth, and anisotropy. The effect of dip is generally accommodated through pre-stack imaging, however, in the case of PS waves this adds to the complexity of deriving the correct sub-surface model which satisfies all of the data including P-waves. Traub (2004) analysed the accuracy and sensitivity of anisotropic parameter estimation using 4C data, however, her study is limited to horizontal-layer models. Dai and Li (2006) studied the effects of migration velocity errors on traveltime accuracy in pre-stack Kirchhoff time migration and the image of PS converted waves, but he only gave a numerical analysis. There is still a lack of understanding of the uncertainties and sensitivities in the parameters, such as γ_0, γ_{eff}, V_c and χ, with regard to the effect of structure. In the thesis I fill this gap by investigating PS-wave imaging sensitivities of anisotropic parameters through the use of a set of dip models.

The second issue is related to the use of PS-waves for fracture analysis. For a 3D wide azimuth dataset, the use of an optimum processing workflow is of great importance, as the fracture analysis is usually applied on the processed results. Li (1998) demonstrated from synthetic modelling that a polarity reversal and amplitude dimming will occur in the azimuthal gathers of the transverse components assuming that the fracture reservoir gives rise to HTI. One can expect that a full azimuthal stack or migration may cause the energy of the fast and slow shear waves to cancel each other. In contrast, the stack or migrated image will be improved from separate processing of fast and slow shear wave data. Various rotation methods have been developed to separate the fast and the slow components (e.g. Alford, 1986; MacBeth *et al.*, 1991). Li and Crampin (1993) presented an efficient linear transform technique for analysing shear wave splitting. However, most of the techniques are developed for pure shear-wave data acquired with shear-wave source. Here I will extend the linear transform technique to handle converted waves and I will investigate how pre-stack time migration of PS-wave will enhance the HTI effects of fracture analysis.

The third issue is to analyse the frequency dependent anisotropy in a reflection survey. In the long wavelength limit, conventional static equivalent medium theories can be used to recover average fracture density and strike. Nevertheless, evidence from a number of measurements supports the idea that anisotropy, or shear-wave splitting, exhibits a frequency dependence. This is generally attributed to properties of the microstructure of the rock and typically assumed to be the result of scattering from oriented inclusions within the rock mass. Theoretical modelling (Chapman, 2003) predicts the frequency dependent anisotropy due to squirt flow in fractured porous rock. A number of recent case studies show the analysis of the frequency dependent anisotropy has the potential to obtain more fracture attribute other than fracture strike and density. However, the current success is limited in the use of VSP datasets. It is valuable to investigate the frequency dependent anisotropy in the reflection dataset.

The fourth one is about P-wave attributes comparison for fracture detection. As we know, we can use several different P-wave attributes, such as amplitudes, velocity, traveltime, etc, for fracture detection (e.g. Corrigan *et. al.* 1997; Sayers and Ebrom, 1997; Lynn and Beckham, 1998; amongst others). It is interesting to check the results from each different attribute. Ideally, each attribute should generate the same results. However, in real case, due to data quality or processing issues, the results may be different. It is also of interest to compare the fracture detection results of PP- and PS-waves together.

The final issue is the use of robust and user-friendly tools for shear wave splitting, especially in a single azimuth distribution condition. Shear wave splitting is widely used for fracture analysis, and the time delay between the fast and slow wave is a particular useful parameter that often can be related to fracture density directly. Time delay is measured over a time window and yields a time-delay curve over depth. This may be not an issue for VSP data. However, for reflection data, it is more convenient to generate attribute sections to aid interpretation. How to generate time delay sections from surface data is an issue. Here I develop a Graphic User Interface (GUI) tool that fills the gap. The tool computes the correlations coefficients between the fast and slow split shear wave and enables one to generate continuous time-delay spectra, which yield a time-delay section. The developed techniques are applied to an onshore multicomponent seismic data.

1.3 Thesis structure

Throughout the whole thesis two dataset have been used. The first dataset is from a 3D multicomponent survey in the Emilio field, made available by Eni-Agip. The Emilio field is fractured and the dataset was shot with the purpose of fracture characterization. The second dataset is a 2D multicomponent survey from the DaQing oilfield in Northeast China. It is a gas reservoir beneath volcanic rocks and

2D multicomponent reflection data were acquired. This data provide a good opportunity for the use of converted wave splitting to delineate the interval reservoir architecture.

In order to understand the main problem in the use of different wave types for fracture detection and imaging, it is necessary to review the PP- and PS-wave fracture analysis methods. In Chapter 2 I give a review of wave propagation in anisotropic media and general methodology fracture detection of using seismic anisotropy in multicomponent PP- and PS-wave seismic data.

In Chapter 3, I begin with a brief review of survey design of the Emilio field and the Emilio data. I review the main procedures for acquisition design and investigate the characteristics of the acquired data. From the analysis of core samples, it was concluded that there is a wide presence of fractures in the Emilio field. In order to characterize the fractured reservoir, the Emilio survey was designed for a full azimuth distribution.

In Chapter 4, the use of P-wave for azimuthal anisotropy analysis is studied. A robust technique is developed for multiple attenuation during data pre-processing. Two techniques are often used to extract fracture parameters from P-wave data: narrow-azimuth/full-offset stacking and full-azimuth/full-offset surface fitting (Li *et al.*, 2003). The first method divides the data into a number of narrow-azimuth volumes and is applicable to the velocity and AVO gradient attributes. The second method fits an elliptical surface to data from all available azimuths and offsets by a least-square fitting technique and is applicable to the amplitude and traveltime attributes. Both methods are used to estimate azimuthal differences of seismic attributes. I confirmed that the narrow-azimuth stacking technique may enhance the acquisition footprint and surface fitting of all azimuths and offsets is recommended.

In Chapter 5, I first introduce various PS-wave anisotropic processing approaches. Due to the strong azimuthal anisotropy appearance in the wide-azimuth dataset, I

process the PS-wave data using the common azimuthal component technique. A recently developed graphic user interface tool at Edinburgh Anisotropy Project (EAP) is used for PS-wave imaging. I also create and process a number of anisotropic synthetic datasets to understand and quantify model-building sensitivities associated with PS-wave imaging in the presence of varying dip and polar anisotropy. The models embody a variation in complexity from simple 1D reflectors to a range of dips, as well as lateral velocity variations. I generate pre-stack time migration impulse responses for the different models. The goal of the analysis is to understand how errors in any one parameter translate into errors in positioning, conversion-point smearing, mis-stacking, and the ultimate degradation in image quality. I achieve this through a combination of parameter perturbation and remigration with a PS migration velocity analysis workflow.

The focus of Chapter 6 is the analysis of the PS-wave for azimuthal anisotropy. For the PS-wave analysis, instead of rotating the raw data into the radial and transverse components, the data were rotated directly into the principal anisotropy directions in the pre-processing stage. This strategy has greatly improved the processing efficiency. The processed azimuthal components show strong correlation with the estimated fracture directions. To analyse the fracture attributed in the Emilio field, I extend the linear transform technique of Li and Crampin (1993) for converted reflection data. The fracture strike and density maps are well correlated with the drilled well locations.

In Chapter 7 I analyse frequency dependent anisotropy in the post-stack migrated data. For this purpose I use both band-pass filtering and several time-frequency analysis methods. Several different methods have been tested, such as the Fourier transform, the short window Fourier transform (STFT) and the continuous wavelet transform (CWT). The results show the variation of the anisotropy with different frequencies and I argue that there is frequency dependent anisotropy in the Emilio field. This finding has a potential to help recover more fracture properties.

In Chapter 8 I carry out a detailed anisotropic processing and converted-wave splitting for a 2D onshore multi-component dataset. I design a technique for evaluating converted-wave splitting for 2D or 3D data with a narrow-azimuth distribution. I adopt a rotation-scanning procedure that maximizes the separation of the fast and slow split shear-waves. I then construct time-delay spectra between the fast and slow waves that allow the picking of time delays as a function of the vertical traveltime. The method is specially designed for a dataset with a single azimuth distribution or a narrow azimuth 3D dataset. A graphic user-interface picking tool is developed which enables one to analyse splitting conveniently and interactively.

In Chapter 9 I draw a summary of the main results of this thesis and discuss the outstanding areas of future research.

Chapter 2

Seismic anisotropy and fracture detection using multicomponent seismic data

2.1 Introduction

Here I begin with an overview of fundamental anisotropy theories and an introduction of different anisotropy classifications. Then I summarize the P- and S-wave responses in the anisotropic media. Since the thesis principally concerns the study of anisotropy in the use of multicomponent seismic datasets, I outline some basic concepts of multicomponent technology as well as the methodology of fracture detection using seismic anisotropy.

2.2 Fundamental anisotropy theory

The Earth is a complex system made up of different layers of material which have undergone a number of tectonic processes, for example, compression and folding.

The present widely used seismic exploration methods are based on the theory of acoustic and elastic wave propagation. Certain assumptions, such as an isotropic medium, a homogeneous medium, and that stresses are linearly related to strains, are usually made (Helbig, 1994, 1998). Nevertheless, real media have deviations from these ideal assumptions and the attempts to deal with such deviations lead to the development of anisotropy theory.

Seismic anisotropy is the variation of elastic properties with direction and it has been identified in the Earth's crust mantle for many years. In Hooke's Law, the relationship between the stress tensor σ_{ij}, strain tensor ε_{kl} and elastic modulus tensor c_{ijkl} satisfies the following equation:

$$\sigma_{ij} = c_{ijkl}\varepsilon_{kl} \tag{2.1}$$

where c_{ijkl} is a fourth rank tensor and in general it has 81 components. However, due to the stress and the strain tensor being symmetric, as well as energy constraints, there are at most 21 independent elastic constants required to describe an anisotropic material uniquely.

Substituting Eq. 2.1 into Newton's Second Law relating force, density and acceleration, leads to the elastodynamic wave equation for infinitesimal displacements of an elementary volume:

$$\rho\ddot{u}_j = c_{ijkl}u_{k,lj} \tag{2.2}$$

where ρ is the density and $u_{k,lj} = \partial^2 u_k / \partial x_l \partial x_j$. A general expression for a homogeneous plane-wave travelling in a chosen direction of the form $u_k = U_k \exp[i\omega(t - p_j x_j)]$ can be substituted into Eq. 2.2 to yield three simultaneous (Kelvin-Christoffel) equations. One way to solve these equations is to find numerical solutions by reformulating the equations as the following linear eigenvalue problem:

$$(\Gamma_{ik} - \rho v^2 \delta_{ik})U_k = 0 \tag{2.3}$$

where Christoffel matrix $\Gamma_{ik} = c_{ijkl} n_j j_l$, U is the polarization vector, p=n/v is the slowness vector, v is the plane-wave (phase) velocity in the chosen propagation direction which is defined as the number of wavelengths per unit distance normal to the wavefront, that is, the velocity with which plane-wave crests and roughs travel through a medium is expressed as the ratio of frequency of vibration and the wave number.

Eq. 2.3 yields three real positive roots for ρv^2 with orthogonal eigenvectors since Γ is a real symmetric positive-definite matrix. It indicates that along the direction of plane-wave propagation there are, in general, three body-waves travelling with different velocities and fixed orthogonal polarization vectors: one quasi P-wave (qP) with approximate longitudinal particle motion; and two *quasi* shear-waves (*qS1* and *qS2*) with particle motion approximately transverse to the direction of propagation in two orthogonal directions. The phase velocities of these three body waves vary with propagation direction in a way determined by the symmetry properties of the elastic constants within the stiffness tensor. Shear-wave splitting refers to the two shear waves, which propagate with different velocities and polarizations.

2.3 Classification of anisotropy

The general 21 independent parameters can be further reduced as long as there are spatial symmetries in the medium. The symmetry of the medium determines the spatial pattern of velocities, polarizations and amplitudes of elastic waves.

2.3.1 Isotropy

In the case of spherical symmetry, the velocity is the same in all directions and there are only two independent elastic parameters, i.e., Lamé parameters λ and μ. μ is the so-called shear-wave modulus which together with the velocity controls the velocity of the shear wave. The elastic tensor of a system of isotropic elastic symmetry can be written:

$$\begin{pmatrix} \lambda+2\mu & \lambda & \lambda & 0 & 0 & 0 \\ \lambda & \lambda+2\mu & \lambda & 0 & 0 & 0 \\ \lambda & \lambda & \lambda+2\mu & 0 & 0 & 0 \\ 0 & 0 & 0 & \mu & 0 & 0 \\ 0 & 0 & 0 & 0 & \mu & 0 \\ 0 & 0 & 0 & 0 & 0 & \mu \end{pmatrix}$$

2.3.2 Cubic crystals

The cubic matrix has the same form as the isotropic matrix except that the lower three diagonal elements are independent. However there are no geophysical objects which show cubic symmetry so that cubic symmetry is ignored in exploration industry.

2.3.3 Transverse isotropy

Media with hexagonal symmetry are transversely isotropic (TI) and five independent stiffness constants are required to define them. Every plane perpendicular to the axis of symmetry is a plane of symmetry and the properties of elastic waves travelling through such media depend on the angle between the propagation direction and the symmetry axis. It is the next simplest material and of particular interest in seismic exploration. According to the direction of the symmetry plane, a TI medium can be further classified as a VTI medium (with vertical axis of symmetry) or a HTI medium (with horizontal axis of symmetry). Horizontal fracturing and horizontal fine-layering are typical of VTI media as shown below in form of stiffness matrix:

$$\begin{pmatrix} c_{11} & c_{11}-2c_{66} & c_{13} & 0 & 0 & 0 \\ c_{11}-2c_{66} & c_{11} & c_{13} & 0 & 0 & 0 \\ c_{13} & c_{13} & c_{33} & 0 & 0 & 0 \\ 0 & 0 & 0 & c_{44} & 0 & 0 \\ 0 & 0 & 0 & 0 & c_{44} & 0 \\ 0 & 0 & 0 & 0 & 0 & c_{66} \end{pmatrix}$$

Vertical fractures in isotropic media produce HTI media and the stiffness tensor has the following form:

$$\begin{pmatrix} c_{11} & c_{13} & c_{13} & 0 & 0 & 0 \\ c_{13} & c_{33} & c_{33}-2c_{44} & 0 & 0 & 0 \\ c_{13} & c_{33}-2c_{44} & c_{33} & 0 & 0 & 0 \\ 0 & 0 & 0 & c_{44} & 0 & 0 \\ 0 & 0 & 0 & 0 & c_{66} & 0 \\ 0 & 0 & 0 & 0 & 0 & c_{66} \end{pmatrix}$$

VTI and HTI symmetry are also referred to as polar and azimuthal anisotropy. It was found that the polar anisotropy can be as big as 30% while azimuthal anisotropy is small, in general, less than 10%.

It is common to describe VTI media in the use of Thomsen's five parameters which are defined as (Thomsen, 1986):

$$V_{p0} = \sqrt{\frac{C_{33}}{\rho}} \tag{2.4}$$

$$V_{s0} = \sqrt{\frac{C_{44}}{\rho}} \tag{2.5}$$

$$\varepsilon = \frac{C_{11} - C_{33}}{2C_{33}} \tag{2.6}$$

$$\delta = \frac{(C_{13} + C_{44})^2 - (C_{33} - C_{44})^2}{2C_{33}(C_{33} - C_{44})} \tag{2.7}$$

$$\gamma = \frac{C_{66} - C_{44}}{2C_{44}} \tag{2.8}$$

In the above equations, V_{p0} is the vertical P-wave velocity, V_{s0} is the vertical S-wave velocity, ε refers to the fractional difference in vertical and horizontal velocities of P-waves, γ refers to the fractional difference between vertical and horizontal velocities of S-waves. δ is a nonintuitive combination of elastic constants which controls the shape of the slowness surface at the intermediate angles. We can use the three parameters, ε, γ and δ, to define the strength of anisotropy. When all the three parameters become zero, the medium is isotropic. When ε and δ are both

much less than 0.2, the medium has weak anisotropy (Thomsen, 1986). It is observed that most marine sediments show weak anisotropy (Wang, 2002).

For HTI, the Thomsen's three anisotropy parameters are defined as:

$$\varepsilon = \frac{C_{33} - C_{11}}{2C_{11}} \tag{2.9}$$

$$\delta = \frac{2C_{66} + C_{13} - C_{11}}{C_{11}} \tag{2.10}$$

$$\gamma = \frac{C_{44} - C_{66}}{2C_{66}} \tag{2.11}$$

Note the definition of δ is a simplified version for weak anisotropy in these equations. These parameters can be measured from seismic data.

In most of this thesis, I will focus on HTI. I will also discuss converted wave imaging in a VTI medium in Chapter 5.

2.3.4 Orthorhombic

Nine independent elastic constants are required to describe a medium with orthorhombic symmetry. Such a medium has three mutually orthogonal symmetry planes. Typical examples of orthorhombic media include: a thin-layered sequence, e.g., shale, with a single set of vertical fractures or orthogonal sets of vertical fractures in it; a massive isotropic sandstone with orthogonal sets of vertical fractures in it.

2.3.5 Monoclinic

Monoclinic media contain a single plain of mirror symmetry and are described by 13 independent stiffness components. Due to the large number of independent parameters, it is very difficult to identify monoclinic anisotropy from seismic data. If a medium has no rotational symmetry except the trivial one which is 180^0 symmetry about the origin point, it is triclinic, and the full set of 21 stiffness constants is required to describe it.

2.4 Overview of multicomponent seismic

2.4.1 Multicomponent data recording

Recent advances in seismic technology, especially in the field of 4-component (4C) ocean-bottom-cable (OBC) data, have shown that the P-to-SV converted wave (or simply C-wave) can provide further valuable insight into earth properties compared to P-waves. This wave type is, due to its shear wave content, more sensitive to the internal structure of subsurface media than the pure P-wave and is easier to acquire and of better quality than pure shear wave data. Furthermore, it can be used to acquire dense 3D data in well-explored regions populated with producing platforms and pipelines which would make a streamer survey difficult.

Conventional surface seismic surveys record only P-waves, however, multicomponent seismic surveys record both P-waves and S-waves. This is realized by recording all components of the returning wavefield: each sensor within a multicomponent recording cable comprises three orthogonally oriented geophones for land acquisition, plus a hydrophone in marine acquisition. P-waves are recorded primarily by the Z-component geophone and the hydrophone, while S-waves are recorded primarily by the X- and Y-component geophones.

Land recording

Land multicomponent acquisition can utilize either conventional P-wave sources (dynamite or vibroseis) or S-wave sources, depending on the specific survey requirements.

Marine Ocean Bottom Cable (OBC) recording

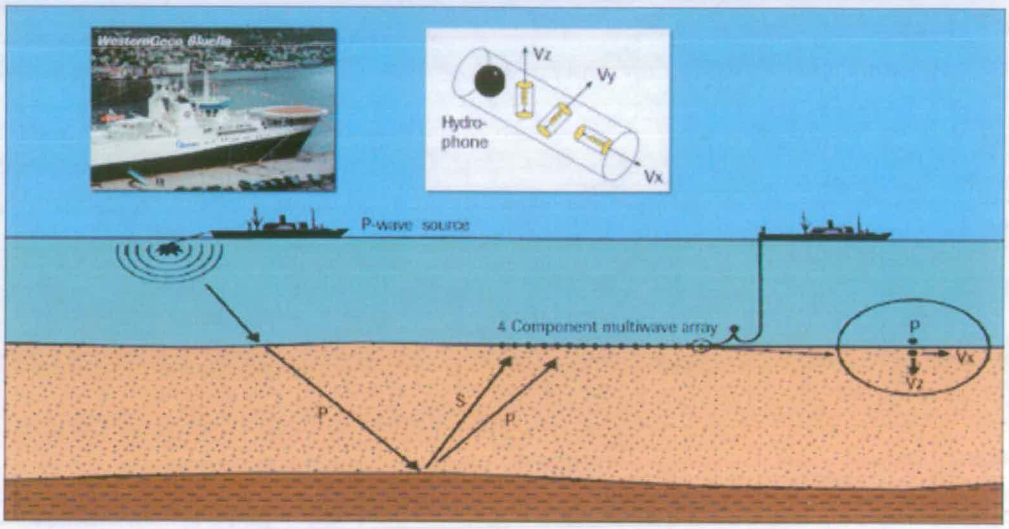

Figure 2.1: Outline of marine multicomponent acquisition (courtesy of WesternGeco).

Subsurface imaging is often improved through wide azimuth illumination, and multicomponent technology offers a cost effective means of acquiring such data in an offshore environment. Marine multicomponent acquisition operations typically consist of two or three vessels, one acting as a source vessel and the others as cable deployment and recording vessels. A seabed recording cable (Ocean Bottom Cable, or OBC) is required because S-waves cannot travel through water. The source vessel generates P-waves; however, at every interface, S-waves are reflected as well as P-waves. The receiver vessel positions the cable and remains stationary while the source vessel shoots either parallel to the OBC or perpendicular to it. At the end of the line the cable is moved and re-positioned. Converted waves are recorded using standard air-gun sources and receiver arrays deployed on the sea-floor. The receiver array is composed either of single nodes or, more often nowadays, of receivers

contained in OBC, which is easier to move and deploy. Due to the presence of a low velocity layer just below the water bottom, it is generally observed that the PP and the PS converted waves tend to separate. The low velocity layer causes the seismic raypath to be closer to the vertical, especially for the S-waves since they are normally slower. Thus PP waves are recorded on both the hydrophone and the vertical component of the geophone, and PS converted waves are recorded on the in line horizontal components. Figure 2.1 is schematic diagram of marine multicomponent acquisition.

2.4.2 Multicomponent applications

Multicomponent seismic technology can be applied to many seismic and geological challenges, including:

Improved imaging

S-waves have showed their capability when imaging areas where traditional P-waves have not obtained satisfactory results. Two typical situations include areas affected by gas clouds and areas with weak P and strong S acoustic impedance contrasts, so-called "transparent" reservoirs.

S-waves help clarify the subsurface image because they are less affected by pore fluids, an important attribute that can improve seismic imaging and highlight information valuable for reservoir characterization, reservoir monitoring, and well planning. However, P-waves are distorted and are slowed down while they pass through gas, resulting in amplitude dimming and "pull-downs". Gas clouds can block the main reservoir which is of exploration interest because they are often generated by gas escaping from the reservoir. The first multicomponent seismic in the North Sea aimed to solve the gas-cloud problem and obtained clear imaging success in the gas-affected areas even with some basic processing. Other well-known examples

include the Tommeliten Alpha field (Granli et al., 1999) and the Valhall field (Thomsen et al., 1997, Li et al., 2001), and the Lomond field (Pope et al., 2000).

The second case of improved imaging is in areas of low P-wave and high S-wave acoustic impedance. P-wave data have difficulty in imaging sand-shale sequences since the impedance contrast between them is usually small. Sometimes the S-wave acoustic impedance is much higher, resulting in a strong reflection so that using S-waves is advantageous. The Alba field (MacLeod at al., 1999) falls into this category and the final converted-wave (C-wave) image shows clear improvement in comparison with the P-wave one.

Fractured reservoir characterization

When a P-S conversion occurs at a reflector and the medium above the reflector is azimuthally anisotropic, the converted shear wave splits into a fast and a slow shear wave, and this is referred to as converted-wave splitting (Li, 1998). Multicomponent seismic data have been applied to study fractured reservoirs based on measurement of shear-wave azimuthal anisotropy. Analysis of shear wave splitting leads to fracture orientation (from the direction of the fast and the slow shear wave) and fracture density (from the time delay between the fast and the slow shear wave). There is a wide interest from industry to use converted-wave splitting to evaluate the internal architecture of hydrocarbon reservoirs. The splitting can be caused by the alignment of cracks, fractures, and small heterogeneities in the reservoirs. There is a vast amount of literature on the use of converted-wave splitting to characterize fractured reservoirs (e.g. Gaiser and Van Dok 2001; Granger *et al.* 2001; Vetri *et al.* 2003; amongst others).

Improved sub-salt illumination

Converted-waves (C-waves) have also been successfully applied to sub-salt imaging. It is believed the C-wave travel path offers better sub-salt illumination than the P-

wave travel path. A good example is in the Mahogany field (Kendall *et al.*, 1998) in the Gulf of Mexico. In this field the top and bottom salt reflectors and some potentially sub-salt reflector events were well imaged.

Direct hydrocarbon and lithology indication

Because S-waves can provide valuable insights into the nature of subsurface lithologies and pore-saturating fluids, highlighting reservoirs not previously visible using only P-waves, the joint use of S-wave and P-wave information enables lithology and fluid prediction. P-velocity on its own is not enough for distinguishing lithologies, for example a V_p of 4000 m/s could indicate gas-bearing sandstones, brine-bearing sandstones or shales. However, P and S-wave velocity ratios can be used for lithology discrimination and for fluid prediction, as shown, for instance, by Garotta *et al.* (2002).

Strong P-wave multiples

The combination of the signals recorded by the hydrophone and the Z-component geophone can help to reduce water-borne multiple contamination.

During production or injection, reservoir fluid saturation and pressure can change dramatically, S-waves can help monitor time-lapse variations and investigate quantitative saturation and pressure changes. Moreover, since methods such as pore-pressure prediction can highlight the presence of shallow gas, S-waves are also used to identify drilling hazards.

2.5 Fracture detection using multicomponent data

Fractures play an important part in reservoir development and enhanced oil recovery and it is of great significance to make a through investigation of fracture networks in

order to produce economical hydrocarbon. Fractured reservoirs act like anisotropic media on seismic waves travelling through them when the fracture dimensions are small in comparison to the seismic wavelength. There are fundamental differences between wave propagation in isotropic and anisotropic media (Crampin, 1977, 1981, 1985). A transverse isotropic medium with a vertical symmetry axis (VTI) is recognized as the equivalent medium for horizontal fractures, while a transversely isotropic medium with a horizontal symmetry axis (HTI) describes vertical fractures.

Natural fracture systems occur widely in the Earth's crust, and the detection of fracture distribution is an important part of reservoir assessment. Figure 2.2 shows some examples of natural fractures. Naturally-fractured reservoirs are an important component of the global hydrocarbon reserve and production base. It has long been recognized that the presence of naturally occurring fracture networks can lead to unpredictable heterogeneity within many reservoirs. Conversely, fractures provide high permeability pathways that can be exploited to extract reserves stored in otherwise low permeability matrix rock. In many parts of the world, including the Middle East and Mexico, fractured reservoirs account for the bulk of production. In other areas, such as the Rockies of North America, low permeability formations that were once considered unconventional hydrocarbon resources are now quickly becoming mainstream.

Techniques to investigate fracture properties include earthquake focal plane mechanisms, outcrop mapping, remote sensing imagery and airborne surveys, core analysis, borehole televiewer or formation logging and borehole stress evaluation from breakout logs, and so on. However, these techniques have limitations in providing fracture information of a 3D area at the depth of interest. Seismic reflection techniques based on anisotropic wave propagation theory have been shown to be very powerful and very valuable in investigating subsurface structure. Polar anisotropy and azimuthal anisotropy are the two basic concepts used by the oil and gas industry to characterize fractured reservoirs. Information on the horizontal fine

layering or fractures may be obtained from the analysis of polar anisotropy and information on vertical fractures may be provided from the analysis of azimuthal anisotropy. In particular, using either multicomponent seismic data or P-wave seismic data for an analysis of azimuthal anisotropy may give us the vertical fracture orientation and density information.

Figure 2.2: Examples of fracture presence in the wild.

A significant body of published work has developed establishing fracture-related seismic anisotropy as an observable effect. Crampin and his colleagues observed shear wave splitting when they carried out three-component studies of microearthquakes in Turkey in 1985. It is the first time theoretical phenomena of VTI or HTI media and the cracks and fractures in the Earth's crust are linked. Following this observation, a number of multi-component VSP seismic surveys (Johnston, 1986; Becker and Perelberg, 1986), surface-to-surface seismic reflection

surveys (Alford, 2000; Willies *et al.*, 1986), and multi-component surveys of microseismic events (Crampin, 1987) confirmed this phenomenon. Moreover, they also confirmed the wide existence of crustal seismic anisotropy with a horizontal symmetry axis in many different geological and tectonic regimes.

In terms of elastic constants, a fractured medium is often represented by equivalent medium theory. There are a number of fracture models. The Hudson model (Hudson, 1981) and the Thomsen model (Thomsen, 1995) are two widely accepted ones. Others commonly used include those of Hudson (1990), Hudson et al. (1996), Liu et al. (2000, 2000) and Schoenberg (1994, 1998).

The Hudson model assumes zero permeability and that there is no connection between cracks. It is therefore a high frequency theory in respect of fluid effects, while the wavelength has to be longer than the crack radius. In contrast, the Thomsen model assumes only low frequency seismic responses and allows fluid flow between interconnected cracks. It can have perfect permeability, which is similar to the Brown-Korringa's (1975) model. Using these two models, one can obtain the same fracture strike, but a different estimate of fracture density. However, for any given case, there is no clear advantage between the two models.

Much excellent work (Schoenberg and Sayers, 1995; Sayers and Kachanov, 1995; Pointer *et al.*, 2000) has been done to improve the above two models. On the other hand, fluid-filled permeable fracture models have attracted wide interest in recent years to improve fractured reservoir characterization (Hudson *et al.*, 1996; Tod, 2001; van der Kolk *et al.*, 2001; Chapman, 2003). Using a frequency dependent anisotropic model, the fracture radius may be potentially obtained (Chapman, 2003) and the saturation class may be distinguished (Chapman *et al.*, 2003).

2.5.1 P-wave responses

In recent years both theoretical studies and field data show that P-waves are rather sensitive to fractures. A set of P-wave attributes, such as azimuthal P-wave AVO, azimuthal traveltime or azimuthal moveout or velocity, may be used to invert for fracture information. In a medium containing fracture-related horizontal transverse isotropy (HTI), the AVO gradient (Chen, 1995; Ruger, 1996a; Ruger, 1996b; Teng and Mavko, 1996; Krasoves *et al.*, 1998; Li *et al.*, 1996), the NMO velocity (Sena, 1991; Tsvankin, 1995; Alkhalifah, 1996; Sayers and Ebrom, 1997) and the azimuthal travel time (Schoenberg *et el.*, 1991; Kendall et al., 1998; Li, 1997; Li, 1999) show elliptical variation with azimuth. This feature forms the basis of many P-wave techniques for fracture detection (MacBeth, 1990; Mallick *et al.*, 1996; Grechka and Tsvankin, 1998; Li, 1999).

To demonstrate the P-wave responses in a HTI medium, a numerical calculation for a three-layer model is shown in Figure 2.3 after Liu (1999). The first layer is composed of an isotropic medium, and the second and third layers are composed of anisotropic media (Table 2.1). The x-axis is aligned parallel to the fracture strike. Through solving the Kelvin-Christoffel equations (Helbig, 1994), the amplitude, slowness (inverse of the velocity) and travel time of all three body waves in every direction can be calculated. The above numerical results confirm that for fracture related azimuthal anisotropy, the three P-wave attributes which are associated with layer 2, as illustrated in Figure 2.4, show near-elliptical variations with azimuth. Moreover, the major axis of the ellipse points along the fracture strike, and the ellipticity indicates the fracture intensity.

To gain insight into how the variation of a particular physical parameter affects the overall trend of seismic attributes, analytical expressions are formed based on Thomsen (1986) for weak anisotropy (Rüger, 1996a, 1996b; Tsvankin, 1997; Li, 1997, 1999). The resulting formulae can be generalized to capture all of the

azimuthal variations for the three P-wave attributes, amplitude, slowness and traveltime:

$$F(\theta,\phi) = A(\theta) + B(\theta)\cos 2\phi + C(\theta)\cos^2 2\phi \qquad (2.12)$$

where $F(\theta,\phi)$ represents either the P-wave amplitude, the inverse of the squared NMO velocity ($1/v_{NMO}^2$), or the travel time. θ is the incidence angle, ϕ is the azimuthal angle measured from the fracture strike, and $A(\theta)$, $B(\theta)$ and $C(\theta)$ are azimuthally invariant coefficients.

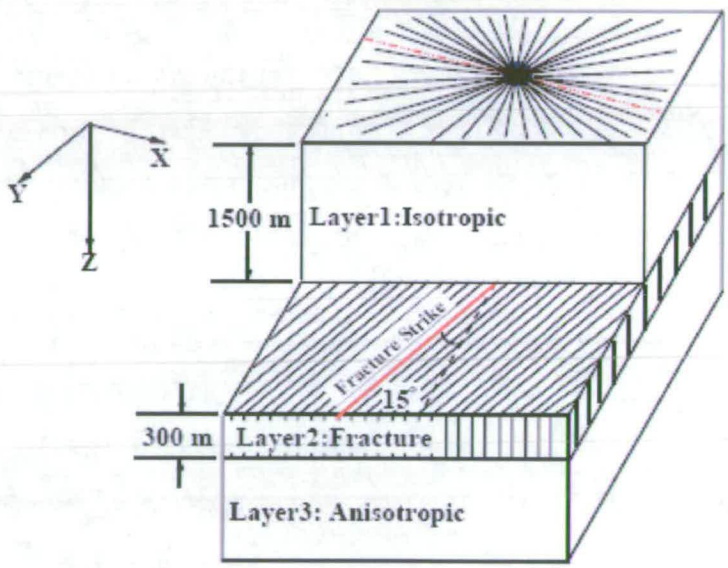

Figure 2.3: Three-layered model used in this study. Layer 1 is isotropic and layer 2 contains aligned fractures giving rise to HTI (after Liu, 1999).

Layer 1: Isotropic	ρ=2.3 g/cm^3, V_p = 3048m/s, V_s = 1574m/s
Layer2: Anisotropic	ρ=2.19 g/cm^3, V_p = 2183m/s, V_s = 1502m/s Aspect ratio: 0.01, Crack density: 10%
Layer3: Anisotropic	ρ=2.0 g/(cm*cm*cm) $\begin{bmatrix} 10.0 & 3.5 & 2.5 & -5.0 & 0.1 & 0.9967 \\ & 8.0 & 1.5 & 0.29 & -0.90 & -0.15 \\ & & 6.0 & 1.0 & 0.42 & 1.5 \\ & & & 5.0 & 0.45 & -0.3532 \\ & & & & 3.0 & -1.0 \\ & & & & & 3.0 \end{bmatrix}$

Table 2.1: The elastic parameters of the model in Figure 2.1.

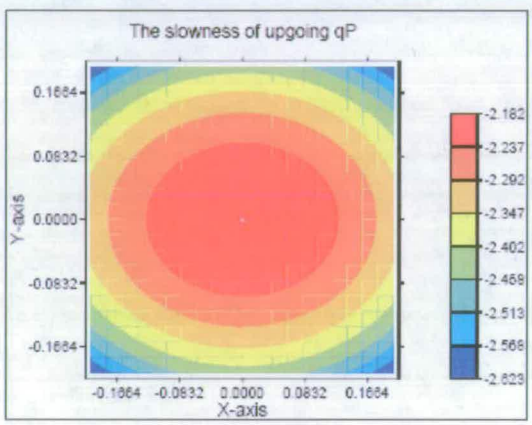

(a)

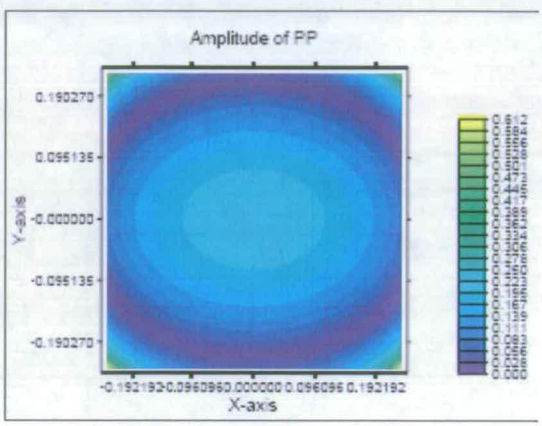

(b)

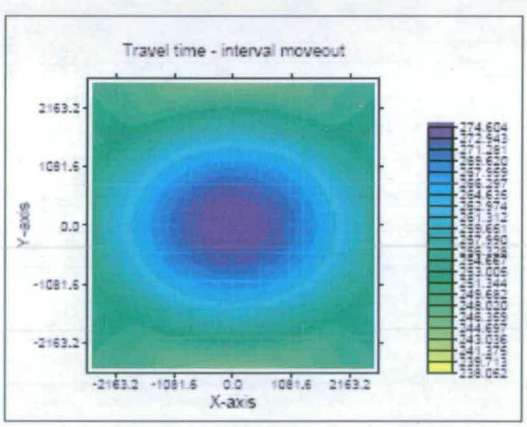

(c)

Figure 2.4: Azimuthal variations of (a) vertical slowness in layer 2, (b) amplitude at the interface between layers 1 and 2, and (c) interval travel time for layer 2 (bottom minus top). The X- and Y -axes represent horizontal slowness along those axes (after Liu, 1999).

2.5.2 Using P-waves for fracture detection

For 3D data acquired with wide azimuthal coverage, four types of attributes, traveltime, amplitude, velocity and AVO gradient, may be used to study azimuthal anisotropy for fracture detection. Two methods (narrow-azimuth stacking and full-azimuth surface fitting) can be used to extract the fracture information. The first method is to sort the data into narrow azimuth bins and then perform an azimuthal bin-stack to reduce the number of azimuths to a few selected azimuths. The second method fits an elliptical surface of $\cos 2(\varphi - \Phi)$ and $\cos 4(\varphi - \Phi)$ to data from all available azimuths and offsets by a least-square fitting technique.

There are several successful case studies which have used P-waves for fracture detection. Here I show one example of this technique. The study area is in the Yellow River delta in East China and most of the area is known to be heavily faulted. The target is fractured mud-rock and oil production mainly relies on the knowledge of fracture information (Li *et al.*, 2003). After data preprocessing, test processing, a full-field processing and analysis is made in the use of the surface-fitting method and the interval traveltime attribute. The final fracture intensity map (Figure 2.5) shows that along the faults the fracture intensity seems to increase. It compares reasonably well with the fault and fracture pattern in the area.

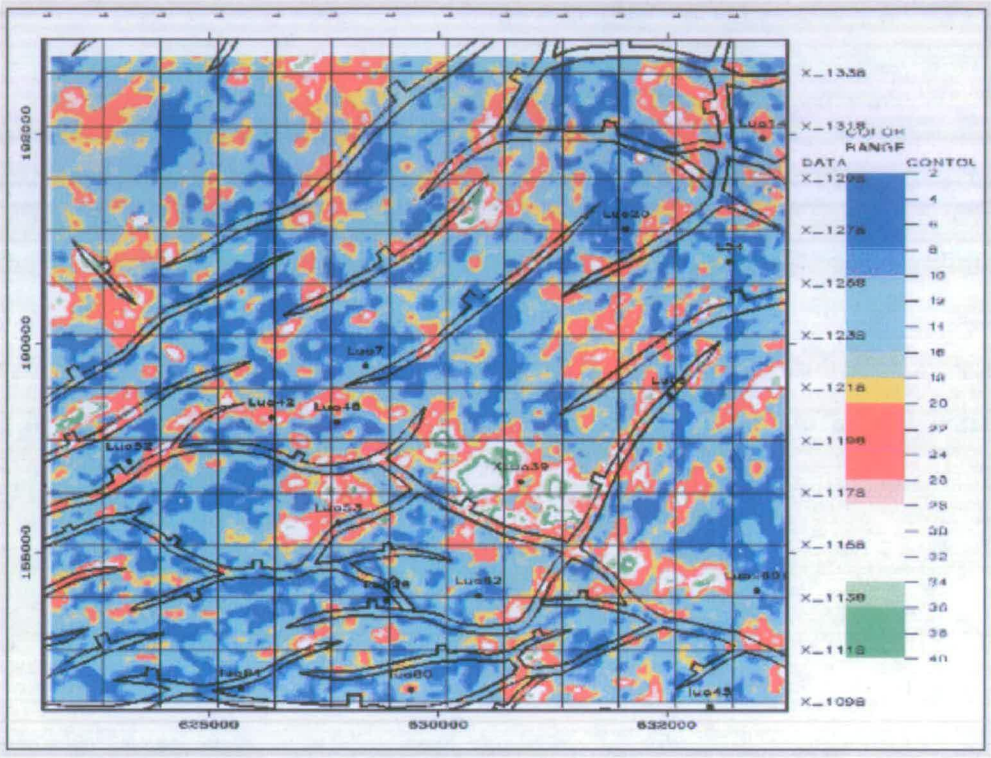

Figure 2.5: Fracture intensity map from the Yellow River Delta, China (Li, et al., 2003).

2.5.3 Shear-wave splitting

The observation of shear-wave splitting in field data was a significant advance in the application of anisotropy to exploration (Crampin and Booth, 1985). In its very early stages, the shear wave splitting analysis method relied upon direct excitation and recording of shear waves in land multicompent acquisitions (Mueller, 1991; Li, 1998). Shear wave splitting is most observable and is greatest in HTI media at vertical incidence so that the method is suitable to near-offset VSP and post-stack surface seismic.

2.5.4 Using S-waves for fracture detection

As a result of azimuthal anisotropy, S-waves usually split into two waves, a fast (s1) and a slow (s2) mode, and these provide information on fracture density and orientation (e.g. Winterstein and Meadows, 1991a, 1991b). For near-vertical propagation the S1 polarization is parallel to the fracture strike, whereas the increase in time delay with depth is a measure of the magnitude of azimuthal anisotropy which is determined by fracture density. Shear-wave splitting analysis can be used to gain more insight of rock anisotropy and it is widely used to provide information about the internal structure of a reservoir (e.g. Crampin, 1985; Willis *et al.*, 1986; Winterstein and Meadows, 1991a; MacBeth et al., 1992; Li and Crampin, 1993; Li, 1997).

2D rotation analysis for P-S wave

In case of 2D acquisition over horizontally stratified media with uniform azimuthal anisotropy, further assume a P-S raypath with the conversion point at the reflector, and a displacement vector confined to the horizontal plane, ϕ representing the polarization azimuth of the fast shear wave (Figure 2.4), the recorded radial and transverse components can be written as,

$$\begin{pmatrix} V_r(t) \\ V_t(t) \end{pmatrix} = \begin{pmatrix} \cos\phi & -\sin\phi \\ \sin\phi & \cos\phi \end{pmatrix} \begin{pmatrix} S_1(t) \\ S_2(t) \end{pmatrix} = R(\phi) \begin{pmatrix} S_1(t) \\ S_2(t) \end{pmatrix} \tag{2.13}$$

where $R(\phi)$ is the 2D rotation matrix, and $S_1(t)$ and $S_2(t)$ represent the amplitudes of the fast and slow waves respectively. Assuming that the fast and slow shear-waves have similar waveforms with only a time delay Δt, $S_1(t) = S(t)$, $S_2(t) = S(t - \Delta t)$, the above equation can be solved by rotation analysis based on an objective function which measures the similarity of the two waveforms. Rotating the radial and

transverse components with an angle α gives the rotated components $R_{vr}(\alpha,t)$ and $R_{vt}(\alpha,t)$ as,

$$\begin{pmatrix} R_{vr}(\alpha,t) \\ R_{vt}(\alpha,t) \end{pmatrix} = R^T(\alpha) \begin{pmatrix} V_r(t) \\ V_t(t) \end{pmatrix} \tag{2.14}$$

An objective function $F(\alpha,\tau)$ may be defined as,

$$F(\alpha,\tau) = \sum_t R_{vr}(\alpha,t) R_{vt}(\alpha,t+\tau) \tag{2.15}$$

Thus, the optimization process is to search for a rotation angle $\alpha = \phi$ and time shift $\tau = \Delta t$, which maximizes $F(\alpha,\tau)$. MacBeth and Crampin (1991) give a good review of this kind of technique. For processing land converted waves, Donati and Brown (1995) introduced the cross-correlation sum of the radial and transverse components as the objective function.

In Chapter 8 I further develop the technique of 2D rotation in the use of PS-waves. The method I use includes two main steps: rotation scanning to obtain the fast split shear polarization and time-delay spectra for picking time delays between the faster and the slower shear wave. This approach has been successfully applied in an onshore multicomponent data set.

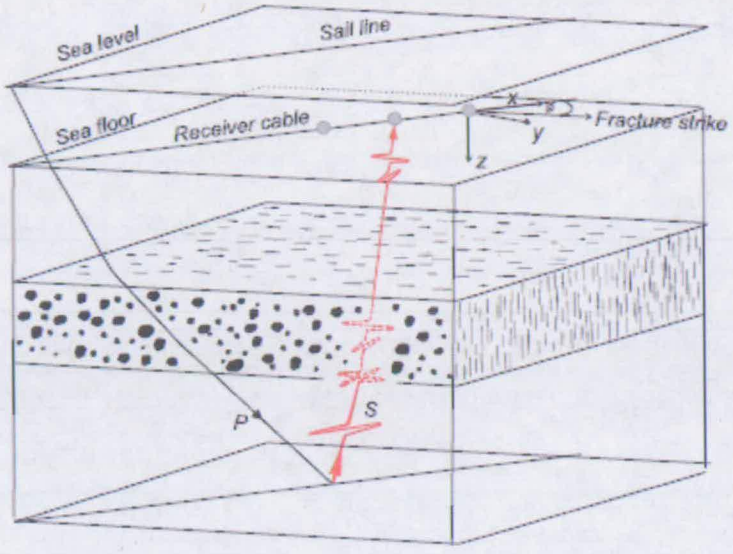

Figure 2.6: Converted shear-waves in 3C sea-floor seismic acquisition over fractured media. The survey line is at angle ϕ to the fracture strike, and a conversion at the reflection point is assumed (Li, 1998).

Azimuthal rotation for 3D data

Various techniques have been developed for shear-wave splitting analysis with the aim to identify the azimuth of the S1 and S2 polarizations and the time delay between them. Alford rotation (1986) is a widely used method for separating "fast" and "slow" split waves for a variety of multicomponent seismic data. With an assumption of a homogeneous medium between sources and receivers and independently propagating pure modes, Alford (1986) gave the following equation for the linear convolution model:

$$D(t) = [R^T(\theta_G)\Lambda(t;t_f,t_s)R(\theta_S)] * S(t) \qquad (2.16)$$

where D(t) is the 4-component data matrix of the displacement recorded at the two horizontal geophone component and S(t) is the matrix of the two orthogonal shear-wave horizontal sources,

$$D(t) = \begin{pmatrix} d_{xx} & d_{xy} \\ d_{yx} & d_{yy} \end{pmatrix} \tag{2.17}$$

$$S(t) = \begin{pmatrix} s_x & 0 \\ 0 & s_y \end{pmatrix} \tag{2.18}$$

The Alford model assumes two orthogonal pure-shear modes, such as might occur for a zero-offset experiment over a horizontally layered vertically fractured earth, or for a crossed dipole survey through a transversely isotropic earth. Although this model assumes zero-offset propagation, in practice, it has also worked well for finite offsets. The application of the rotation matrix $R(\theta)$ describes rotation of the source vectors into the polarization direction of S1 and S2 and then back again into the geophone directions. The operator $\Lambda(t;t_f,t_s)$ extrapolates the S1 and S2 wave modes from the source to the receiver where they have arrival times t_f and t_s.

$$R(\theta) = \begin{pmatrix} \cos\theta & \sin\theta \\ -\sin\theta & \cos\theta \end{pmatrix} \tag{2.19}$$

$$\Lambda(t;t_f,t_s) = \begin{pmatrix} \lambda_f & 0 \\ 0 & \lambda_s \end{pmatrix} \tag{2.20}$$

If the data are rotated into the coordinate system of the S1 and S2 polarizations the off-diagonal energy should become zero. A solution of Eq. 2.16 therefore finds the angles θ_G and θ_S that minimize off-diagonal components of the matrix

$$\Lambda(t;t_f,t_s) * S(t) = R(\theta_g) D(t) R^T(\theta_S) \tag{2.21}$$

In the years since Alford's method was published, several generalization of Alford rotation have been proposed to perform this process. All of these methods are consistent for the original Alford geometry, but can produce different results for more general data.

In the early stages, the optimum angle was found by scanning through a range of θ-values and performing numerical rotation of the recorded data matrix (Alford, 1986; Thomsen, 1988). Naville (1986) and Nicoletis *et al.* (1988) adopted a similar rotation procedure, but minimized off-diagonal elements in the propagation matrix. Murtha (1989) developed an analytical expression for a rotation angle in a specified time-window. MacBeth and Crampin (1991a) minimized the spectral interference of two split shear waves in the frequency domain. MacBeth and Crampin (1991b) adapted the independent source-geophone rotation technique of Igel and Crampin (1990) to an exploration context. However, their methods require intensive computations.

Li and Crampin (1993) present a fast linear transform technique for analyzing shear-wave splitting in four-component seismic data, which is flexible and widely applicable. The technique transforms the four-component data by simple linear transforms so that the complicated shear-wave motion is linearized in a variety of circumstances. It allows various attributes to be measured, such as the polarizations of faster split shear waves and the time delays between faster and slower split shear waves, as well as allowing the time series of the faster and slower split shear waves to be separated deterministically. Moreover, with minimal assumptions, the geophone orientations can be estimated for zero-offset vertical seismic profiles (VSPs), and the polarizations of the slower split shear waves can be measured for offset VSPs. The time series of the split shear-waves can be separated before stack for reflection surveys. The technique has been successfully applied to a number of field VSPs and reflection data sets. Another technique of efficient algebraic solutions is given by Zeng and MacBeth (1993), which also allows the condition that sources and geophones are aligned to be relaxed. These algebraic solutions are based upon a convolutional model for shear waves propagating through an anisotropic model.

In 2001, Dellinger et al. developed a generalized rotation technique, namely "tensor rotation", for the case that the S1 and S2 polarizations measured at the two horizontal receiver components are not orthogonal. The tensor rotation uses a (2 X 2) matrix of

the horizontal vector data, not just the radial component. The matrix is exactly analogous to the (2 X 2) matrix produced by conventional multicomponent land shear-wave processing, but with the C-wave source-azimuth vector filling the role of the S-wave source polarization vector. However, unlike the orthogonally polarized pairs of balanced sources used in traditional land S-wave acquisition, the C-wave source-azimuth distribution is typically not uniformly sampled in azimuth, creating a bias that must be accounted for in the algorithm. Once this has been done, however, the fast and slow directions can then be determined via Alford rotation of the tensor image in the usual way.

In Chapter 6 I present a detailed analysis of 3D fracture detection using the Emilio dataset. I develop programs in the Seismic Unix format to apply the linear transform technique for OBC reflection survey.

2.6 Summary

The stiffness tensor structure is determined by anisotropic symmetry systems and it can used to derive the variation of the elastic response with propagation direction of seismic waves. In a HTI medium, P-wave propagation characteristics show elliptical variations in the horizontal planes. The directions of long and short axes indicate the fracture strike and normal and the ratio between them is proportional to the fracture density. These features of P-waves lay a foundation for the determination of fracture properties, which are of importance for the economical production of oil and gas. Analysis of shear-wave splitting yields the symmetry directions and the degree of anisotropy. Multicomponent seismic data have been widely used for fractured reservoir characterization.

Chapter 3

The Emilio field and data acquisition

3.1 Introduction

In this Chapter I give a brief introduction to the Emilio field and the Emilio dataset, which are used throughout this thesis. The study area is a gas-oil reservoir in the central part of the Adriatic Sea that resides in Eocene carbonate rocks characterized by low primary porosity and fractures. A detailed overview of the acquisition design procedures is given and the data characteristics are examined. In addition to this offshore 3D/4C dataset, I also analyse another onshore 2D/4C dataset, as described in Chapter 8.

3.2 The Emilio field

The Emilio field is located in the central part of the Adriatic Sea, close to the eastern coast of Italy (on the right of Figure 3.1). The target of the Emilio field is the Top Paleocene at the depth of 2850m, as seen in the black rectangle on the left of Figure 3.1.

As shown in the structural model (Figure 3.2), the Emilio Field is in a highly complex structural area with a number of folds and faults. The main structure in the reservoir is associated with an anticline formed by east-west compression. On top of the reservoir, there is a very pervasive Gessoco Solfifera reflector with a strong reflective behaviour for both PP and PS waves. On the left of Figure 3.2, an acoustic log collected in the area shows clear evidence of this behaviour. There is gas present in the shallowest part of the reservoir, the Scaglia Formation (Figure 3.2) (Vetri, 2003).

The lithology in this area includes sands, shales, and evaporates in the overburden, and limestones at the target. A number of wells were drilled into the reservoir recently. Much information about fracture properties in the reservoir was obtained from borehole data through the analysis of breakouts, induced fractures and cores.

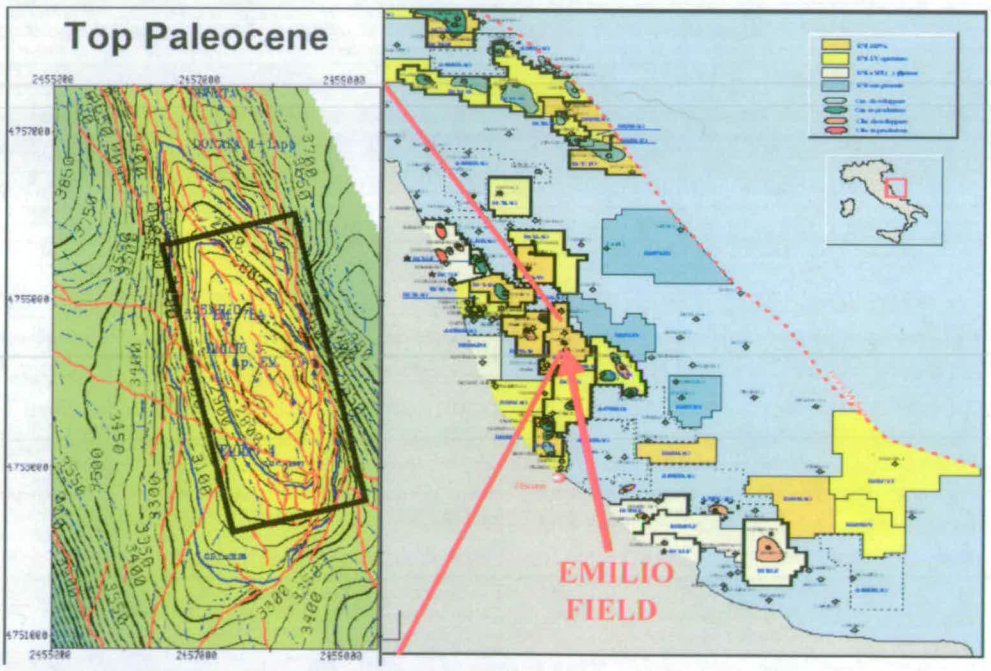

Figure 3.1: The Emilio field is located in the central part of the Adriatic Sea and the target is the Top Paleocene at a depth of 2850m.

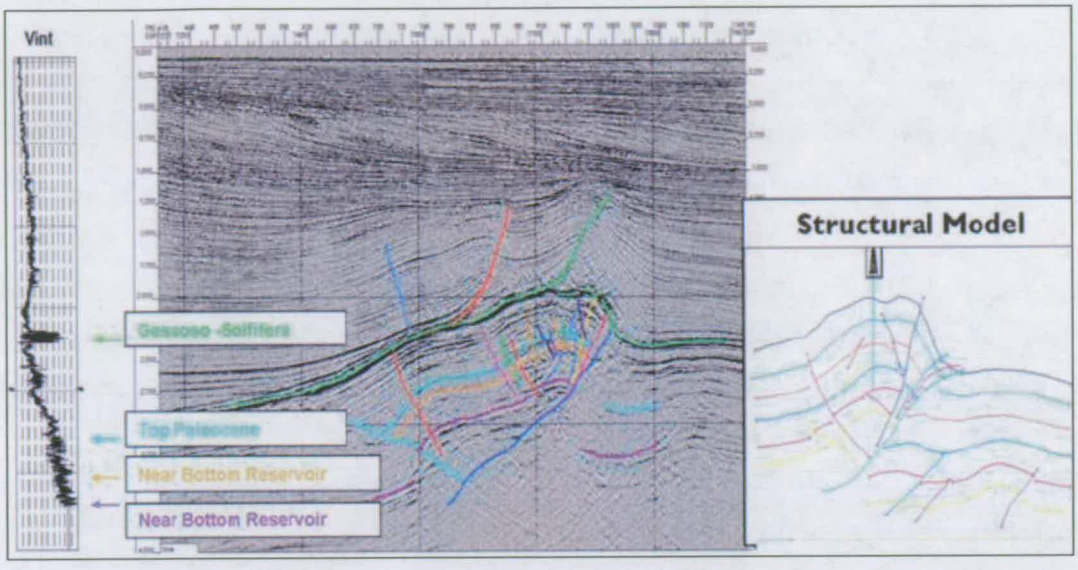

Figure 3.2: Emilio reservoir interpretation together with one of the acoustic logs acquired in the area (left) and a structural model (right) (after Vetri *et al.*, 2003).

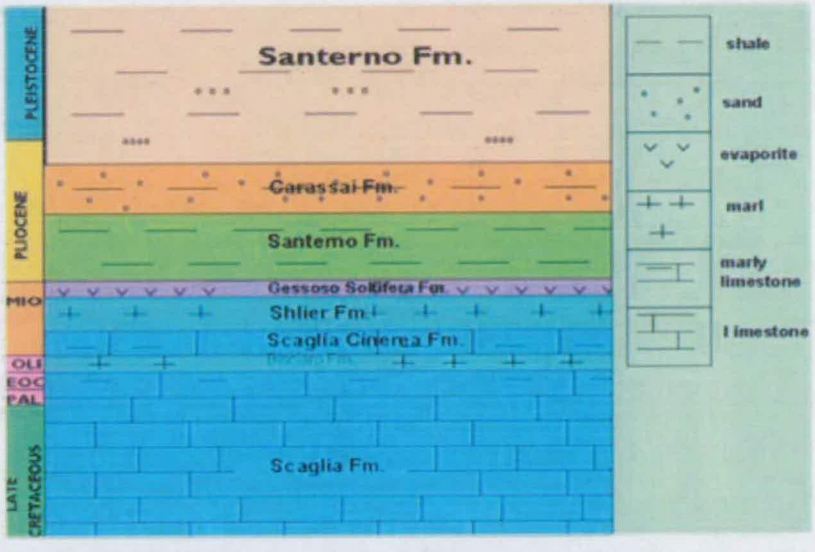

Figure 3.3: A typical lithology column map from the Emilio field (Vetri *et al.*, 2003).

3.3 Acquisition design

The 3D/4C survey in the Emilio field was planned for both the short and long term targets. The short-term targets were reservoir production improvement, to minimize dry-hole risk and to increase proven reserves; the long term ones were reservoir fluid monitoring (4D) and field life extension by planning an optimized enhanced recovery. In order to match these aims a 3D/4C acquisition methodology was chosen. The feasibility study and the acquisition parameters design were much more critical and complex than in traditional surveys. Different types of data were used: borehole information (logs, cores etc), production profiles and preexisting 3D seismic were analyzed for generating a reliable earth model; then PS anisotropic and P-PS isotropic modelling were performed.

3.3.1 Reconnaissance data

The first part of the study was the collection of non-seismic reconnaissance data, which included geological studies, core sample analysis, and borehole and production logs interpretations. The main purpose of this information is to achieve a detailed reservoir physical model with which to plan the survey. Moreover, reconnaissance data are useful to determine an approximate Vp/Vs ratio from VSP, sonic or density logs for successive modelling. The core sample analysis (Figure 3.4) represented the first part of the study: it aimed to characterize all the features that could play a role in generating seismic anisotropy. The position, density, dip and type of filling were accurately checked on the cores extracted in the wells Emilio 5 and Emilio 3. However, at this stage it was impossible to identify fracture azimuthal directions because the assessed samples were not oriented. At the end of the study of the reconnaissance data, as a result, it was observed that highly fractured zones were present at the target level (Top Paleocene) and that the open cracks were mainly subvertical which result in an HTI medium. These data suggest the existence of two

orthogonal fracture sets oriented ENE and NNW, and that the presence of dipping fractures should be considered (Angerer *et al.*, 2002) (Figure 3.5).

From borehole data (log, dipmeter, FMS) it was possible to get information on structural features and on the horizontal in-situ stress; the determination of this parameter is important because it is related to the direction of open fractures, since their strike is usually parallel to the maximum horizontal stress direction. In order to estimate the dips of the layers, the dipmeter responses of five wells were examined; a gentle slope of 15 degrees (average) towards the West was observed (this could have effects on azimuthal anisotropy). The study to determine the orientation of the principal axis of the stress required the use of both dipmeter (Emilio 4) and FMS tools (Emilio 7); from dipmeter data a breakout analysis was performed, while from FMS images, drilling induced fractures were investigated. The merging and averaging of all the information led to an inferred minimum stress direction of approximately $N350^0$, thus indicating a possible open fracture direction of $N80^0$ (Figure 3.6).

A further step for acquiring useful details on the field was the inspection of production profiles; it appeared immediately evident that the Emilio reservoir produces both through fractures and primary porosity.

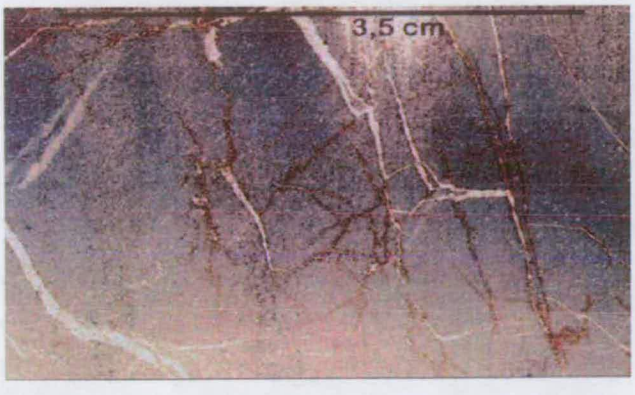

Figure 3.4: Reconnaissance data that show evidence of fracturing from core samples.

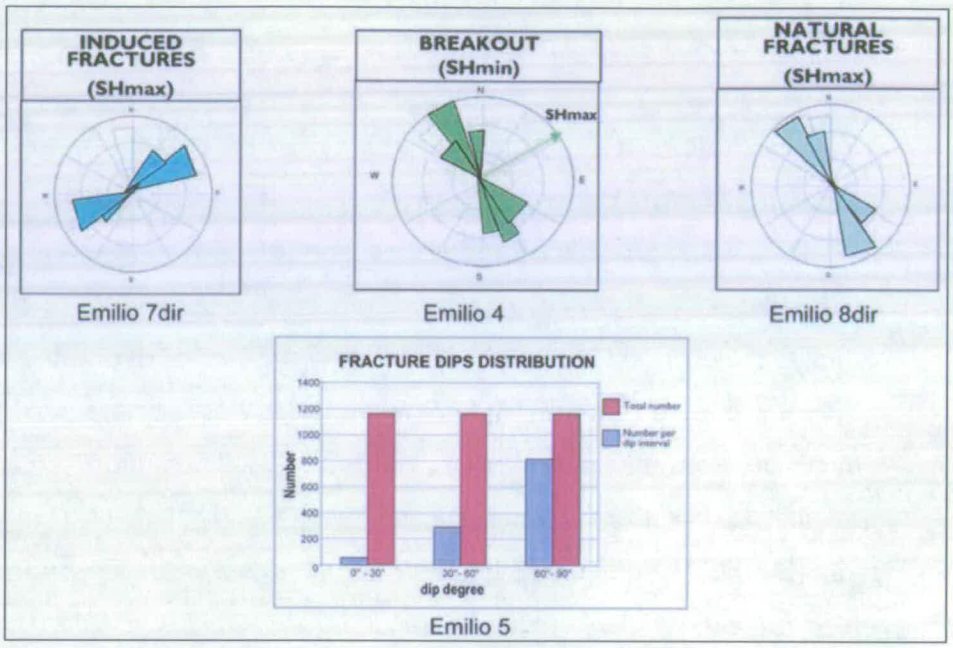

Figure 3.5: Information about fractures and SHmax azimuth collected from Emilio borehole data. Indications of two orthogonal fracture trends are evident. The analysis of bottom cores in well Emilio 5 reveals the presence of subvertical fractures (Vetri *et al.*, 2003).

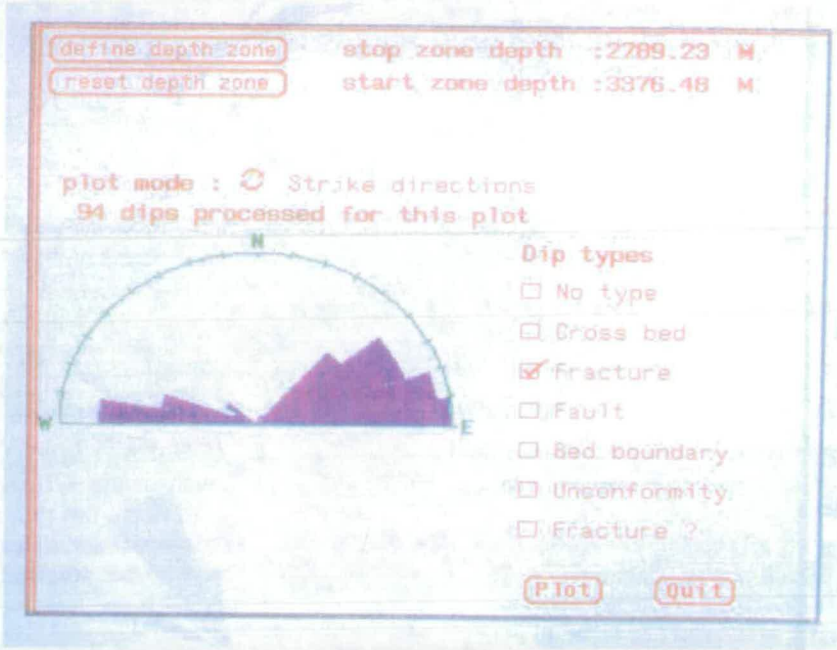

Figure 3.6: Reconnaissance data show direction of induced fractures (from FMS).

3.3.2 Preexisting 3D seismic

The second part of the study was a detailed investigation on preexisting seismic data. The aim was to collect information on general seismic quality in the area and related problems, give a preliminary estimation of survey parameters (frequency, bin-size etc), and approximately evaluate anisotropy from P wave attributes.

Preexisting seismic data on Emilio field consists of two 3D surveys; the last one was shot in cross-shooting mode, i.e., the same area was shot both in dip and strike directions. It was an optimum candidate for checking anisotropy along near minimum (strike volume) and maximum (dip volume) horizontal stress directions. From the comparison between the two seismic volumes at target level it was possible to highlight differences both in frequency and in velocity; these differences were maximum (up to 10%) on producing well locations and minimum on dry (tight) ones (Emilio 4), thus confirming a possible relationship with open fractures. It became also apparent that the magnitude of the inconsistencies between the two volumes was high near the crest of the Emilio's structure and low on the flanks (Figure 3.7); this phenomenon reinforced the idea of a connection with crack density (expected maximum near the crest). It should be noted that contrarily to frequency and velocity it was impossible to extract useful information on possible anisotropy from seismic amplitude.

As a general comment on the preexisting seismic data, it can be noticed that the reflectivity and the signal to noise ratio in the area (with conventional seismic) is high, also the frequency content, thus encouraging the acquisition of a converted waves survey.

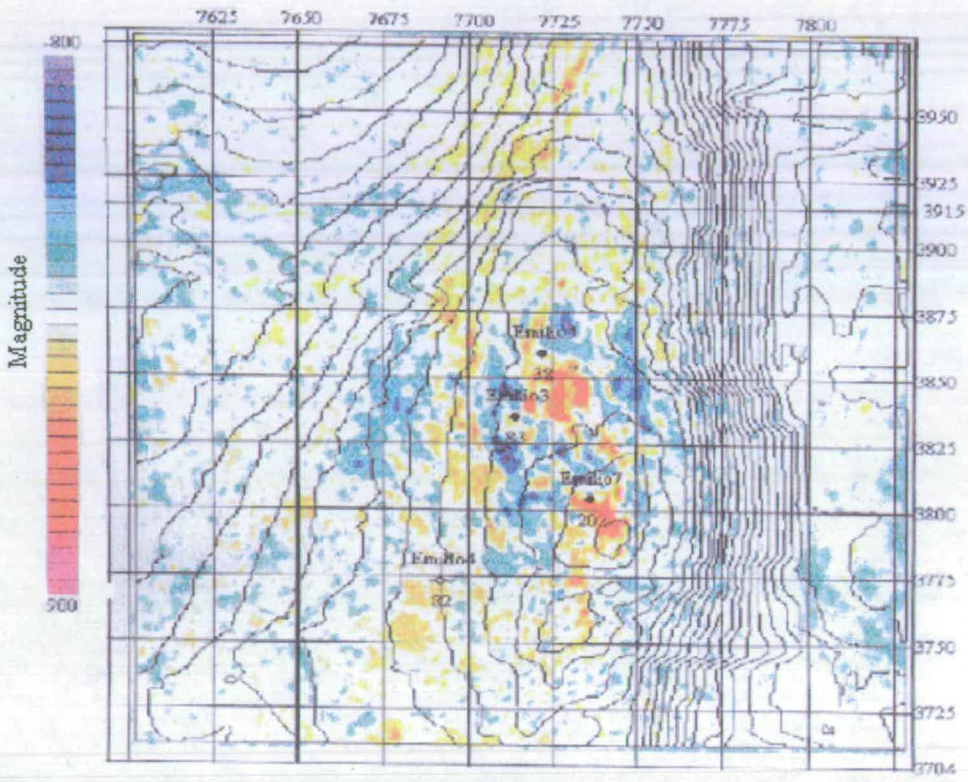

Figure 3.7: Preexisting seismic magnitude difference map at Top Paleocene. Note that the magnitude difference was high on producing well locations, near the crest of the Emilio's structure, and low on dry holes (Emilio 4), the Emilio's flank (courtesy of ENI-Agip).

3.3.3 1D anisotropic modelling

The third part of the feasibility study was the 1D anisotropic reflectivity modelling. The aim of this step consisted of predicting azimuthal anisotropic effects on S waves (splitting) and optimizing the acquisition geometry and processing strategies. A PS frequency estimate at target level was also attempted. In order to perform the above modelling a 1D anisotropic earth model was created (Table 3.1) on which a full azimuth 3D synthetic survey was shot. The velocity anisotropy percentage was extracted from the preexisting seismic analysis, and the layers of the model and relevant fracture directions from reconnaissance data. The resultant seismic was

Thickness,m	Pvel	Svel	Density	% ani
100	1500	-------	1	----
800	2040	907	2	----
800	2815	1440	2.1	----
550	3080	1588	2.15	10
750	3515	1893	2.4	8
1000	4800	2462	2.6	7
4000	5300	2718	2.8	----

Table 3.1: 1D anisotropic earth model (after Buia *et al.*, 2001).

processed and rotated into radial and transverse directions. The synthetic seismograms of Fig. 3.8 demonstrate that large amplitudes in the transverse component of the reflected shear wave are generated at intermediate offset when shooting perpendicular to the direction of anisotropy in the reflecting medium (in this case layer 4). Note that there is a polarity reversal in trace 3 because it is near the critical angle. If the properties of the medium are not known in advance, it is therefore important to shoot at a range of azimuths and offsets, otherwise the strong reflection off layer 4 shown in the transverse component of Fig 3.8 will not be seen, and the best diagnostic of seismic anisotropy will be missed.

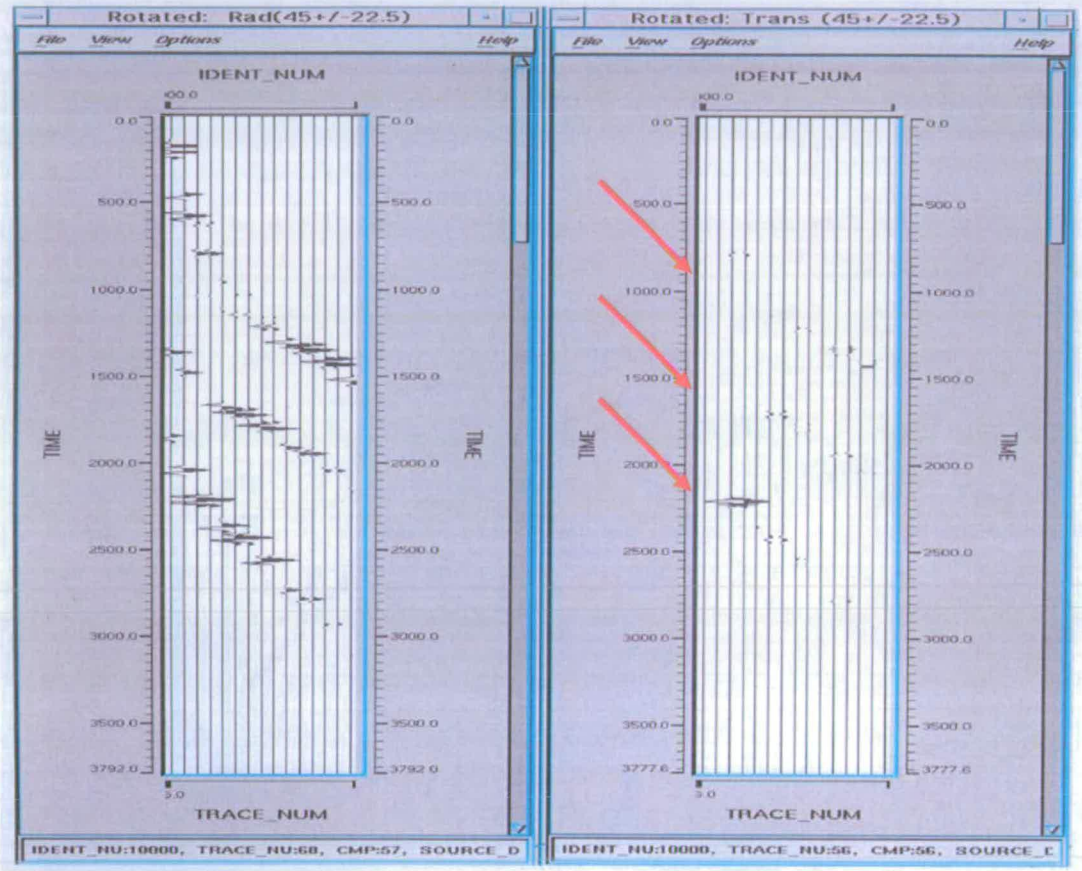

Figure 3.8: Synthetic seismograms for the radial (left diagram) and transverse (right diagram) components corresponding to reflections at increasing offset (expressed by the trace number) for shot-receiver pairs oriented in a direction orthogonal to the long axis of the shear-wave anisotropy in layer 4 for the Earth model of Table 3.1 (after Buia et al., 2001). The red arrows indicate the expected arrival time for shear waves at near zero offset for the first three reflections expected from Table 3.1. The first two reflections are negligible but the third has a large amplitude on Trace 3 that can be used as a diagnostic of anisotropy in layer 4.

3.3.4 2D and 3D isotropic modelling

The fourth part of the feasibility study consisted of 2D and 3D isotropic ray-tracing modelling. The aims of this step were both to perform the final estimation of acquisition parameters and to assess the target illumination. In order to perform the 2D ray tracing, a 2D isotropic velocity model was created from a previous prestack depth migration and then a synthetic 2D-4C survey was shot over it and processed. The shear wave velocities for the model were calculated from reconnaissance data. Modelled 2D P and PS CMP/CCP gathers were produced, together with the relevant stacked sections (Figure 3.9). It was immediately clear from the simulated PP and PS gathers and sections that structural effects were very significant on the crest of the Emilio reservoir structure. The most important parameters calculated making use of 2D modelling were the following: PP/PS maximum reflection time, PP maximum offset and PS min/max offset.

The 3D modelling was used for evaluating the migration border at target level; all the depth horizons, with relevant velocity, were loaded into the software and then demigrated thus permitting the evaluation of the necessary extension of the survey. Furthermore 3D ray tracing was performed on the target depth horizon (Top Paleocene) in order to assess the illumination and the conversion point scattering in case of dip (Figure 3.10) or strike cable orientation; it was seen that strike cable orientation provided a better and more homogenous conversion point distribution in the subsurface thus creating a better stacked section.

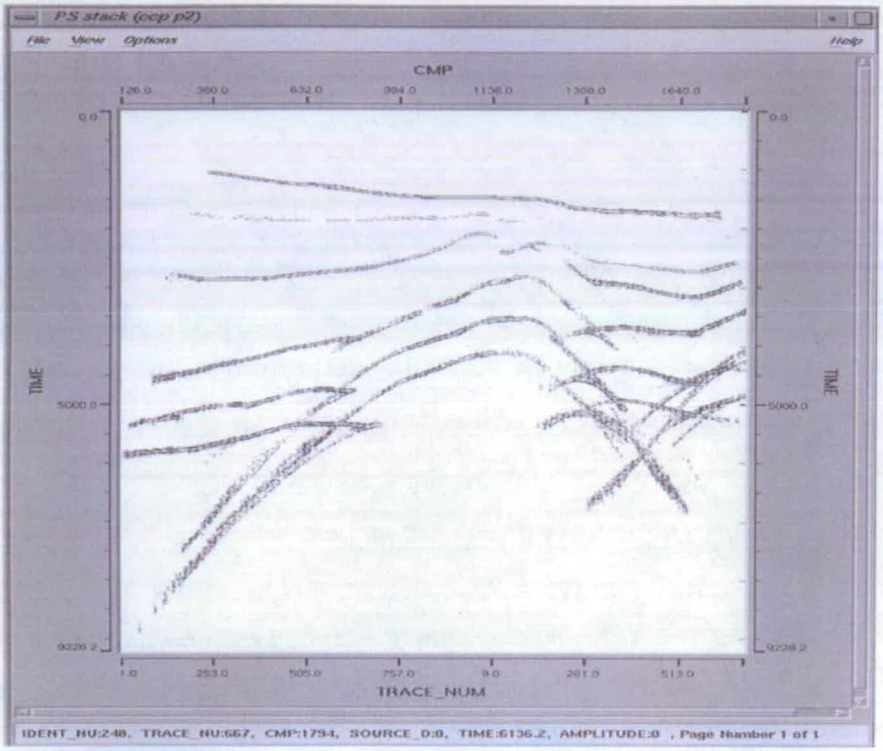

Figure 3.9: PS synthetic stacked section from 2D isotropic modelling (Buia *et al.*, 2001).

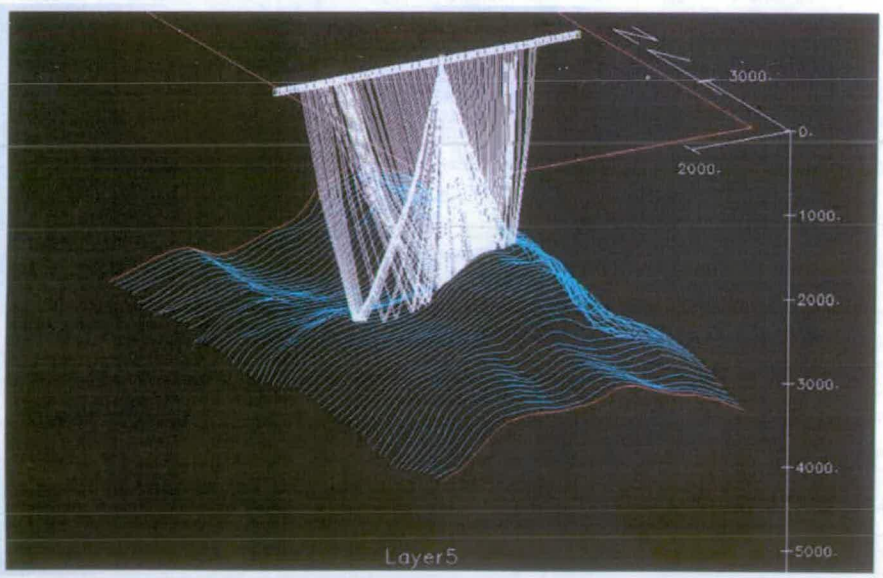

Figure 3.10: PS synthetic stacked section from 3D isotropic modelling (Buia *et al.*, 2001).

3.3.5 Source configuration

The last part of the study was the source directivity optimization; a source array was created to achieve isotropic energy spreading in all directions; this was designed and checked by creating synthetic plots of energy vs. azimuth at various frequencies (Figure 3.11).

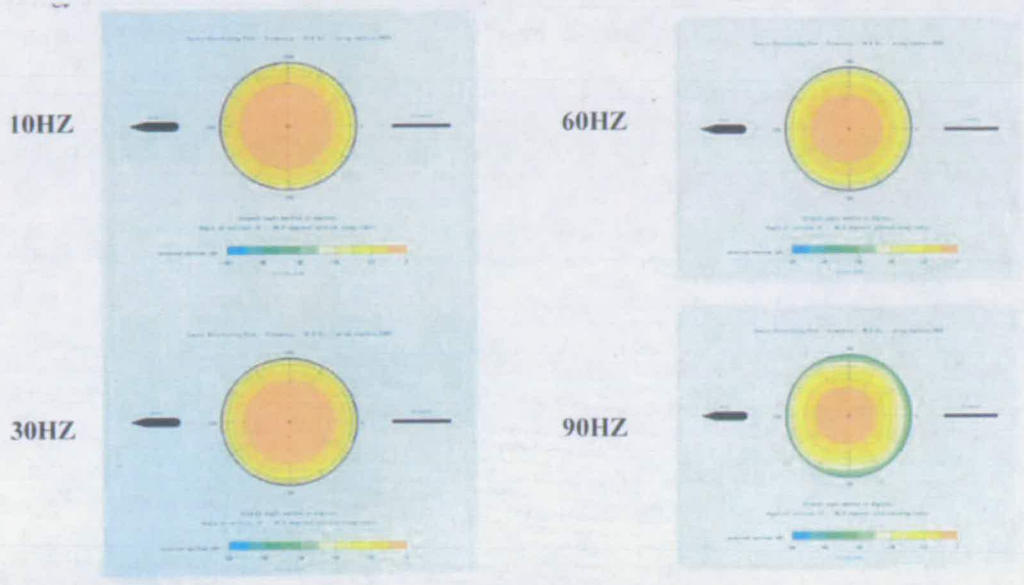

Figure 3.11: Isotropic source configuration at all frequencies.

3.4 The Emilio data

The Emilio data, which were collected at the beginning of 2000, was the product of the first marine 3D/4C survey specially designed for characterizing fractured carbonate reservoir. The whole area covered by receivers was 50 km^2, with a full-fold area about 20km^2. The data were saved in 267 IBM 3590 tapes.

To acquire 3D/4C OBC seismic data, the conventional practice is to lay the two receiver cables on the seabed and to shoot in patches with direction perpendicular to the cables in order to achieve a good azimuthal coverage. Since the Emilio dataset is a huge dataset and includes twelve patches, here I only use patch seven for a detailed study. The analysis of the loaded geometry in SEG-Y trace headers show that an orthogonal acquisition pattern (Figure 3.12) was designed to collect a high fold (Figure 3.13) and uniform azimuth and offset trace distribution (Figure 3.14). Shot lines were oriented N80^{0}E. There are thirty shot lines and two receiver lines in this patch (Figure 3.12). Details of the acquisition parameters are listed in Table 3.2.

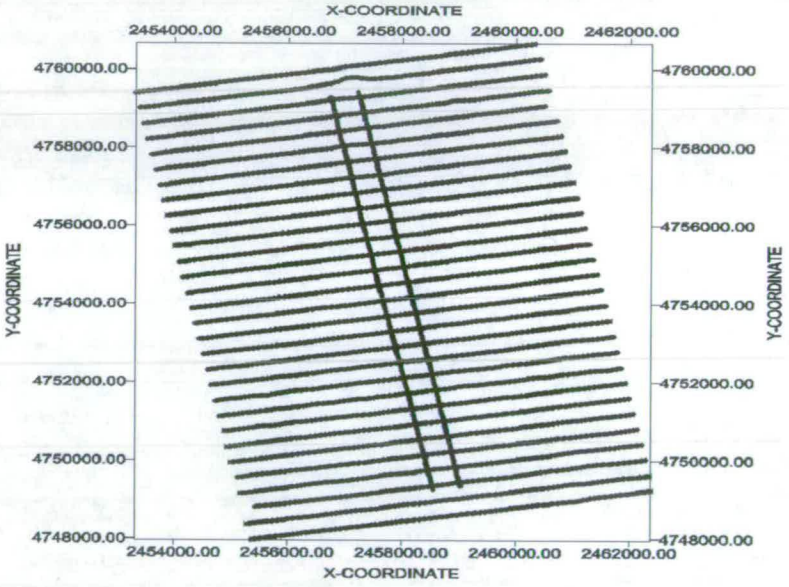

Figure 3.12: Geometry of the Emilio 3D/4C data (Patch seven). An orthogonal acquisition pattern is used for data collection.

Source line spacing	400 m	Receiver line spacing	500 m
Source line length	12,200 m	Receiver line length	+ - 4000 m
Shot point interval	25 m	Group interval	50 m
Sampling rate	2 ms	Record length	8 s
Number of channels	410	Bin size	12.5 m X 25 m

Table 3.2: Acquisition parameters.

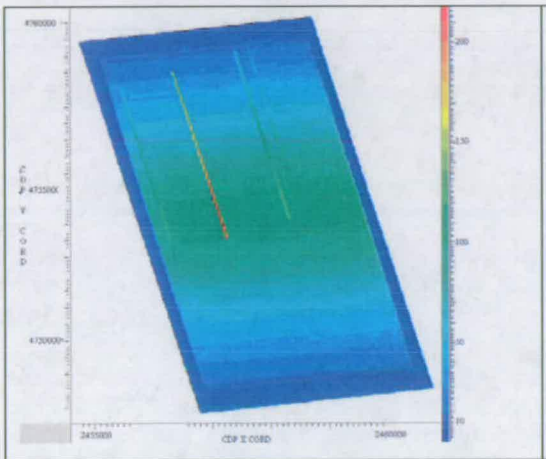

Figure 3.13: CMP fold map of the Emilio 3D/4C data in patch seven.

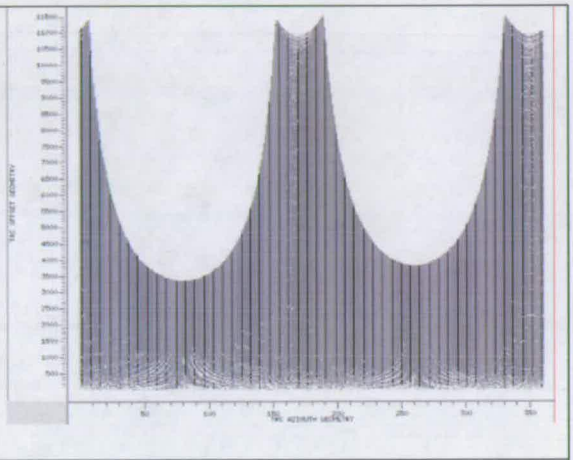

Figure 3.14: Azimuth versus offset distribution map.

3.5 The data characteristics

Figures 3.15 and 3.16 respectively show typical common shot and receiver gathers. The overall quality of the acquired data is good, especially for converted PS data. The hydrophone shows strong water-column multiples, and there is shear energy leakage at near offsets on the vertical geophones due to coupling. The transverse component amplitude is much lower than the radial component, but it tends to build up with time. This is likely to be the result of S-wave azimuthal anisotropy.

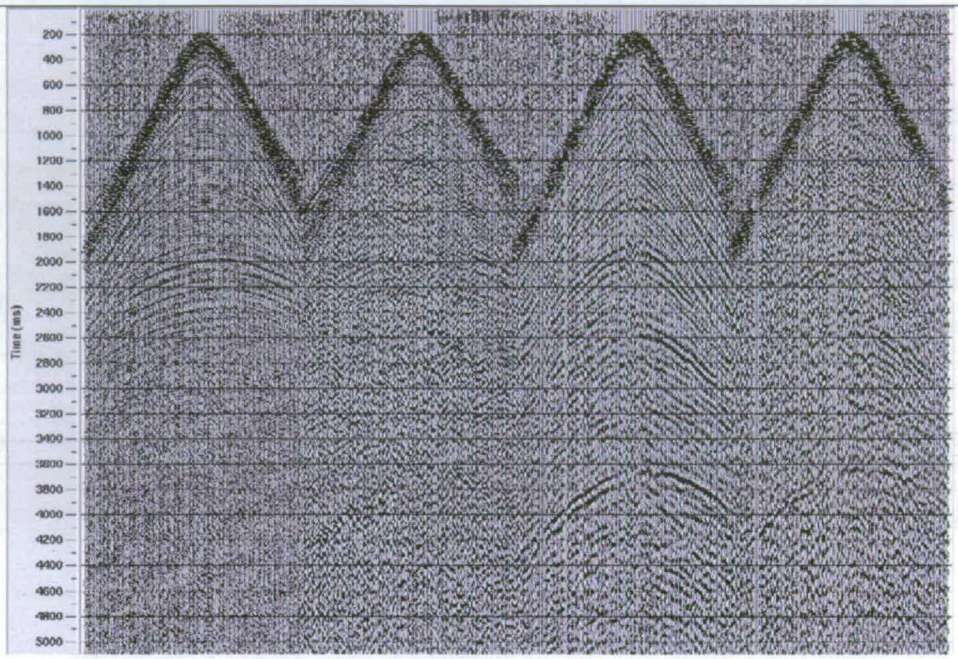

(a) Hydrophone	(b) Vertical geophone	(c) Radial component	(d) Transverse component

Figure 3.15: A common shot gather (shot 150) from the Emilio data. AGC is applied for display purposes.

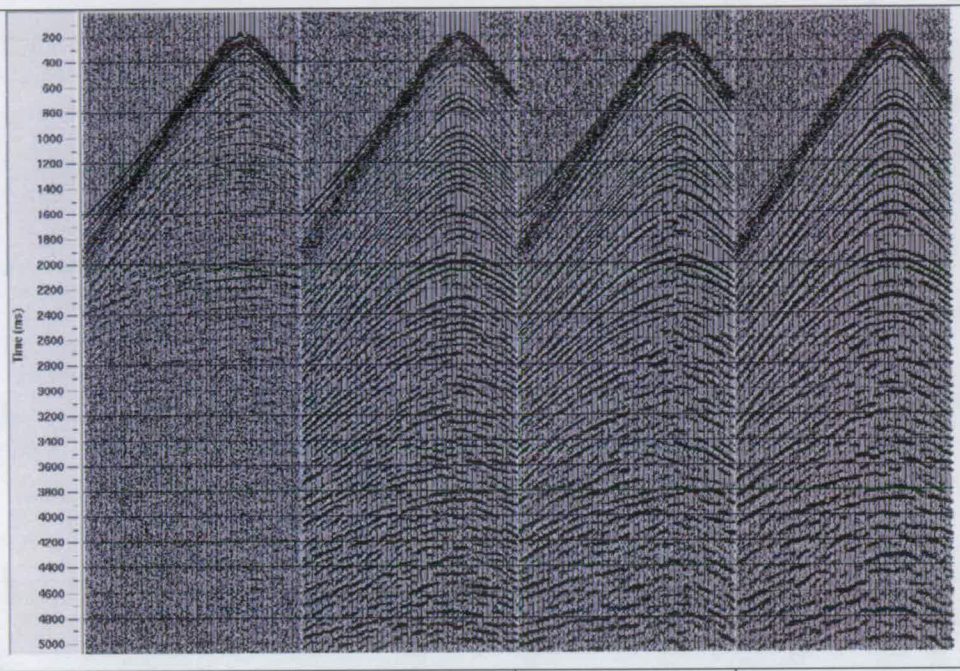

(a) Hydrophone	(b) Vertical geophone	(c) Radial component	(d) Transverse component

Figure 3.16: A common receiver gather (receiver channel 112) from the Emilio data. AGC is applied for display purposes. Note the leakage of radial shear-wave energy to the vertical geophone.

3.6 Summary

The Emilio field is a gas-oil reservoir in the Adriatic Sea and a 3D/4C survey aiming to assess crack direction and density was planned. 3D/4C methodology for fracture detection requires a stronger effort in the survey design phase in comparison with usual techniques. A large amount of reconnaissance non-seismic data should be checked and interpreted to create a reliable reservoir model for the successive anisotropic and isotropic P and PS modelling phase. From this feasibility study, it is easy to realize that the most important feature to take care of, when designing a 3D-4C survey for fracture characterization, is the survey isotropy (full azimuth, offset and energy distribution), so that the occurrence of anisotropy in the recorded data can be related only to geology. Good quality data were acquired, especially for converted PS data.

Chapter 4

Analysis of the Emilio P-wave data for azimuthal anisotropy

4.1 Introduction

In this Chapter I present the fracture analysis results using the P-wave data from the Emilio dataset. I carry out the azimuthal anisotropy analysis in two steps. First, I check the data quality, geometry, and data characteristics. I develop a simple and robust technique to attenuate multiples at the stage of data preprocessing. Second, I use both the narrow-azimuth stacking method and the full-azimuth surface fitting method for azimuthal anisotropy analysis. I examine two seismic attributes (stacking velocity and interval travel time) to map fracture distributions (both orientation and intensity). The final fracture orientation and intensity maps are shown and they compare reasonably well with the fault and fracture patterns in the study area.

4.2 Data preprocessing

During the data preprocessing stage, I check geometry, inspect data quality and evaluate data characteristics. The preprocessing includes: dual sensor summation, surface-consistent amplitude correction and conventional image processing. The dual sensor summation technique is designed to remove multiples, and is discussed in more detail in next section. Care must be taken during surface-consistent amplitude correction processing to maintain the relative amplitude and phase information among different azimuths. Image processing is to produce the initial image volumes for identifying the target horizons. Figure 4.1 shows the flowchart of the pre-processing steps. Table 4.1 shows the resetting of FFID for geometry definition.

Figure 4.2 shows a super CDP gather with 75m x 75m bin size. The data are of good quality. However, some contamination by multiples can be observed and dual summation to reduce multiples is necessary.

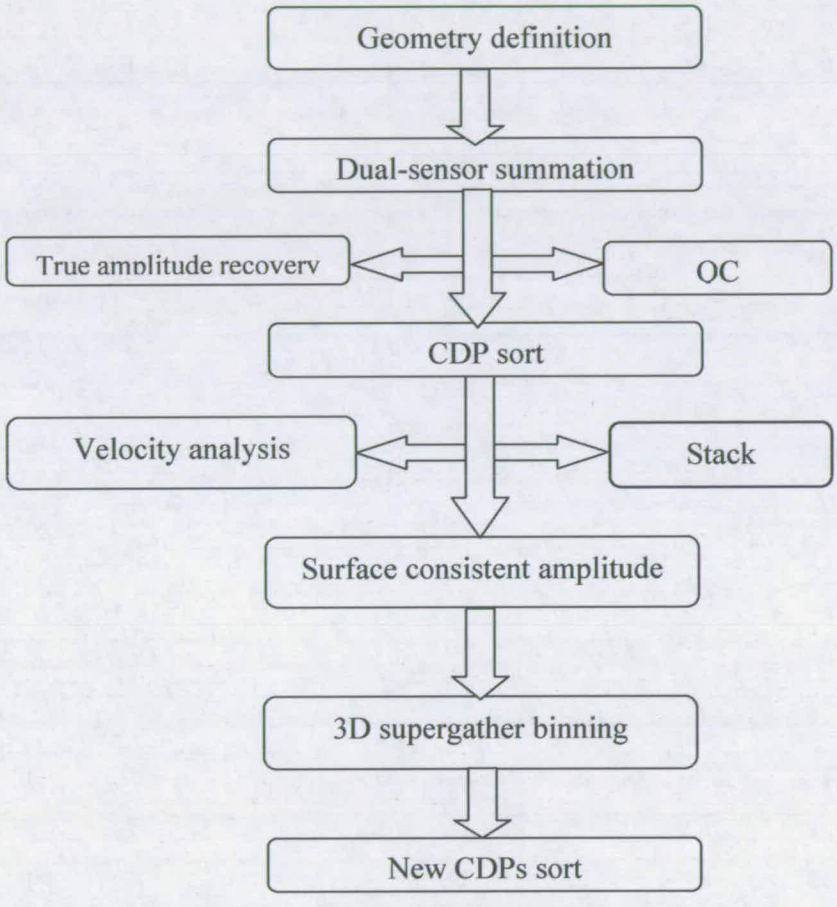

Figure 4.1: Processing flowchart: data preparation.

Line No.	FFID	New SIN
C1	2-287	1-286(-1)
C2	2-289	287-574(+285)
C3	339-626	575-862(+236)
C4	291-577	863-1149(+572)
C5	629-914	1150-1435(+521)
C6	579-866	1436-1723(+857)
C7	1446-1733	1724-2011(+278)
C8	868-1154	2012-2298(+1144)
C9	1735-2022	2299-2586(+564)
C10	1157-1444	2587-2874(+1430)
C11	2023-2310	2875-3162(+852)
C12	2890-3146	3163-3419(+273)
C13	2312-2599	3420-3707(+1108)
C14	3161-3448	3708-3995(+547)
C15	2601-2888	3996-4283(+1395)
C16	3450-3737	4284-4571(+834)
C17	2-289	4572-4859(+4570)
C18	3986-4271	4860-5145(+874)
C19	359-646	5146-5433(+4787)
C20	3697-3984	5434-5721(+1737)
C21	648-935	5722-6009(+5074)
C22	3408-3695	6010-6297(+2602)
C23	937-1220	6298-6581(+5361)
C24	3119-3406	6582-6869(+3463)
C25	1237-1579	6870-7212(+5633)
C26	2765-3046	7213-7494(+4448)
C27	1581-1886	7495-7800(+5914)
C28	2465-2757	7801-8093(+5336)
C29	1888-2175	8094-8381(+6206)
C30	2177-2463	8382-8668(+6205)

Table 4.1: FFID of each line are reset for geometry definition.

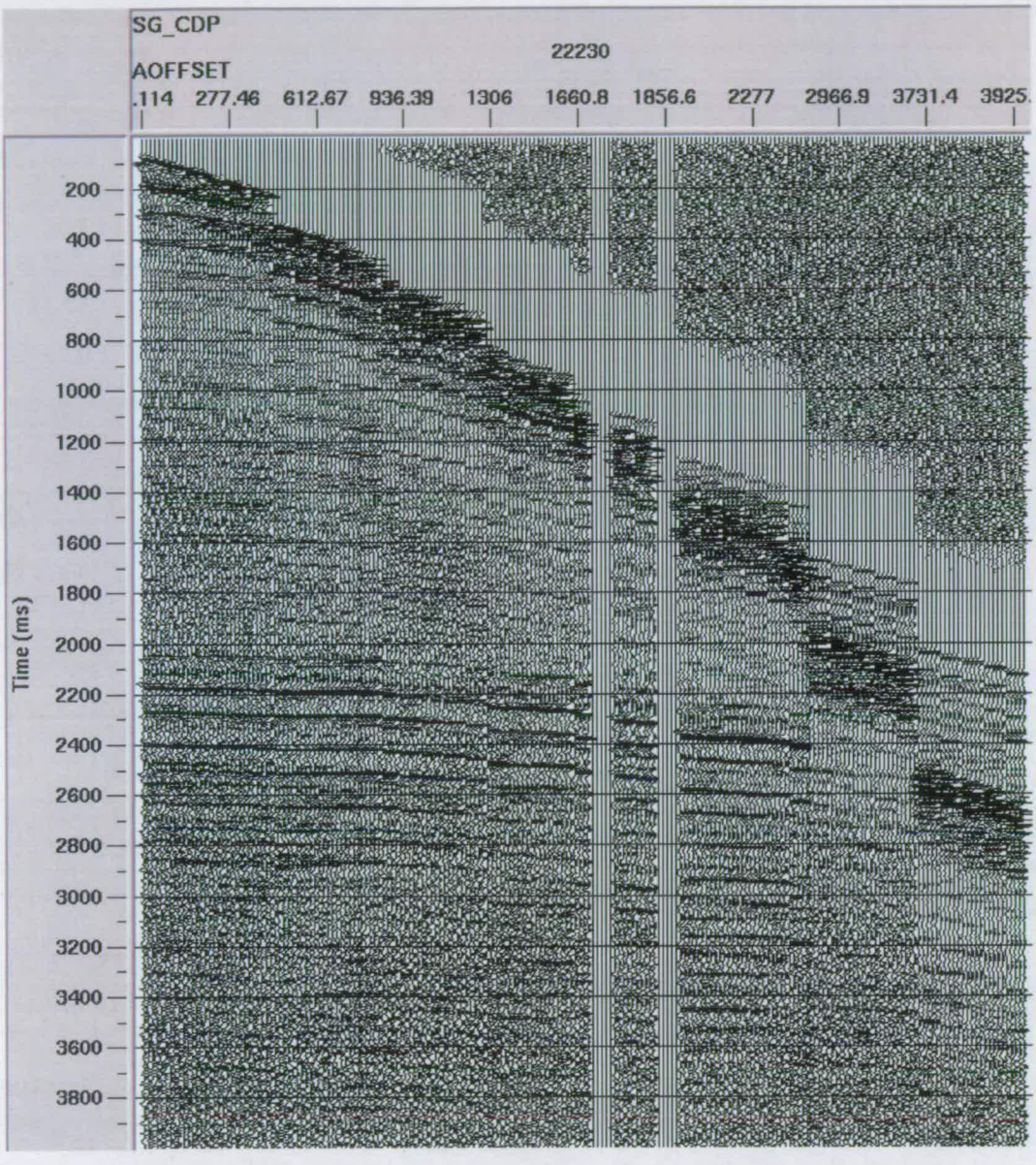

Figure 4.2: A super gather with bin-size of 75 X 75m.

4.3 Dual-sensor summation

It is well known that one of the shortcomings of acquiring seismic data in the marine environment is the presence of water-column reverberations that produce undesirable multiples. As a single upgoing reflection wavelet arrives at the ocean-bottom from below, it continues to travel upwards until it impinges upon the ocean's surface where it is completely reflected. Upon arrival at the ocean-bottom, this downgoing wavelet is again partially reflected back towards the water's surface. This cycle repeats producing second and subsequent multiple arrivals of the original reflection at time lags equal to the two-way travel time through the water column. This arrival of primary reflection energy at the ocean-bottom and its subsequent water-column multiples is illustrated schematically in Figure 4.3. it is thus very important for marine seismic data processing to remove these multiple arrivals and preserve the primaries.

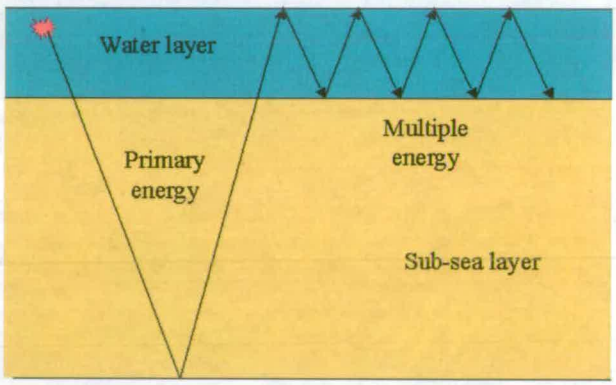

Figure 4.3: Diagram of the ray path geometry for the receiver-side multiples.

In early OBC technology, both down- and up-going fields are recorded in the cable system and these wavefields may then be separated from the original data. The concept of wavefield separation eventually led to the concept of combining both hydrophone and vertical geophone recordings for removal of multiples. This happens because a surface-reflected event recorded by a geophone has the opposite polarity to

the same event recorded by a hydrophone. This approach is commonly referred to as the dual-sensor method. Numerous methods have been published on the combination of dual-sensor OBC data for multiple removal (Ball and Corrigan, 1996; Bale, 1998; Barr and Sanders, 1989). However, all of these methods require the computation of an accurate estimate of the ocean-bottom reflection coefficient in order for them to be effective.

Here I tackle the problem in a much simpler manner and use a very simple and robust method for dual-sensor combination, based on Hoffe *et al.*, 1999. I wrote a Seismic Unix (SU) program, *supzsum*, to realize Hoffe's methodology. A time-variant scalar trace is computed for every hydrophone-geophone trace pair. Application of these time-variant scalar traces essentially forces the amplitudes of the geophone traces to equal that of the hydrophone traces. Therefore, when summed, I can achieve cancellation of multiples due to their opposing polarity in each of the hydrophone-geophone trace pairs.

The methodology for computing these time-variant scalar traces is as follows:

1. The data is first sorted so that the hydrophone-geophone trace pairs are properly matched for each common receiver location.
2. Since the hydrophone amplitudes are usually an order of magnitude greater than that of the geophone amplitudes, the hydrophone trace is divided by the geophone trace on a sample-by-sample basis, which produces a quotient trace.
3. A median smoothing filter is then applied to the absolute value of this quotient trace over a small time window, typically 80-100ms, and this yields a scalar trace for output.
4. These scalar traces are then applied to the appropriate geophones traces via trace multiplication and the scaled geophone traces are then simply added to the corresponding hydrophone traces to complete the dual-sensor summation.

Application of this method to the Emilio data has demonstrated that it can effectively attenuate multiple energy. Figure 4.4 and 4.5 show a shot gather and a stack section

from the survey. The summed result in Figure 4.4(c) and Figure 4.5(c) show a considerable reduction in the amplitude of the multiples compared to the originals.

Figure 4.6 shows an example of the selected inline data after preprocessing. I marked two horizons, the Gessoso Solfifera and the target (the Top Palaeocene), in the map. The horizons are handpicked from the stack section and are used as control points for pre-stack analysis.

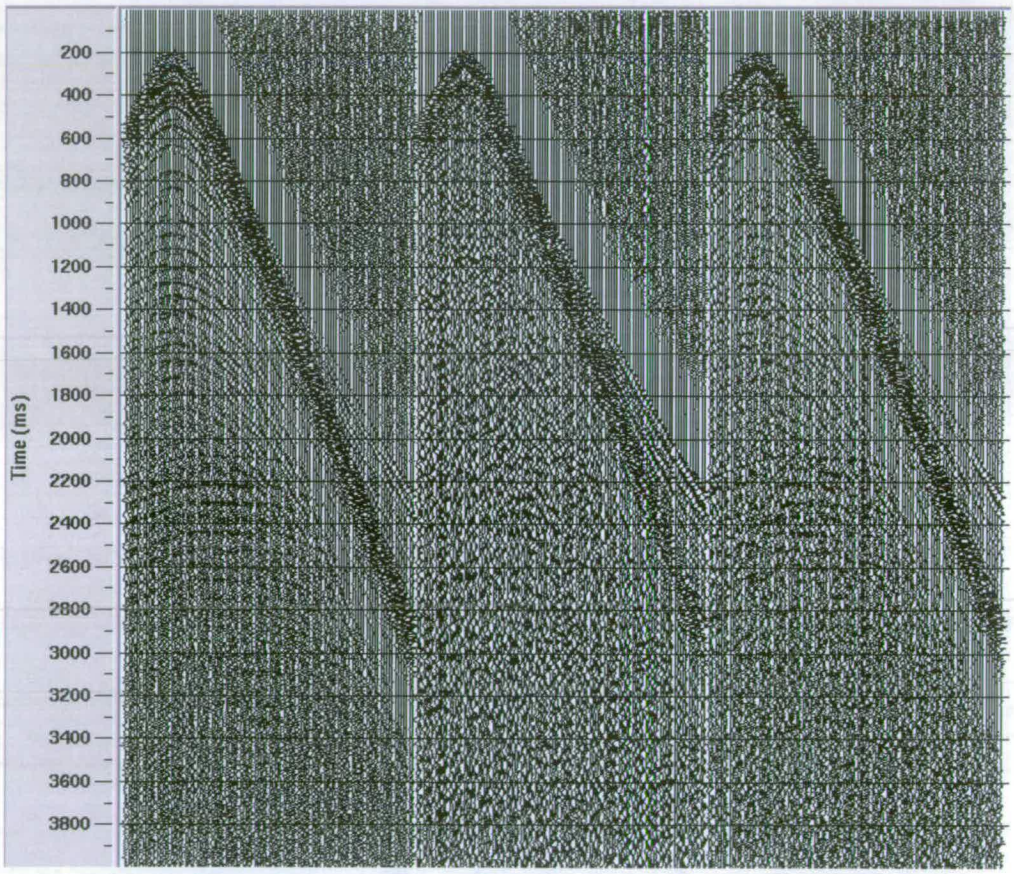

(a) Hydrophone (b) Vertical geophone (c) Summed result

Figure 4.4: A common shot gather showing dual-sensor summation result. AGC is applied for display purposes. Note the considerable reduction in the amplitudes of the multiples on the summed result, as compared to the original hydrophone data in (a).

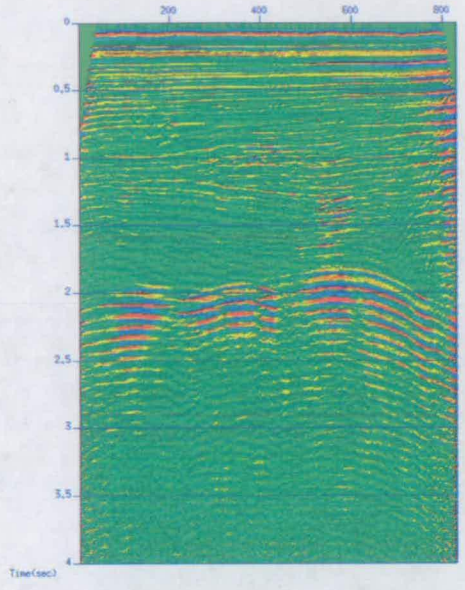

(a) Hydrophone stack section

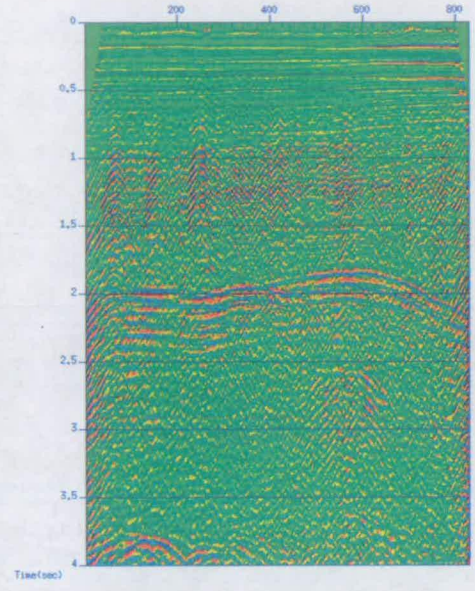

(b) Vertical geophone stack section

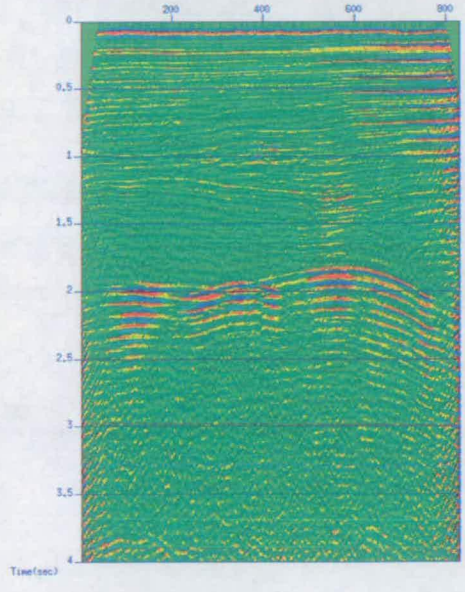

(c) Summed result stack section

Figure 4.5: Stacked sections before and after dual-sensor summation. The receiver-side multiples are greatly reduced in amplitude. Note that the amplitude of the hydrophone component is an order of magnitude greater than that of the vertical geophone, thus the vertical geophone stack section looks noisier.

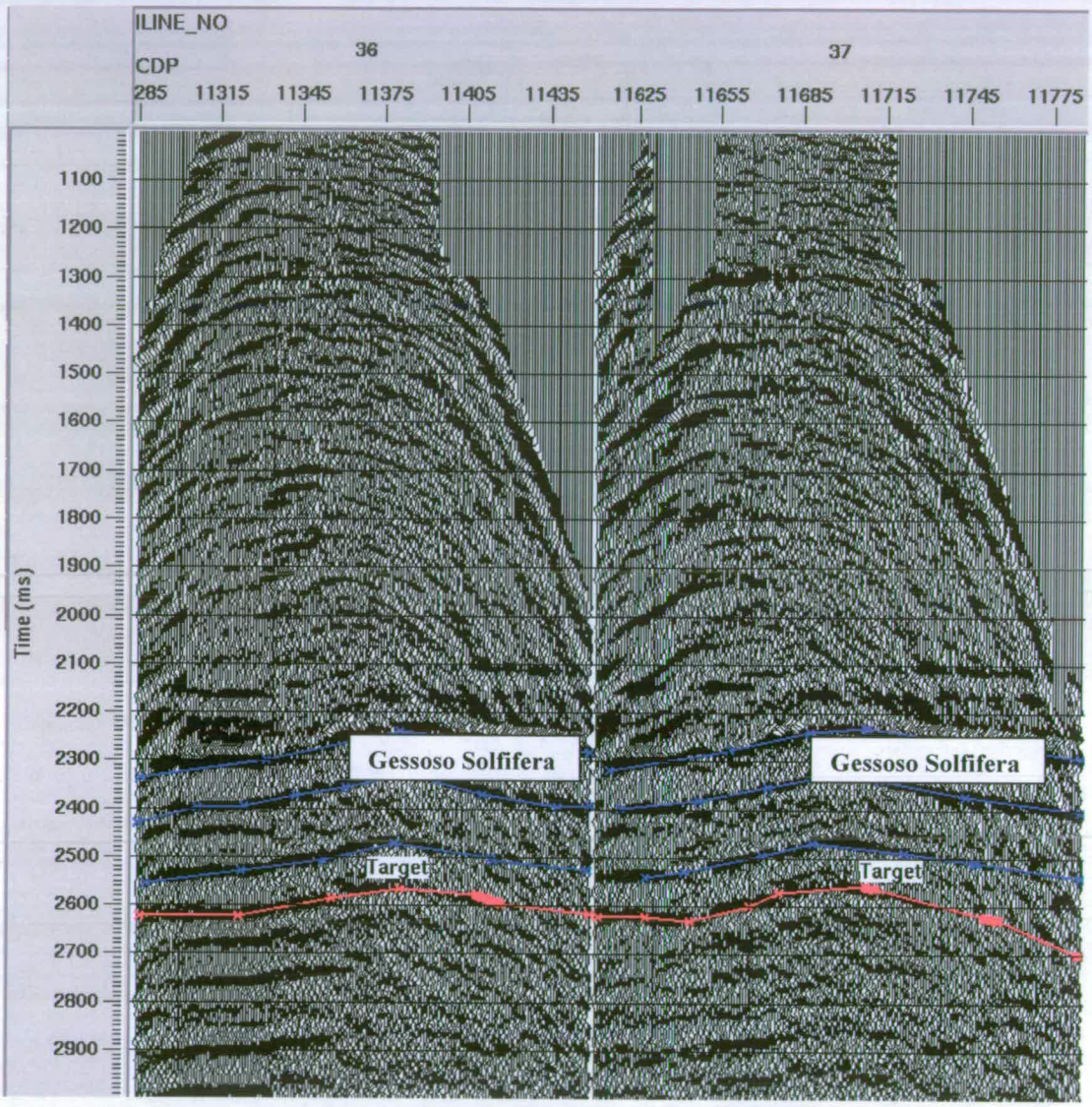

Figure 4.6: Example of image processing for two inline profiles. Two horizons have been identified.

4.4 Narrow azimuth stack

I carry out two methods for azimuthal anisotropy analysis. I choose a 75m x 75m bin size for the surface-fitting method and a 125m x 125m bin size for the narrow azimuth stacking method. I have performed a full test of two seismic attributes, stacking velocity and interval traveltimes, in the target. The final result from the interval traveltimes using the surface-fitting method compares well with the fault and fracture patterns in the area (Figure 4.10).

Figure 4.7 outlines the processing flowchart of azimuthal attribute analysis using the narrow azimuth stacking method. I divide the data into four azimuthal bins with 45^0 bin size, and then perform narrow azimuth velocity analysis stacking. To apply the method, velocity picking for every CDP in all four data volumes (every 45^0 for each azimuthal component) is carried out, followed by NMO correction and automatic picking of traveltimes. Inverse NMO is then applied and a least-square traveltime inversion method is used to obtain the stacking velocity. Each CDP has four velocities corresponding to the four azimuths. An elliptical fitting technique is applied.

Figure 4.8 show the fracture orientation map and fracture map using the narrow azimuth stacking analysis method. The fracture orientation map is mainly yellow colour (around 80 degrees), which is along the source and receiver line azimuth $N80^0E$. In the fracture map, the arrows mainly point to the acquisition source-receiver direction. Thus we can see the narrow azimuth stacking analysis results are dominated by the acquisition footprint (noise correlated to the geometric distribution of sources and receivers on the earth's surface).

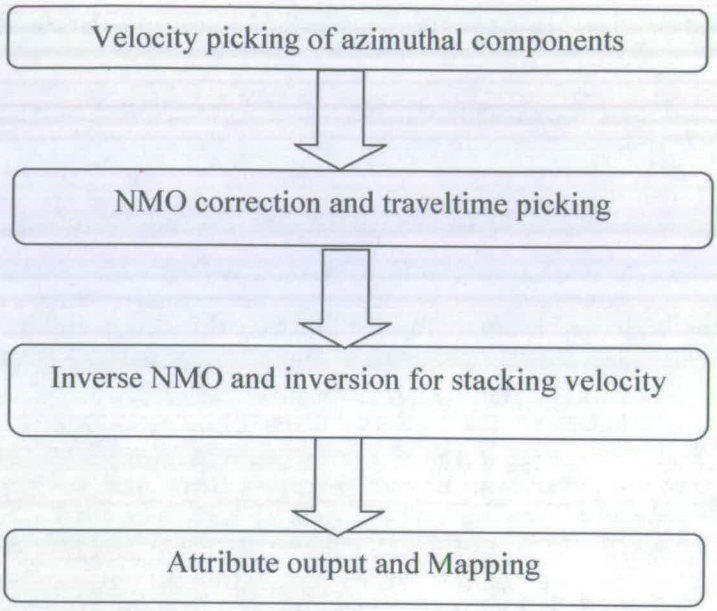

Figure 4.7: Processing flowchart for P-wave azimuthal attribute analysis using the narrow azimuth stacking method.

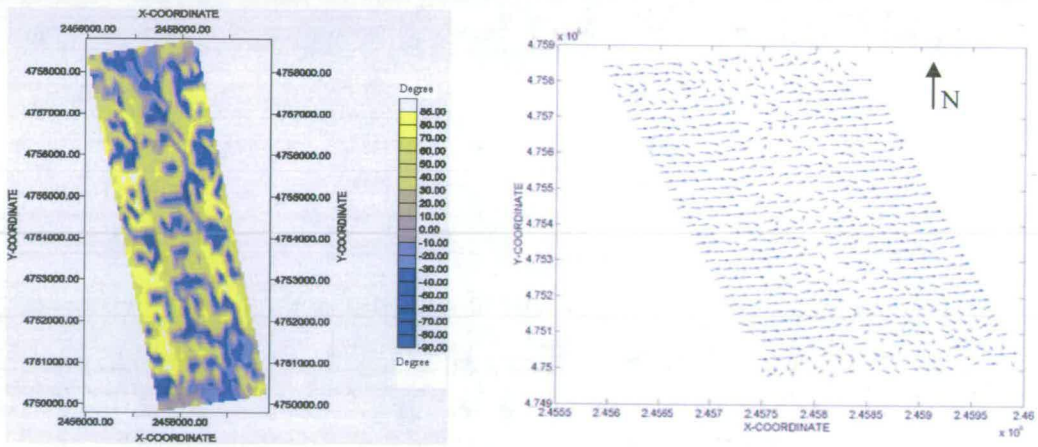

(a) Orientation (b) Fracture map

Figure 4.8: Narrow-azimuth method of stacking velocity inversion from the target: (a) fracture orientation map and (b) interpreted fracture map. Note that yellow colour in (a) and arrows in (b) are both $N80^0E$, the acquisition source-receiver direction.

4.5 Surface fitting results (full-azimuth and full-offsets)

Figure 4.9 outlines the processing flowchart for azimuthal attri bute analysis using the full-azimuth least-square inversion method. Surface fitting fits an elliptical surface through all the available azimuths and offsets for a given CDP gather. It is necessary to pick traveltimes of the top and bottom of the target horizons. It is impossible to do this manually due to the workload and also the picking errors can be large. Here an automatic picker is used. To ensure reliable picking, the horizons are first manually picked from the post-stack volumes and then used to control points for pre-stack picking.

After the picking, a least-squares inversion method including all azimuths and offsets is applied to the picked interval traveltimes. Figure 4.10 shows the analysis results. In Figure 4.10(a), two main sets of fracture are shown, at N75^{0}E indicated by the yellow colour, and at N165^{0}E (-75^0 in the colour bar) indicated by the light blue colour. In Figure 4.10(b), the average anisotropy is about 2-5%. These results are consistent with the published results (Vetri *et al.*, 2003), which showed there are two main set of orthogonal fractures (N75^{0}E and N165^{0}E) in the Emilio field. Note the marked Well7d position lies in both the principal anisotropy direction and the higher anisotropy density locations. Furthermore, the impact of acquisition footprint on the estimated orientation is negligible as shown in Figure 4.11.

4.6 Effects of overburden anisotropy

It is necessary to know is there is any anisotropy in the overburden as we are generally interested in the anisotropy in the target zones. Li (1999) found that if the events immediately above the target horizon are flattened using the NMO correction,

any anisotropy in the overburden will be almost removed and the data can then be used for anisotropy analysis in the underlying layer.

To examine the overburden anisotropy, surface fitting is applied to the traveltimes through the overburden (Figure 4.11). The orientation appears very random and the anisotropy is very weak. This confirms that the overburden is almost isotropic which increases confidence in the result. However, the use of the interval traveltime will compensate for the effect even if there is anisotropy in the layer above.

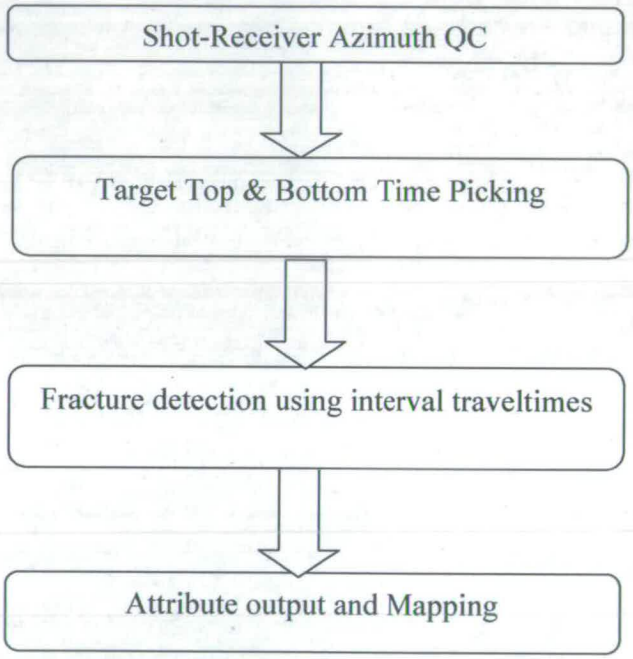

Figure 4.9: Processing flowchart for P-wave azimuthal attribute analysis using the full-azimuth least-square inversion method.

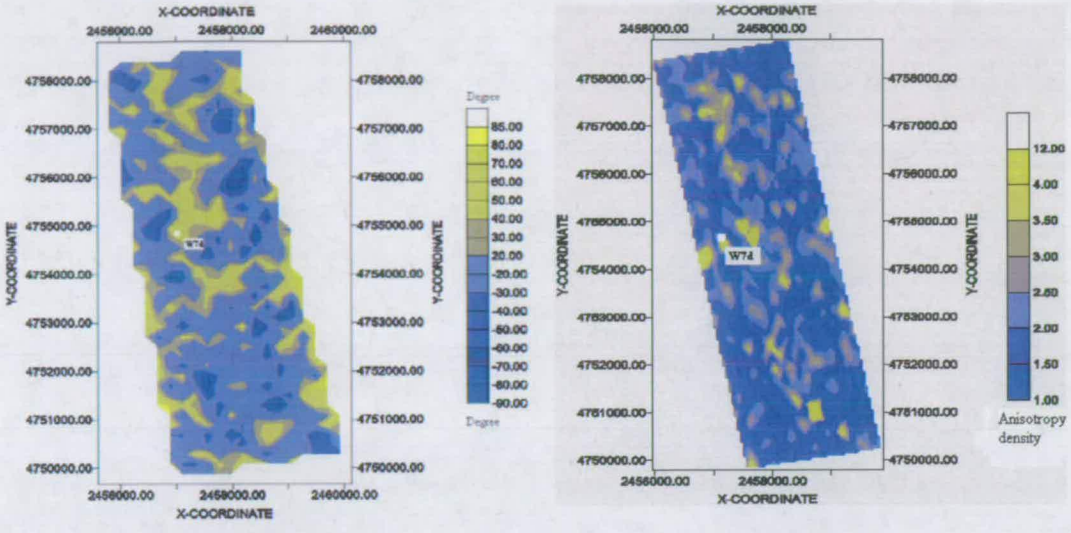

(a) Orientation **(b) Intensity**

Figure 4.10: Full-azimuth and full-offset interval traveltime inversion from the target: (a) fracture orientation map and (b) fracture intensity map.

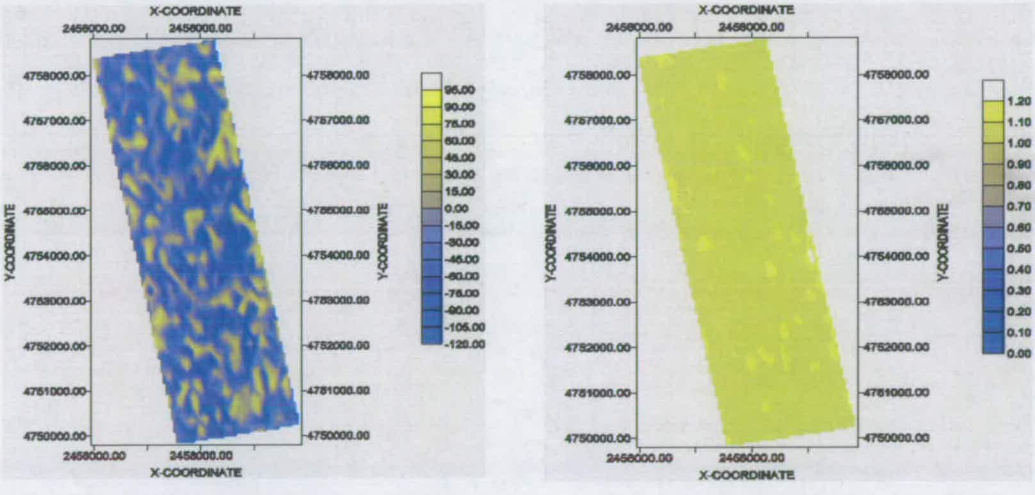

(a) Orientation **(b) Intensity**

Figure 4.11: Full-azimuth and full-offset traveltime inversion from the overburden: (a) fracture orientation map and (b) fracture intensity map.

4.7 Summary

I have proposed a simple and robust method of combining dual-sensor OBC data for multiple attenuation during the data preprocessing stage. A critical assumption required of this method is that both the hydrophone and vertical geophone elements are matched in phase. Application of the method to the Emilio data as shown in the report has clearly demonstrated that it can effectively attenuate multiple energy.

I have carried out a detailed and robust analysis of the azimuthal variation in P-wave attributes for patch seven of the Emilio 3D/4C dataset. Two methods, full-azimuth/full-offset and narrow-azimuth/full-offset, have been used and two seismic attributes have been analysed for fracture parameter estimation. The final fracture orientation and intensity maps from the interval traveltime attributes compare reasonably well with the published result (Vetri *et al.*, 2003). The analysis shows that there are two main orthogonal fracture sets in $N75^0E$ and $N165^0E$ direction, which agrees with Figure 3.5 in Chapter 3, and P-wave anisotropy intensity is about 2-5% in the Emilio field.

Chapter 5

Sensitivity of PS-wave imaging to dip, azimuth, velocity and anisotropy

5.1 Introduction

In this Chapter I study the PS-wave imaging sensitivities to dip, azimuth, velocity and anisotropy in a VTI medium. First I give an introduction of general PS-wave processing techniques and I present the EAP's approach for converted wave imaging. Then I overview various modelling methods and demonstrate the effect of a low shear wave velocity layer on OBC data recording. A suite of 2D models have been built to generate converted wave synthetics for evaluating PS-wave imaging sensitivities. These synthetic datasets are processed using a tool recently developed by EAP. The imaging sensitivities of four parameters, γ_0, γ_{eff}, V_c and χ, are investigated.

5.2 Basic theory

Imaging the earth's interior using PS converted waves is a non-trivial problem and faces a number of challenges. It is difficult to build a migration velocity model even in the simplest of 1D earth structures since the migration velocity analysis is complicated by the asymmetric propagation path, reflector dip, source-receiver azimuth, and anisotropy. In a 2D case, an incorrect velocity model may result in the smearing of the common-image point within the sub-surface by forward and reverse offsets. Further complications arise in the presence of dip and anisotropy.

As I discussed in Chapter 2, P- and S-wave propagation in a VTI medium can be described by the four Thomsen's (1986) parameters (V_{p0}, V_{s0}, ε, and δ). Anisotropy parameters include η_{eff}, related to P-wave anisotropy (Alkahalifah, 1997), ζ_{eff}, related to S-wave anisotropy, and χ_{eff}, related to PS-waves (Li and Yuan, 2003). They are defined in terms of the Thomsen parameters ε and δ as:

$$\eta_{eff} = \frac{\varepsilon - \delta}{1 + 2\delta} \tag{5.1}$$

$$\zeta_{eff} = \gamma_{eff}^2 \eta \tag{5.2}$$

$$\chi_{eff} = \gamma_0 \gamma_{eff}^2 \eta_{eff} - \zeta_{eff} = (\gamma_0 - 1)\gamma_{eff}^2 \eta_{eff} \tag{5.3}$$

where γ_0 and γ_{eff} are vertical and effective velocity ratios.

The PS-wave travel time t_{ps} in layered anisotropic media can be derived in Taylor series form,

$$t_{ps}^2 = t_{ps0}^2 + \frac{x^2}{V_{ps2}^2} + \frac{A_4 x^4}{1 + A_5 x^2} \tag{5.4}$$

The coefficients A_4 and A_5 are derived as (Li and Yuan, 2003),

$$A_4 = -\frac{(\gamma_0 \gamma_{eff} - 1)^2 + 8(1 + \gamma_0)\chi_{eff}}{4 t_{ps0}^2 V_{ps2}^4 \gamma_0 (1 + \gamma_{eff})^2} \tag{5.5}$$

and

$$A_5 = \frac{A_4 V_{c2}^2 (1+\gamma_0)\gamma_{eff}[(\gamma_0 - 1)\gamma_{eff}^2 + 2\chi_{eff}]}{(\gamma_0 - 1)\gamma_{eff}^2 (1-\gamma_0\gamma_{eff}) - 2(1+\gamma_0)\gamma_{eff}\chi_{eff}} \tag{5.6}$$

where V_{ps2} is the stacking velocity for PS-waves. The Equations (5.4), (5.5), and (5.6) can be used to estimate V_{ps2} and χ_{eff}.

The t_{ps} in prestack time migration (PKTM) for anisotropic media is approximately calculated using the double-square root (DSR) equation derived by Li *et al.* (2001):

$$t_{ps} = \sqrt{t_{p0}^2 + \frac{(h+x)^2}{v_p^2} - \frac{2\eta_{eff}(h+x)^4}{v_p^2[t_{p0}^2 v_p^2 + (1+2\eta_{eff})(h+x)^2]}} + \sqrt{t_{s0}^2 + \frac{(h-x)^2}{v_s^2} + \frac{2\zeta_{eff}(h-x)^4}{v_s^2[t_{s0}^2 v_s^2 + (h-x)^2]}} \tag{5.7}$$

where h is the half-offset; x is the distance from the midpoint to the scatter-point; t_{p0} is the vertical travel-time for the P-wave; t_{s0} is the vertical travel-time for S-wave; V_p is the migration velocity for the P-wave and V_s is the migration velocity for the S-wave. η_{eff} and ζ_{eff} are VTI anisotropy parameters for the P- and S-waves.

Various parameters, such as velocities (V_{p2}, V_{s2} and V_{ps2} for stacking velocities, V_p, V_s, and V_{ps} for migration velocity, for P-, S- and PS-waves), velocity ratios (γ_0 and γ_{eff} for vertical and effective velocity ratios) and anisotropy parameters (η and σ) have been derived from different combinations of the four Thomsen's parameters. Depending on how one parameterizes the reflection moveout, each parameter may have a contribution to it. A number of approaches have been developed for processing the PS converted waves based on different parameter derivations.

5.3 EAP's approach for PS-wave imaging in VTI media

EAP has been working on PS-wave imaging for many years and has developed its own tools for anisotropy velocity analysis and anisotropy migration. Instead of using the conventional time processing workflow (Asymptotic Conversion Point (ACP) binning, DMO, anisotropic NMO, stacking and post-migration), EAP chooses a prestack Kirchhoff time migration (PKTM) approach since it can cope with varying velocity. EAP's approach is based on a four parameter equation (V_{ps2}, γ_0, γ_{eff} and χ_{eff}) for PS wave travel-time and a five parameter DSR equation (V_p, V_s, γ_0, η_{eff} and ζ_{eff}) for prestack time migration of PS waves. However, in PKTM, it is impossible to separate t_{ps} into t_p and t_s, resulting in difficulty to obtain V_p and V_s from field data directly. Thus another set of the combined parameters is used, including V_{ps2} for PS-wave stacking velocity, γ or γ_{eff} for the velocity ratio, γ_0 for the vertical velocity ratio and χ for PS-wave anisotropy. The relationships among these parameters are,

$$V_{ps2}^2 = \frac{1}{t_{p0} + t_{s0}}(t_{p0}V_{p2}^2 + t_{s0}V_{s2}^2) \tag{5.8}$$

$$\gamma_2 = \frac{V_{p2}}{V_{s2}} \quad \text{or} \quad \gamma_{eff} = \frac{\gamma^2}{\gamma_0} \tag{5.9}$$

$$\gamma_0 = \frac{t_{s0}}{t_{p0}} \tag{5.10}$$

$$\chi_{eff} = \eta_{eff}\gamma_{eff}^2\gamma_0 - \zeta_{eff} \tag{5.11}$$

$$\zeta_{eff} = \eta_{eff}\gamma_{eff}^2 \tag{5.12}$$

A practical workflow (Figure 5.1) is recommended for anisotropy velocity analysis and migration. The P-waves are required in joint analysis with the PS converted-waves (C-waves) to estimate γ_0. V_{ps2}, γ_{eff}, and χ_{eff} are obtained in the PS-wave processing. η_{eff} and ζ_{eff} are then calculated from V_{ps2}, γ_0, γ_{eff}, and χ_{eff}. The estimated stacking velocity V_{ps2} can be used for the initial values in the prestack

Kirchhoff time migration and needs to be updated by constructing the common image point (CIP) gathers before the final migrated image is obtained.

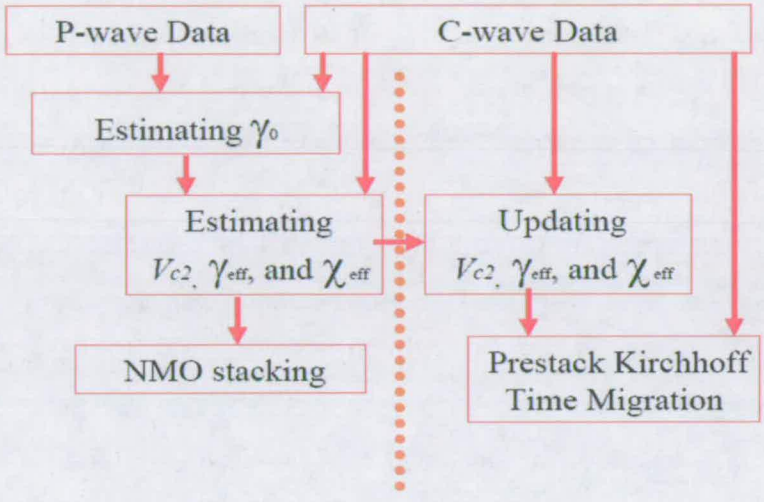

Figure 5.1: PS-wave imaging workflow in the use of EAP's Cx-tools.

With these procedures, EAP has also developed a processing package, so-called Cx-tools, in the format of Seismic Unix. The package provides GUI (Graphic User Interface) tools for parameter estimation and parallel PKTM for migration on a PC cluster, so that it greatly extends the ability of Seismic Unix in processing real data. It also provides tools for dealing with large datasets and geometry setting. Using this package, we have efficiently processed several marine and land multi-component (3D and 2D) datasets and obtained improved results at low cost (Dai *et al.*, 2000, 2003a, 2003b; Fabio *et al.*, 2005).

5.4 Modelling OBC PS-waves

5.4.1 Overview of modelling techniques

To study PS-wave imaging sensitivities requires the use of synthetic modelling methods. There are a number of methods, which may be used to simulate how seismic waves will propagate through the real earth, and then affect the sensors that will be used to record them. The nature of seismic wave propagation can be very complex, and the various methods use compromises of various types in order to make the problem solvable. Usually modelling seismic waves requires the adoption of a particular theory of wave propagation and an analysis of the corresponding wave equation. Such theories include, for example, acoustic-wave theory and elastic-wave theory. All wave theories have a corresponding ray theory. The ray theories are approximate theories, generally applicable to "high" frequencies that track the flow of wave energy along ray paths rather than wave fronts. Central tasks in ray theory are the computation of raypath geometry, the traveltime along a raypath, and the expected amplitude behaviour along the raypath. Though approximate, ray theories are popular because they are fundamentally local theories. In principle, to predict the wave amplitude at a particular point in space and a future time, wave theories require the contributions of all parts of the present wavefield that are causally connected to the particular point to be calculated. In contrast, ray theory asserts that most of these calculations will contribute little to the final result and seeks only to calculate the particularly important contributions. The latter turn out to be from points lying on raypaths that pass through the particular point. While this gives great efficiencies, it can also be very wrong if the approximations of ray theory are violated. It can be very difficult to know when a particular result is correct or what additional effects might be missing from the calculation.

Common methods for simulation of seismic wave propagation include ray tracing, convolutional modelling, the reflectivity method, 1-D theoretical seismograms, finite difference simulation, the pseudo spectral method, the finite element method,

Gaussian beam modelling, and Kirchhoff modelling (e.g. Liu *et al.*, 1997). Many, though not all, modelling methods proceed through a technique called time stepping. If we consider a wavefield in n spatial dimensions to be an $n+1$ dimensional object where the extra dimension is time, then by snapshot we will refer to a slice through this wave object at constant time. Time stepping is the process of calculating a wavefield snapshot at some future time, given snapshots of the present and a few past times. Most commonly, time stepping is used in finite difference modelling but it is also used in raytracing and Gaussian beam methods.

1-D synthetic seismograms are usually the first type of modelling done in an area where wells have been drilled and sonic logs have been run. The idea is over 50 years old and is often credited to Goupillaud. He suggested that a layer model might be constructed from well logs such that all layers have an identical two-way traveltime that is equal to the desired sample rate of the seismogram. Then any primary or multiple will fall exactly upon a particular sample. Later algorithms dispensed with the need for equal traveltime sampling but were still able to calculate all possible multiples.

Ray tracing is usually done through a model of the earth which is divided into blocks of relatively constant velocity. The raypaths obey Snell's law at block boundaries, and so make realistic deviations and record realistic amplitude changes as they cross these boundaries. The amount of raypath spreading may be used to define part of the energy amplitude changes. A great difficulty with ray theory is knowing when and how to calculate a sufficiently dense set of rays to accurately represent a model. Additionally, ray tracing is almost always iterative because there is no known way to calculate directly the raypath between a specific source and receiver in an arbitrarily complex medium.

Gaussian beams technique is similar to the ray tracing method except that the rays are simulated with a finite width. The ray width is typically a Gaussian shape, hence the name. Amplitude variation across the beam is calculated with a local approximation to the wave equation. A beam is affected by the entire range of material properties that it encounters, and so is not as vulnerable to small anomalies or discontinuities in the slopes within the geologic model. A great advantage of the Gaussian beam method is that it is far easier than raytracing to obtain a set of beams that fully covers a model. Conceptually Gaussian beams lie midway between rays and waves.

The finite difference method may be used to model sonic wave propagation through a geologic model with very few of the problems mentioned above, but a completely different set of problems appear. The new problems are associated with numerical analysis, involving dispersion and edge effects. In this method, the propagating waveform is specified from its starting point as a complete wave, and the geologic model is specified throughout by its density and compressibility, or with the additional specification of shear strength. The waves then propagate very naturally in response to the laws of physics (the wave equation).

A major problem with the finite-difference method is that simple finite-difference operators require many samples per wavelength in order to control artefacts such as grid dispersion. One way to improve this is to go to more sophisticated finite-difference operators. Yet another alternative is the pseudo spectral method where the spatial derivatives are calculated in the wavenumber domain. This gives theoretically optimum performance requiring only two samples per wavelength but at the price of Fourier wrap-around artefacts. The method proceeds by time-stepping in exactly the same fashion as the finite difference technique.

Rather than employ an approximate derivative estimate at each point in a grid, the finite-element method breaks a complex body into a finite number of polygonal regions and solves the wave equation exactly within each region. Though capable of great accuracy, this method requires very sophisticated model-building software.

To summarize, a great many tools are available for seismic modelling and there is no single best method that suits for all purposes. I now show a modelling of OBC multicomponent recording. I choose the finite difference method because, on one hand, it can generate good modelling result, and on the other hand, it is available in BP.

5.4.2 Modelling OBC multicomponent seismic

One purpose of OBC multicomponent survey is to acquire both hydrophone (pressure) and vertical geophone (particle velocity) data. The P-wave velocity in the seafloor sediments is often equal to or slightly above the acoustic velocity of the water (Dunn et al., 1986), and the S-wave velocity is very low (Theilen et al., 1997). Thus one would expect little shear wave energy in the vertical geophone, because the angle of approach should be nearly vertical. This characteristic has been studied by Gaiser (1998). Based on the consideration of different acquisition technologies, especially the cable type, he concluded that the shear wave energy recorded on the vertical geophone in the data he analyzed is energy leaked from the crossline horizontal geophone, due to poor geophone isolation.

Here I show synthetic modelling records using the finite difference method. Figure 5.2 shows velocity models for the shallow layers. I calculate full-wave synthetics for the two models in Figure 5.2 of which one has a high velocity seafloor and the other has a low-to-high shear-wave gradient.

Figure 5.3 and 5.4 presents the modelling results. Four components have been modelled, including PS wave (X displacement), PP wave (Z displacement), pressure and shear wave potential, and they are shown from left to right in each of these two figures. If the shear velocity of the seafloor is a constant high velocity, as shown by Figure 5.3 which is 500 m/s, there is a strong contamination of PS-data (X displacement) by PP waves (Z displacement). In this case, we could hardly see any energy in the shear potential component (Figure 5.3(d)).

However, by using a shear velocity gradient at the seafloor which is from 100m/s to 500m/s, the PP contamination (Z displacement) on the PS-data (X displacement) has been removed (Figure 5.4(a)). We can also see clear events in the shear potential component (Figure 5.4(d)). This modelling study shows the effect of the presence of the low velocity layer. The suppression of shear energy in the vertical geophone is due to that its propagation angle is nearly vertical so that it leaves almost no energy on the horizontal geophone.

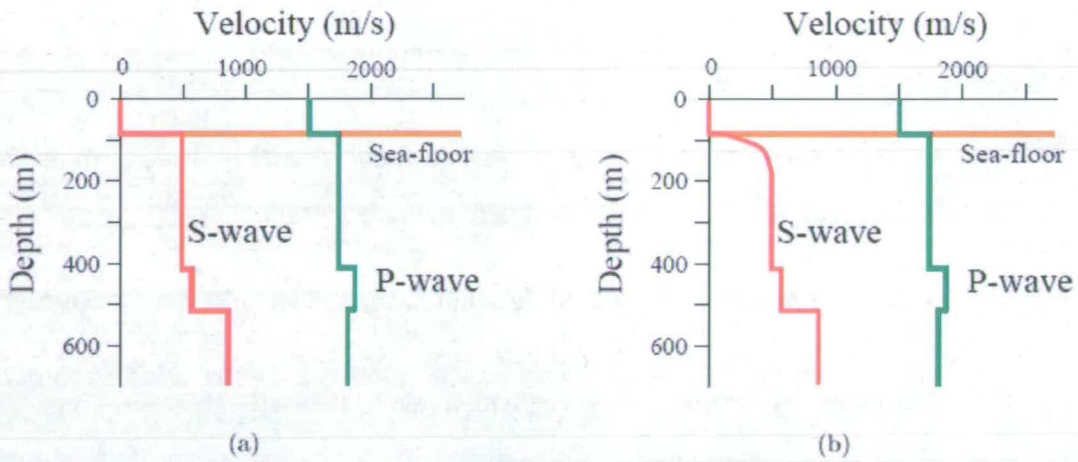

Figure 5.2: Models (shallow layers) (a) without and (b) with shear velocity gradient. The shear velocity gradient is from 100 m/s to 500 m/s in a depth of 90 meters.

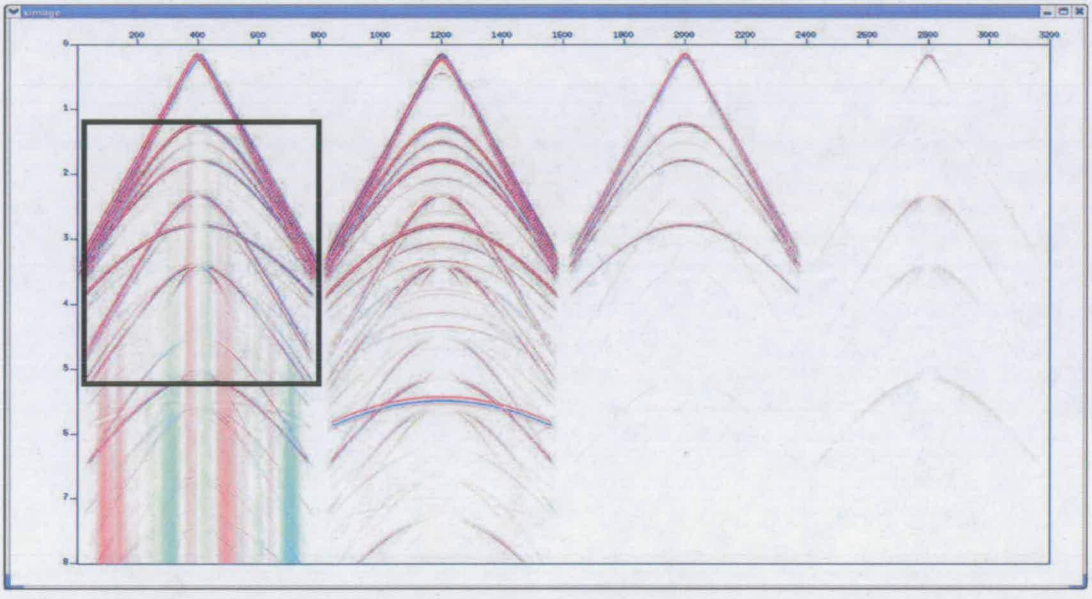

(a) x displacement (b) z displacement (c) pressure (d) shear potential

Figure 5.3: OBC synthetics in the use of finite difference modelling method without a low shear wave velocity layer. Note in the black box, the contamination of PS-data (x displacement) with PP waves (z displacement).

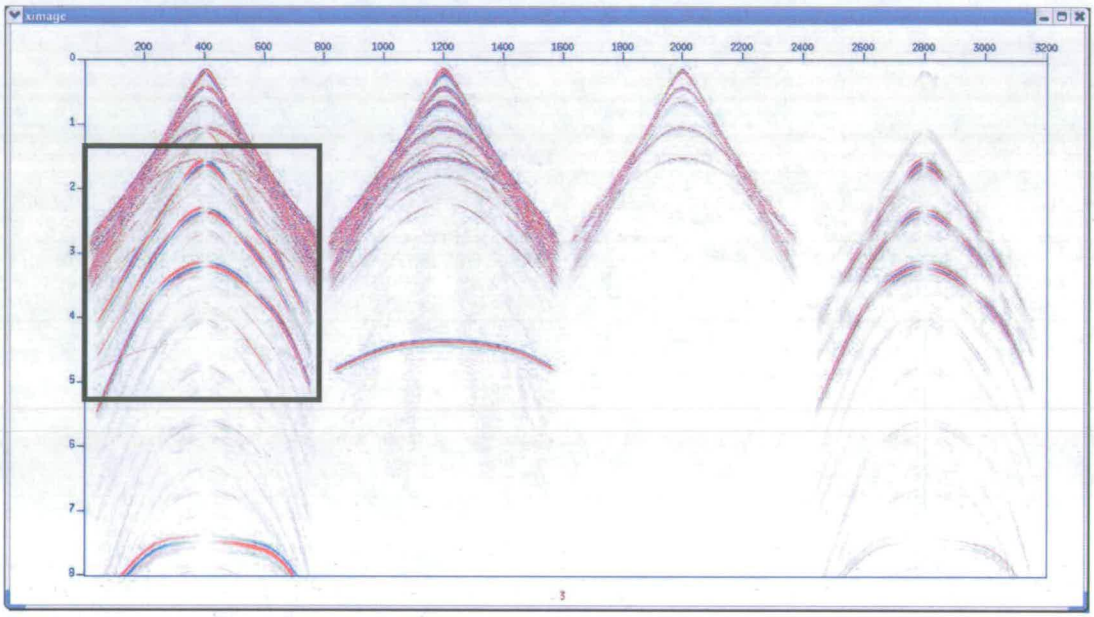

(a) x displacement (b) z displacement (c) pressure (d) shear potential

Figure 5.4: OBC synthetics in the use of finite difference modelling method with a low shear wave velocity layer. Note that in the black box, the low shear wave velocity layer removes PP waves (z displacement) contamination of PS-data (x displacement).

5.5 Sensitivity analysis results

A study of the PS-wave imaging sensitivity is useful for our understanding of PS-wave behaviour and for PS-wave imaging. Intensive efforts have been invested in this subject. For instance, Traub (2004) analysed the accuracy and sensitivity of anisotropic parameter estimation using 4C data, but her study is limited to horizontal-layer models. Dai (2006) studied the effects of migration velocity errors on traveltime accuracy in prestack Kirchhoff time migration and the image of PS converted waves. However, he only gave a numerical analysis. Here I bridge this gap by investigating C-wave imaging sensitivity of anisotropic parameters in the use of a set of dip models. I use ray-tracing synthetics and EAP's Cxtools for processing. Key factors are γ_0, P-to-S vertical velocity ratio, γ_{eff}, effective P-to-S velocity ratio, V_c, PS velocity and χ, the PS-wave anisotropic parameter.

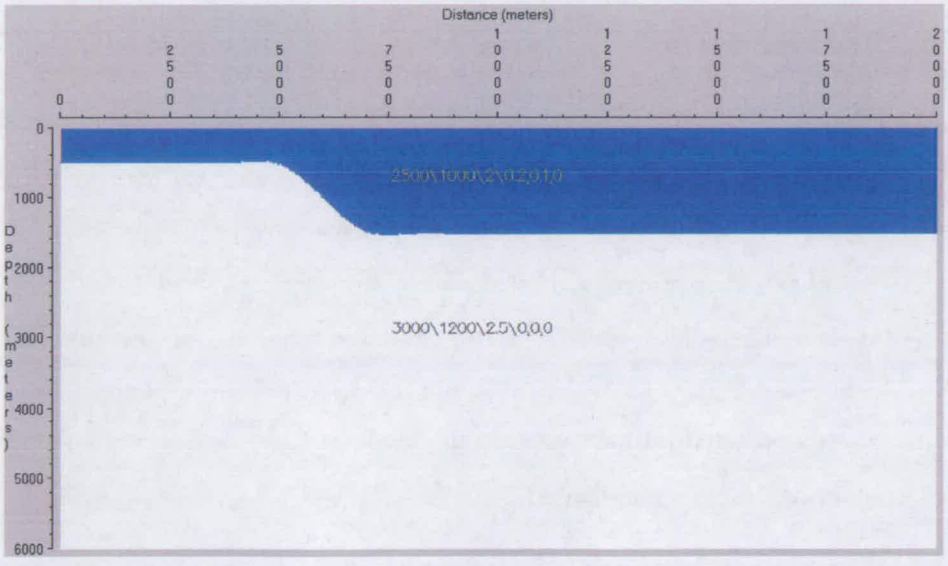

Figure 5.5: The single layer model used for sensitivity analysis with 27^0 dip right to left. Note that only the right part of the model is shown, the left part contains a 27^0 dip layer left to right direction.

Layer1	V_p	2500 m/s
	V_s	1000 m/s
	ρ	2.0 g/cm^3
	ε	0.2
	δ	0.1
Layer2	V_p	3000 m/s
	V_s	1200 m/s
	ρ	2.5 g/cm^3

Table 5.1: Layer properties of the model in Figure 5.5.

Shot point interval	25 m	Receiver line length	+ - 3000 m
Sampling rate	2 ms	Group interval	50 m
Number of channels	121	Record length	4 s

Table 5.2: Acquisition system parameters of the model in Figure 5.5.

Figure 5.5 shows a simple model I used for a C-wave imaging sensitivity study. In order to analyse the structural effect, there is one 27^0 dip layer contained in the model. The dip layer is symmetric and only the right part is shown. Table 5.1 shows the physical parameters used for modelling and Table 5.2 describes the acquisition system. The velocity ratio γ in this model is fixed at 2.5. The generated synthetics are processed in the use of Cx-tools and the migration images are obtained. To study the parameter sensitivities, I perturb the value of one parameter at each time and keep the other parameters unchanged.

5.5.1 Effects of γ_0 errors on migration images

The first parameter checked is γ_0. To investigate the relationship between γ_0 and the dipping events, I migrate the data set with various values of γ using PKTM. From Table 5.1, the exact value of γ_0 should be 2.5 in order to obtain the true image. I sort the whole dataset into two parts, the negative offset and the positive offset, and migrate them separately in order to investigate any horizontal movement between them. In Figures 5.6, 5.7 and 5.8, γ_0 is set to 1.5, 2.5 and 3.5. Compared with Figure 5.7, the images in Figure 5.6 and 5.8 show very little difference and minimal positioning error, even when the error in γ_0 is as large as 45% (Figure 5.6), but there is a weakened stack response for flanks dipping away from shooting direction (left to right). Since the effect of the error in γ_0 is small, it is impossible to estimate γ_0 accurately, but is not necessary to do so.

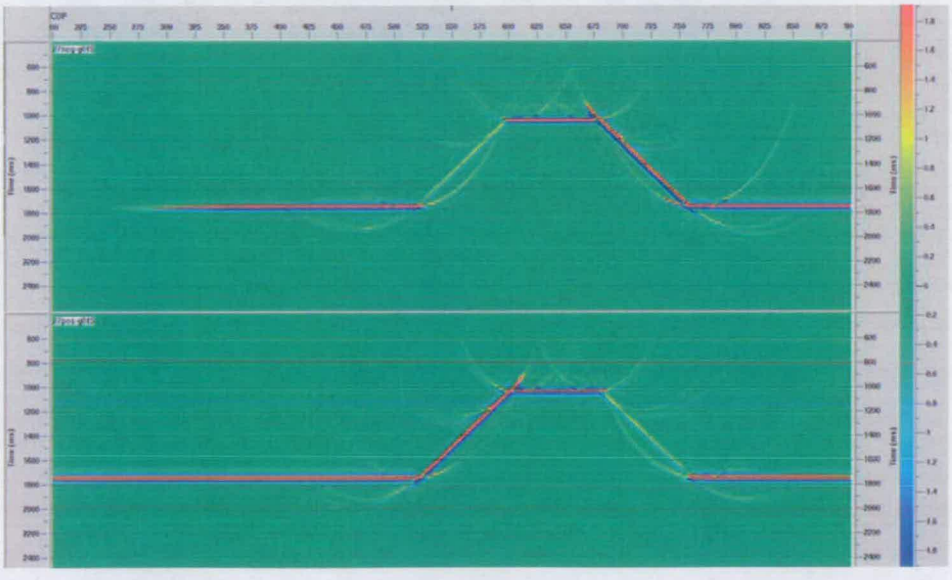

Figure 5.6: Migration images of the 27^0 dip isotropic model with γ_0 set to 1.5. The negative offset image is on top and the positive offset image is at the bottom.

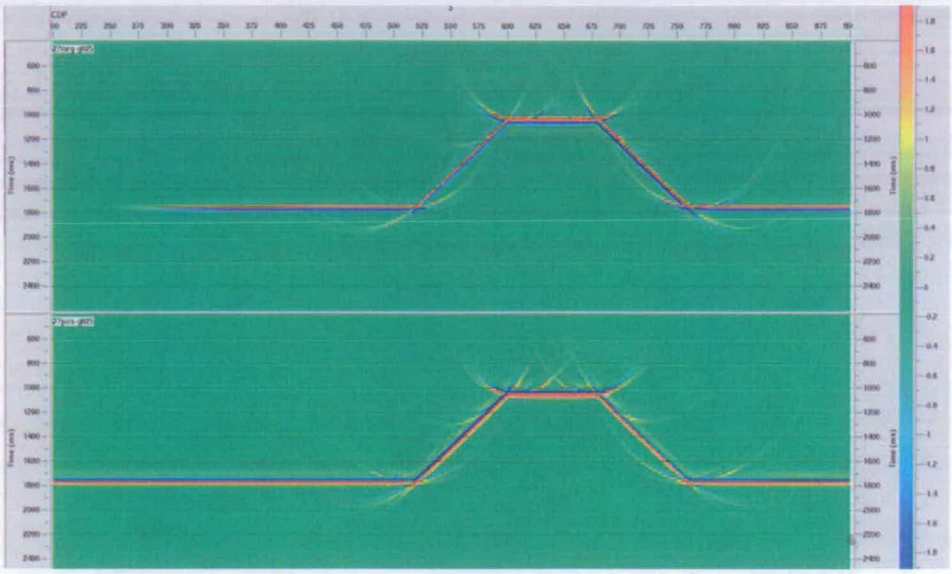

Figure 5.7: Migration images of the 27^0 dip isotropic model with γ_0 set to 2.5 (the true value). The negative offset image is on top and the positive offset image is at the bottom.

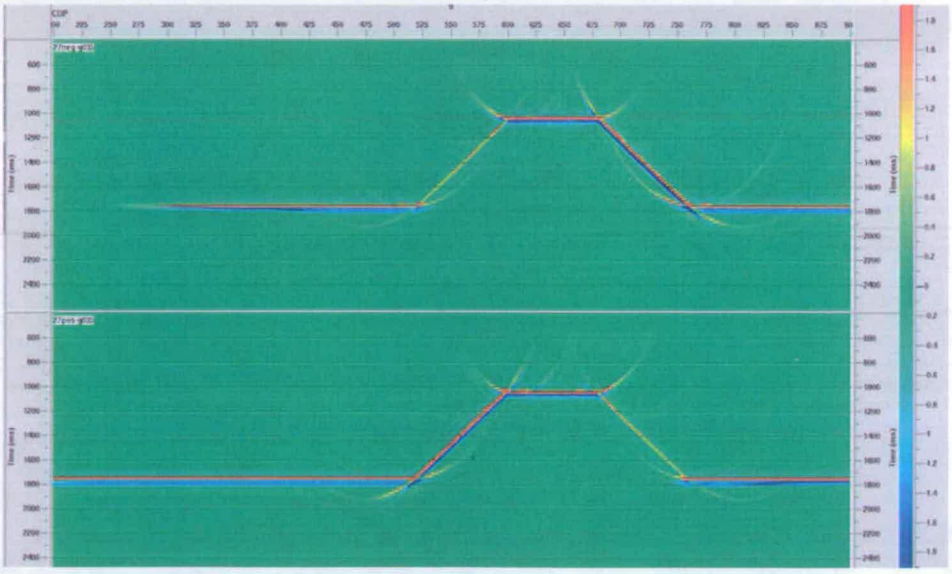

Figure 5.8: Migration images of the 27^0 dip isotropic model with γ_0 set to 3.5. The negative offset image is on top and the positive offset image is at the bottom.

5.5.2 Effects of γ_{eff} errors on migration images

Next I check the γ_{eff} effect. As we know, in PKTM processing, the image at a point in the CIP gather is constructed by summing the energy from all possible scatter points with given vertical traveltime and offset over all different available source and receiver locations. The image point is the intersection of all diffraction curves that have the same offset but a different source and receiver. Figure 5.9 presents a series of CIP gathers with different γ_{eff} values: γ_{eff} is set to 1, 1.5, 2, 3, 3.5 and 4 from the top down. Note the exact value of γ_{eff} should be 2.5 to flatten the CIP gather. In Figure 5.9, the differences among these CIP gathers are significant, and it is clear that γ_{eff} controls the symmetry of different offsets, and errors in γ_{eff} may result in large mispositioning in images. It is also interesting that the movement of positive dip direction is larger than that of negative dip direction. From Figure 5.10 to 5.14, PKTM images are shown with various γ_{eff} perturbations from 1.5 to 3.5. If there are γ_{eff} errors, images of the negative offset part and positive offset part are located incorrectly in positions to both sides of the correct position. This indicates that the average position of positive and negative images does not give the correct position.

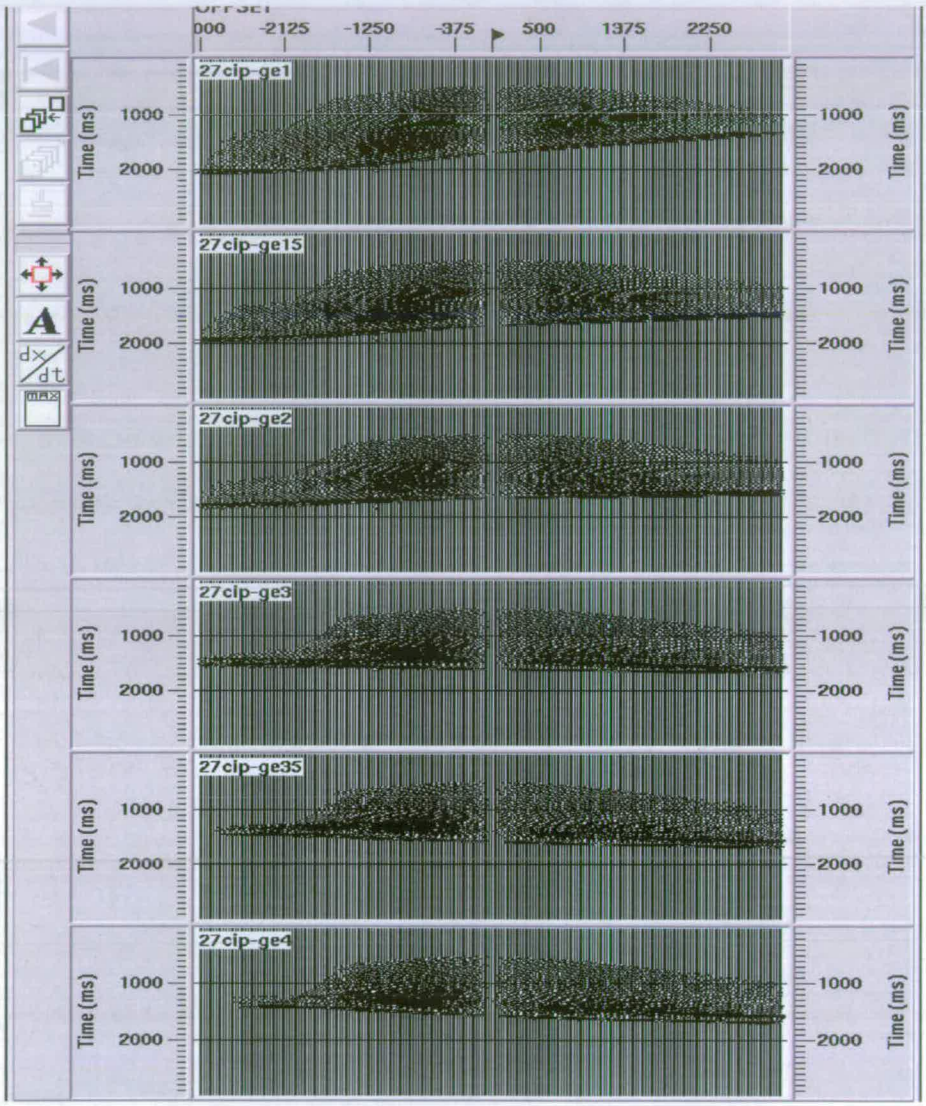

Figure 5.9: CIP gather images with various γ_{eff} values. From top to bottom, γ_{eff} values are set to 1, 1.5, 2, 3, 3.5 and 4. The exact value needed to flatten the gather is 2.5.

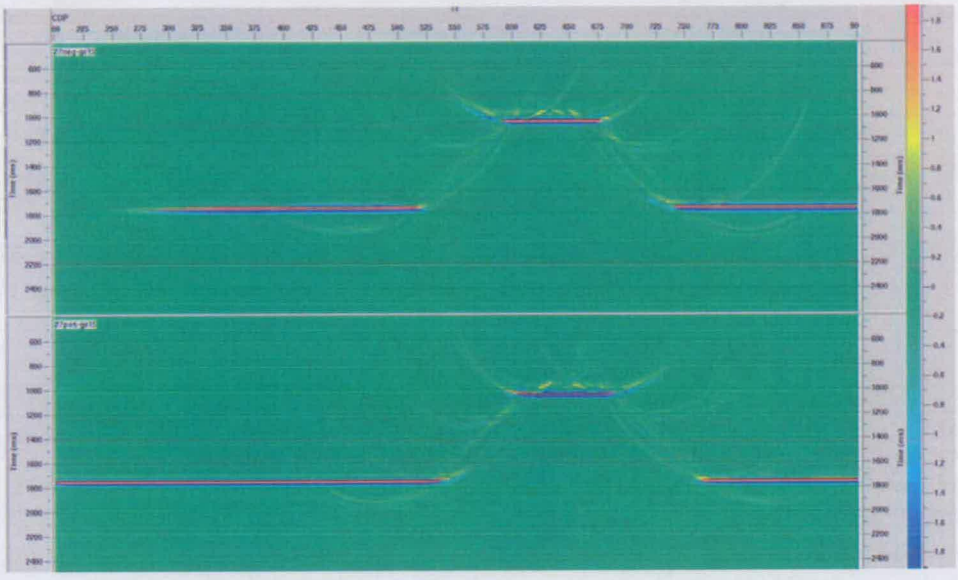

Figure 5.10: Migration images of the 27^0 dip isotropic model with γ_{eff} set to 1.5. The negative offset image is on top and the positive offset image is at the bottom.

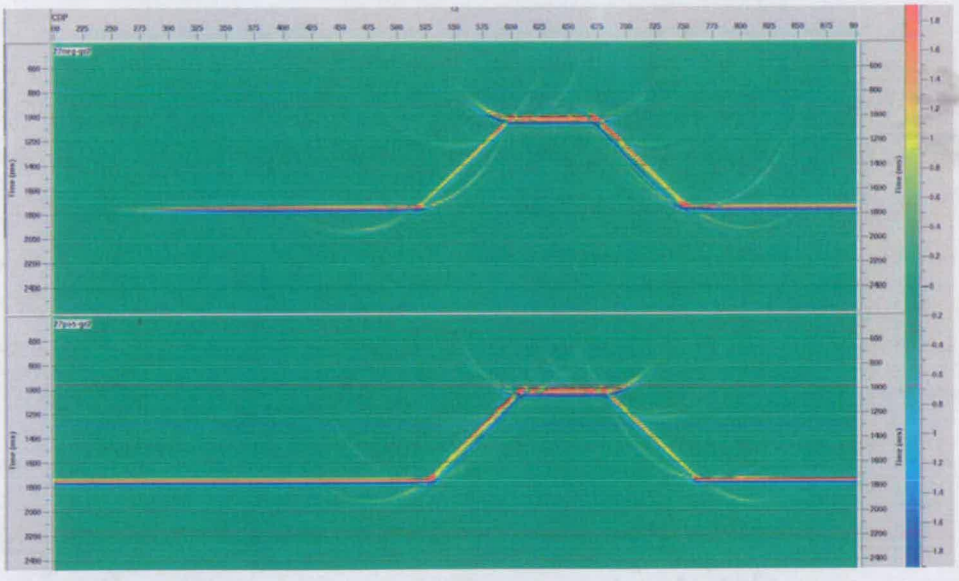

Figure 5.11: Migration images of the 27^0 dip isotropic model with γ_{eff} set to 2. The negative offset image is on top and the positive offset image is at the bottom.

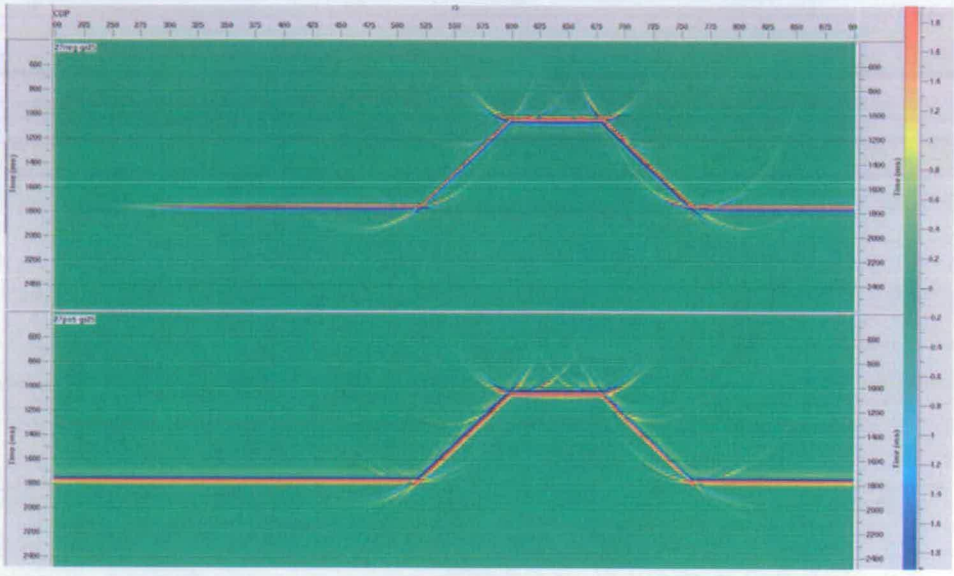

Figure 5.12: Migration images of the 27^0 dip isotropic model with γ_{eff} set to 2.5. The negative offset image is on top and the positive offset image is at the bottom. This is the exact value needed for the same results from the negative and positive offsets.

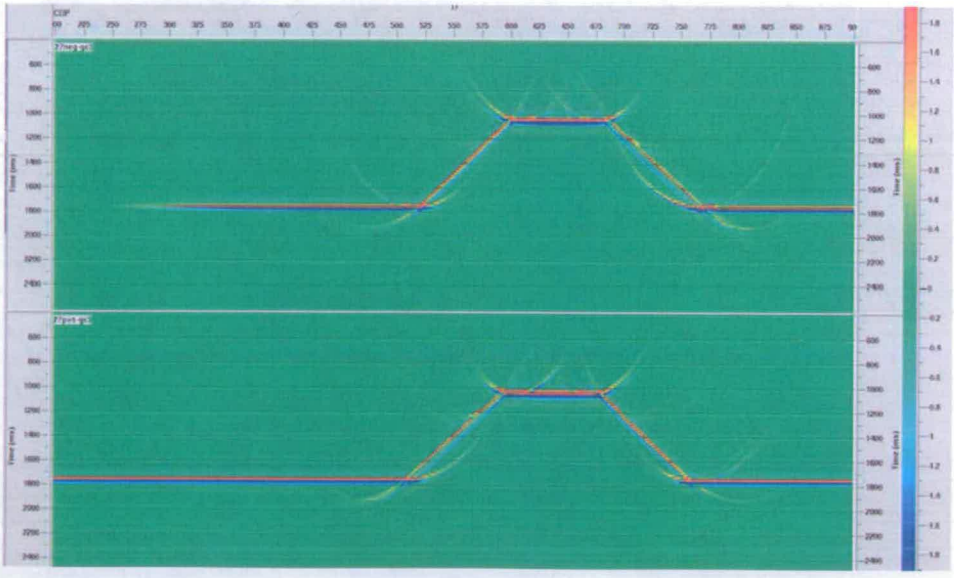

Figure 5.13: Migration images of the 27^0 dip isotropic model with γ_{eff} set to 3. The negative offset image is on top and the positive offset image is at the bottom.

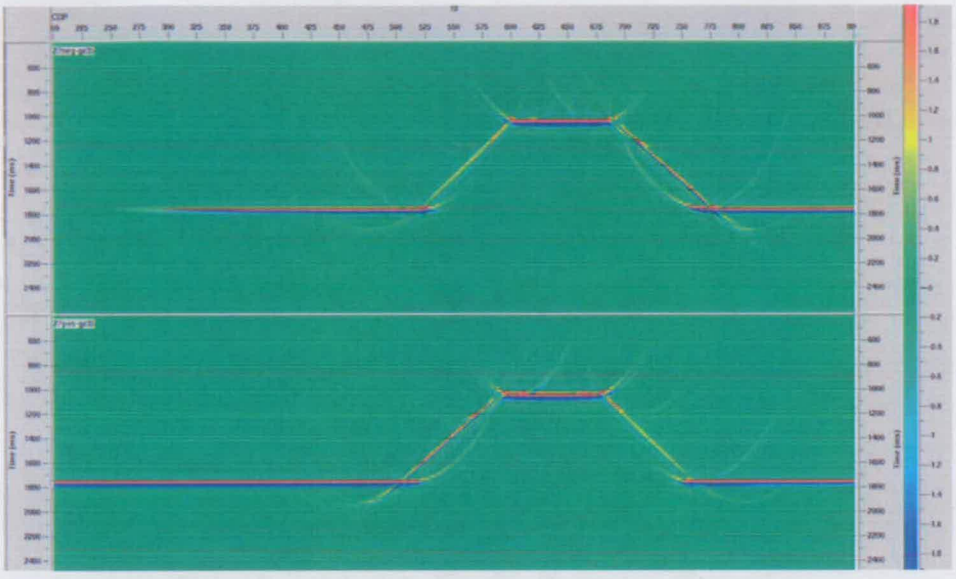

Figure 5.14: Migration images of the 27^0 dip isotropic model with γ_{eff} set to 3.5. The negative offset image is on top and the positive offset image is at the bottom.

5.5.3 Effects of velocity errors on migration images

Velocity errors are investigated in this section. Figure 5.15 shows a set of CIP gathers with velocity variation. From the top down, velocities are set to 95%, 98%, 99%, 101%, 102% and 105% of the exact value. In contrast to γ_{eff}, errors in velocity make dips flap, but there is the same effect for both the positive and negative offsets. Migration images of both offsets are shown from Figure 5.16 to 5.20, using different velocities. Figure 5.18 shows the results obtained using the true velocity model. Images are quite sensitive to velocity errors: even one percent of velocity error can cause an obvious degradation of the images. Compared with Figure 5.10 to 5.14, the location of images of velocity errors are worse relative to the correct position than the mislocation caused by γ_{eff} errors: 10% of the error in γ_{eff} has comparable effects on the migrated image to an error in velocity of 2%. In reality, we usually first update velocity based on the flatness of events. Once the events are flattened, we can assume focusing the image is mainly determined by γ_{eff} error and then update γ_{eff}

based on focusing the image, following the workflow suggested in Figure 5.1 by Dai and Li (2005).

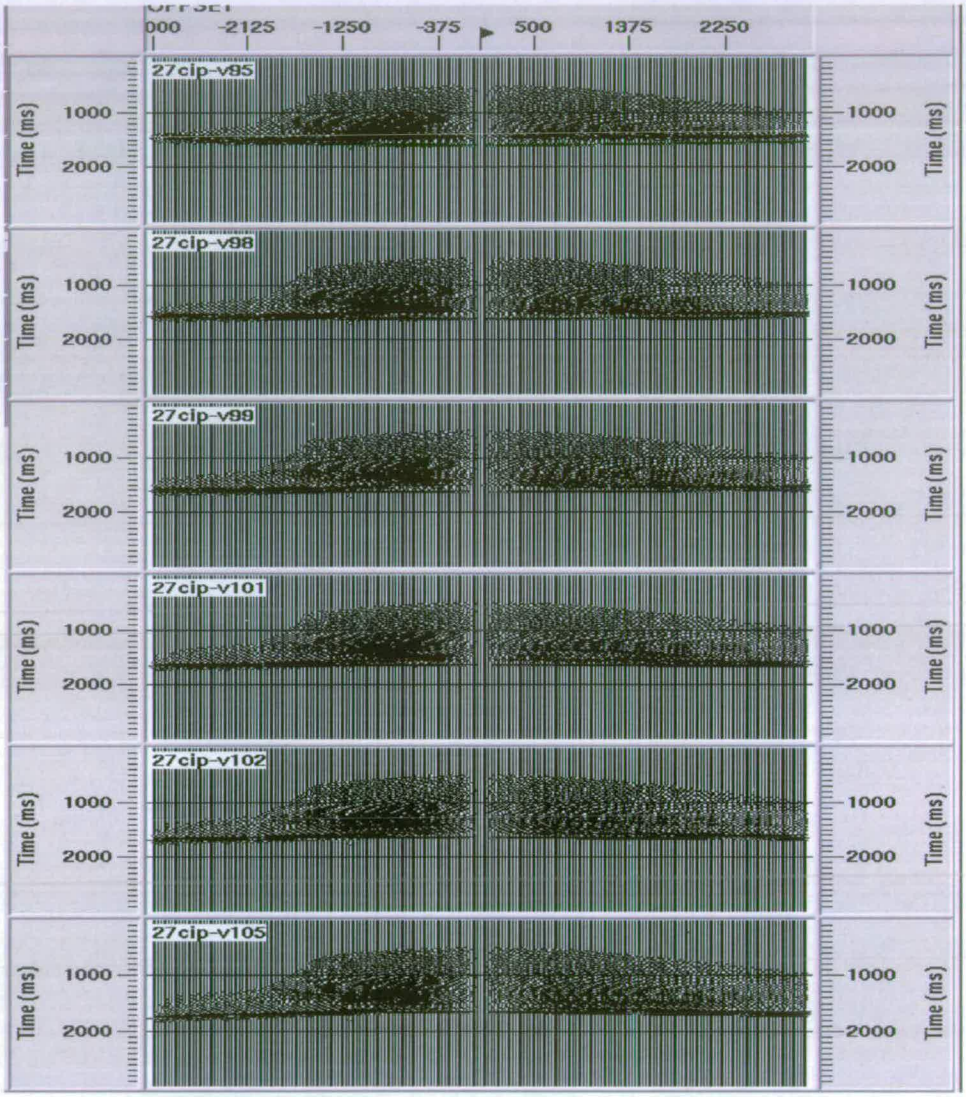

Figure 5.15: CIP gather images with various velocity values. From top to bottom, velocities are set to 95%, 98%, 99%, 101%, 102% and 105% of the exact value.

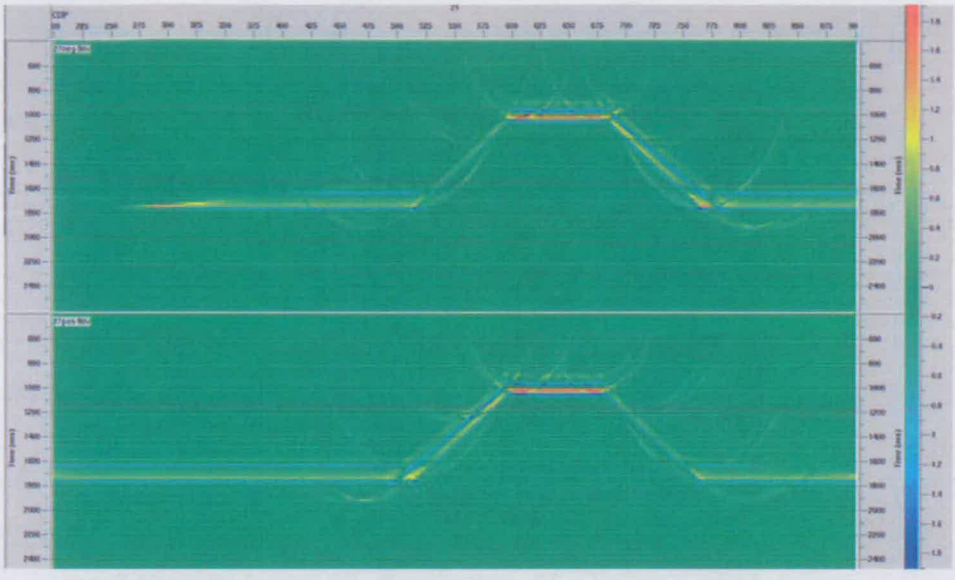

Figure 5.16: Migration images of the 27° dip isotropic model with velocity set to 90% of the exact value. The negative offset image is on top and the positive offset image is at the bottom.

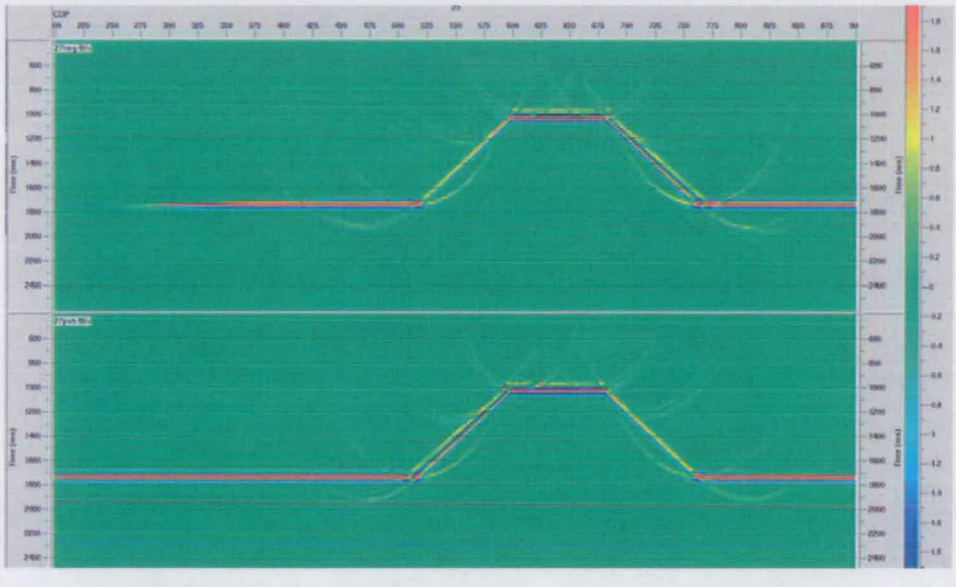

Figure 5.17: Migration images of the 27° dip isotropic model with velocity set to 95% of the exact value. The negative offset image is on top and the positive offset image is at the bottom.

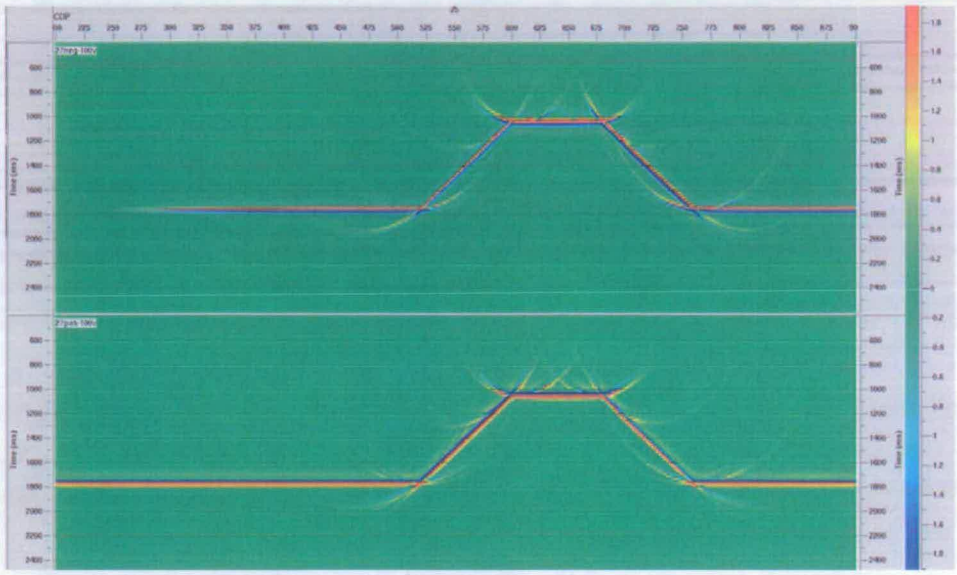

Figure 5.18: Migration images of the 27^0 dip isotropic model with velocity set to the exact value. The negative offset image is on top and the positive offset image is at the bottom.

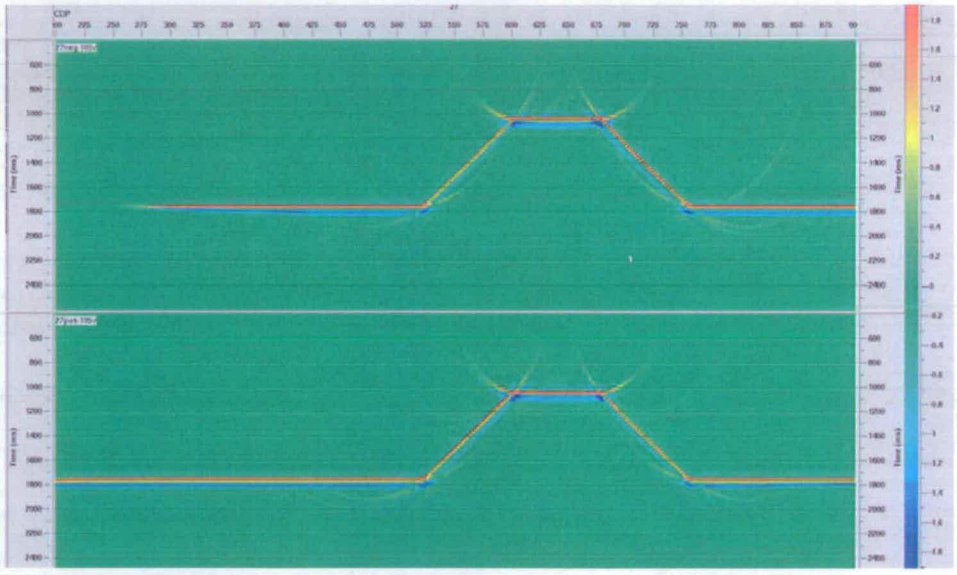

Figure 5.19: Migration images of the 27^0 dip isotropic model with velocity set to 105% of the exact value. The negative offset image is on top and the positive offset image is at the bottom.

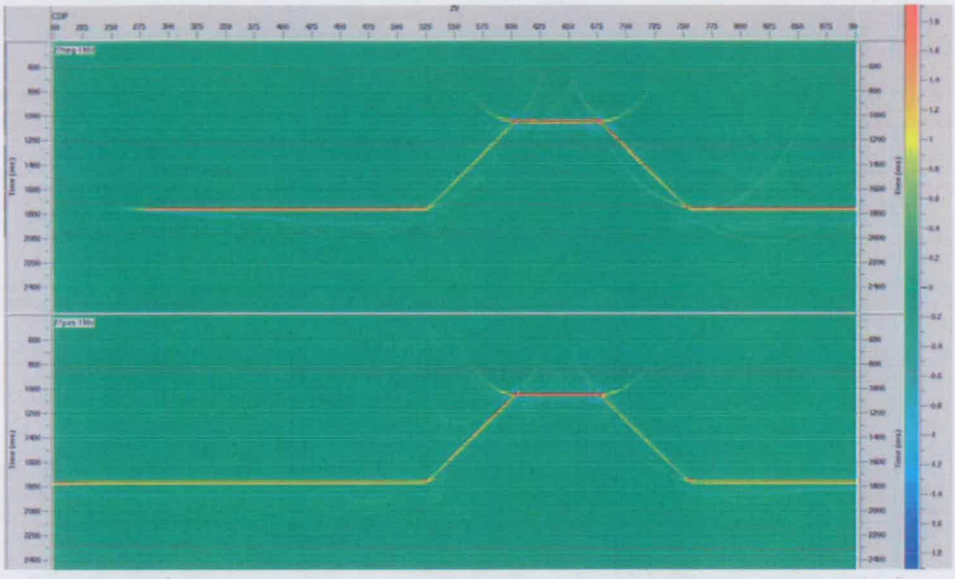

Figure 5.20: Migration images of the 27^0 dip isotropic model with velocity set to 110% of the exact value. The negative offset image is on top and the positive offset image is at the bottom.

5.5.4 Effects of anisotropy errors on migration images

Anisotropy plays an important role in PS-wave imaging. Following the same procedures, I check the imaging sensitivities caused by χ errors. Figure 5.21 shows CIP gathers with different χ values of -0.2, -0.1, -0.05, 0.05, 0.1 and 02. The exact value of χ to flatten the CIP gather should be 0.1. It is obvious that χ also controls the symmetry of different offsets, similar to γ_{eff}, and errors in χ_{eff} can cause mispositioning in images. From Figure 5.22 to 5.24, PKTM images of both directions of offsets are shown. Images are located incorrectly in positions on both sides of the correct position so that the average position of both positive and negative images is not correct. However, due to the correlation between γ_{eff} error and χ error, it is difficult to separate them in real data analysis. This partially explains why PS-wave imaging requires more effort.

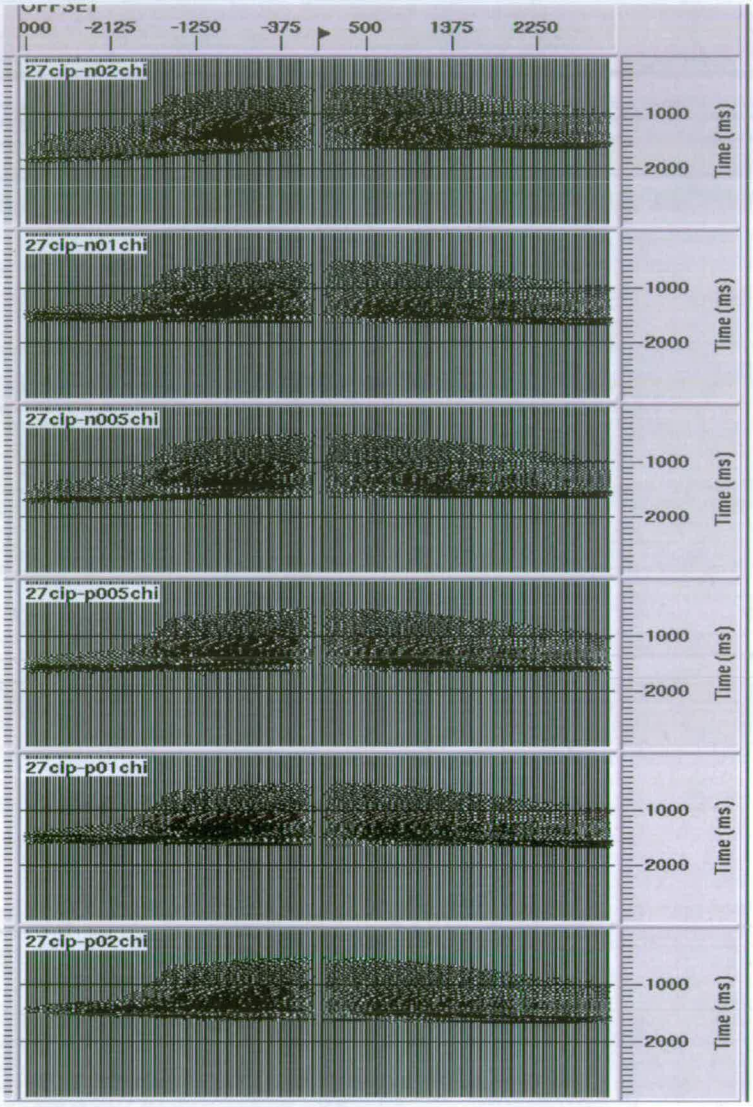

Figure 5.21: CIP gather images with anisotropic χ values. From top to bottom, χ is set to –0.2, -0.1, -0.05, +0.05, +0.1 and +0.2. The exact value required to flatten the CIP gather is 0.1.

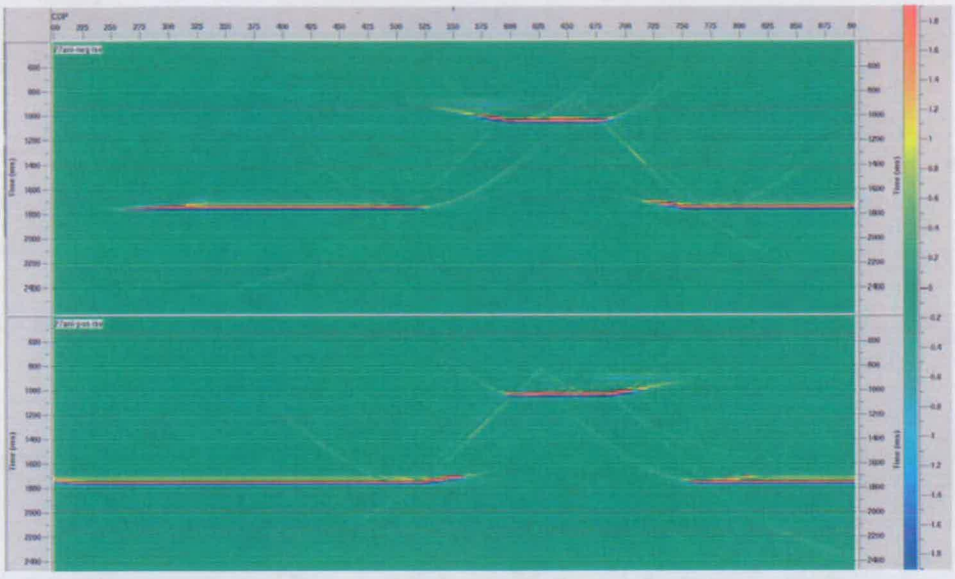

Figure 5.22: Migration images of the 27^0 dip anisotropic model with χ set to 0. The negative offset image is on top and the positive offset image is at the bottom.

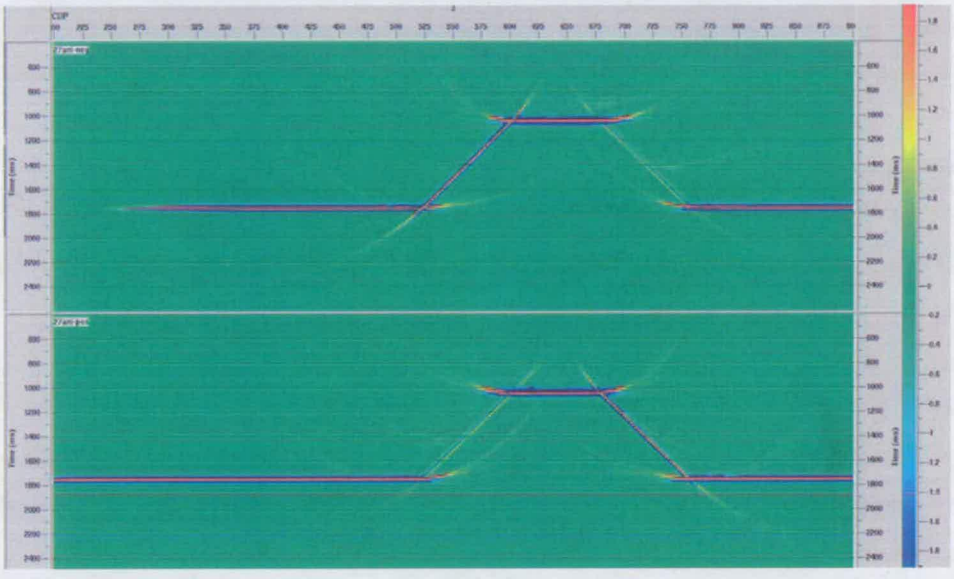

Figure 5.23: Migration images of the 27^0 dip anisotropic model with χ set to 0.1 (true value). The negative offset image is on top and the positive offset image is at the bottom.

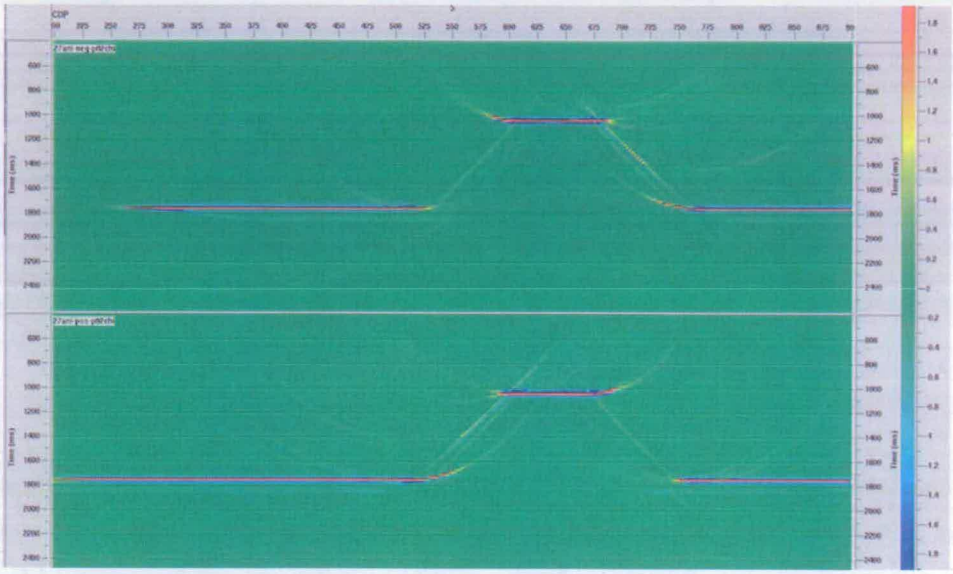

Figure 5.24: Migration images of the 27^0 dip anisotropic model with χ set to 0.2. The negative offset image is on top and the positive offset image is at the bottom.

5.5.5 Effects of γ_{eff} errors on various dipping targets

So far I have discussed error effects on the migrated image for 27^0 dip targets. To further understand the structural effect on imaging, I will now discuss the γ_{eff} error effect on the migrated image for a 45^0 dip target. From Figure 5.25 to 5.28, images with γ_{eff} of 2, 2.5, 3 and 3.5 are shown. As we expect, due to γ_{eff} errors, images are located incorrectly in positions on both sides of the correct position. Moreover, in comparison to Figures 5.10 to 5.14, the positioning errors are bigger. This synthetic example confirms the theoretical finding (Dai, 2006) that the effect of error in γ increases with increasing dip angle of a target. The larger the dip angle is, the larger will be the effect of the error in γ_{eff}.

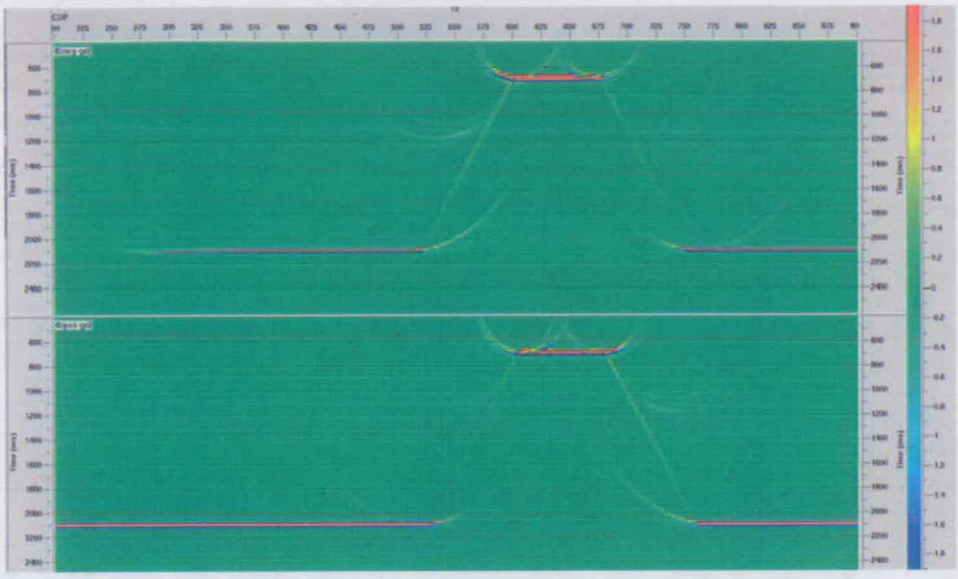

Figure 5.25: Migration images of the 45^0 dip isotropic model with γ_{eff} set to 2. The negative offset image is on top and the positive offset image is at the bottom.

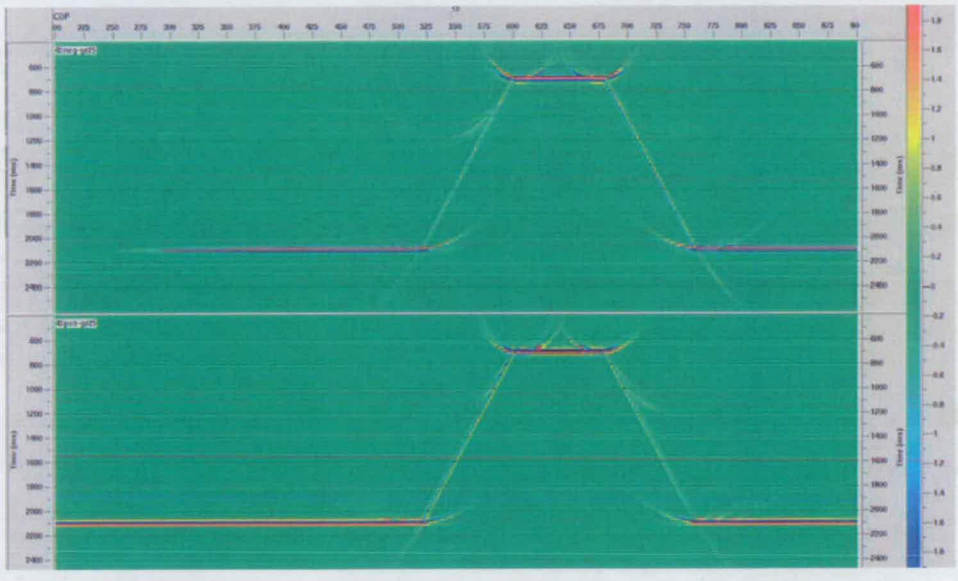

Figure 5.26: Migration images of the 45^0 dip isotropic model with γ_{eff} set to 2.5 (true value). The negative offset image is on top and the positive offset image is at the bottom.

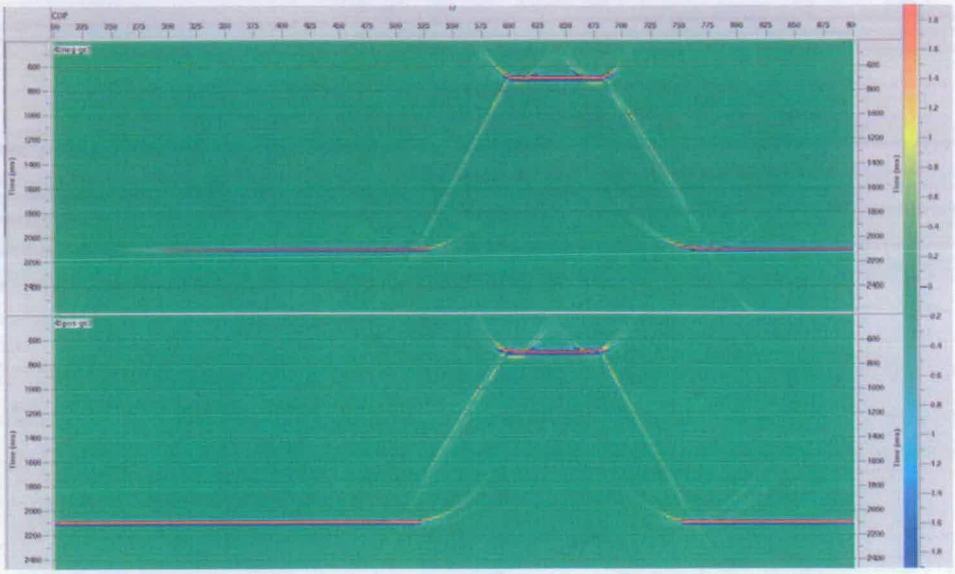

Figure 5.27: Migration images of the 45^0 dip isotropic model with γ_{eff} set to 3. The negative offset image is on top and the positive offset image is at the bottom.

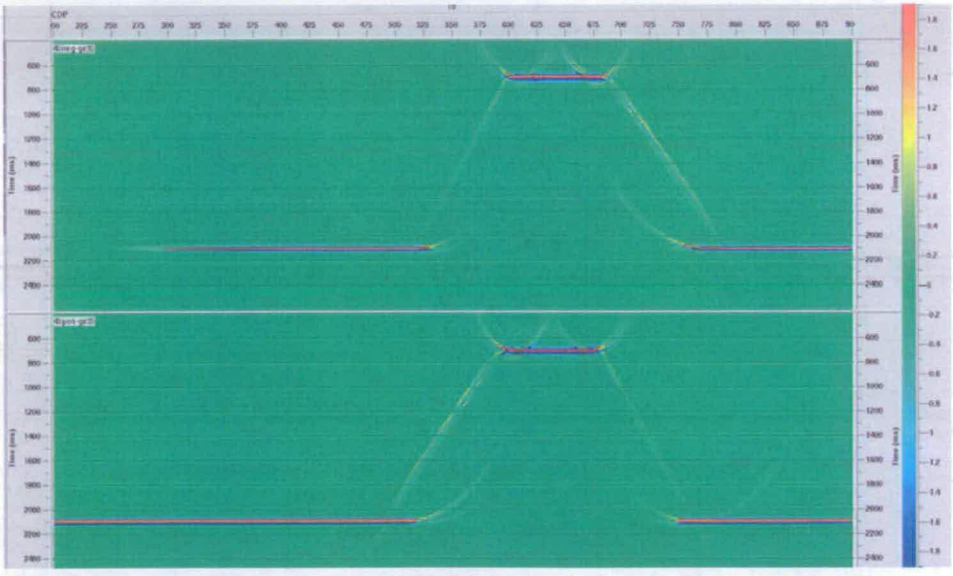

Figure 5.28: Migration images of the 45^0 dip isotropic model with γ_{eff} set to 3.5. The negative offset image is on top and the positive offset image is at the bottom.

5.6 Summary

In this Chapter I have created and processed a number of isotropic and anisotropic synthetic datasets for understanding and quantifying model-building sensitivities associated with PS imaging in the presence of varying dip and polar anisotropy. I have reviewed various PS-wave processing techniques, especially the EAP's PS migration velocity analysis workflow. I have also reviewed a number of modelling methods and used finite difference modelling synthetics to demonstrate the effect of a shear wave low velocity layer.

The sensitivity analysis is to understand how errors in any one parameter translate into errors in positioning, conversion-point smear, mis-stacking, and ultimate degradation in image quality. Four parameters, γ_0, γ_{eff}, V_c and χ, are perturbed and different dipping targets are included in the models. It is found that γ_0 errors can cause minimal positioning error, but weaken the stack response for flanks dipping away from the shooting direction. γ_{eff} error can result in large horizontal mispositioning and the average positions of positive and negative images do not give the correct position. V_c errors make dips 'flap' but have the same effect for both directions of offsets. Moreover, the PS wave is affected more severely by error in velocity than error in γ_{eff}. Thus, in PS-wave data processing only V_c needs to be estimated accurately, and a rough estimation value of γ_{eff} can be used in PKTM for imaging. The degree of γ_{eff} error is proportional to the angle of dip. Anisotropy errors in χ and errors in γ_{eff} are correlated and errors in them have the same effect. These findings are useful for processing PS-wave data, understanding PS-wave behaviour, and for PS-wave imaging.

Chapter 6

Analysis of the Emilio PS-wave data for azimuthal anisotropy

6.1 Introduction

In this Chapter I present the fracture analysis results in the use of PS wave data. Firstly I give an overview of the Emilio post-stack migrated dataset. Then I review the linear transform technique (LTT). I extend the LTT to hand the PS-wave and develop a Seismic Unix program, *sultt,* which is specially designed for reflection acquisition system. A special case of four-component acquisition system, two orthogonal sources and two orthogonal receivers, has been studied to demonstrate the use of the technique. The application of this program allows fracture strike and fracture intensity properties to be estimated. These results are correlated with the subsurface fracture systems in the Emilio field.

6.2 The Emilio post-stack migrated dataset

The Emilio post-stack migrated dataset is made available by Eni-Agip. For the 3D/4C Emilio processing, a preliminary azimuthal analysis of PS prestack data allowed an early orientation of horizontal geophones into the overburden principal component directions. This strategy greatly benefited the entire processing flow (Gaiser *et al.*, 2001; Vetri *et al.*, 2002; Vetri *et al.*, 2003).

Vetri *et al* (2003) firstly selected twenty-seven azimuth-receiver super-gathers (the combination of seven adjacent receivers) on a regular grid and at well locations to investigate azimuthal anisotropic effects. These consist of stacked radial and transverse traces at every 10^0 in azimuth (Figure 6.1a). They found out that the principal azimuth (fast) was dominantly $N75^0E$, but in some places $N165^0E$, over the entire area down to Gessoso Solfifera (the very bright easily registered PP and PS reflector, see Figure 3.2). Then, all horizontal geophones were rotated from conventional radial and transverse into $N75^0E$ and $N165^0E$ directions. This produced fast, PS1, and slow, PS2, converted-wave volumes.

They then independently tested processing parameters were in two butterfly restricted azimuth volumes (centred on $N75^0E/N255^0E$ and $N165^0E/N345^0E$). However, they applied the same processing sequence and parameters to both data sets; the split shear-wave reflections had their own appropriate move out functions applied.

The wide-azimuth acquisition geometry allowed the data to be split into eight separate common-azimuth volumes, each including an azimuth range of 45^0. Due to the asymmetry of PS-raypaths, opposite azimuths were kept separate, resulting in eight PS volumes (Figure 6.1b). The Emilio migrated data contain nearly a half million CDPs. Figure 6.2 is the cdp distribution map. CDP ranges from 353785 to 729795.

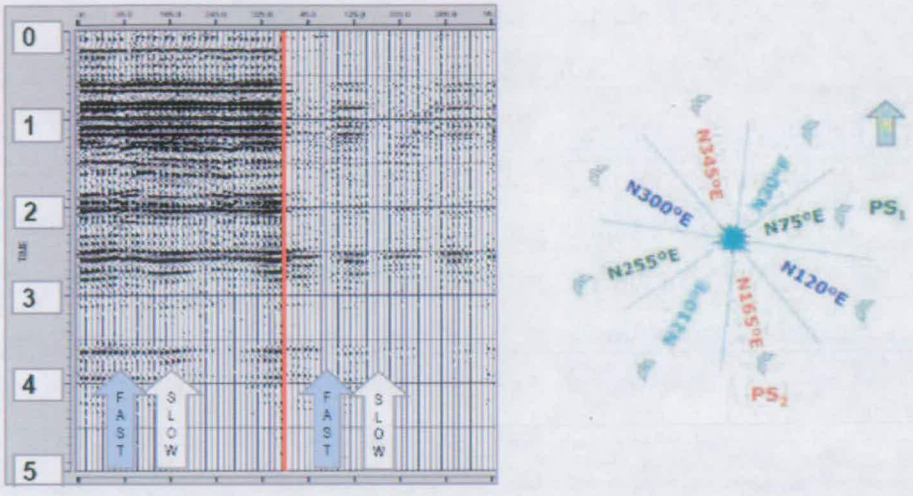

(a) (b)

Figure 6.1: The principal azimuth (fast) was dominantly $N75^0E$ and the orientation of eight PS common azimuths created for azimuthal processing: (a) stacked radial and transverse traces in one location (Vetri, *et al.*, 2002) (b) coordinate system used for consequent common-azimuthal processing (*Vetri, et al*, 2003).

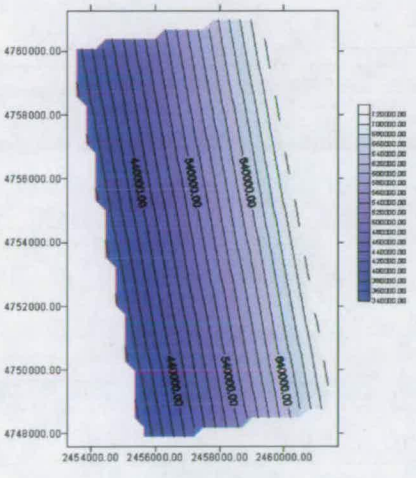

Figure 6.2: The whole CDP map of the Emilio migrated data. CDP ranges from 353785 to 729795 and CDP number is used for the colour bar. X-axis is Rec-x and Y-axis is Rec-y.

The comparison between the eight PS1 and the eight PS2 migrated volumes highlights evident energy variation due to azimuthal anisotropy (Figures 6.3 and 6.4). Clearly when the azimuths are consistent with the principal anisotropy axes, the energy is at maximum, orthogonal azimuths show almost no energy at all. Note the principal anisotropy direction is from the top section before 3 seconds, where the black box is, we can only see energy changes within this range. However, orthogonal azimuthal components show an increase in energy with time as expected with azimuthal anisotropy.

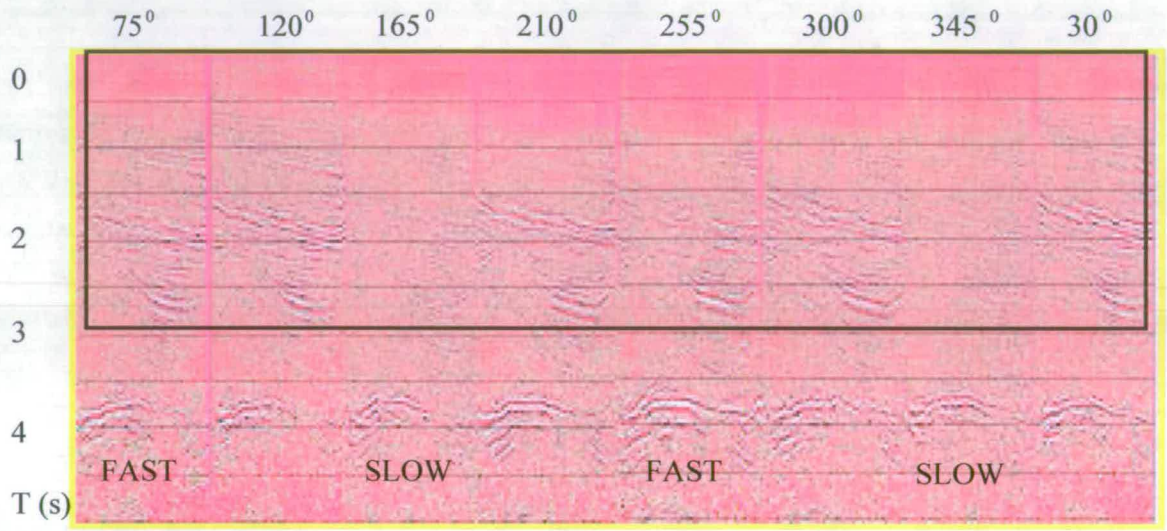

Figure 6.3: PS1 migrated data volume. In particular where the wavefield is oriented in the same direction as the horizontal geophone, the energy in the corresponding panel is at a maximum (75^0 and 255^0). When they are orthogonal (165^0 and 345^0), energy is very low but increasing with time as expected with azimuthal anisotropy. Note the principal anisotropy direction is from the top section before 3 seconds, where the black box is, we can only see energy changes within this range.

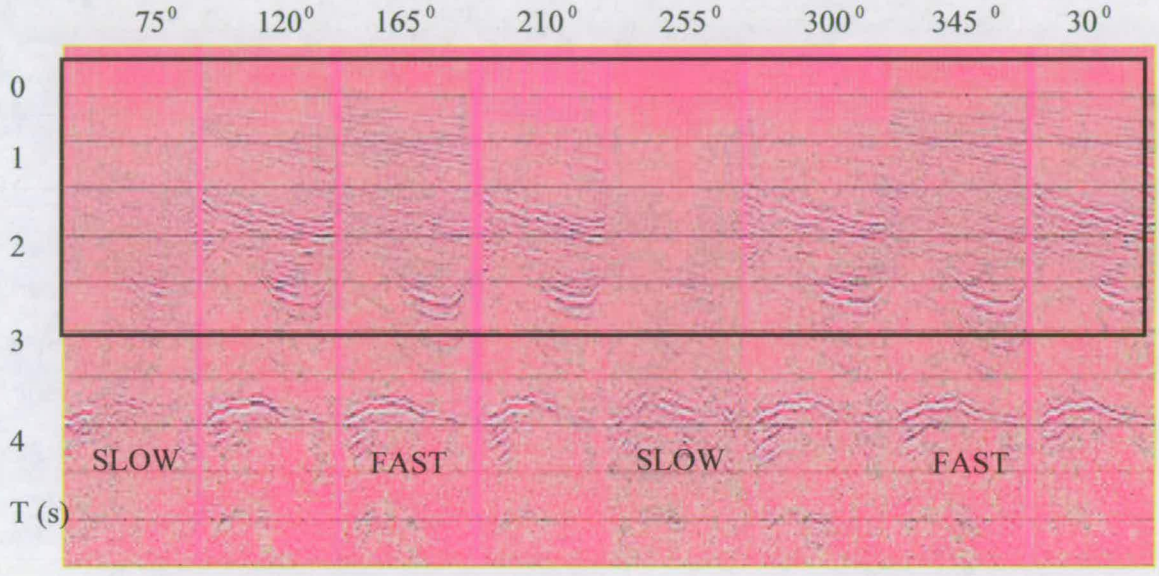

Figure 6.4: PS2 migrated data volume. In particular where the wavefield is oriented in the same direction as the horizontal geophone, the energy in the corresponding panel is at a maximum (165^0 and 345^0). When they are orthogonal (75^0 and 255^0), energy is very low but increasing with time as expected with azimuthal anisotropy. Note the principal anisotropy direction is from the top section before 3 seconds, where the black box is, we can only see energy changes within this range.

6.3 The linear transform technique

As we know, in a homogeneous crack-induced anisotropic medium caused by a single set of parallel vertical cracks in an isotropic matrix rock, the recorded four components can be expressed in terms of the properties of the uncracked matrix and the properties of the faster and slower split shear-waves. The properties of the matrix and the faster and slower split shear-waves can be determined from the recorded components. However, the success of such applications depends on the success of the processing techniques for determining the faster and the slower split shear-waves.

Most techniques for analysing shear-wave splitting employ rotation procedures and tend to be computing intensive (Alford, 1986; MacBeth and Crampin, 1991). Li and Crampin suggested a linear transform technique which showed efficiency and simplification. The technique transforms the recorded four-component seismic data (two source orientations recorded by two receivers) by four linear transforms so that the shear-wave motion is linearized under many conditions.

This linear transform technique can be used to invert the polarizations of faster split shear-wave, and the time delays between faster and slower split shear-waves. Moreover, it allows the time series of the faster and the slower split shear-waves to be separated deterministically.

6.3.1 Basic definitions

Figure 6.5 shows the coordinate system with origin at the surface. Figure 6.5a shows the source geometry. Unit vectors *e1* and *e2* are at angles of α' and β' from the X-direction respectively. Figure 6.5b shows the surface projection of the geophone geometry, where e1 and e2 are at angles α and β from the x-direction, respectively. All angles are measured clockwise form the X- and x- directions.

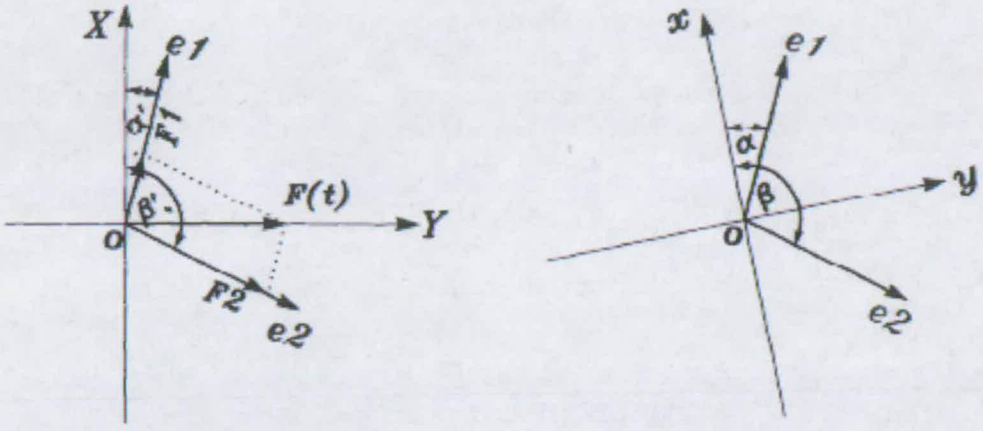

(a) Source geometry (b) Geophone geometry

Figure 6.5: Diagrams showing the acquisition geometry and coordinate system in the horizontal plane. (a) Source geometry, where X and Y are two orthogonal sources with signature F(t), e1 and e2 are the directions of faster and slower split shear-waves received at the geophone position, and F1 and F2 are two decompositions of the source vector F. (b) Geophone geometry, where x and y are two orthogonal geophones possibly in a different orientation from the sources, and e1 and e2 are the same as (a) (Li and Crampin, 1993).

We can further assume that the angle between the faster and slower split waves is preserved throughout the homogeneous material, that is, $\beta' - \alpha' = \beta - \alpha$. Here I define the principal time series qS1(t) of the faster split shear-wave is the time series received at a receiver when the receiver and a source vector F with signature F(t) are both polarized along e1. Similarly, time series qS2(t) of the slower split shear-waves is the time series received when the receiver and the source vector F are both polarized along e2.

Two transformed time series $V1(t)$ and $V2(t)$ are introduced as the sum and difference of the principal time series $qS1(t)$ and $qS2(t)$:

$$V1(t) = qS1(t) + qS2(t) \quad (6.1)$$
$$V2(t) = qS1(t) - qS2(t) \quad (6.2)$$

6.3.2 Four-component data equations

Here the four-component time series are defined as that $s_{ij}(t)$ recorded from X- and Y- sources (j=1,2) at x- and y- geophones (i=1,2). The four geophone components $s_{11}(t)$, $s_{21}(t)$, $s_{12}(t)$ and $s_{22}(t)$ from the X- and Y-sources can be written as:

$$s_{11}(t) = [qS1(t)\sin\beta'\cos\alpha - qS2(t)\sin\alpha'\cos\beta] = \sin(\beta' - \alpha') \quad (6.3)$$
$$s_{21}(t) = [qS1(t)\sin\beta'\sin\alpha - qS2(t)\sin\alpha'\sin\beta] = \sin(\beta' - \alpha') \quad (6.4)$$
$$s_{12}(t) = [-qS1(t)\cos\beta'\cos\alpha + qS2(t)\cos\alpha'\cos\beta] = \sin(\beta' - \alpha') \quad (6.5)$$
$$s_{22}(t) = [-qS1(t)\cos\beta'\sin\alpha + qS2(t)\cos\alpha'\sin\beta] = \sin(\beta' - \alpha') \quad (6.6)$$

In the LTT, a linear transform is applied to the four-component data sets:

$$\xi(t) = s_{11}(t) - s_{22}(t) \quad (6.7)$$
$$\eta(t) = s_{21}(t) + s_{12}(t) \quad (6.8)$$
$$\varsigma(t) = s_{11}(t) + s_{22}(t) \quad (6.9)$$
$$\chi(t) = s_{12}(t) - s_{21}(t) \quad (6.10)$$

In case of orthogonally polarized shear-waves, as in zero-offset VSPs or stacked sections (e.g., the Emilio migrated data volumes) (Figure 6.2), noting that $\alpha = \alpha'$, $\beta = \beta'$, and $\beta = \pi/2 + \alpha$, the above four equations can be written as:

$$\xi(t) = [qS1(t) - qS2(t)]/\cos(2\alpha) \quad (6.11)$$
$$\eta(t) = [qS1(t) - qS2(t)]/\sin(2\alpha) \quad (6.12)$$
$$\varsigma(t) = qS1(t) + qS2(t) \quad (6.13)$$
$$\chi(t) = 0 \quad (6.14)$$

It shows that the time series V2(t)=qS1-qS2 represents linear motion in coordinate system (ξ, η) with angle $\alpha' + \alpha$ to the axis ξ, and time series V1(t)=qS1+qS2 represents linear motion in coordinate system (ς, χ) with angle $\alpha' - \alpha$ to the ξ axis.

From the properties of linear motion, I can uniquely determine V1 and V2, and $\alpha' + \alpha$ and $\alpha' - \alpha$. Thus, qS1= (V1+V2)/2 and qS2= (V1-V2)/2, and α' and α can be determined, and the orientation of the geophone can be estimated from $\alpha' - \alpha$.

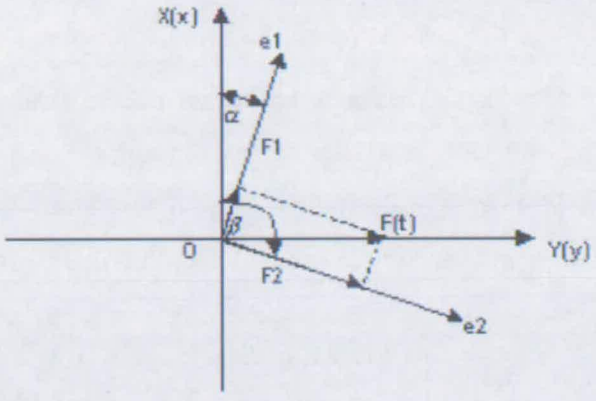

Figure 6.6: Diagram shows the acquisition geometry and coordinate system in the horizontal plane in case of orthogonally polarized shear-waves. X and Y are two orthogonal sources with signature F(t), x and y are two orthogonal geophones in same orientation from the sources, e1 and e2 are the directions of faster and slower split shear-waves received at the geophone position, and F1 and F2 are two decompositions of the source vector F.

6.4 Inversion for fracture strike and density

At the beginning stage of PS-wave analysis, I used the shear-wave analysis package (SWAP), which was developed by the Edinburgh Anisotropy Project (EAP), for a feasibility study. However, the SWAP is designed specially for the vertical seismic profile (VSP) data, so a proper tool has to be developed. As discussed above, the linear transform technique (Li and Crampin, 1993) can handle reflection dataset and can be used here. I develop a program called *sultt* in the Seismic Unix (SU) format.

The migrated data volumes of the Emilio data can be treated as orthogonally polarized shear-waves: $N75^0E$ and $N165^0E$ are two fixed receiver directions and PS1 and PS2 volumes each has eight separate sources from different azimuths.

Therefore, the Emilio migrated data can be seen as a dataset with sixteen sources and each source has two receivers.

6.4.1 Test of the *sultt* program

I developed a SU format program called *sultt* to realize the LTT and tested it on the Emilio dataset. I first select some common-depth points (CDP) to test the sultt program. I select two orthogonally polarized shear-waves and form the following four-component (two source orientations recorded by two receivers) matrix:

$$\begin{bmatrix} PS1AZ120^0\,E(s11) & PS2AZ120^0\,E(s21) \\ PS1AZ210^0\,E(s12) & PS2AZ210^0\,E(s22) \end{bmatrix} \tag{6.15}$$

$$\begin{bmatrix} PS1AZ210^0\,E(s11) & PS2AZ210^0\,E(s21) \\ PS1AZ300^0\,E(s12) & PS2AZ300^0\,E(s22) \end{bmatrix} \tag{6.16}$$

$$\begin{bmatrix} PS1AZ300^0\,E(s11) & PS2AZ300^0\,E(s21) \\ PS1AZ30^0\,E(s12) & PS2AZ30^0\,E(s22) \end{bmatrix} \tag{6.17}$$

$$\begin{bmatrix} PS1AZ30^0\,E(s11) & PS2AZ30^0\,E(s21) \\ PS1AZ120^0\,E(s12) & PS2AZ120^0\,E(s22) \end{bmatrix} \tag{6.18}$$

The selected CDPs range from 529000 to 529050. In total eight different matrices can be formed. Figure 6.7 shows the above four matrices. Figure 6.7(a), 6.7(c), 6.7(e) and 6.7(g) are the input data, and Figure 6.7(b), 6.7(d), 6.7(f) and 6.7(h) are the output after applying *sultt*. We can clearly see the two off-diagonal components, s12 and s21, have been minimized and the faster and the slower shear-waves have been separated.

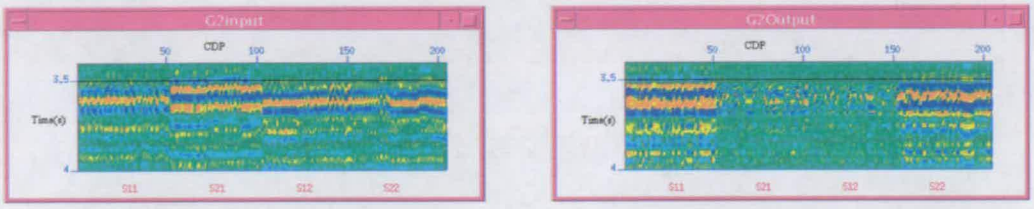

(a) Matrix I (before LTT) **(b) Matrix I (after LTT)**

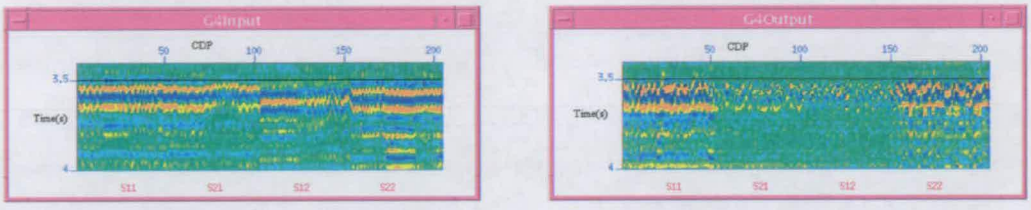

(c) Matrix II (before LTT) **(d) Matrix II (after LTT)**

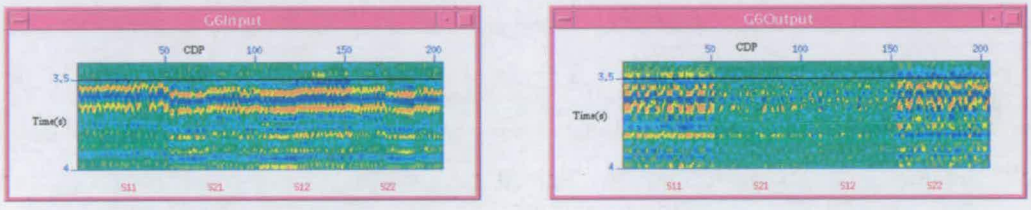

(e) Matrix III (before LTT) **(f) Matrix III (after LTT)**

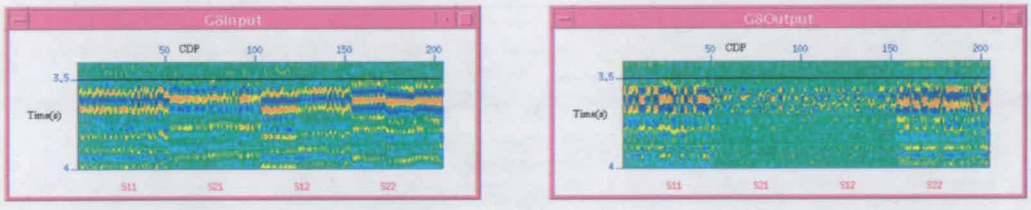

(g) Matrix IV (before LTT) **(h) Matrix IV (after LTT)**

Figure 6.7: Examples of applying the *sultt* program. We can clearly see two off-diagonal components (s12 and s21) have been minimized in each matrix. Note the component names s11, s12, s21, s22 are shown at the bottom of each picture.

6.4.2 Fracture maps

The Emilio migrated data contain nearly a half million CDPs, which range from 353785 to 729795. I choose four azimuthal components as shown below:

$$\begin{bmatrix} PS1AZ75^0\,E(s11) & PS2AZ75^0\,E(s21) \\ PS1AZ165^0\,E(s12) & PS2AZ165^0\,E(s22) \end{bmatrix} \tag{6.19}$$

Then I applied *sultt* to the whole data volume and got the fast PS orientation map (Figure 6.8) and fracture density (time-delay) map (Figure 6.9) at the target interval (time window 3400ms-4000ms). Figure 6.8, the fracture polarization map, shows that there exist two orthogonal fracture systems at the target in the Emilio field (yellow and blue colours mean two different orientations). In some areas the azimuth distribution seems to indicate the existence of fault domains, where there is consistent orientation and density. Note that where there is fast anisotropy direction (yellow colour in Figure 6.8), there is also high fracture density (red colour in Figure 6.9), which means that there is a correlation between fracture orientation and fracture densities. In particular the crest of the anticline, where most of the wells were drilled, is characterized both $N80^0E$ PS1 (PS-fast) azimuth, in good agreement with the highest anisotropy values.

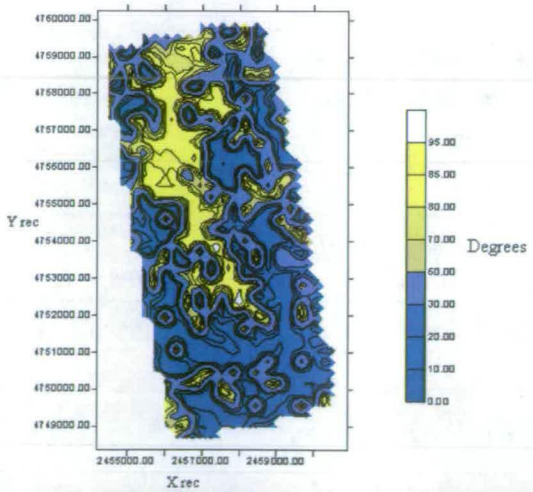

Figure 6.8: Fast PS polarization map at the target in the Emilio field.

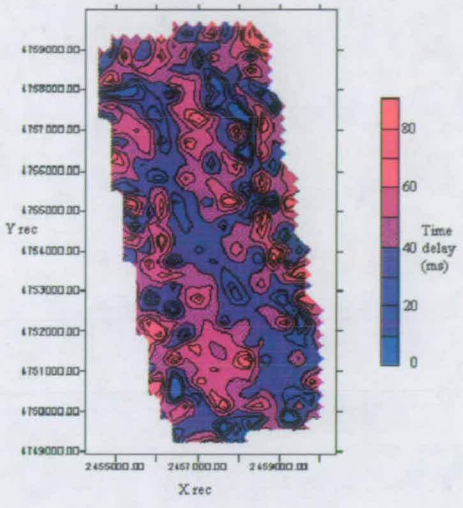

Figure 6.9: Fracture density (time delay) map at the target in the Emilio field. Note that red colour means higher fracture density and blue colour means lower fracture density.

6.5 Comparison with previous results

Figure 6.10 compares the previous analysis results and my analysis results using the PS-waves from the target in the Emilio field. Figure 6.10(a) is the fracture orientation map after Vetri *et al.* (2003). Figure 6.10(b) is my fracture orientation result after applying the *sultt* program. There is a correlation between the two fracture orientation maps, in particular the crest of the anticline ($N80^0E$). However, we do recognize that differences between the two results could be due to a more complicated fracture system (e.g., dipping fractures).

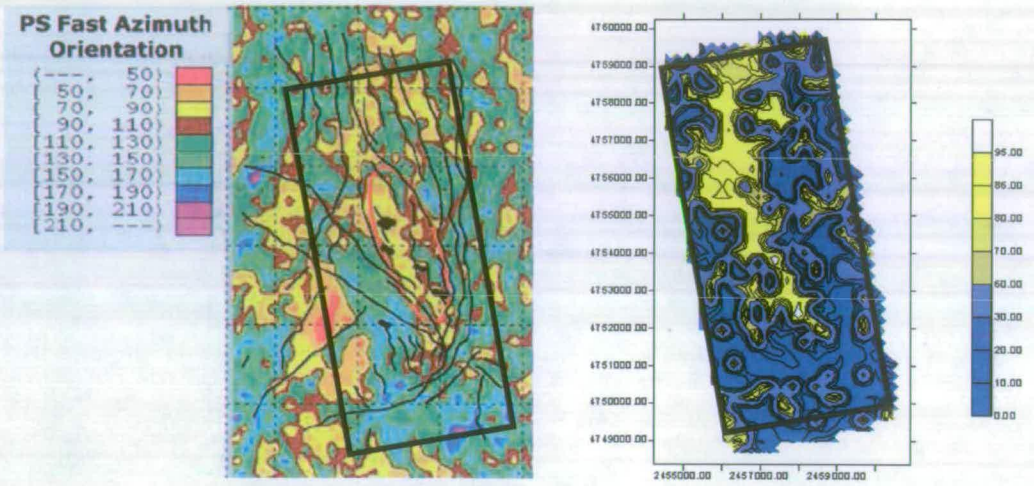

(a) P-wave result (b) PS-wave result

Figure 6.10: Comparison of the previous results and my results using *sultt*: (a) fracture orientation map (Vetri *et al.*, 2003) and (b) fracture orientation map from *sultt*. Note two black rectangles are used to confine the areas for comparison.

6.6 Summary

Early orientation of horizontal geophones into the overburden principal component directions greatly simplifies the whole process flow. This produced PS1 and PS2 converted-wave components. Each component can be split into eight common azimuth volumes with an azimuth range of 45^0. The comparison between the eight PS1 and eight PS2 migrated volumes shows obvious energy variation due to azimuthal anisotropy.

The linear transform technique is applied to recover various fracture attributes. I develop a *sultt* program especially for the reflection survey. The program is firstly tested and then is used in the Emilio post-stack migrated data. The analysis results are presented in form of fracture strike and density map. There is a correlation between the maps and the subsurface fracture systems in the Emilio field and the PS-wave results are consistent with the previous published results.

Chapter 7

Frequency dependent anisotropy in the Emilio post-stack migrated data

7.1 Introduction

As I discussed in Chapter 6, conventional static equivalent medium theories can be used to recover average fracture density and strike in the long wavelength limit. These theories are insensitive to frequencies. However, scattering of seismic waves due to aligned heterogeneities has been recognised to be frequency-dependent (Werner and Shapiro, 1999). Since frequency dependent anisotropy provides a possibility to invert more fracture properties, such as fracture size and spacing, it is worth checking the existence of such phenomena in the Emilio field.

In this Chapter I present the analysis results of frequency dependent anisotropy in the Emilio post-stack migrated data. I test band-pass filtering and several time-frequency analysis techniques, including the Fourier transform, short window Fourier transform and the continuous wavelet transform. The results show there is an existence of frequency dependent anisotropy in the Emilio field.

7.2 Band-pass filtering

Although there are many kinds of artificial sources used to generate seismic energy, two basic categories are represented on the final seismic section. One is minimum phase, which refers to those that begin as an abrupt pulse at the time of the reflected event. The other is zero phase, which refers to those that depict half of the pulse at the time of the event and half after (Figure 7.1).

7.2.1 Minimum Phase Pulse

An explosive source, like dynamite on land or air guns at sea, results in a burst of energy near the time of the event, followed by reverberation that diminishes with time.

7.2.2 Zero Phase Pulse

Instead of an abrupt explosion, vibrations can be sent into the ground as a `sweep' of continuously varying frequencies. In one technique, known as 'Vibroseis', a massive plate beneath a truck vibrates for a few seconds, first with low frequencies, then gradually changing into higher ones (or vice versa). Computer processing of the resulting seismic trace results in a waveform symmetrical about the time of the event.

7.2.3 Choice of band-pass filter

In the SU package (Cohen and Stockwell, 2000), there are two types of band-pass filtering techniques: a minimum-phase Butterworth filter and a zero-phase filter, i.e. *subfilt* and *sufilter*. For minimum phase signals, the phase shift is required to keep all frequencies at the same arrival time after filtering (similar to the geophone acting like a band-pass filter, which also has a non zero phase spectrum in order to maintain arrival times for all frequencies). Since air guns at sea generate minimum phase physical signals, the Butterworth filter (i.e., *subfilt*) must be used.

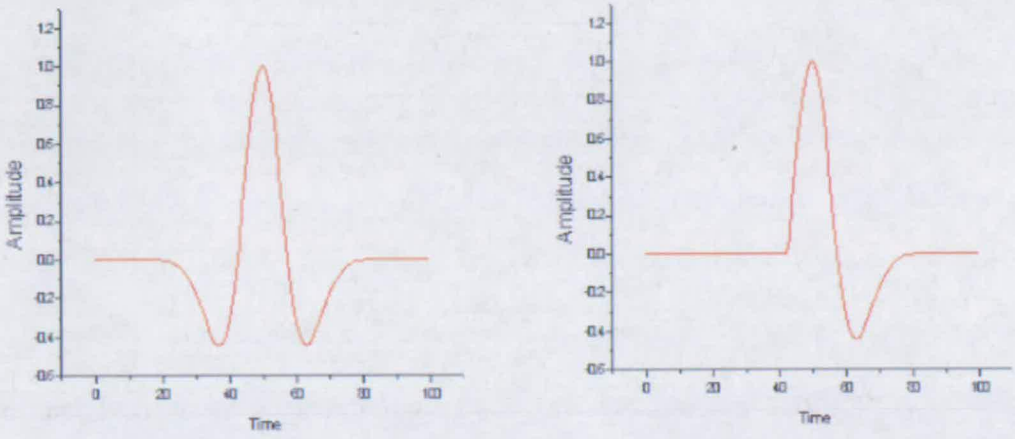

(a) Zero-phase (b) Minimum-phase

Figure 7.1: Diagram of two different types of seismic signals. (a) Zero-phase. (b) Minimum-phase.

7.2.4 Band-pass filtering analysis results

I choose two azimuthal components of the principal anisotropy axes, $PS1AZ75^0E$ and $PS2AZ165^0E$, since the data have already been separated naturally for these two components. Then I use correlation to obtain the time-delays between the fast ($PS1AZ75^0E$) and the slow ($PS2AZ165^0E$) split shear-waves.

I check the frequency range by the Ormsby bandpass filter (the minimum phase filter option) in Promax. The frequency ranges from 1Hz to 20Hz and can be filtered into two frequency bands, i.e., one low frequency band (1-4-10-14Hz) and one high frequency band (5-9-15-19Hz) (Figure 7.2).

The following analysis is done by SU. As mentioned earlier, I choose *subfilt* to filter data. The default option of *subfilt* is zero-phase band-pass filter, so zero-phase option must be set to zero and ensure the suitable filter is chosen.

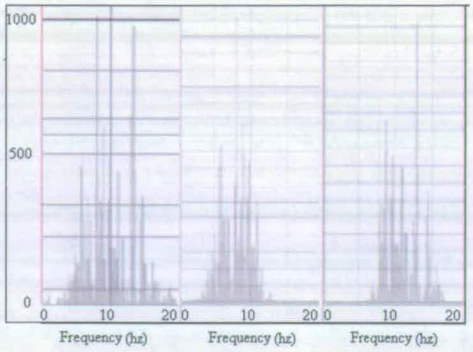

(a) Raw migrated data frequency range (b) Low frequency data (c) High frequency data

Figure 7.2: Frequency spectrums of raw, low frequency and high frequency data. Here $PS1AZ75^0$ azimuthal component CDP520759 is used to test band-pass filtering options. (a) Raw migrated data frequency range (0-20Hz). (b) Low frequency (1-4-10-14 Hz) filtered data. (c) High frequency (5-9-15-19Hz) filtered data.

I firstly resampled the fast and slow PS-wave data into 1ms. Then I filtered the data into low and high frequency bands using both zero-phase and minimum-phase filters. Next I chose two time windows, 1500ms-2100ms in the overburden and 3400ms-4000ms at the target, to correlate and generate fracture density maps. The statistics of the time-delay results (Figures 7.3 and 7.4) and time-delay maps (Figures 7.5-7.9) show that there exists difference between the results of zero-phase and minimum-phase band-pass filters.

From the time-delay maps obtained by the minimum-phase filter, Figure 7.8b and Figure 7.9b, we can see slight time-delay differences between the low and high frequency data in some locations in the Emilio field.

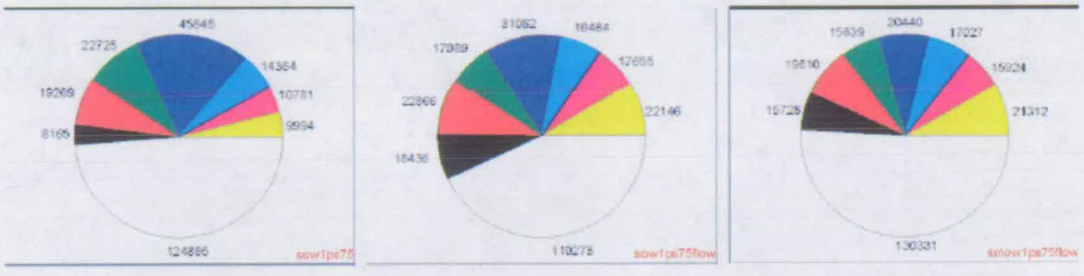

(a) Raw data (b) Zero-phase filtered low frequency (c) Minimum-phase filtered low frequency

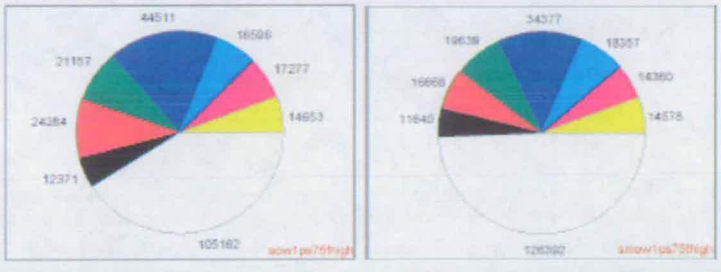

(d) Zero-phase filtered high frequency (e) Minimum-phase filtered high frequency

Figure 7.3: Time-delay statistics in the overburden (1500ms-2100ms) of $PS1AZ75^0E$ and $PS2AZ165^0$ components. Non-zero trace number is 256011 in total, and each colour denotes different time-delay range. Number is the trace number within that time-delay range. White: no data; Black:-69ms to -50ms; Red: -50ms to -30ms; Green:-30ms to -10ms; Blue: -10ms to 10ms; Cyan: 10ms to 30ms; Pink: 30ms to 50ms; Yellow: 50ms to 69ms. (a) Raw migrated data. (b) Low frequency data with zero-phase filter applied. (c) Low frequency data with minimum-phase filter applied. (d) High frequency data with zero-phase filter applied (e) High frequency data with minimum-phase filter applied.

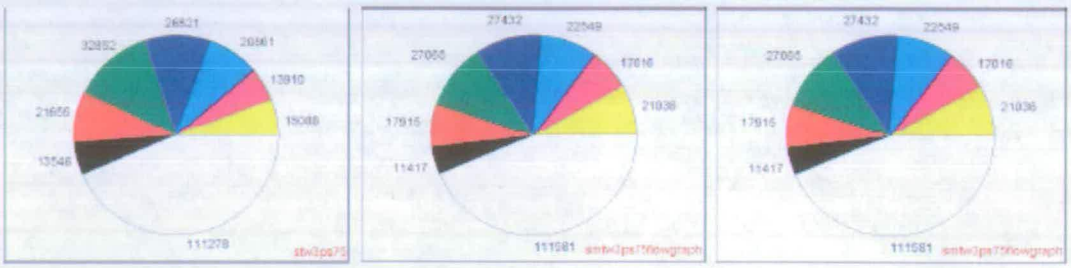

(a) Raw data (b) Zero-phase filtered low frequency (c) Minimum-phase filtered low frequency

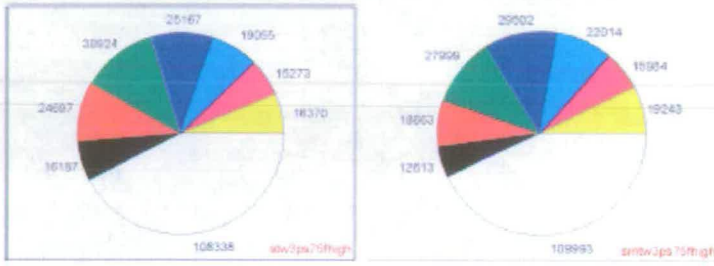

(d) Zero-phase filtered high frequency (e) Minimum-phase filtered high frequency

Figure 7.4: Time-delay statistics in the overburden (3400ms-4000ms) of $PS1AZ75^0E$ and $PS2AZ165^0$ components. Non-zero trace number is 256011 in total, and each colour denotes different time-delay range. Number is the trace number within that time-delay range. White: no data; Black:-69ms to -50ms; Red: -50ms to -30ms; Green:-30ms to -10ms; Blue: -10ms to 10ms; Cyan: 10ms to 30ms; Pink: 30ms to 50ms; Yellow: 50ms to 69ms. (a) Raw migrated data. (b) Low frequency data with zero-phase filter applied. (c) Low frequency data with minimum-phase filter applied. (d) High frequency data with zero-phase filter applied (e) High frequency data with minimum-phase filter applied.

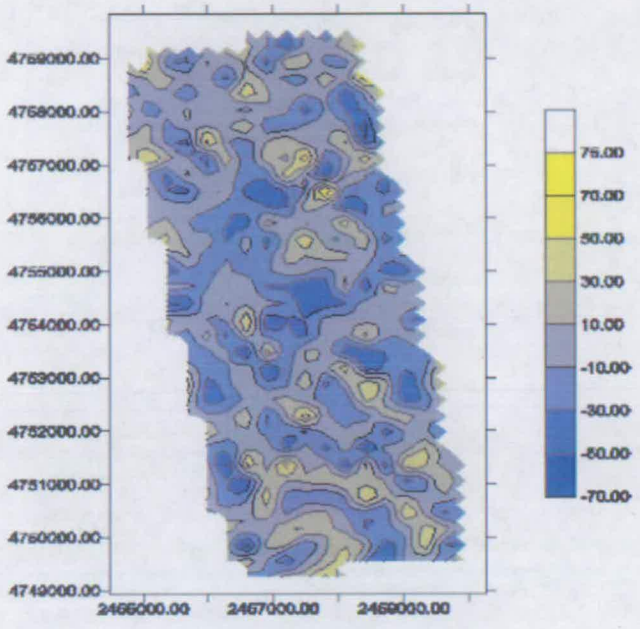

(a) Overburden (1500ms-2100ms)

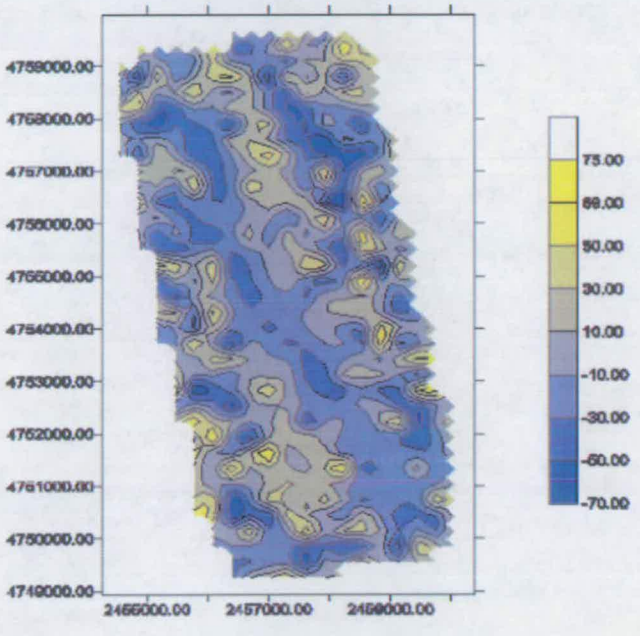

(b) Target (3400ms-4000ms)

Figure 7.5: Fracture density (time-delay) map of the raw migrated data volumes. (a) The overburden (1500ms-2100ms) fracture density (time-delay) map. (b) The target (3400ms-4000ms) fracture density map.

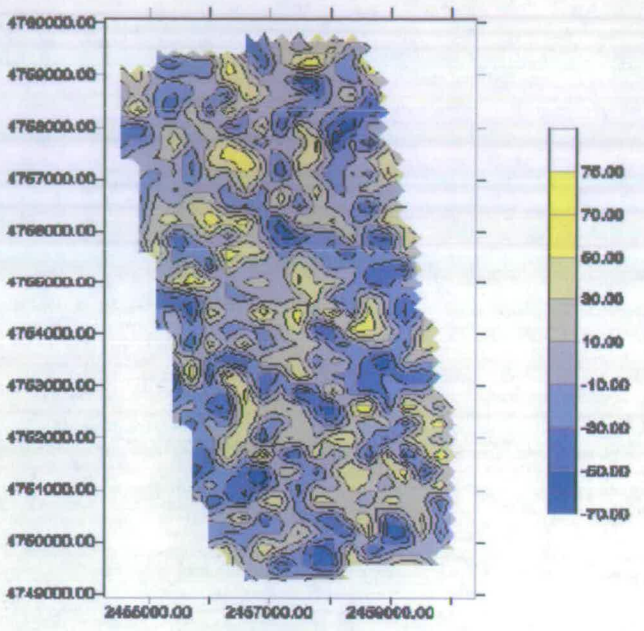

(a) Zero-phase filter

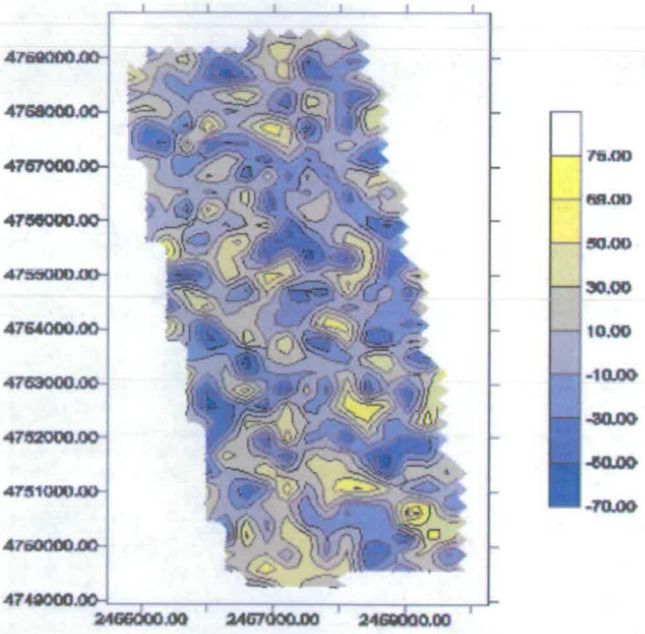

(b) Minimum-phase filter

Figure 7.6: Low-frequency data fracture density (time-delay) map of the overburden (1500ms-2100ms) with different band-pass filters. (a) Zero-phase filter. (b) Minimum-phase filter.

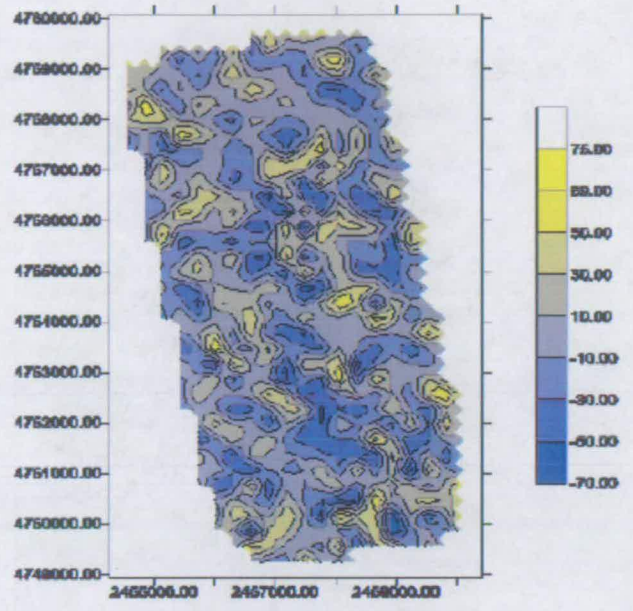

(a) Zero-phase filter

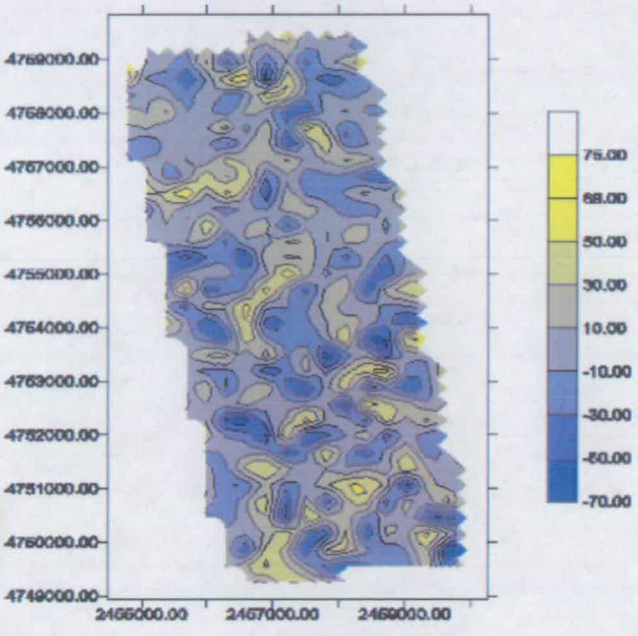

(b) Minimum-phase filter

Figure 7.7: High-frequency data fracture density (time-delay) map of the overburden (1500ms-2100ms) with different band-pass filters. (a) Zero-phase filter. (b) Minimum-phase filter.

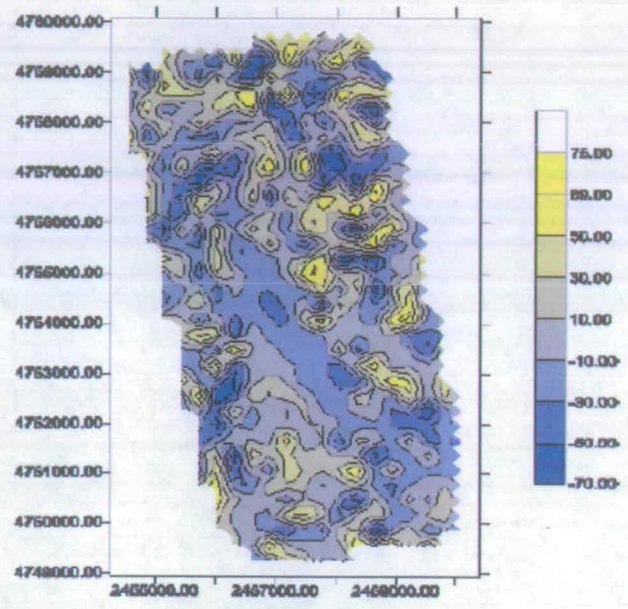

(a) Zero-phase filter

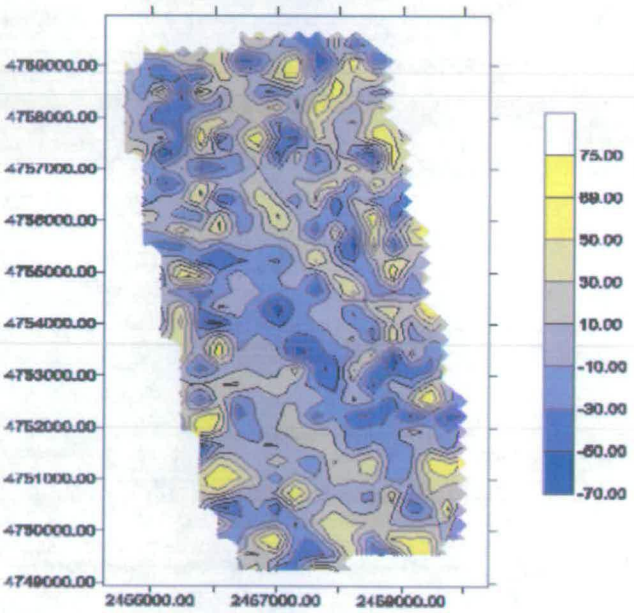

(b) Minimum-phase filter

Figure 7.8: Low-frequency data fracture density (time-delay) map of the target (3400ms-4000ms) with different band-pass filters. (a) Zero-phase filter. (b) Minimum-phase filter.

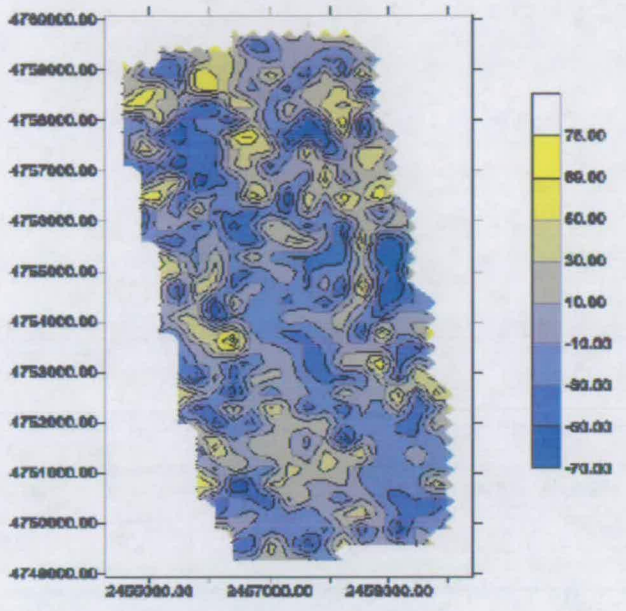

(a) Zero-phase filter

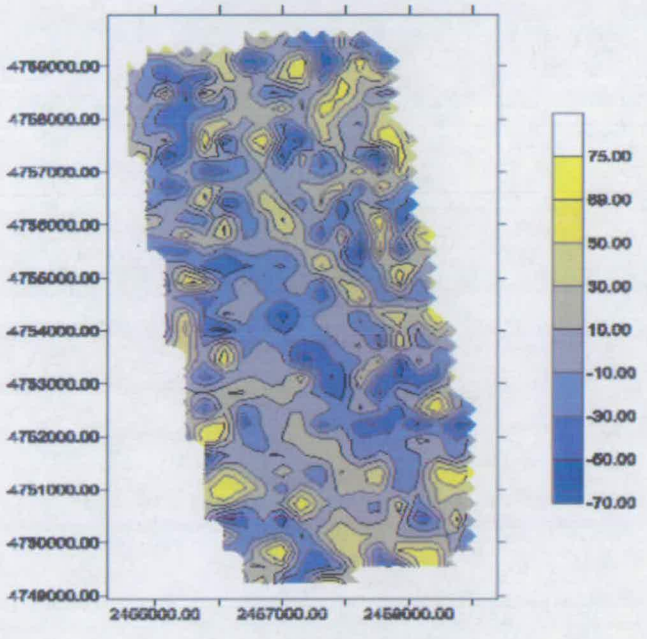

(b) Minimum-phase filter

Figure 7.9: High-frequency data fracture density (time-delay) map of the target (3400ms-4000ms) with different band-pass filters. (a) Zero-phase filter. (b) Minimum-phase filter.

7.3 Time-frequency analysis

The time-frequency (TF) analysis is the basis for a number of processing algorithms and interpretive methods. For a nonstationary signal such as a seismogram, the frequency content changes with time. The representation of the spectral behaviour in the TF plane may allow an improved analysis (Chakraborty and Okaya, 1995; Castagna et al., 2003). For instance, frequency content from multiple arrivals, such as split shear-waves, can be identified (Liu et al., 2003b).

In this part, I first give an overview of various TF analysis methods. I write a SU program (*sutfan*), which includes these TF analysis approaches. TF analysis results of the Emilio data are shown in the next section.

7.3.1 The Fourier transform

The Fourier transform (FT) The Fourier transform (FT) can be expressed as:

$$X(f) = \int_{-\infty}^{\infty} x(t) e^{-2j\pi ft} dt \qquad (7.1)$$

$$x(t) = \frac{1}{2\pi} \int_{-\infty}^{\infty} X(f) e^{2j\pi ft} df \qquad (7.2)$$

where t stands for time, f stands for frequency, x denotes the signal in time domain and X denotes the signal in frequency domain.

7.3 2 The short time Fourier transform (STFT)

The definition of STFT is:

$$STFT_x^{\omega}(t,f) = \int_{-\infty}^{\infty} [x(t')\omega^*(t-t')] e^{-j2\pi ft} dt \qquad (7.3)$$

$x(t)$ is the signal itself, $\omega(t)$ is the window function, * is the complex conjugate.

In STFT, the signal is divided into small enough series, where these segments of the signal can be assumed to be stationary. So the STFT of the signal is just the FT of the signal multiplied by a window function. The window function that we use is a Gaussian function in the form:

$$\omega(t) = \frac{\alpha}{\pi^{-1/4}} e^{-\alpha t^2/2} \qquad (7.4)$$

where α determines the length of the window, and t is the time.

7.3.3 The continuous wavelet transform (CWT)

The continuous wavelet transform (CWT) is used to decompose a signal into wavelets, small oscillations that are localized in time. For a given signal *x(t)*, the CWT of *x(t)* with respect to the basic wavelet (t) is defined as follows:

$$W(\tau, s) = \int_{-\infty}^{\infty} \frac{1}{\sqrt{s}} x(t) \psi^*\left(\frac{t-\tau}{s}\right) dt \qquad (7.5)$$

where τ is a modulation parameter, s is the scale that affects the width of the window.

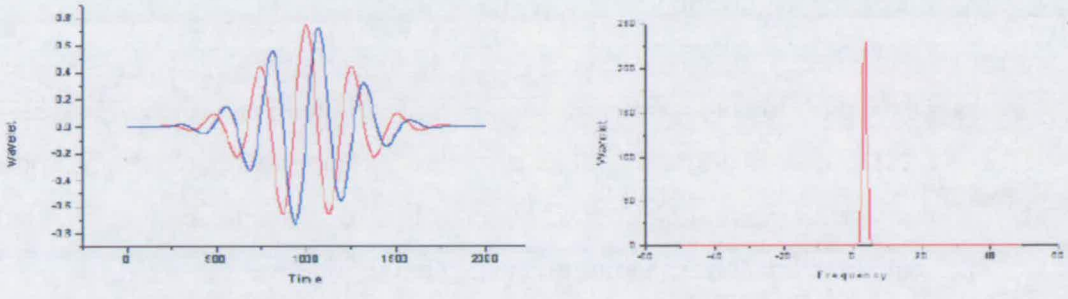

(a) Time domain (b) Frequency domain

Figure 7.10: The Morlet wavelet used for the TF analysis in the CWT. Here wavenumber is 6.0. (a) The red curve is the real component and the blue curve is the complex component. (b) Frequency domain representation is a single symmetric Gaussian peak.

Unlike a Fourier decomposition, which always uses complex exponential (sine and cosine) basis functions, a wavelet decomposition uses a time-localized oscillatory function as the analyzing or mother wavelet. The mother wavelet is chosen to serve as a prototype for all windows in the process. All the windows that are used are the dilated (or compressed) and shifted versions of the mother wavelet. The most commonly used CWT wavelet is the Morlet wavelet, a Gaussian-windowed complex sinusoid that is defined as follows in the time and frequency domains:

$$\Psi_0(\eta) = \pi^{-1/4} e^{im\eta} e^{-\eta^2/2} \tag{7.6}$$

$$\hat{\Psi}_0(s\omega) = \pi^{-1/4} H(\omega) e^{-(s\omega - m)^2/2} \tag{7.7}$$

In these equations, η is a non-dimensional time parameter, m is the wavenumber, and H is the Heaviside step function.

In the time domain plot, the Morlet wavelet is shown with an adjustable parameter m (wavenumber) of 6. This is the smallest wavenumber that allows for an accurate signal reconstruction. Figure 7.10a is the time domain representation of the Morlet wavelet. The red curve is the real component and the blue curve is the complex component. The Gaussian's second order exponential decay results in good time localization. In Figure 7.10b, the frequency domain representation is a single symmetric Gaussian peak. While not the sharp spectral peak of a sinusoid, the frequency localization is very good.

Once the mother wavelet is chosen the computation starts with scale=1 and the CWT is computed for all values of scales. For practical purposes, computation of the transform for a limited interval of scales is usually adequate. Figure 7.11 shows some scales and the corresponding frequency representations.

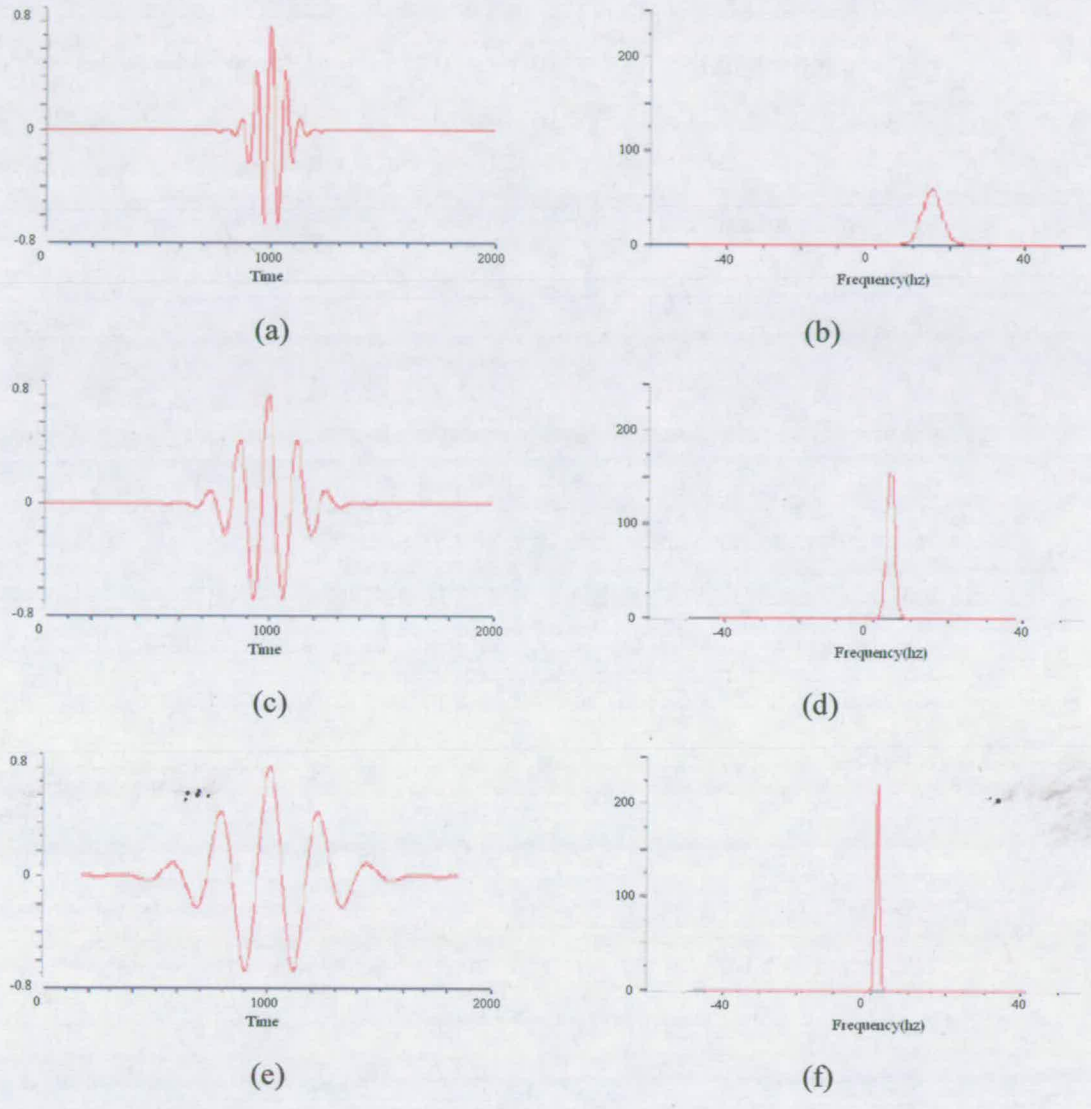

Figure 7.11: Different scales of the mother wavelet. As the scale is increased, the wavelet will dilate. Left is in time domain, right is in frequency domain. (a,b) Scale=1 (Frequency=32Hz) (c,d) Scale=2 (Frequency=16Hz) (e,f) Scale=4 (Frequency=8Hz) (j,h) Scale=8 (Frequency=4Hz).

7.3.4 Results of time-frequency analysis

I first test the SU program (*sutfan*) on synthetic data. I use four different wavelets whose centre frequencies are 10 Hz, 20 Hz, 30 Hz and 40 Hz. At a given time, the seismogram trace is summed by these four wavelets. Figure 7.12 (a) and (b) show two synthetic seismic traces summed by these four wavelets but at different time locations. Figure 7.13 is the amplitude spectrum of the two synthetic traces. We cannot see the time location of each frequency, as FT doesn't show any information of time domain.

Figure 7.14 is the time-frequency analysis using the *sutfan* program. It decomposes the seismogram into constituent wavelets since the frequency spectrum of a seismogram is the sum of the frequency spectra of the wavelets that sum to produce that seismogram. At any given time, the frequency spectrum is the superposition of weighted wavelet spectra in the vicinity of that time sample. The output of the program is the time-frequency plot which shows amplitude spectra for each time sample.

The first arrival (event 1 in Figure 7.14) on the synthetic seismogram is the spectrum results from an isolated reflector. The frequency spectrum is the spectrum of the wavelet. Note that the duration of the spectrum is identical to the duration of arrival in the time domain as opposed to Fourier-based methods in which the time duration is equal to the window length. The second event (event 2 in Figure 7.14) is a composite of two events of differing centre frequency arriving precisely at the same time. The frequency spectrum indicates a low-frequency arrival spread over time and a higher-frequency arrival that is more localized in time. The third event (event 3 in Figure 7.14) is caused by two interfering arrivals of the same frequency. The fourth event (event 4 in Figure 7.14) is a composite of four waveforms arriving at two distinct times evident on the time-frequency analysis. The final event (event 5 in

Figure 7.14) consists of three arrivals of the same frequency that are very closely spaced in time. The three distinct arrivals cannot be resolved at low frequencies, but it is slightly better separation on the time-frequency analysis at high frequency. It is apparent that the wavelet transform provides a useful representation of the information contained in a seismic trace.

I use one fast ($PS1AZ75^0E$) and one slow ($PS2AZ165^0E$) azimuthal components for TF analysis. Figure 7.15 is an example from CDP 529050 (time window is 3500ms to 3900ms). Horizontal coordinate is time (ms) and the vertical coordinate is frequency (Hz). In the colour bar, the amplitude increases from blue to red. Figure 7.15a is the TF spectra of the fast shear-wave. Figure 7.15b is the TF spectra of the slow shear-wave. The vertical axis is frequency and the horizontal axis is time. From the time-frequency spectra, we can see the difference in travel times between the fast and slow shear-waves, and also the differences in frequency spectra between the fast and slow shear-waves (two white spots in Figure 7.15).

I then pick the maximum amplitudes and their corresponding arrival times for each frequency in the fast and slow components. The time-delays between split shear-waves for each frequency are obtained by subtracting the travel-times of the fast and slow components corresponding to the maximum amplitudes (or power spectra). Figure 7.16 shows some typical traces. In some traces, time-delay keeps almost unchanged (a,b). In other traces, we can see two change trends: the time-delay either increases (c,d) or decreases (e,f) with frequency. These differences could potentially be related to different fracture dips, because there are dipping fractures present in the Emilio field (see Figure 3.5 in Chapter 3).

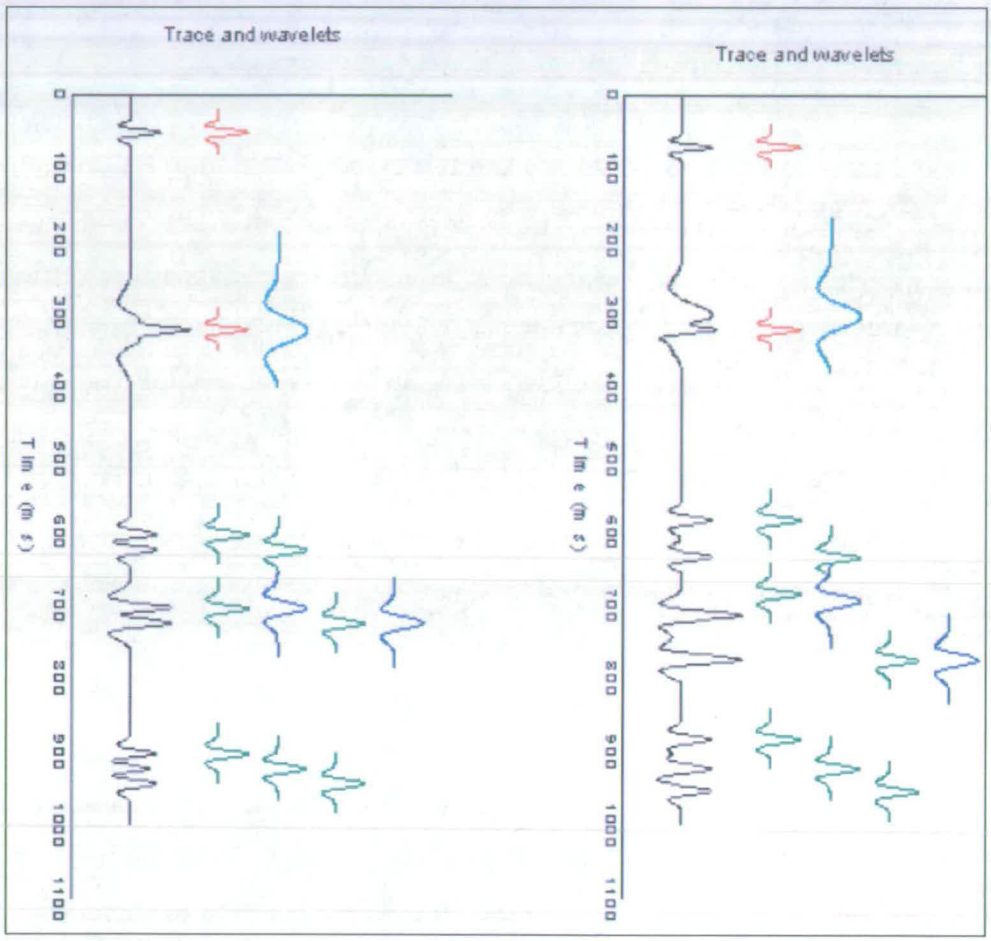

(a) (b)

Figure 7.12: Synthetic waveform with transient arrivals (black seismogram), constituent wavelets (colour coded by center frequency. Red: 40Hz; Green: 30Hz; Blue: 20Hz; Cyan: 10Hz). (a) data1. (b) data2. Data2 is of different TF location from data1.

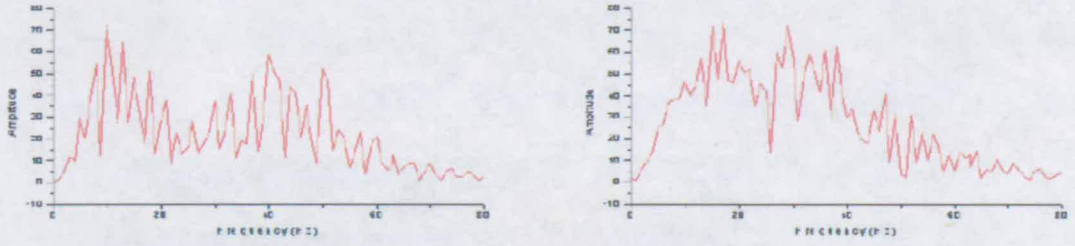

(a) (b)

Figure 7.13: The Fourier transform of the two synthetic traces. (a) FT of data1. (b) FT of data2.

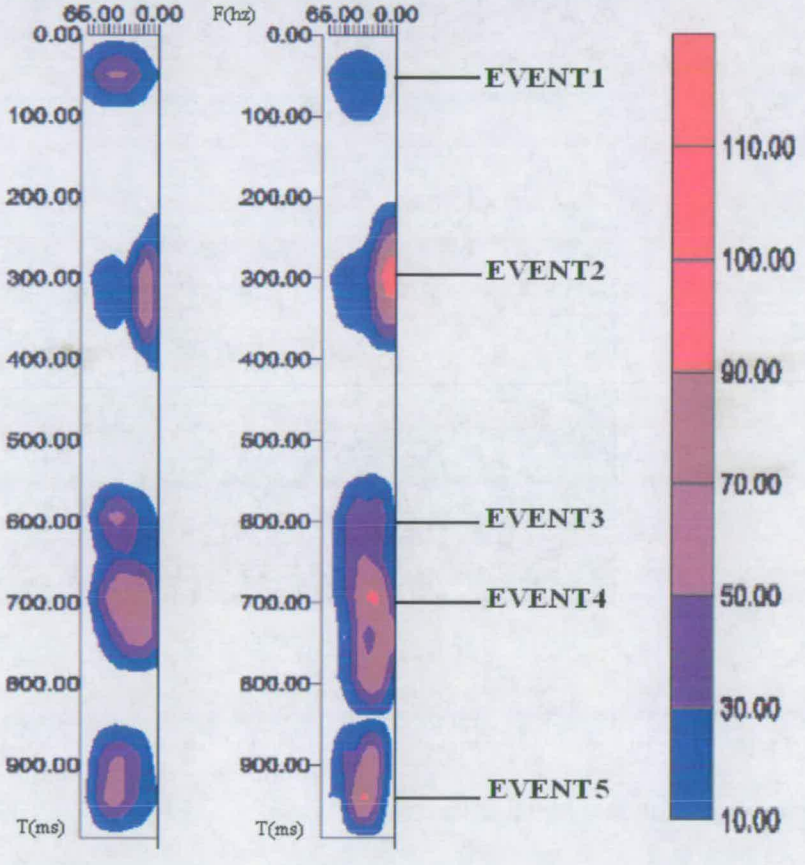

(a) Data1 TF (b) Data2 TF

Figure 7.14: Time-frequency analysis of a synthetic data. (a) Data1. (b) Data2. Instantaneous spectral analysis (ISA) (red represents high amplitude and horizontal coordinate is frequency).

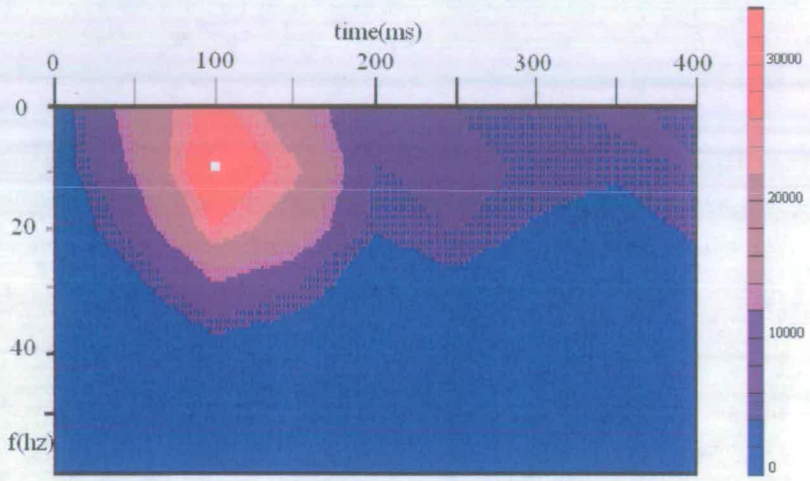

(a) S1 wave

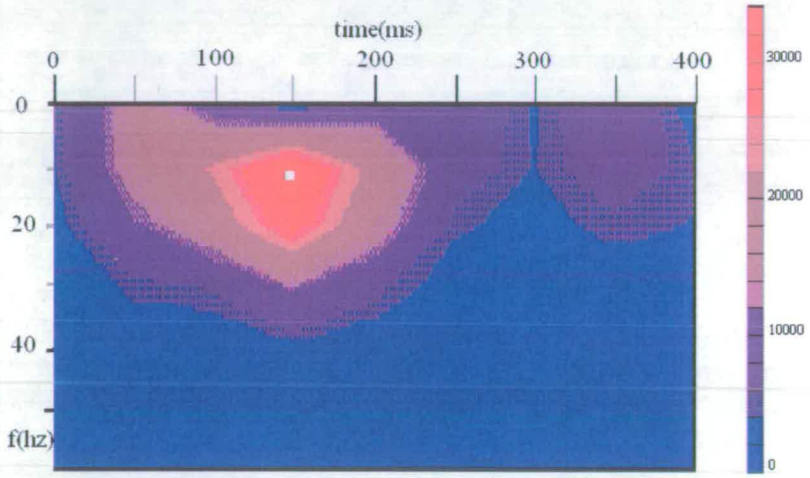

(b) S2 wave

Figure 7.15: Time-frequency spectra of the Emilio migrated data. CDP number is 529050. Time-window is chosen 3500ms-3900ms. (a) Fast shear-wave. (b) Slow shear-wave. Note that the white spots indicate the frequency and time differences between the fast and the slow shear waves.

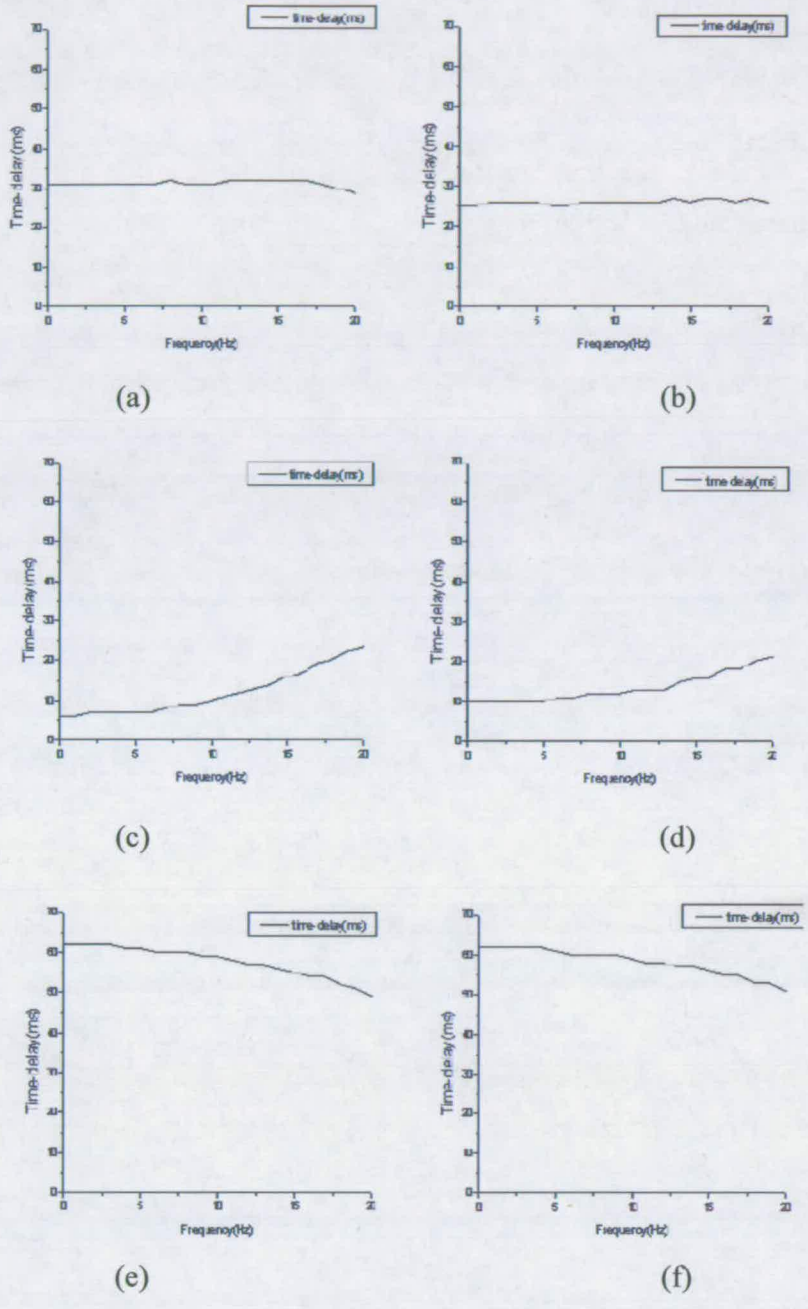

Figure 7.16: A number of sample CDPs choosen for TF analysis. Time-window is choosen at the target (3500ms-3900ms) and the moving window length is set 70ms at maximum. In (a) and (b), time-delay keeps almost unchanged. In (c) and (d), the time-delay increases with frequency. In (e) and (f), the time-delay decreases with frequency. The CDP numbers are: (a) 545418. (b) 440384. (c) 545700. (d) 529050. (e) 440251. (f) 440250.

7.4 Summary

In this Chapter I have used various analysis methods to check the existence of frequency anisotropy in the Emilio field. I have tested different filters and find out that results of minimum filtered data indicate frequency dependent anisotropy in some locations in the Emilio field. Time-frequency analysis constructs a time-frequency representation of a signal and the continuous wavelet transform technique can give a continuous variation of time-delays with frequency. We can see the differences in traveltimes and in frequency spectra between the fast and the slow converted split shear-waves in some locations. This confirms the analysis by band-pass filtering and helps us to analyse frequency dependent anisotropy more effectively.

Chapter 8

Using onshore data for converted-wave splitting analysis

8.1 Introduction

In this Chapter I present a case study of an onshore 2D multicomponent dataset from China. The data were acquired over volcanic gas reservoirs in Northeast China with a mixed sand and shale sequence in the overburden, which revealed a significant amount of shear-wave splitting over the volcanic formation as well as anisotropic moveout effects.

I firstly give an overview of various method used to image and characterize gas reservoirs. Next I develop a converted-wave splitting analysis technique to extract the shear-wave polarization and time delay. The technique is particularly designed for evaluating converted-wave splitting for 2D or 3D data with a narrow-azimuth distribution. I adopt a rotation-scanning procedure that maximizes the separation of the fast and slow split shear-waves. Then I evaluate a converted-wave seismic dataset. It is interesting that the amount of splitting determined from the data can be correlated to the known gas reservoirs, revealing a potential to use shear-wave splitting to delineate gas reservoirs in volcanic rocks.

Furthermore, following the Chapter 5, I use a four-parameter theory to evaluate the effects of non-hyperbolic moveout due to an asymmetric raypath and transverse isotropy (TI). These four parameters include the PS converted wave stacking velocity

(V_{c2}), the vertical velocity ratio (γ_0), the effective velocity ratio (γ_{eff}), and the anisotropy parameter (χ). This four-parameter theory leads to an improvement in imaging quality and correlation between the P-waves and converted-waves.

8.2 Methods to characterize volcanic reservoirs

With more and more gas and oil found in volcanic reservoirs, characterizing volcanic reservoirs has attracted considerable attention in the oil and gas industry. Various methods have been used to image and characterize gas reservoirs, such as spectral decomposition, model based impedance inversion and seismic wave attenuation.

Spectral decomposition provides a tool for mapping and imaging temporal bed thickness and geological discontinuities over large 3D seismic surveys (Partyka *et al.*, 1999). This technique has been used to delineate facies and depositional environments such as channel sands and incised vally-fill sands (Peyton *et al.*, 1998). The use of the wavelet transform allows a seismic signal to be examined in both the time and frequency domains simultaneously (van den Berg, 1999; Gao *et al*, 1999; Castagna and Sun, 2003). Shen *et al* (2003) introduce a workflow and illustrate the application of instantaneous spectral analysis with the aid of a case study on fractured shale reservoirs. This technique provides energy and phase spectra that can delineate temporal reservoir thickness variability and indicate lateral geological discontinuities. It allows interpreters to quickly and efficiently image and quantify local rock property variability within the 3D seismic data volume.

The model based impedance inversion technique is used to characterize the heterogeneity of reservoir lithology and internal structure. The geological constraints from interpreted structure and stratigraphic frames and geological characteristics from instantaneous spectral analysis are very helpful for model building in the impedance inversion. The inverted impedance can be used to estimate lateral changes

in reservoir thickness and acoustic properties. Under the constraints of the interpreted reservoir lithology using inverted seismic impedance, seismic attenuation variation within reservoirs can also be efficiently used to characterize reservoir properties.

Seismic wave attenuation is observed as a pronounced loss of high frequency energy, and these attenuation anomalies can be a useful hydrocarbon indicator. As the instantaneous spectral analysis allows us to obtain a frequency spectrum at each time sample for a seismic trace, seismic attenuation can be described as frequency-dependent spectral variations. These variations enable us to detect high-frequency attenuation associated with gas-bearing volcanic reservoirs.

Converted shear-wave splitting provides a practical means for evaluating azimuthal anisotropy in hydrocarbon reservoirs that may give some insights into the internal architecture of the reservoirs. Shear-wave splitting in volcanic rocks has also been reported (e.g. Crampin and Lovell, 1991). Volcanic rocks are known to be heterogeneous and can contain a large amount of fractures and vuggy pores, as well as other small heterogeneities. When these small-scale features are aligned, it will introduce azimuthal anisotropy, giving rise to shear-wave splitting. Angerer *et al.* (2002) observed significant changes in shear-wave splitting before and after CO_2 injection in a carbonate reservoir where the presence of CO_2 kept the fractures and cracks open and increased the amount of splitting. Based on similar ideas, here I present a study of using converted-wave splitting to delineate gas reservoirs in volcanic rocks.

8.3 Analysis methods for shear-wave splitting

Rotation of horizontal components of shear-wave data is one of the key processing procedures in anisotropy analysis, as discussed in Chapter 2 and 6. Through rotation,

the effects of anisotropy can be compensated for and the fast and slow shear waves can be separated. Several algorithms for the rotation of shear-wave seismic data have been devised. As we know, tensor rotation algorithms such as Alford's rotation require multi-azimuth distribution (Gaiser and Van Dok, 2001).

However, the converted-wave data used in this study is acquired using digital MEMS (micro-electro-mechanical-system) sensors with a 2D configuration and single-azimuth source and receiver distribution. Single azimuth two-component birefringence-analysis schemes that do not involve hodograms have largely been based upon either the autocorrelation or crosscorrelation of rotated components (Narville 1986; Peron, 1990). Harrison (1992) presented an algorithm using the autocorrelation and crosscorrelation of rotated radial and transverse components, which is particularly suitable for converted waves and is robust in the presence of noise. Esmersoy (1990) presented an algorithm to obtain the rotation parameters by an inversion method. For single-azimuth data, a rotation scanning procedure is often needed that searches for optimum solutions according to certain criteria. The common criteria include waveform similarity between the fast and slower shear-waves, or minimum spectral interference of split shear-waves (MacBeth and Crampin, 1991). Here I adopt a criterion that maximizes the separation of the fast and slow shear-waves, following the approach of Yuan (2001). Once the split shear-waves are separated, I construct a time-delay spectrum between the fast and slow waves that allows the picking of time delays as a function of the vertical travel time, yielding a time-delay section for interpretation purposes.

8.3.1 Basic equations for rotation scanning

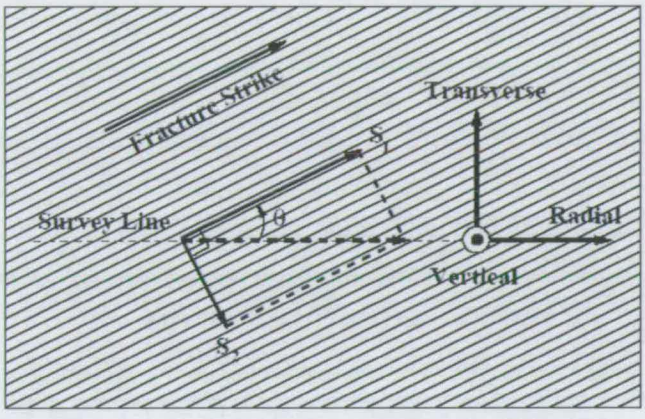

Figure 8.1: Map view of shear wave splitting when an up-going converted shear wave travels in a vertically fractured medium.

Figure 8.1 shows a map view of shear wave splitting when an up-going converted shear wave travels in a medium with a preferred distribution of heterogeneities. The principal direction of the medium forms an oblique angle θ with the survey line. The orientation of the three component geophone forms a right-handed coordinate system: radial component R, transverse component T and vertical component V, pointing to the reader. The polarization of the fast split shear wave S_1 is parallel to the principal direction and that of the slow shear wave S_2 perpendicular to it.

To process the split shear waves, it is common to use the convolution model of seismic wave propagation. Thus, in the frequency domain, the wavefield recorded by the radial and transverse components can be written as,

$$\begin{bmatrix} R(\omega) \\ T(\omega) \end{bmatrix} = \begin{bmatrix} \cos\theta & \sin\theta \\ \sin\theta & -\cos\theta \end{bmatrix} \begin{bmatrix} S_1(\omega) \\ S_2(\omega) \end{bmatrix} + \begin{bmatrix} N_R(\omega) \\ N_T(\omega) \end{bmatrix} \tag{8.1}$$

where $N_R(\omega)$ and $N_T(\omega)$ are the noise components in the radial and transverse directions. To maximize the separation between the fast and slow shear-waves, one may calculate the residual errors between the fast and slow waves as

$$E(\theta, \Delta t, \omega) = S_1(\omega) - S_2(\omega) e^{i\omega\Delta t} \tag{8.2}$$

where Δt is the time delay between the fast and slow waves. Substituting into Equation 8.1 and changing into the time domain, it becomes,

$$\begin{aligned} E(\theta, \Delta t, t) &= (R(t)\cos\theta + T(t)\sin\theta) - (R(t-\Delta t)\sin\theta - T(t-\Delta t)\cos\theta) \\ &- (N_R(t)\cos\theta + N_T(t)\sin\theta) + (N_R(t-\Delta t)\sin\theta - N_T(t-\Delta t)\cos\theta) \end{aligned} \tag{8.3}$$

Equation 8.3 forms the basis for single-azimuth two component (2C) vector rotation analysis. One can perform double scanning over the rotation angle θ and time delay Δt, and the objective function $F(\theta, \Delta t)$ to minimize the summed $E(\theta, \Delta t, t)$:

$$F(\theta, \Delta t) = \left(\sum_{k=0}^{n} E(\theta, \Delta t, t_k)^p\right)^{1/p} \tag{8.4}$$

for a time window length with n samples.

8.3.2 Time-delay spectra

The time-delay spectra can be constructed by scanning over vertical time using the correlation method. According to the 2C rotation analysis results, I am able to rotate the data into the fast and slow components. First I form a trace pair from traces of the fast and slow components. I then set a time window and use the correlation method to compute the correlation coefficients within the window. The time window slides downwards and therefore a time-delay spectrum is constructed.

8.4 DaQing data processing and analysis

It has become increasingly common knowledge that anisotropy is widely present in the Earth subsurface. Sedimentary layers such as shales and thin bedding sequences in the overburden often give rise to vertical transverse isotropy (VTI, or polar anisotropy), whilst the presence of near-vertical fractures in sand or carbonate hydrocarbon reservoirs may result in horizontal transverse isotropy (HTI, or azimuthal anisotropy). For VTI, a major seismic effect is non-hyperbolic moveout, whilst for HTI, I have shear-wave splitting, both of which are intensively studied in the literature (e.g. Helbig and Thomsen, 2005; Crampin and Lovell, 1991). However, due to data quality issues, it is not very common to find both of these effects present in a land shear-wave dataset that can be clearly identified and used for reservoir characterization.

As a result, here I present an example of using MEMS-based converted-wave technology for jointly evaluating shear-wave splitting and the effects of non-hyperbolic moveout in Northeast China. The data were recorded over a volcanic gas reservoir buried at depths ranging from 2800m to 3600m, and the overburden is primarily composed of a mixed sand and shale sequence.

8.4.1 Data acquisition

The Daqing oilfield is located in northeast China. It is the largest oilfield for hydrocarbon production in China, and it has been in production for more than forty years. Shallow targets at depth less than 2km have largely been exhausted and the current focus is to explore deep targets buried at depths ranging from 2800m to 3600m, which provide a good potential for reserve growth. These deep targets are mostly volcanic gas reservoirs, and often give rise to an incoherent P-wave response. Past multicomponent seismic experiments reveal some potential to use PS converted

waves to image these targets, but the results are limited due to data quality issues. Recent advances in digital MEMS sensors have rekindled the interests of using converted-wave data to delineate these volcanic reservoirs in this area. For this purpose, a multicomponent experiment was set up in 2005.

The experiment consists of six 2D lines with about 90km of full-fold coverage, as shown in Figure 8.2. The six lines form several intersection points passing through ten boreholes drilled into the volcanic reservoirs. Multicomponent VSPs have also been acquired from three of the boreholes for helping in correlating the PP- and PS-sections, together with some P- and S-wave sonic logs. Four of the lines were acquired with a split spread with a maximum offset of 6605m, nominal receiver interval of 10m, and shot interval of 40m. The number of channels for each component is 1220, giving rise to a nominal fold of 152. Two other lines were acquired with a single-side spread with a maximum offset of 5805m, a receiver interval of 5m, shot interval of 20m, and nominal fold of 145.

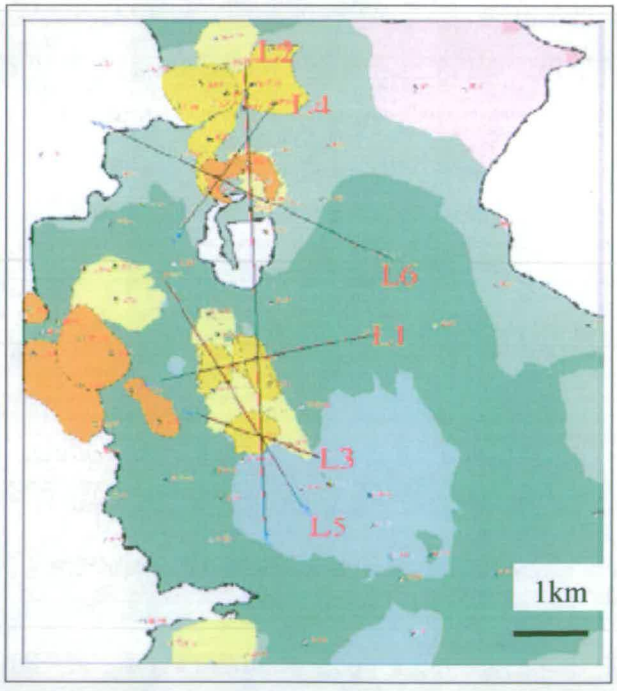

Figure 8.2: Survey map and line locations of the DaQing data.

Land shear-wave data have usually been of poor quality, which limited the application of multicomponent technology to some degree. However, the use of digital MEMS (micro-electro-mechanical system) sensors has substantially improved the quality of land converted-wave data and has led to the acquisition of several land multicomponent surveys recently (e.g. Roche *et al.,* 2005; Mattocks *et al.,* 2005; Calvert *et al.*, 2005, and amongst others). The use of MEMS sensors has lead to the acquisition of very high quality shear-wave data (Figure 8.3), and major events can be clearly identified in the original shot record, although some ground roll can be observed. Dominant frequency is about 40hz for P-wave and about 20hz for converted-wave.

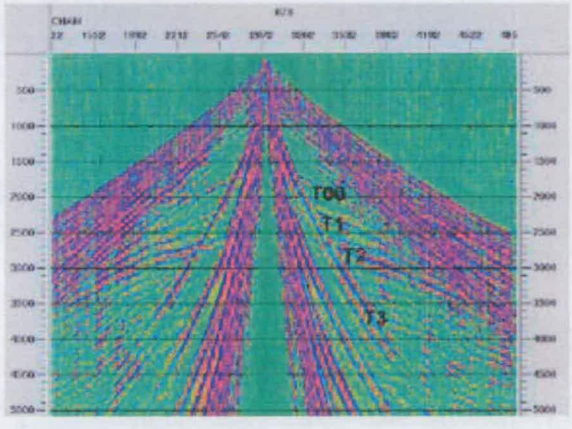

Figure 8.3: PS Converted-wave, X-component.

8.4.2 Non-hyperbolic moveout analysis

Due to the improved data quality, the processing is relatively straightforward. The following nine steps are applied to both the vertical (PP-) and horizontal (PS-) components: 1) geometry loading; 2) static correction; 3) noise attenuation (ground roll); 4) CMP bin for PP, but ACP (Asymptotic conversion point) bin for PS with

binning velocity ratio γ=2.0; 5) velocity analysis, 6) moveout correction; 7) stack; 8) migration velocity analysis and 9) final prestack time migration.

Converted-wave (C-wave) moveout is inherently non-hyperbolic due to the asymmetric raypath. The moveout signature is often further complicated by the presence of vertical transverse isotropy (VTI). According to Li and Yuan (2003), four parameters are required for performing converted-wave velocity analysis and moveout correction. These four parameters are the vertical P- and S-wave velocity ratio γ_0, the effective velocity ratio γ_{eff}, the converted-wave stacking velocity V_{C2} and anisotropic parameter χ_{eff}. The following work flow may be used to determine these four parameters (V_{C2}, γ_0, γ_{eff} and χ_{eff}) (see Chapter 5):

1) obtain γ_0 by a coarse correlation between the P- and C-wave stacked sections;

2) Estimate V_{C2} from the near-offset moveout signature (offset-depth ratio x/z<1.0);

3) Estimate γ_{eff} from the intermediate-offset moveout (x/z<1.5) and χ_{eff} from the far offset moveout (x/z<2.0). An interactive velocity tool has been developed by Dai (2003), which can be used to perform the above steps interactively (Figure 8.4).

The analysis is performed on the radial component (PSV-wave). Figure 8.4 compares C-wave velocity analysis with and without consideration of anisotropic effects. In the shallow section there is significant residual moveout without considering anisotropy (Figure 8.4a – setting χ_{eff} to zero), whereas the event is properly aligned after taking account for anisotropy (Figure 8.4b – non-zero χ_{eff}). Using the interactive tools, I can determine values of V_{C2}, γ_{eff} and χ_{eff} across the whole section, as shown in Figure 8.5. As where the arrows are, we can see that the amount of anisotropy is very significant for the events around 2.0 seconds (Figure 8.5d). In comparison, the other quantities (V_{C2}, γ_0 and γ_{eff}) all vary very smoothly. V_{C2}, γ_0, γ_{eff} and χ_{eff} are referred to as the anisotropic velocity model for stacking and migration.

Figure 8.6 compares the corresponding stacking results with and without considering anisotropy. The horizons in the zone around 2.0 seconds are only slightly better resolved with anisotropy (Figure 8.6b) than without anisotropy (Figure 8.6a). This is because the contribution of the far-offset C-waves to the final stack is relatively small compared with the C-waves in the intermediate offsets, as in Figure 8.4.

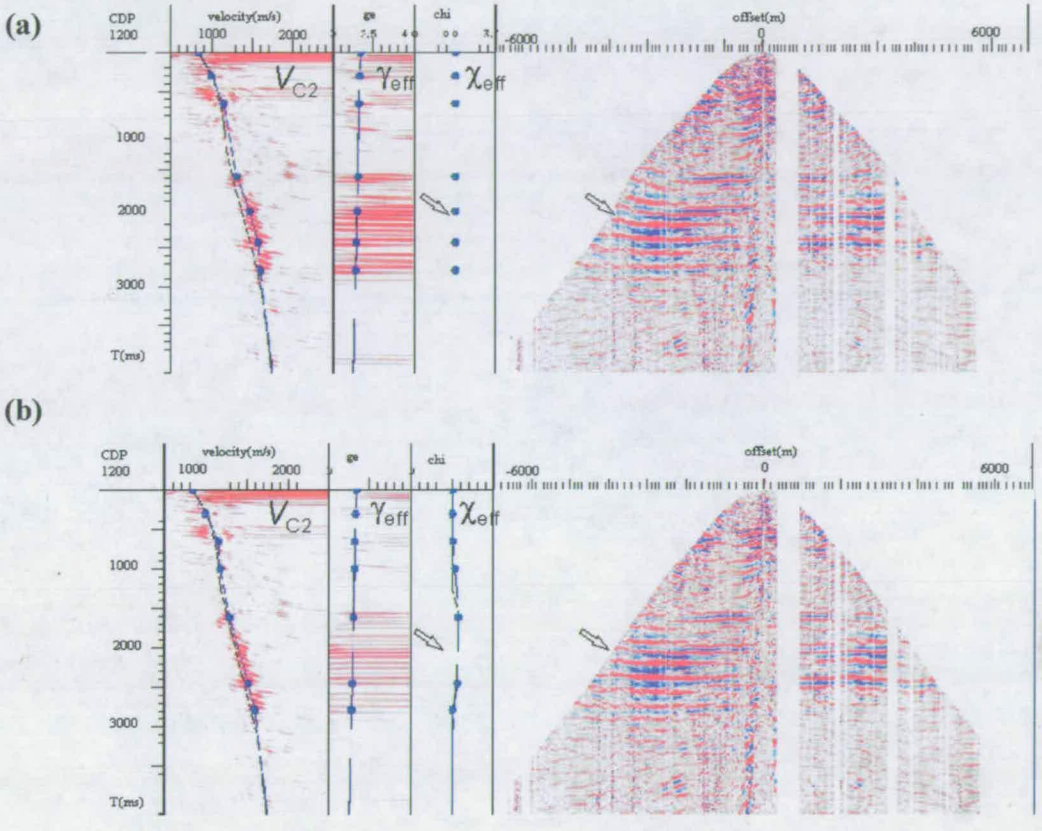

Figure 8.4: Analysis of the effects of anisotropy on converted-waves: velocity analysis and moveout correction (a) without and (b) with anisotropy. Note that from left to right, the three panels show the semblance analyses for V_{C2}, γ_{eff} and χ_{eff}, respectively.

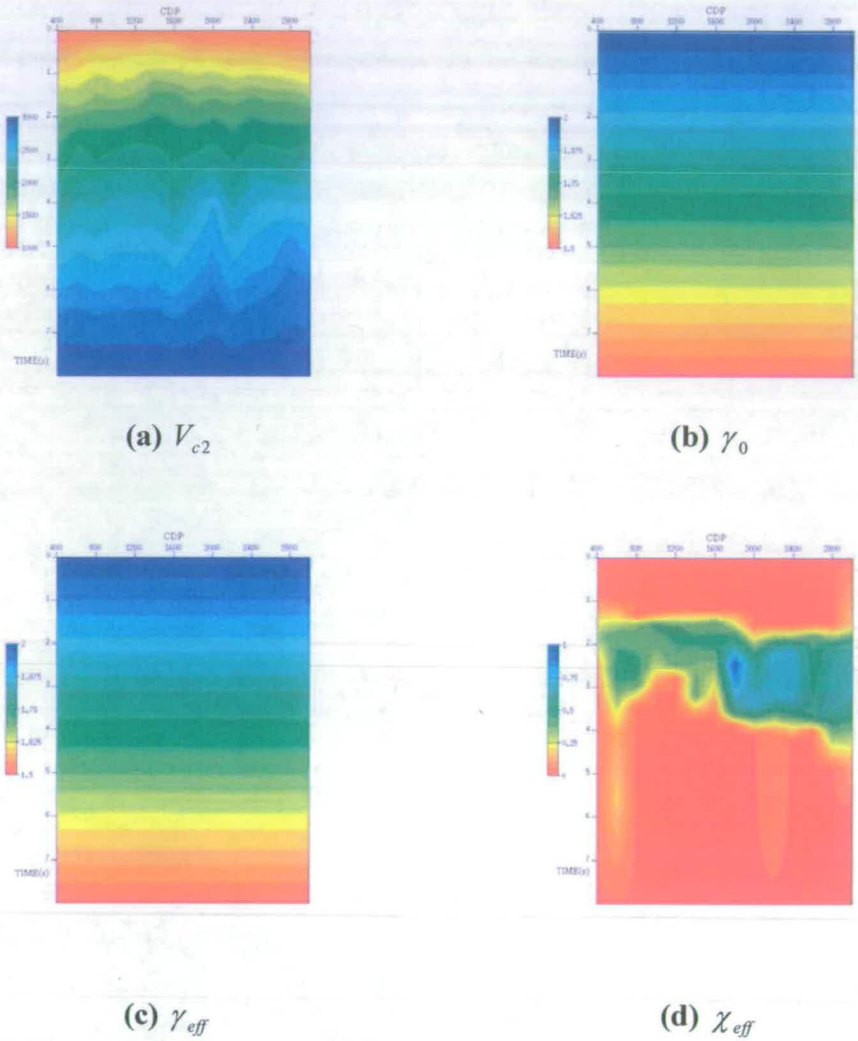

(a) V_{c2} (b) γ_0

(c) γ_{eff} (d) χ_{eff}

Figure 8.5: The four parameters (a) V_{c2}, (b) γ_0..(c)γ_{eff} and (d) χ_{eff} estimated from C-wave moveout analysis using the interactive tools as shown in Figure 8.3 for the radial component (PSV-wave).

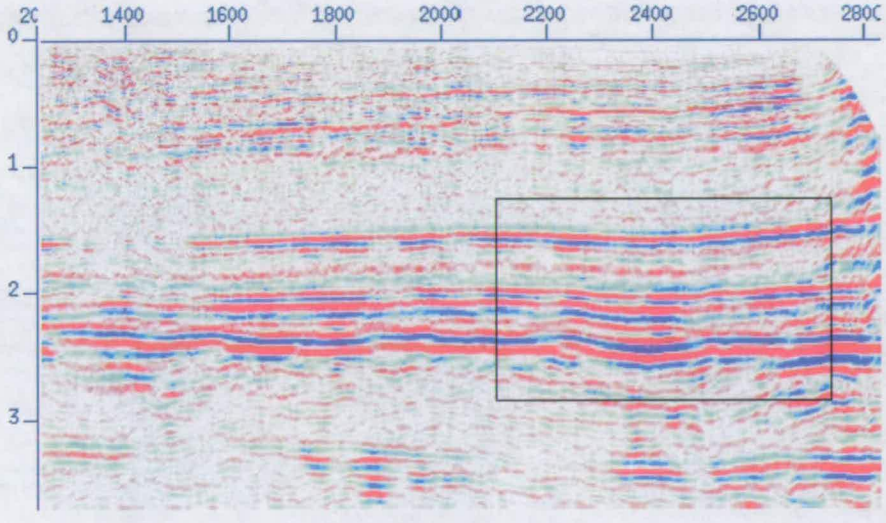

(a) Isotropic stack

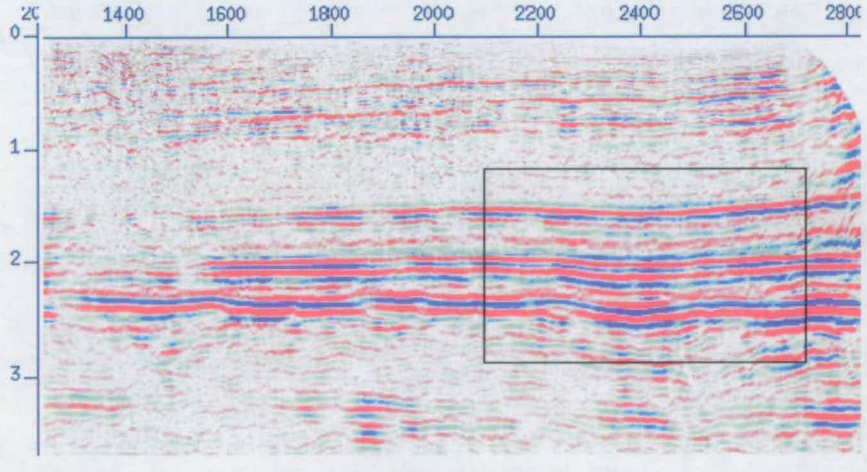

(b) Anisotropic stack

Figure 8.6: Comparison of converted-wave stacked sections: (a) without and (b) with anisotropy for radial component (PSV-wave).

8.4.3 Shear-wave splitting analysis

As I mentioned earlier, the data used in this study are acquired with a 2D configuration and single-azimuth source and receiver distribution. For single-azimuth data, a rotation scanning procedure is often needed that searches for optimum solutions according to certain criteria. I applied the developed rotation approach, which adopts a criterion that maximizes the separation of the fast and slow shear-waves. Once the split shear-wave are separated, I construct a time-delay spectrum between the fast and slow waves using a sliding window that allows the picking of time delays as a function of the vertical travel time, yielding a time-delay section for interpretation purposes.

Here the converted-wave data reveal a significant amount of splitting over the volcanic formations, indicated by the strong coherent energy in the transverse component (Figure 8.7). As shown in Figure 8.7, I select the reservoir target as indicated by the lines for the 2C rotation analysis and Figure 8.8 shows the scanning results, the objective function calculated from Equation 8.4.

Figures 8.9 and 8.10 are picked rotation angles and time delays at a 50 CDP interval. The average orientation angle is about 40 degrees from the inline X-direction (anticlockwise) and the average time delay is 25-30 milliseconds, indicating about 2% shear-wave splitting. The data are then rotated into the Fast/Slow components, which are shown in Figure 8.11. Figure 8.12 shows time-delay spectra from selected CDP locations, from which a time-delay section can be obtained. The time-delay section was sent to PetroChina Dqaing and they marked the wells on the section. The reservoir target and shallow gas were also interpreted. Figure 8.13 is the interpretation results on the time-delay gradient section.

As shown in Figure 8.13, areas of volcanic rocks with high gas accumulation show a significant amount of splitting (SS1), whilst no-gas bearing rocks show little splitting (SS201). For Well SS1, the splitting anomalies seem to be good indicators of gas accumulation. However, there is an inconsistency for Well S202, and this maybe due to more complex geology.

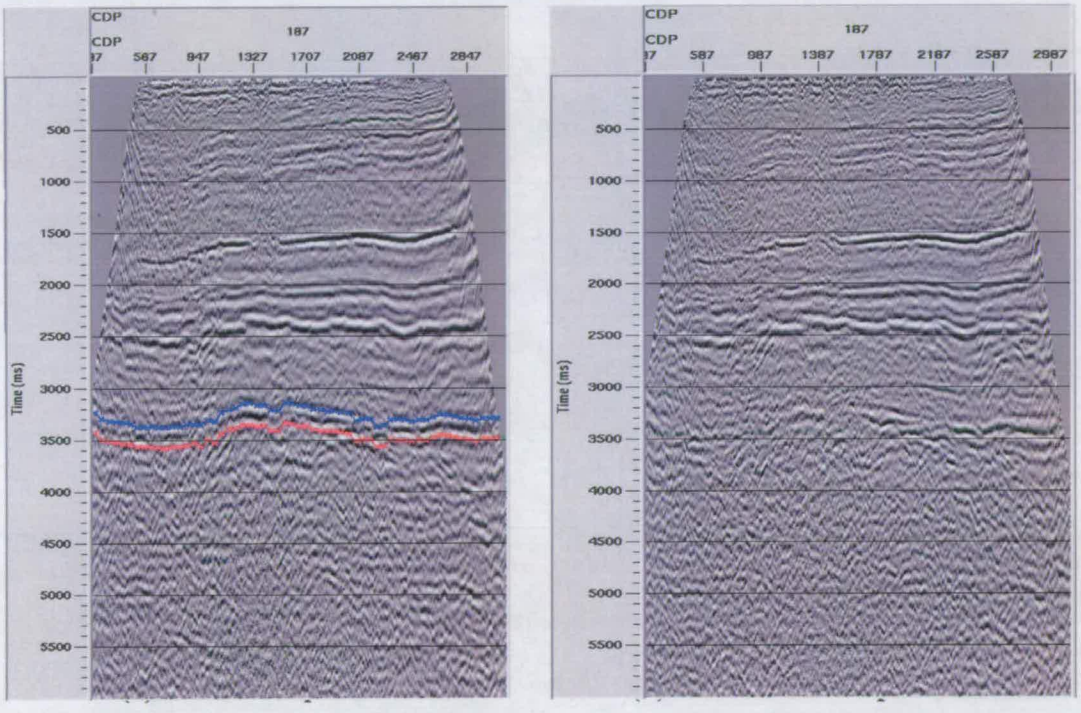

Figure 8.7: Input data for 2C rotation analysis. The blue and red lines show the top and bottom of the target.

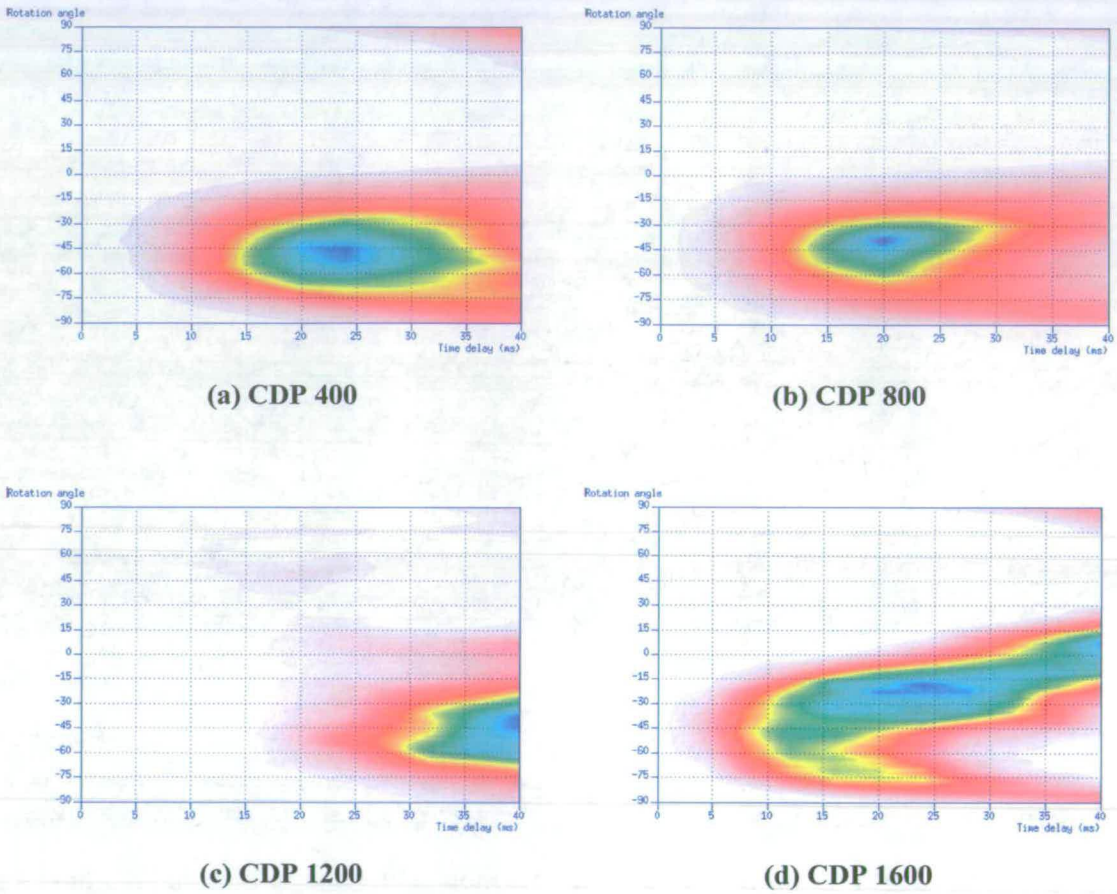

(a) CDP 400

(b) CDP 800

(c) CDP 1200

(d) CDP 1600

Figure 8.8: Rotation analysis for the data in Figure 8.7. The scanning is looking for a minimum value (in blue). The vertical axis is rotation angle, and the horizontal axis is time-delay.

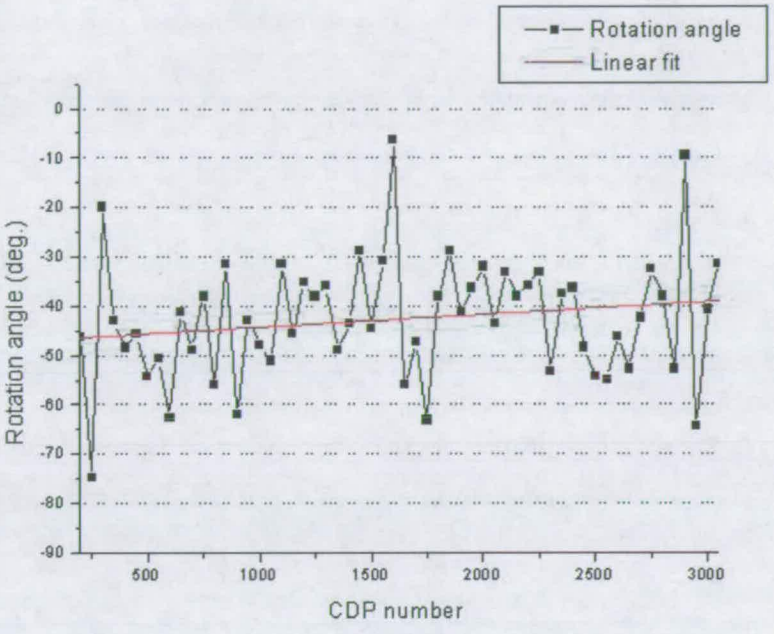

Figure 8.9: Picked rotation angles of selected CDPs.

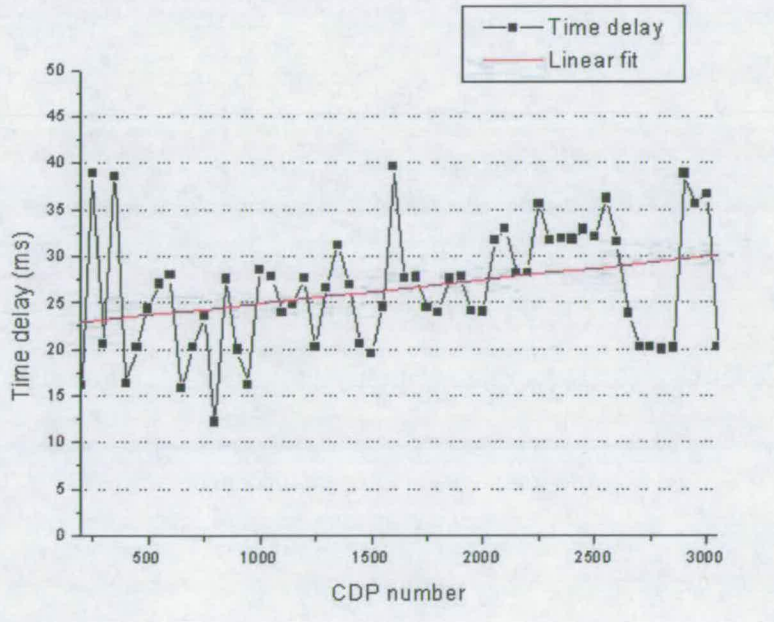

Figure 8.10: Picked time delays of selected CDPs.

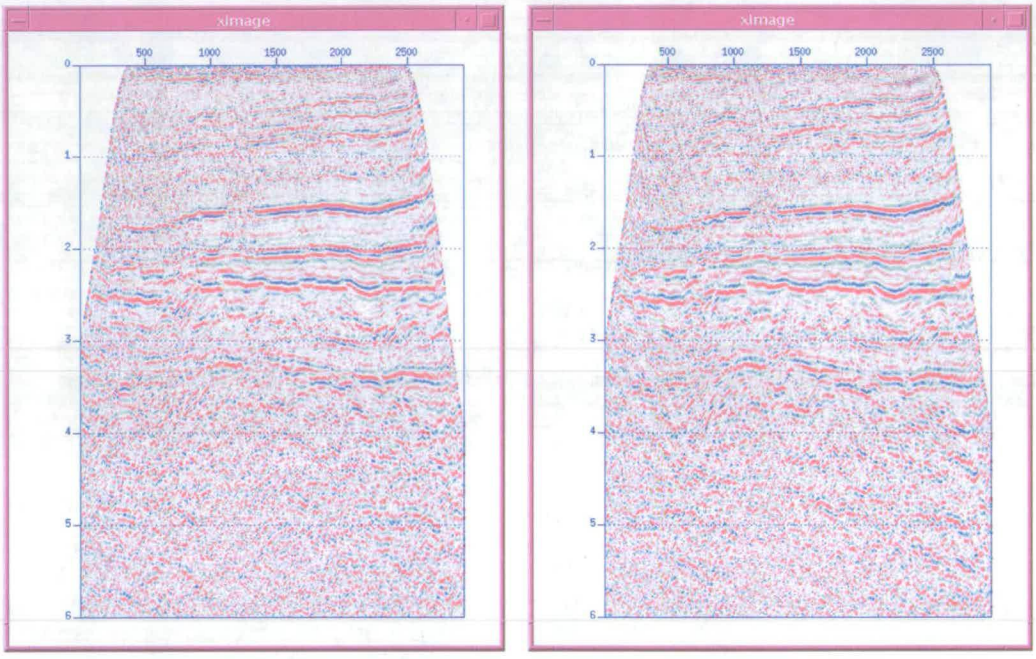

(a) Fast component (b) Slow component

Figure 8.11: Data after rotation. Note that the fast and slow components have been separated.

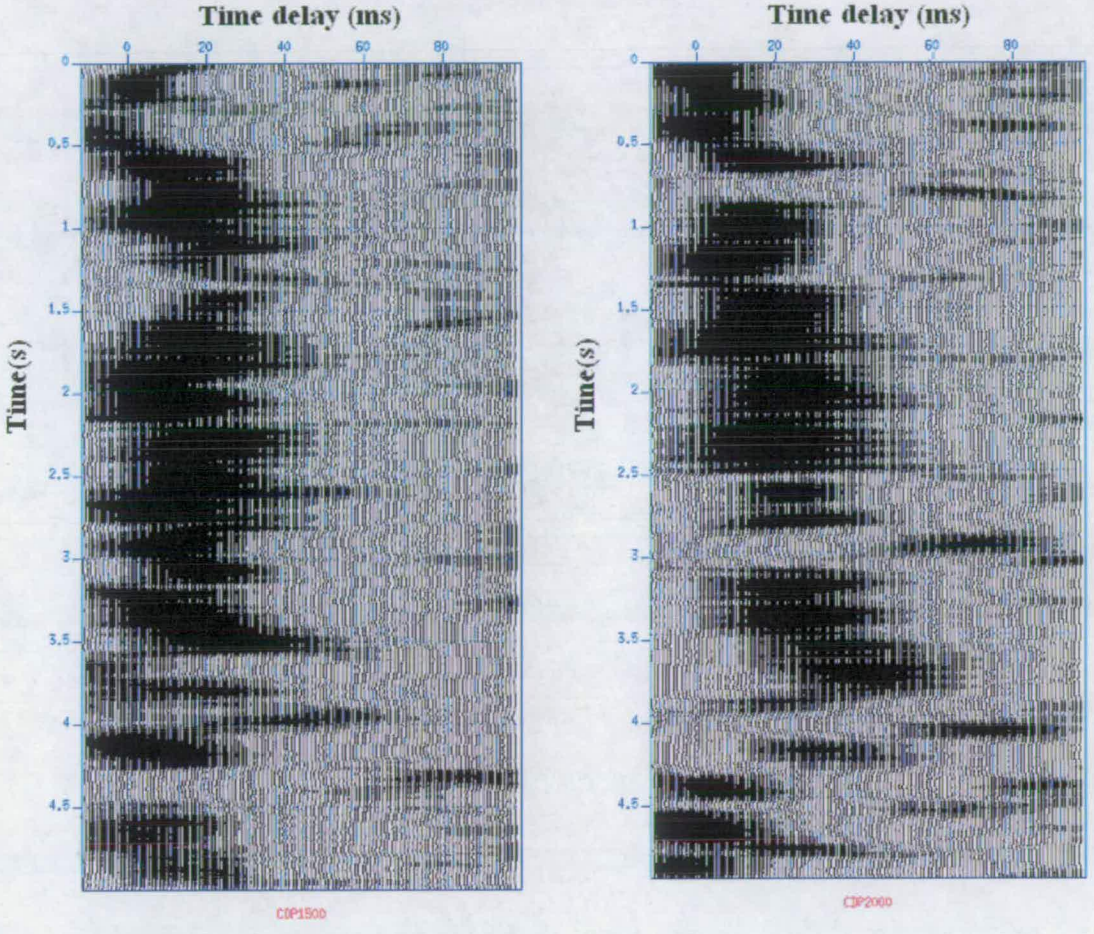

(a) CDP 1500 (b) CDP 2000

Figure 8.12: Time-delay spectra of selected CDPs. The horizontal axis is time-delay, and vertical axis is travel time.

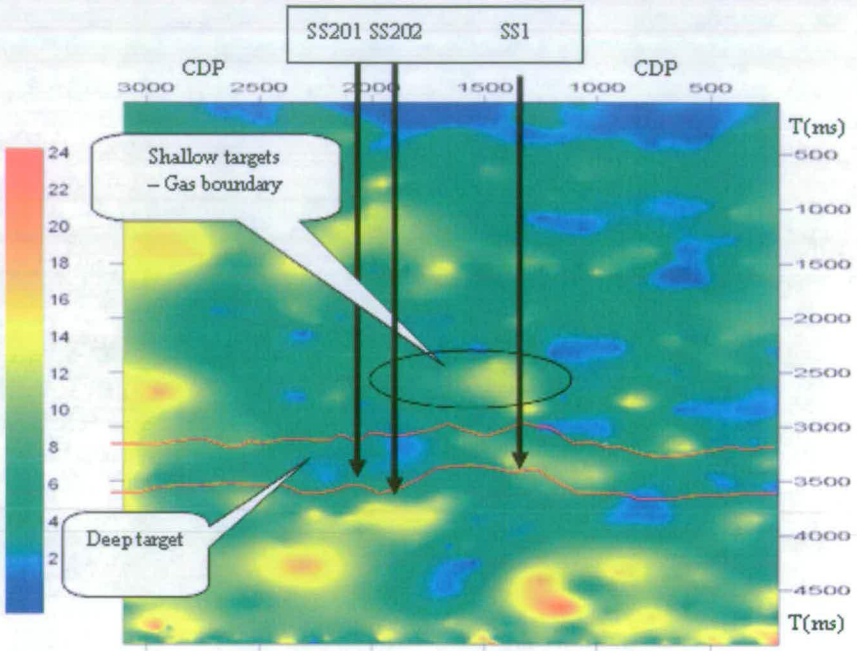

Figure 8.13: Interpretation results on the time-delay gradient section. SS202 and SS1 are gas-producing wells, and SS201 is a dry hole. Scales on the colour bar shows the anisotropy density and arrows show the extent of wells.

8.5 Summary

In this case study, I have applied the newly developed shear-wave splitting analysis method. The efficient and convenient method is specially designed for single-azimuth distribution converted-wave data. My approach includes two key steps: rotation scanning to maximize the separation of the split shear-waves and small-window correlation to build time-delay spectra. I find that the degree of shear-wave splitting in some wells can be correlated to the known gas reservoirs. Higher values of shear-wave splitting in the presence of gas saturation is consistent with equivalent medium modelling, as in the case studied by Angerer *et al.* (2002). However, there is an inconsistency in one well in the dataset and more case studies need to be shown.

Additionally, I have evaluated non-hyperbolic moveout in converted-wave data. I have shown that the converted-wave non-hyperbolic moveout in the presence of anisotropy can be fully compensated for using the four-parameter theory of Li and Yuan (2003), which leads to an improvement in both imaging quality and event correlation between PP and PS converted-waves.

Chapter 9

Conclusions

9.1 Thesis conclusions

In this thesis I have focused on the analysis of multicomponent reflection data in the presence of seismic anisotropy with the objective of addressing a range of current issues in multicomponent data imaging and fracture characterization. I have studied both an onshore 2D/4C dataset from the DaQing oilfield and a marine 3D/4C dataset acquired over the Emilio field and performed extensive synthetic modelling. The main technical achievements are: first, a multiple removal technique, second, extending the linear transform technique to handle PS-waves, and third, the development of a tool for time delay spectra. Applications of these developments to the real data reveal that fracture-related seismic anisotropy can be efficiently detected. Moreover, the shear-wave splitting is sensitive to gas saturation in some wells in Daqing oilfield and the observed shear-wave splitting is frequency dependent in some locations in the Emilio field.

The Emilio field has a wide presence of fractures, which give rise to a HTI medium. In data processing, I recommended the early rotation of the horizontal geophones

into the principal component directions, instead of conventional radial and transverse component directions, to optimize the PS-wave processing workflow (Vetri *et al.*, 2003). In order to deal with the effects of HTI, I have extended the linear transform technique, originally developed for pure shear-wave data, to handle PS converted waves and determine the principal S-wave directions and percentage anisotropy. I have found that the inverted fracture polarization and intensity in the Emilio dataset correlate with the previous results obtained from Alford rotation. I recommend the linear transform technique since it shows efficiency and simplification and doesn't require intensive computation.

In the Emilio P-wave data, I developed a technique for multiple attenuation during data pre-processing. I computed a time-variant scalar trace for every hydrophone-geophone trace pair. Therefore, when summed, it is possible to achieve cancellation of multiples, when summed, due to their opposing polarity in each of the hydrophone-geophone trace pairs. Compared with various previous methods (e.g. Ball and Corrigan, 1996; Barr and Sanders, 1989), the advantage of this approach is that it doesn't need the computation of reflection coefficients and it can also attenuate multiples.

For the P-wave fracture analysis, I have used two methods, the narrow-azimuth/full-offset method and the full-azimuth/full-offset method, to estimate the azimuthal differences of seismic attributes. I confirmed that the narrow-azimuth stacking technique may enhance the acquisition footprint and recommended surface fitting of all azimuths and offsets (Li *et al.*, 2003). I also found the PS-wave results are more consistent and clear than scattered P-wave results.

I developed and applied various techniques to investigate the existence of frequency-dependent anisotropy for application to multicomponent reflection seismic data. The

statistics results show that converted-wave splitting changes with frequency in some locations in the Emilio field.

For 2D or 3D multicomponent data with a narrow-azimuth distribution, I have developed a tool for evaluating PS converted-wave splitting. I adopted a rotation-scanning procedure that maximizes the separation of the fast and slow split shear-waves and then I constructed spectra of the time-delay between the fast and slow waves that allow the picking of time delays as a function of the vertical traveltime. The technique was applied to the onshore multicomponent DaQing dataset acquired over volcanic gas reservoirs. I have found that the amount of splitting determined from the data can be correlated to the known gas reservoirs. This finding also agrees with the case study of Angerer *et al.* (2002). However, there is an inconsistency for one well in the Daqing dataset which needs more investigation.

In addition to the real data analyses, I have performed synthetic modelling to study the effect of structural variation on anisotropic parameter estimation using PS converted waves. I generated and processed a number of isotropic and anisotropic synthetic datasets in the presence of varying dip and polar anisotropy. I found that the errors in velocity ratio of PP- and PS-wave result in large horizontal mis-positioning, and erroneous PS-wave stacking velocities make dips vary significantly but produce the same effects for both directions of offsets if the data are separated into positive and negative offsets. Errors in the velocity ratio have the same effects as errors in the anisotropy measurements. These findings are valuable for processing PS-wave data, understanding PS-wave behaviour, and for PS-wave imaging, especially in the case of the DaQing dataset which shows VTI effects.

9.2 Future work

As I found narrow azimuth stacking method to detect the P-wave fractures is affected by acquisition footprint, to further develop P-wave fracture detection technology, the

effects of the acquisition footprint and the effects of dipping layers and complex overburden merit further study. Still more needs to be done on C-wave imaging, as there are more complex anisotropic geometries, such as the Tilted Transverse Isotropy (TTI), which are more difficult to parameterise for processing purposes. How the frequency content affects C-wave prestack migration is also an open question.

The use of time-frequency transforms is a broad field that could be the subject of further investigations. Although I have applied a number of methods to measure effects of frequency-dependent anisotropy, it is by no means a comprehensive study of the merits and limitations of different techniques. In the thesis I observed the frequency-dependent anisotropy only exists in some locations in the Emilio field, more case studies should be studied so that we can have a better understanding of this phenomena in reflection datasets. Data processing is also an issue as high quality processed products are essential to extract subtle anisotropy changes with frequency. Furthermore, the methods of measuring attenuation could be used for frequency dependent anisotropy analysis (Maultzsch, 2005).

For the Daqing dataset, there is an inconsistency in one well and further research is required for gas reservoirs beneath volcanic rocks. In addition, a joint interpretation unifying P and S-wave information has a high potential for providing information on lithology and fluids. However, this faces the challenge of finding a methodology to correlate the two imaged volumes with a high degree of accuracy, since this process is easily affected by errors in horizon interpretation, different frequency content of P- and C-wave sections, and mis-match with well data. This topic is certainly worthy of further studies.

References

Alford, R.M., 1986, Shear data in the presence of azimuthal anisotropy, In *56th Ann. Internat. Mtg., Soc. of Expl. Geophys.*, **Expanded Abstracts**, 476-479.

Alford, R.M., 2000, Shear data in the presence of azimuthal anisotropy, *70th Ann. Internat. Mtg: Soc. Expl. Geophys.*, **Expanded Abstracts**, 372-374.

Alkhalifah, T.A., 1996, Velocity analysis using nonhyperbolic moveout in transversely isotropic media, *66th Ann. Internat. Mtg: Soc. Expl. Geophys.*, **Expanded Abstracts**, 1499-1502.

Alkhalifah, T.A., 1997, Velocity analysis using nonhyperbolic moveout in transversely isotropic media, *Geophysics*, **62**(8), 1839-1854.

Alkhalifah, T.A., and Tsvankin, I., 1995, Velocity analysis for transversely isotropic media, *Geophysics*, **60**(5), 1550-1566.

Angerer, E., Crampin, S., Li, X.Y. and Davis, T.L., 2002, Processing, modelling and predicting time-lapse effects of overpressured fluid-injection in a fractured reservoir. *Geophysical Journal International*, **149**, 267-280.

Angerer, E., Horne, S., Gaiser, J.E., Walters, R., and Vetri, L., 2002, Azimuthal analysis of shear-wave splitting for the characterization of dipping cracks: EAGE 64th Conference & Technical Exhibition-Florence, Italy, **Expanded Abstracts**, P256.

Bale, R., 1998, Plane wave deghosting of hydrophone and geophone OBC data: *68th Ann. Internat. Mtg., Soc. Expl. Geophys.*, **Expanded Abstracts**, 730-733.

Ball, V. and Corrigan, D., 1996, Dual-sensor summation of noisy ocean-bottom data: *71th Ann. Internat. Mtg., Soc. Expl. Geophys.*, **Expanded Abstracts**, 28-31.

Barr, F.J. and Sanders, J.I., 1989, Attenuation of water-column reverberations using pressure and velocity detectors in a water-bottom cable: *59th Ann. Internat. Mtg., Soc. Expl. Geophys.*, **Expanded Abstracts**, 653-656.

Becker, D., and Perelberg, A.I., 1986, Seismic detection of subsurface fractures: *56th Ann. Internat. Mtg: Soc. Expl. Geophys.*, **Expanded Abstracts**, Session: S9.2.

Brown, R., and Korringa, J., 1975, On the dependence of the elastic properties of a porous rock on the compressibility of the pore fluid, *Geophysics*, **40**, 608-616.

Buia, M., Delaney, D., Tomasi, V. D., and Vetri, L., 2001, 3D-4C acquisition design for fractures characterization in carbonate reservoir - a case history in offshore Adriatic, the Emilio field: *EAGE 63th Conference & Technical Exhibition-Amsterdam, Netherlands*, **Expanded Abstracts**, F33.

Calvert, A.S., Novak, J.M., Maher, J., Burch, D.N., Bird, D., Larson, R., 2005, A tale of two surveys: experiences processing two similar but different land 3D-3C MEMS surveys, *75th SEG meeting, Houston, USA*, **Expanded Abstracts**, 975-978.

Castagna, J.P., Sun, S., and Siegfried, R.W., 2003, Instantaneous spectral analysis: Detection of low-frequency shadows associated with hydrocarbons: *The Leading Edge*, **22**, 120-127.

Chakraborty, A., and Okaya, D., 1995, Frequency-time decomposition of seismic data using wavelet-based methods: *Geophysics*, **60**, 1906-1916.

Chapman, M., 2003, Frequency dependent anisotropy due to meso-scale fractures in the presence of equant porosity, *Geophysical Prospecting*, **51**, 369-379.

Chapman, M. and Liu, E., 2003, The frequency dependent azimuthal AVO response of fractured rock, In *73rd Ann. Internat. Mtg., Soc. of Explor. Geophys.*, **Expanded Abstracts**, 105-108.

Chapman, M., Maultzsch, S., Liu, E. and Li, X.-Y., 2003, The effect of fluid saturation in an anisotropic multi-scale equant porosity model, *Journal of Applied Geophysics*, **54**, 191-202.

Chen, W., 1995, AVO in azimuthally anisotropic media: fracture detection using P-wave data and a seismic study of naturally fractured tight gas reservoirs: *PhD Thesis, The University of Stanford*, 1-143.

Cohen, J., and Stockwell, J.J.W., 2000, CWP/SU: Seismic Unix Release: Centre for Wave Phenomena: No.3.2: *A Free Package for Seismic Research*, Colorado School of Mines.

Corrigan, D., Withers, R., Darnall, J., and Skopinski, T., 1997, Fracture mapping from azimuthal velocity analysis using 3D surface seismic data, *67th Ann. Internat. Mtg: Soc. Expl. Geophys.*, **Expanded Abstracts**, 1834-1837.

Crampin, S., 1977, A review of effects of anisotropic layering on the propagation of surface waves, *Geophys, J. Roy. Astr. Soc.*, **49**, 9-27.

Crampin, S., 1981, A review of wave motion in anisotropic and cracked elastic media, *Wave Motion*, **3**, 343-391.

Crampin, S., 1985, Evaluation of anisotropy by shear-wave splitting, *Geophysics*, **50**, 142-152.

Crampin, S., 1987, Geological and industrial implications of extensive-dilatancy anisotropy, *Nature*, **328**, 491-496.

Crampin, S., and Booth, D., 1985, Shear-wave polarizations near the North Anatolian fault II, Interpretation in terms of crack induced anisotropy, *Geophys. J. Roy. Astr. Soc.*, **83**, 75-92.

Crampin, S. and Lovell, J.H., 1991, A decade of shear-wave splitting in the Earth's crust what does it mean? What use can we make of it? And what should we do next? *Geophysical Journal International*, **107**, 387-407.

Dai, H., 2003a, Interactive estimation of anisotropic parameters and velocities from PS converted waves, *73th Internat. Mtg. Soc. Expl. Geophys.*, **Expanded Abstracts**, 1577-1580.

------2003b, Sensitivity analysis of migration velocities for P-S converted wave (C-wave) imaging, *64th Mtg.: Eur. Assn. of Expl. Geophys.*, Session, **P008**.

Dai, H. and Li, X.-Y., 2001, Anisotropic migration and model building for Alba 4C data, *71st Internat. Mtg. Soc. Expl. Geophys.*, **Expanded Abstracts**, 795-798.

Dai, H., and Li, X.-Y., 2006, The effects of migration velocity errors on traveltime accuracty in prestack Kirchhoff time migration and the image of PS converted waves, *Geophysics*, **71**, 73-83.

Dai, H., Li, X. –Y, and Gonway, P., 2004, 3D pre-stack Kirchhoff time migration of PS-waves and migration velocity model building, *74th Ann. Internat. Mtg: Soc. Expl. Geophys.*, **Expanded Abstracts**, N29.

Dai, H., Li, X.-Y., and Mueller, M., 2000, Compensating for the effects of gas clouds by prestack migration: A case study from Valhall, *70th Internat. Mtg. Soc. Expl. Geophys.*, **Expanded Abstracts**, 1047-1050.

Dellinger, J., Brandsberg-Dahl, S., Clarke, R., and Thomsen, L, 2001, Alford rotation after tensor migration, *71th Ann. Internat. SEG Mtg.*, **Expanded Abstracts**, 982-985.

Donati, M. and Brown, R.J., 1995, Birefringence study on 3-C/2-D: Barinas Basin (Venezuela): *65th Internat. Mtg., Soc. Explor. Geophys.*, **Expanded Abstracts**, 723-726.

Dunn, D.A., Biat, B.N.M., and Johns, M.V., 1986, Physical properties data, deep sea drilling project: *Init. Reports Deep Sea Drill Proj.*, **93**, 445-464.

Esmersoy, C., 1990, Split-shear wave inversion for fracture evaluation: *60th Ann. Internat. Mtg., Soc. Expl. Geophys.*, 1440-1403.

Gaiser, J.E., 1998, Compensating OBC data for variations in geophone coupling: *68th Annual Internat. Mtg., Soc. Expl. Geophys.*, **Expanded Abstracts**, 1429-1432.

Gaiser, J., 2000, 3D PS-wave data – unravelling shearwave birefringence for fracture detection. In *62nd Ann. Internat. Mtg., , Eur. Assn. Geosci. Eng.*, **Expanded Abstracts**, C0015.

Gaiser, J.E., Loinger, E., and Laura, V., 2001, PS-wave birefringence analysis at the Emilio field for fracture characterization: EAGE 63th Conference & Technical Exhibition-Amsterdam, Netherlands, **Expanded Abstracts**, N07.

Gaiser, J. and Van Dok, R., 2001, Green River basin 3D/3C case study for fracture characterization: Analysis of PS-wave birefringence: *71th Ann. Internat. Mtg., Soc. Of Expl. Geophys.*, 764-767.

Gao, J., Wang, W. and Li, Y., 1999, Instantaneous parameters extraction via wavelet transform: *IEEE Trans. On Geoscience and Remote Sensing*, **37**, 867-870.

Garotta, R., 2000, Shear waves from acquisition to interpretation, *SEG Distinguished Instructor short course, Distinguished instructor series*, **N.3.**

Garotta, R., Granger, P.-Y., and Dariu, H., 2002, Combined interpretation of PP and PS data provides direct access to elastic rock properties, *The Leading Edge*, **21**, N.6.

Granli, J. R., Arntsen, B., Sollid, A., and Hilde, E., 1999, Imaging through gas-filled sediments using marine shear wave data, *Geophysics*, **64**, 668-677.

Grechka, V., and Tsvankin, I., 1998, Feasibility of nonhyperbolic moveout inversion in transversely isotropic media, *Geophysics,* **63**(3), 957-969.

Grechka, V., and Tsvankin, I., 1998, Inversion of azimuthally dependent NMO velocity in transversely isotropic media with a tilted axis of symmetry, *68th Ann. Internat. Mtg: Soc. Expl. Geophys.*, **Expanded Abstracts**, 1483-1486.

Harrison, M.P., 1992, Processing of P-SV surface datga: Anisotropy analysis, dip moveout, and migratio: Ph.D Thesis, The University of Calgary, Alberta, Canada.

Helbig, K., 1994, Foundations of anisotropy for exploration seismics: *Handbook of Geophysical Exploration Section I. Seismic Exploration*, **22**, 1-485.

Helbig, K., 1998, A formalism for the consistent description of non-linear elasticity of anisotropic media: *The 8th International Workshop on Seismic Anisotropy,* 89-90.

Helbig, K. and Thomsen, L., 2005, 75-plus years of anisotropy in exploration and reservoir seismics: A historical review of concepts and methods: *Geophysics*, **70**, 9ND-23ND.

Hoffe, B.H., Cary, P.W. and Lines, L., 1999, A simple and robust method for combing dual-sensor OBC data? *CREWES Research Report*, Volume **11**.

Horne, S.A., 2003, Fracture characterization from walkaround VSPs. *Geophysical Prospecting*, **51**, 493-499.

Hudson, J., 1981, Wave speeds and attenuation of elastic waves in material containing cracks, *Geophys. J. Roy. Astr. Soc.*, **64**, 133-150.

Hudson, J., 1990, Overall elastic properties of isotropic materials with arbitrary distribution of circular cracks, *Geophys. J. Int.,* **102**, 465-469.

Hudson, J., Liu, E., and Crampin, S., 1996, The mechanical properties of materials with interconnected cracks and pores, *Geophys. J. Int.*, **124**, 105-112.

Igel, H. and Crampin, S., 1990, Extracting shear-wave polarizations from different source orientations: synthetic modelling: *J. Geophys. Res.*, **96**, 11283-11292.

Johnston, D., 1986, VSP detection of fracture-induced velocity anisotropy, *56th Ann. Internat. Mtg: Soc. Expl. Geophys.*, **Expanded Abstracts**, Session: S9.1.

Kendall, R.R., Gray, S.H. and Murphy, G.E., 1998, Subsalt imaging using prestack depth migration of converted waves, *68th Mtg. Soc. Expl. Geophys.,* **Expanded Abstracts**, 2052-2055.

Kendall, R., Hall, S.A., Kendall, J.-M., and Sondergeld, C., 1998, Analysis of anisotropic velocities in a fractured, vuggy carbonate and AVOA, *68th Ann. Internat. Mtg: Soc. Expl. Geophys.*, **Expanded Abstracts**, 1057-1059.

Krasover, M.L., Rodi, W., and Toksöz, M.N., 1998, Sensitivity analysis of amplitude variation with offset (AVO) in fractured media, *68th Ann. Internat. Mtg: Soc. Expl. Geophys.*, **Expanded Abstracts**, 201-203.

Li, X.-Y., 1997, Fractural reservior delineating using multicomponent seismic data, *Geophysical Prospecting,* **54**, 39-64.

Li, X.-Y., 1997, Viability of azimuthal variation in P-wave moveout for fracture detection: *67th Ann. Internat. Mtg: Soc. Expl. Geophys.*, Expanded Abstracts, II, 1555-1558.

Li, X.-Y., 1998, Fracture detection using P-P and P-S wave in multicomponent sea-floor data: *68th Ann. Internat. Mtg: Soc. Expl. Geophys.*, **Expanded Abstracts**, 2056-2059.

Li, X-Y., 1998, Processing PP and PS waves in multicomponent sea-floor data for azimuthal anisotropy: theory and overview, *Procedding of the Eighth International Workshop on seismic Anisotropy (Revue De L'institut francia du petrole)*, **53**, 607-620.

Li, X.-Y., 1999, Fracture detection using azimuthal variation of P-wave moveout from orthogonal seismic survey lines, *Geophysics*, **64**(4), 1193-1201.

Li, X.-Y. and Crampin, S., 1993, Linear transform techniques for analysing split shear-waves in four-component seismic data, *Geophysics,* **58**, 240-256.

Li, X.-Y., Dai, H., Mueller, M.C., and Barkved, O.I., 2001, Compensating for the effects of gas clouds on C-wave imaging: A case study from Valhall, *The Leading Edge*, **20**, 111-117..

Li, X.–Y., Dai, H., and Yuan, J., 2001, Converted-wave imaging in inhomogeneous, anisotopic media: part II – prestack migration, *63nd Mtg.: Eur. Assn. of Expl. Geophys.,* **Expanded abstracts**, L01.

Li, X.-Y., Kühnel, T., and MacBeth, C., 1996, Mixed mode AVO response in fractured media, *66th Ann. Internat. Mtg: Soc. Expl. Geophys.,* **Expanded Abstracts**, 1822-1825.

Li, X.-Y., Liu, Y., Liu, E., Feng, S., Qi, L. and Qu, S., 2003, Fracture detection using land 3D seismic from the Yelow-River delta, China, *The Leading Edge*, **22**, 680-683.

Li, X.-Y., and Yuan, J., 2003, Converted-wave moveout and conversion-point equations in layered VTI media revisited: Theory and applications, *Journal of Applied Geophysics*, **54**, 297-318.

Liu, E., Crampin, S. and Hudson, J.A., 1997, Diffraction of seismic waves with application to hydraulic fracturing, *Geophysics*, **62**, 253-265.

Liu, E., Hudson, J., and Pointer, T., 2000, Equivalent medium representation of fractured rock, *J. Geophys. Rec.*, **105**, 2981-3000.

Liu, E., and Li, X.-Y., 2000, Seismic detection of fluid saturation in aligned fractures, *70th Ann. Internat. Mtg: Soc. Expl. Geophys.*, **Expanded Abstracts**, 2373-2375.

Liu, E., Queen, J.H., Li, X.-Y., Chapman, M., Maultzsch, S., Lynn, H.B. and Chesnokov, E.M., 2003, Observation and analysis of frequency-dependent anisotropy from a multicomponent VSP at Bluebell-Altamont Field, Utah, *Journal of Applied Geophysics*, **54**, 319-333.

Liu, E., Maultzsch, S., Chapman, M., Li, X.-Y., Queen, J.H., and Zhang, Z., 2003a, Frequency-dependent seismic anisotropy and its implication for estimating fracture size in low porosity reservoirs: *The Leading Edge*, **22**, 662-665.

------2003b, Observation and analysis of frequency-dependent anisotropy from a multicomponent VSP at Bluebell-altamont field, Utah: *Journal of Applied Geophysics*, **54**, 319-333.

Liu, Y., Li, X.-Y., MacBeth, C., and Anderton, P., 1999, Analysis of azimuthal variation in P-wave signature from orthogonal steamer lines, *69th Ann. Internat. SEG Mtg.*, **Expanded Abstracts**, 1959-1962.

Lynn, H., and Beckham, W., 1998, P-wave azimuthal variations in attenuation, amplitude and velocity in 3-D field data: Implications for mapping horizontal permeability anisotropy, *68th Ann. Internat. Mtg: Soc. Expl. Geophys.*, **Expanded Abstracts**, 193-196.

MacBeth, C., 1999, Azimuthal variation in P-wave signatures due to fluid flow, *Geopohysics*, **64**, 1181-1192.

MacBeth, C. and Crampin, S., 1991a, Examination of a spectral method for measuring the effects of anisotropy, *Geophysical Prospecting*, **39**, 667-689.

-----1991b, Comparison of signal processing techniques for estimating the effects of anisotropy in VSP data, *Geophysics Prospecting*, **39**, 357-385.

MacBeth, C., and Li, X.-Y., 1999, AVD-An emerging new marine technology for reservoir characterization: Acquisition and application, *Geophysics*, **64**, 1153-1159.

MacBeth, C., Li, X.-Y., Crampin, S., and Muller, M., 1992, Detecting lateral viability in crack parameters from surface data, *62nd Ann. Internat. Mtg: Soc. Expl. Geophys.*, **Expanded Abstracts**, 816-819.

MacLeod, M., Hanson, R., Hadley, M. Reyholds, K., Lumley, D., MacHugo, S., and Probert, T., 1999, The Alba Field OBC seismic survey, *69th Internat. Mtg. Soc. Expl. Geophys.*, **Expanded Abstracts**, 725-727

Mallick, S., Craft, K. L,. J., Meister, L. J., and Chambers, R. E., 1996, Computation of principal directions of azimuthal anisotropy from P-wave seismic data, *66th Ann. Internat. Mtg: Soc. Expl. Geophys.*, **Expanded Abstracts**, 1862-1865.

Mancini, F., Li, X. –Y., and Pointer, T., 2005, Imaging Lomond Field using C-wave anisotropic PSTM, *The Leading Edge*, **24**(6), 614-620.

Mattocks, B., Li, J. and Roche, S.L., 2005, Converted-wave azimuthal anisotropy in a carbonate foreland basin: *75th SEG meeting, Houston*, **Expanded Abstracts**, 897-890.

Maultzsch, S., Chapman, M., Liu, E. and Li, X.-Y., 2003, Modelling frequency-dependent seismic anisotropy in fluid-saturated rock with aligned fractures: implication of fracture size estimation from anisotropic measurements, *Geophysical Prospecting*, **51**, 381-392.

Mueller, M., 1991, Prediction of lateral variability in fracture intensity using multicomponent shear wave surface seismic as a precursor to horizontal drilling, *Geophys. J. Int.*, **107**, 409-415.

Murtha, P.E., 1989, Preliminary analysis of the ARCO multicomponent seismic group experiment: SEG Research Workshop, Recording and Processing Vector Wavefield Data, *Soc. Expl. Geophys.*, **Expanded Abstracts**, 61-63.

Naville, C., 1986, Detection of anisotropy using shear-wave splitting in VSP survey: Requirements and application, *56th Ann. Internat. Mtg., Soc. Expl. Geophys.*, **Expanded Abstracts**, 391-394.

Nicoletis, L., Client, C., and Lefeuvre, F., 1988, Shear-wave splitting measurements from multishot VSP data: *58th Ann. Internat. Mtg., Soc. Expl. Geophys.*, **Expanded Abstracts**, 527-530.

Partyka, G., Gridley, J. and Lopez, J., 1999, Interpretational applications of spectral decomposition in reservoir characterization: *The Leading Edge*, **18**, 353-360.

Peron, J., 1990, Estimation of fracture directions from zero-offset VSP by two- and four-component rotation: *60th Ann. Internat. Mtg., Soc. Of Expl. Geophys.*, 1443-1446.

Peyton, L., Bottjer, R. and Partyka, G., 1998, Interpretation of incised valleys using new 3-D seismic techniques: A case history using spectral decomposition and coherency: *The Leading Edge*, **17**, 1294-1298.

Pointer, T., Liu, E., and Hudson, J., 2000, Seismic wave propagation in cracked porous media, *Geophysical Journal International*, **142**, 199-231.

Pope, D., Kimmedal, J. and Hansen, J., 2000, Using 3D 4C Seismic to drill beneath the Lomond gas cloud, *62nd Mtg.: Eur. Assn. of Expl. Geophys.*, **Expanded abstracts**, L01.

Roche, S.L., Wagaman, M., and Watt, H.J., 2005, Analysis of P-wave and Converted-wave 3D seismic data, Anadarko Basin, Oklahoma, USA: *75th SEG meeting, Houston*, **Expanded Abstracts**, 979-982.

Rüger, A., 1996a, Variation of P-wave reflectivity with offset and azimuth in anisotropic media, *66th Ann. Internat. Mtg: Soc. Expl. Geophys.*, **Expanded Abstracts**, 1810-1813.

------ 1996b, Analytic insight into shear-wave AVO for fractured reservoirs, *66th Ann. Internat. Mtg: Soc. Expl. Geophys.*, **Expanded Abstracts**, 1801-1804.

Sayers, C.M., and Ebrom, D., A., 1997, Seismic traveltime analysis for azimuthally anisotropic media: Theory and experiment, *Geophysics*, **62**, 1570-1582.

Sayers, C.M., and Kachanov, M., 1995, Microcrack-induced elastic wave anisotropy of brittla rocks, *J. Geophys. Res.*, **100**, 4149-4156.

Schoenberg, M., Hsu, K., and Walsh, J.J., 1991, Anisotropy from polarization and moveout, *Geophysics*, 1526-1529.

Schoenberg, M., 1994, Transverse isotropic media equivalent to thin isotropic layers, *Geophysical Prospecting*, **42**, 885-915.

Schoenberg, M.A., 1998, Acoustic characterization of underground fractures, *68th Ann. Internat. Mtg: Soc. Expl. Geophys.*, **Expanded Abstracts**, 1624-1627.

Schoenberg, M., and Sayers, C.M., 1995, Seismic anisotropy of fractured rock, *Geophysics*, **60**, 204-211.

Sena, A.G., 1991, Seismic traveltime equations for azimuthally anisotropic and isotropic media: Estimation of interval elastic properties, *Geophysics,* **56**, 2090-2101.

Shen, F., Gary, C.R. and Jiang, T., 2003, Instantaneous spectral analysis applied to reservoir imaging and productability characterization: *73th Ann. Internat. Mtg., Soc. Of Expl. Geophys.*, 1406-1409.

Teng, L., and Mavko, G., 1996, Fracture signatures on P-wave AVOZ, *66th Ann. Internat. Mtg: Soc. Expl. Geophys.*, **Expanded Abstracts**, 1818-1821.

Theilen, F., Ayres, A., and Lange, G., 1997, Physical properties of near surface marine sediments: *59th EAGE Conference*, **Expanded Abstracts**, P064.

Thomsen, L., 1986, Weak elastic anisotropy, *Geophysics*, **51**, 1954-1966.

Thomsen, L., 1988, Reflection seismology over azimuthally anisotropic media, *Geophysics*, **53**, 304-313.

Thomsen, L., 1995, Elastic anisotropy due to aligned cracks in porous rock, *Geophysics Prospecting*, **43**, 805-829.

Thomsen, L., Barkved, O. I., Haggard, B., Kimmedal, J. H., Rosland, B., 1997, Converted-wave imaging of Valhall reservoir, *59th Mtg.: Eur. Assn. of Expl. Geophys.*, **Expanded Abstracts**, B048.

Tod, S.R., 2001, The effects on seismic waves of interconnected nearly aligned cracks, *Geophys. J. Int.*, **146**, 249-263.

Traub, B., and Li, X.-Y., 2004, Can we constrain a VTI model by joint non-hyperbolic moveout inversion of P- and Converted-wave data? *66nd Mtg.: Eur. Assn. of Expl. Geophys.*, **Expanded abstracts**, Z99.

Tsvankin, I., 1995, Inversion of moveout velocity for horizontal transverse isotropy, *65th Ann. Internat. Mtg: Soc. Expl. Geophys.*, **Expanded Abstracts**, 735-738.

Tsvankin, I., 1997, Reflection moveout and parameter estimation for horizontal transverse isotropy, *Geophysics*, **62**, 614-629.

Tsvankin, I., and Thomsen, L., 1994, Nonhyperbolic reflection moveout in anisotropic media, *Geophysics*, **59**(8), 1290-1304.

Tsvankin, I., and Thomsen, L., 1995, Inversion of reflection traveltimes for transverse isotropy, *Geophysics*, **60**(4), 1095-1107.

van den Berg, J., 1999, Wavelets in physics: Cambridge University Press, Cambridge, England.

van der Kolk, C.M., Guest, W.S., and Potters, J.H.H.M., 2001, The 3D shear experiment over the Natih field in Oman: The effect of fracture-filling fluids on shear propagation, *Geophysical Prospecting*, **49**, 179-197.

Vetri, L, Angerer, E., and Gaiser, J.E., 2002, Emilio field anisotropy analysis from PP and PS data; EAGE 64th Conference & Technical Exhibition-Florence, Italy, **Expanded Abstracts**, F46.

Vetri, L., Loinger, E., Gaiser, J.B., Grandi, A., and Lynn, H., 2003, 3D/4C Emilio: Azimuth processing and anisotropy in a fractured carbonate reservoir: *The Leading Edge*, **22**, 675-679.

Wang, Z., 2002, Seismic anisotropy in sedimentary rocks, part 2: Laboratory data, *Geophysics*, **67**, 1423-1440.

Werner, U. and Shapiro, S.A., 1999, Frequency-dependent shear-wave splitting in thinly layered media with intrinsic anisotropy, *Geophysics*, **51**, 604-608.

Willis, H., Rethford, G., and Bielanski, E., 1986, Azimuthal anisotropy: Occurrence and effects of shear-wave data quality, *56th Ann. Internat. Mtg: Soc. Expl. Geophys.*, **Expanded Abstracts**, Session: S9.7.

Winterstein, D.F. and Meadows, M. A., 1991a, Shear-wave polarization and substructure stress direction at Lost Hill field, *Geophysics*, **56**, 1331-1348.

-----1991b, Changes in shear-wave polarization azimuth with depth in Cymric and Railroad Gap oil fields, *Geophysics*, **56**, 1349-1364.

Yuan, J., 2001, Analysis of four-component sea-floor seismic data for seismic anisotropy: PhD Thesis, The University of Edinburgh.

Zeng, X. and MacBeth, C., 1991, Accuracy of shear-wave splitting estimations from near-offset VSP data, *Can. J. Expl. Geophys.*, **29**, 246-265.

Zeng, X. and MacBeth, C., 1993, Algebraic processing techniques for estimating shear-wave splitting in near-offset VSP data: theory, *Geophysical Prospecting*, **41**, 1033-1066.

Appendix A

The Emilio dataset information

In this appendix I list the information of the Emilio dataset, which has 12 swaths. I made a copy the whole Emilio dataset from IBM 3590 tapes into DLT8000 tapes.

A.1 List of the tape numbers in each swath

EMILIO 3D 4C						
SWATH		START		END		NUMBER
7		FS6403		FS6434		32
8		FS6435		FS6463		29
6		FS6464		FS6494		31
6		FS6545		FS6549		5
5		FS6495		FS6525		31
4		FS6526		FS6544		19
3		FS6550		FS6571		22
2		FS6572		FS6585		14
1		FS6586		FS6597		12
9		FS6598		FS6621		24
10		FS6622		FS6643		22
11		FS6644		FS6657		14
12		FS6658		FS6669		12

A.2 The Emilio data copy list

LOW_REF	HIGH_REF	DOC_TYPE	REEL_LAB	SWATH	DLT8000	FILE_NO
2	347	FIELD	FS6403	7	SWATH07-1	1
348	694	FIELD	FS6404	7		2
695	1040	FIELD	FS6405	7		3
1041	308	FIELD	FS6406	7		4
309	654	FIELD	FS6407	7	SWATH07-2	1
655	1001	FIELD	FS6408	7		2
1002	1347	FIELD	FS6409	7		3
1348	1693	FIELD	FS6410	7		4
1694	2039	FIELD	FS6411	7	SWATH07-3	1
2040	2385	FIELD	FS6412	7		2
2386	2731	FIELD	FS6413	7		3
2732	3077	FIELD	FS6414	7		4
3078	3423	FIELD	FS6415	7	SWATH07-4	1
3424	3769	FIELD	FS6416	7		2
3770	342	FIELD	FS6417	7		3
343	688	FIELD	FS6418	7		4
689	1034	FIELD	FS6419	7	SWATH07-5	1
1035	1380	FIELD	FS6420	7		2
1381	1726	FIELD	FS6421	7		3
1727	2072	FIELD	FS6422	7		4
2073	2418	FIELD	FS6423	7	SWATH07-6	1
2419	2764	FIELD	FS6424	7		2
2765	3110	FIELD	FS6425	7		3
3111	3456	FIELD	FS6426	7		4
3457	3802	FIELD	FS6427	7	SWATH07-7	1
3803	4148	FIELD	FS6428	7		2
4149	4342	FIELD	FS6429	7		3
8	67	FIELD	FS6430	7		4
68	1102	FIELD	FS6431	7	SWATH07-8	1
1103	212	FIELD	FS6432	7		2
213	761	FIELD	FS6433	7		3
4762	972	FIELD	FS6434	7		4
2	347	FIELD	FS6435	8	SWATH08-1	1
348	693	FIELD	FS6436	8		2
694	1039	FIELD	FS6437	8		3
1040	1385	FIELD	FS6438	8		4
1386	1731	FIELD	FS6439	8	SWATH08-2	1
1732	2077	FIELD	FS6440	8		2
2078	2423	FIELD	FS6441	8		3
2424	2769	FIELD	FS6442	8		4

LOW_REF	HIGH_REF	DOC_TYPE	REEL_LAB	SWATH	DLT8000	FILE_NO
2770	3115	FIELD	FS6443	8	SWATH08-3	1
3116	3461	FIELD	FS6444	8		2
3462	3808	FIELD	FS6445	8		3
3809	4154	FIELD	FS6446	8		4
4155	4500	FIELD	FS6447	8	SWATH08-4	1
4501	4846	FIELD	FS6448	8		2
4847	5192	FIELD	FS6449	8		3
5193	5538	FIELD	FS6450	8		4
5539	5884	FIELD	FS6451	8	SWATH08-5	1
5885	6230	FIELD	FS6452	8		2
6231	6577	FIELD	FS6453	8		3
6578	6923	FIELD	FS6454	8		4
6924	7269	FIELD	FS6455	8	SWATH08-6	1
7270	7615	FIELD	FS6456	8		2
7616	7961	FIELD	FS6457	8		3
7962	8307	FIELD	FS6458	8		4
8308	8656	FIELD	FS6459	8	SWATH08-7	1
8657	8790	FIELD	FS6460	8		2
2	550	FIELD	FS6461	8		3
551	1099	FIELD	FS6462	8		4
1100	1466	FIELD	FS6463	8	SWATH08-4	1
2	347	FIELD	FS6464	6	SWATH06-3	2
348	693	FIELD	FS6465	6		3
694	1039	FIELD	FS6466	6		4
1040	1385	FIELD	FS6467	6	SWATH06-2	1
1386	1731	FIELD	FS6468	6		2
1732	2076	FIELD	FS6469	6		3
2077	2422	FIELD	FS6470	6		4
2423	2768	FIELD	FS6471	6	SWATH06-3	1
2769	3114	FIELD	FS6472	6		2
3115	3460	FIELD	FS6473	6		3
3461	3806	FIELD	FS6474	6		4
3807	4152	FIELD	FS6475	6	SWATH06-4	1
4153	4498	FIELD	FS6476	6		2
4499	4844	FIELD	FS6477	6		3
4845	5190	FIELD	FS6478	6		4
5191	5536	FIELD	FS6479	6	SWATH06-5	1
5537	5882	FIELD	FS6480	6		2
5883	6228	FIELD	FS6481	6		3
6229	6574	FIELD	FS6482	6		4
6575	6920	FIELD	FS6483	6	SWATH06-6	1
6921	7266	FIELD	FS6484	6		2
7267	7613	FIELD	FS6485	6		3
7614	7959	FIELD	FS6486	6		4
7960	8305	FIELD	FS6487	6	SWATH06-7	1
8306	8651	FIELD	FS6488	6		2
8652	8758	FIELD	FS6489	6		3
2	347	FIELD	FS6490	6		4

LOW_REF	HIGH_REF	DOC_TYPE	REEL_LAB	SWATH	DLT8000	FILE_NO
348	693	FIELD	FS6491	6	SWATH06-8	1
694	1039	FIELD	FS6492	6		2
1040	1386	FIELD	FS6493	6		3
1387	1465	FIELD	FS6494	6		4
1469	1814	FIELD	FS6495	5	SWATH05-1	1
1815	2160	FIELD	FS6496	5		2
2161	2506	FIELD	FS6497	5		3
2507	2852	FIELD	FS6498	5		4
2853	3198	FIELD	FS6499	5	SWATH05-2	1
3199	3544	FIELD	FS6500	5		2
3545	3890	FIELD	FS6501	5		3
3891	4236	FIELD	FS6502	5		4
4237	4582	FIELD	FS6503	5	SWATH05-3	1
4583	4928	FIELD	FS6504	5		2
4929	5274	FIELD	FS6505	5		3
5275	5620	FIELD	FS6506	5		4
5621	5966	FIELD	FS6507	5	SWATH05-4	1
5967	6312	FIELD	FS6508	5		2
6313	6658	FIELD	FS6509	5		3
6659	7004	FIELD	FS6510	5		4
7005	7350	FIELD	FS6511	5	SWATH05-5	1
7351	7696	FIELD	FS6512	5		2
7697	8042	FIELD	FS6513	5		3
8043	8388	FIELD	FS6514	5		4
8389	8734	FIELD	FS6515	5	SWATH05-6	1
8735	9080	FIELD	FS6516	5		2
9081	9426	FIELD	FS6517	5		3
9527	9772	FIELD	FS6518	5		4
9773	191	FIELD	FS6519	5	SWATH05-7	1
192	342	FIELD	FS6520	5		2
2	347	FIELD	FS6521	5		3
348	693	FIELD	FS6522	5		4
694	1039	FIELD	FS6523	5	SWATH05-8	1
1040	1385	FIELD	FS6524	5		2
1386	1467	FIELD	FS6525	5		3
2	347	FIELD	FS6526	4	SWATH04-1	4
348	693	FIELD	FS6527	4	SWATH04-2	1
694	1079	FIELD	FS6528	4		2
1080	1425	FIELD	FS6529	4		3
1426	1771	FIELD	FS6530	4		4
1772	2117	FIELD	FS6531	4	SWATH04-3	1
2118	2463	FIELD	FS6532	4		2
2464	2809	FIELD	FS6533	4		3
2810	3155	FIELD	FS6534	4		4
3156	3501	FIELD	FS6535	4	SWATH04-4	1
3502	3847	FIELD	FS6536	4		2
3848	4193	FIELD	FS6537	4		3
4194	4539	FIELD	FS6538	4		4

LOW_REF	HIGH_REF	DOC_TYPE	REEL_LAB	SWATH	DLT8000	FILE_NO
4540	4885	FIELD	FS6539	4	SWATH04-5	1
4886	5231	FIELD	FS6540	4		2
5232	5577	FIELD	FS6541	4		3
5578	5923	FIELD	FS6542	4		4
5924	6269	FIELD	FS6543	4	SWATH04-6	1
6270	6396	FIELD	FS6544	4		2
2	349	FIELD	FS6545	6	LAST	1
350	695	FIELD	FS6546	6	SWATH06-9	3
696	1042	FIELD	FS6547	6	SWATH06-1	1
1043	1388	FIELD	FS6548	6		2
1389	1461	FIELD	FS6549	6		3
2	347	FIELD	FS6550	3	SWATH03-1	4
348	694	FIELD	FS6551	3	SWATH03-2	1
695	1041	FIELD	FS6552	3		2
1042	1387	FIELD	FS6553	3		3
1388	1733	FIELD	FS6554	3		4
1734	2079	FIELD	FS6555	3	SWATH03-3	1
2080	2426	FIELD	FS6556	3		2
2427	2772	FIELD	FS6557	3		3
2773	3118	FIELD	FS6558	3		4
3119	3464	FIELD	FS6559	3	SWATH03-4	1
3465	3810	FIELD	FS6560	3		2
3811	4156	FIELD	FS6561	3		3
4157	4502	FIELD	FS6562	3		4
4503	4848	FIELD	FS6563	3	SWATH03-5	1
4849	5194	FIELD	FS6564	3		2
5195	5540	FIELD	FS6565	3		3
5541	5698	FIELD	FS6566	3		4
2	347	FIELD	FS6567	3	SWATH03-6	1
348	693	FIELD	FS6568	3		2
694	1040	FIELD	FS6569	3		3
1041	1386	FIELD	FS6570	3		4
1387	1466	FIELD	FS6571	3	SWATH03-7	1
1	346	FIELD	FS6572	2	SWATH02-3	2
347	692	FIELD	FS6573	2		3
693	1038	FIELD	FS6574	2		4
1039	1384	FIELD	FS6575	2	SWATH02-2	1
1385	1731	FIELD	FS6576	2		2
1732	2077	FIELD	FS6577	2		3
2078	2423	FIELD	FS6578	2		4
2424	2769	FIELD	FS6579	2	SWATH02-3	1
2770	2898	FIELD	FS6580	2		2
2	347	FIELD	FS6581	2		3
348	693	FIELD	FS6582	2		4
694	1039	FIELD	FS6583	2	SWATH02-3	1
1040	1385	FIELD	FS6584	2		2
1386	1467	FIELD	FS6585	2		3
2	347	FIELD	FS6586	1	SWATH01-1	4

LOW_REF	HIGH_REF	DOC_TYPE	REEL_LAB	SWATH	DLT8000	FILE_NO
348	693	FIELD	FS6587	1	SWATH01-2	1
694	1039	FIELD	FS6588	1		2
1040	1385	FIELD	FS6589	1		3
1386	1731	FIELD	FS6590	1		4
1732	2077	FIELD	FS6591	1	SWATH01-3	1
2078	2187	FIELD	FS6592	1		2
2	347	FIELD	FS6593	1		3
348	693	FIELD	FS6594	1		4
694	1039	FIELD	FS6595	1	SWATH01-4	1
1040	1385	FIELD	FS6596	1		2
1386	1456	FIELD	FS6597	1		3
2	345	FIELD	FS6598	9	SWATH09-1	4
346	691	FIELD	FS6599	9	SWATH09-2	1
692	1037	FIELD	FS6600	9		2
1038	1383	FIELD	FS6601	9		3
1384	1729	FIELD	FS6602	9		4
1730	2075	FIELD	FS6603	9	LAST	4
2076	2421	FIELD	FS6604	9	SWATH09-3	1
2422	2767	FIELD	FS6605	9		2
2768	3113	FIELD	FS6606	9		3
3114	3459	FIELD	FS6607	9	SWATH09-4	1
3460	3805	FIELD	FS6608	9		2
3806	4151	FIELD	FS6609	9		3
4152	4497	FIELD	FS6610	9		4
4498	4843	FIELD	FS6611	9	SWATH09-5	1
4844	5189	FIELD	FS6612	9		2
5190	5535	FIELD	FS6613	9		3
5536	5881	FIELD	FS6614	9		4
5882	6227	FIELD	FS6615	9	SWATH09-6	1
6228	6447	FIELD	FS6616	9		2
2	347	FIELD	FS6617	9		3
348	693	FIELD	FS6618	9		4
694	1039	FIELD	FS6619	9	SWATH09-3	1
1040	1385	FIELD	FS6620	9		2
1386	1480	FIELD	FS6621	9		3
2	347	FIELD	FS6622	10	SWATH10-4	4
348	693	FIELD	FS6623	10	SWATH10-2	1
694	1039	FIELD	FS6624	10		2
1040	1385	FIELD	FS6625	10		3
1386	1731	FIELD	FS6626	10		4
1732	2077	FIELD	FS6627	10	SWATH10-3	1
2078	2423	FIELD	FS6628	10		2
2424	2770	FIELD	FS6629	10		3
2771	3116	FIELD	FS6630	10		4
3117	3462	FIELD	FS6631	10	SWATH10-4	1
3463	3808	FIELD	FS6632	10		2
3809	4154	FIELD	FS6633	10		3
4155	4500	FIELD	FS6634	10		4

LOW_REF	HIGH_REF	DOC_TYPE	REEL_LAB	SWATH	DLT8000	FILE_NO
4501	4846	FIELD	FS6635	10	SWATH10-5	1
4847	5192	FIELD	FS6636	10		2
5193	5538	FIELD	FS6637	10		3
5539	5660	FIELD	FS6638	10		4
3	348	FIELD	FS6639	10	SWATH10-6	1
349	694	FIELD	FS6640	10		2
695	1040	FIELD	FS6641	10		3
1041	1386	FIELD	FS6642	10		4
1387	1467	FIELD	FS6643	10	SWATH10-1	1
2	347	FIELD	FS6644	11	LAST	2
348	693	FIELD	FS6645	11	SWATH11-3	2
694	1042	FIELD	FS6646	11		3
1043	1388	FIELD	FS6647	11		4
1389	1734	FIELD	FS6648	11	SWATH11-2	1
1735	2080	FIELD	FS6649	11		2
2081	2426	FIELD	FS6650	11		3
2427	2773	FIELD	FS6651	11		4
2774	3059	FIELD	FS6652	11		
2	347	FIELD	FS6653	11	SWATH11-3	1
348	693	FIELD	FS6654	11		2
694	1039	FIELD	FS6655	11		3
1040	1385	FIELD	FS6656	11		4
1386	1453	FIELD	FS6657	11	SWATH11-4	1
2	347	FIELD	FS6658	12	SWATH12-1	2
348	693	FIELD	FS6659	12		3
694	1039	FIELD	FS6660	12		3
1040	1385	FIELD	FS6661	12		4
1386	1731	FIELD	FS6662	12	SWATH12-2	1
1732	2077	FIELD	FS6663	12		2
2078	2194	FIELD	FS6664	12		3
2	347	FIELD	FS6665	12		4
348	693	FIELD	FS6666	12	SWATH12-3	1
694	1039	FIELD	FS6667	12		2
1040	1385	FIELD	FS6668	12		3
1386	1468	FIELD	FS6669	12		4

A.3 The Emilio dataset (Swath 7, 35 lines)

LINE	FFID START	FFID END	TAPE
P1	8	489	6430
P2	2	486	6432 6433
P3	69	480	6431
P4	968	1438	6431 6432
P5	488	972	6433 6434
C1	2	287	6403
C2	2	289	6406
C3	339	626	6404
C4	291	577	6406 6407
C5	629	914	6405
C6	579	866	6407 6408
C7	1446	1733	6410 6411
C8	868	1154	6408 6409
C9	1735	2022	6411
C10	1157	1444	6409 6410
C11	2023	2310	6411 6412
C12	2890	3146	6414 6415
C13	2312	2599	6412 6413
C14	3161	3448	6415 6416
C15	2601	2888	6413 6414
C16	3450	3737	6416
C17	2	289	6417
C18	3986	4271	6428 6429
C19	359	646	6418
C20	3697	3984	6427 6428
C21	648	935	6418 6419
C22	3408	3695	6426 6427
C23	937	1220	6419 6420
C24	3119	3406	6425 6426
C25	1237	1579	6420 6421
C26	2759	3046	6425
C27	1581	1886	6421 6422
C28	2465	2757	6424 6425
C29	1888	2175	6422 6423
C30	2177	2463	6423 6424
TAPE	PART ONE	PART TWO	
6430	1_7	8_489	
6431	69_480	967_1103	
6432	1_213	1104_1439	
6433	214_762		
6434	763_972		

A.4 Swath 7 information

NAME	LOW_REF	HIGH_REF	DOC_TYPE	REEL_LAB	SWATH
EMILIO 3D 4C	2	347	FIELD	FS6403	7
EMILIO 3D 4C	348	694	FIELD	FS6404	7
EMILIO 3D 4C	695	1040	FIELD	FS6405	7
EMILIO 3D 4C	1041	308	FIELD	FS6406	7
EMILIO 3D 4C	309	654	FIELD	FS6407	7
EMILIO 3D 4C	655	1001	FIELD	FS6408	7
EMILIO 3D 4C	1002	1347	FIELD	FS6409	7
EMILIO 3D 4C	1348	1693	FIELD	FS6410	7
EMILIO 3D 4C	1694	2039	FIELD	FS6411	7
EMILIO 3D 4C	2040	2385	FIELD	FS6412	7
EMILIO 3D 4C	2386	2731	FIELD	FS6413	7
EMILIO 3D 4C	2732	3077	FIELD	FS6414	7
EMILIO 3D 4C	3078	3423	FIELD	FS6415	7
EMILIO 3D 4C	3424	3769	FIELD	FS6416	7
EMILIO 3D 4C	3770	342	FIELD	FS6417	7
EMILIO 3D 4C	343	688	FIELD	FS6418	7
EMILIO 3D 4C	689	1034	FIELD	FS6419	7
EMILIO 3D 4C	1035	1380	FIELD	FS6420	7
EMILIO 3D 4C	1381	1726	FIELD	FS6421	7
EMILIO 3D 4C	1727	2072	FIELD	FS6422	7
EMILIO 3D 4C	2073	2418	FIELD	FS6423	7
EMILIO 3D 4C	2419	2764	FIELD	FS6424	7
EMILIO 3D 4C	2765	3110	FIELD	FS6425	7
EMILIO 3D 4C	3111	3456	FIELD	FS6426	7
EMILIO 3D 4C	3457	3802	FIELD	FS6427	7
EMILIO 3D 4C	3803	4148	FIELD	FS6428	7
EMILIO 3D 4C	4149	4342	FIELD	FS6429	7
EMILIO 3D 4C	8	67	FIELD	FS6430	7
EMILIO 3D 4C	68	1102	FIELD	FS6431	7
EMILIO 3D 4C	1103	212	FIELD	FS6432	7
EMILIO 3D 4C	213	761	FIELD	FS6433	7
EMILIO 3D 4C	4762	972	FIELD	FS6434	7

Appendix B

Theory of PZ summation

In Chapter 4, I have developed a simple and robust technique for multiple attenuation during data pre-processing stage. Here I review some theories of PZ summation, the possibility of summing the hydrophone and the vertical component responses.

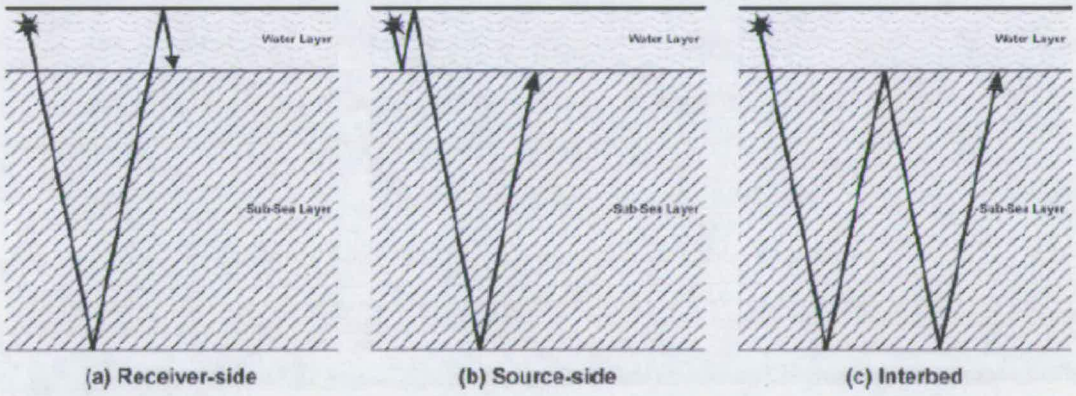

Figure B.1: Most common first order multiples, from Hoffe et al. (1999). (a) the receiver side multiple (ghost), (b) the source side multiple (peg-leg) and (c) the interbed.

Ghosts and peg–legs are commonly referred to water-column reverberation. The problem of water-column reverberation can be greater in OBC acquisition than in traditional streamer acquisition. The reason is that the receivers are at a greater depth, i.e. a greater distance from the water surface. This translates into having receiver ghosts at a much lower frequency. The frequency of the ghost no*tc*hes is in fact dependent on the receivers depth: [$f=k(v/2\Delta z)$], where k is an integer, v is the water

velocity and Δz is the receivers depth. This lower frequency makes difficult to eliminate the ghosts using a deconvolution operator (Soubaras, 1996). Figure B.1 shows three of the most common first order multiples which affect marine-acquired seismic data.

Ghost effects can instead be removed by summation of the hydrophone and the vertical geophone records (PZ summation) (Barr and Sanders, 1986, Soubaras, 1996). This technique exploits the fact that the response of the hydrophone and the vertical component are opposite in sign. The hydrophone measures a total pressure fields and it is not directional while the vertical component records a velocity and is directional. If we call H the pressure recorded at the hydrophone and G the vertical velocity recorded at the geophone we can see that their response at the receivers is (Ball et al., 1996):

$$H = \frac{(1-z)}{(1+rz)} A \tag{B.1}$$

$$G = \frac{(1+z)}{1+rz} A \tag{B.2}$$

r is the water-bottom reflection coefficient, z is the two way propagation of sound in the water layer and A is the subsurface response.

To remove the ghost effect, Barr and Sanders (1989) proposed to add the two responses as follow:

$$\frac{(1-r)}{2} H + \frac{(1+r)}{2} G \tag{B.3}$$

Here the value of r is needed. Barr and Sanders (1986) used an empirical estimation of it, 0.32, derived for a sandy water bottom with a velocity contrast of 1.13. Ball and Corrigan (1996) proposed to calculate r using a more complicated function, which has the property of being unbiased by the effects of source side reverberation. In practice, prior to summation, the amplitude and phase, if needed, have to be carefully matched; usually the geophone is scaled to match the hydrophone.

Analysis of converted-wave splitting in volcanic rocks: a case study from northeast China

Lifeng Wang[1,2], Xiang-Yang Li[1] and Xianyi Sun[3]

[1] British Geological Survey, Murchison House, West Mains Road, Edinburgh EH9 3LA, UK

[2] School of GeoSciences, The University of Edinburgh, West Mains Road, Edinburgh EH9 3JW, UK

[3] PetroChina Daqing Oilfield Ltd, Henglong Jiang, China

Summary

Converted shear-wave splitting provides a practical means for evaluating azimuthal anisotropy in hydrocarbon reservoirs that may give some insights into the internal architecture of the reservoirs. In this paper, we evaluate converted-wave seismic data acquired over volcanic gas reservoirs. The converted-wave data reveals a significant amount of shear-wave splitting over the volcanic formation, and we develop a technique to extract the shear-wave polarization and time delay from the data. The technique is particularly designed for evaluating converted-wave splitting for 2D or 3D data with a narrow-azimuth distribution. We adopt a rotation-scanning procedure that maximizes the separation of the fast and slow split shear-waves. It is interesting that the amount of splitting determined from the data can be correlated to the known gas reservoirs, revealing a potential to use shear-wave splitting to delineate gas reservoirs in volcanic rocks.

Introduction

When a P-S conversion occurs at a reflector and the medium above the reflector is azimuthally anisotropic, the converted shear wave splits into a fast and a slow shear wave, and this is referred to as converted-wave splitting. There is a wide interest from the industry to use converted-wave splitting to evaluate the internal architecture of hydrocarbon reservoirs. The splitting can be caused by the alignment of cracks, fractures, and small heterogeneities in the reservoirs. There is a vast amount of literatures on the use of converted-wave splitting to characterize fractured reservoirs (e.g. Gaiser and Van Dok 2001; Granger et al. 2001; Vetri et al. 2003; amongst others).

Shear-wave splitting in volcanic rocks has also been reported (e.g. Crampin and Lovell 1990). Volcanic rocks are known to be heterogeneous and can contain a large amount of fractures and vuggy pores, as well as other small heterogeneities. When these small-scale features are gas-charged and stress-aligned, it will introduce azimuthal anisotropy, giving rise to shear-wave splitting. Angerer et al. (2002) observed significant changes in shear-wave splitting before and after CO_2 injection in a carbonate reservoir where the presence of CO_2 kept the fractures and cracks open and increased the amount of splitting. Based on similar ideas, here we present a study of using converted-wave splitting to delineate gas reservoirs in volcanic rocks.

Analysis methods for shear-wave splitting

As we know, tensor rotation algorithms such as Alford's rotation require multi-azimuth distribution (Gaiser and Van Dok 2001). However, the converted-wave data used in this study is acquired using digital MEMS (micro-electro-mechanical-sysmtem) sensors with a 2D configuration and single-azimuth source and receiver distribution. For single-azimuth data, a rotation scanning procedure is often needed that searches for optimum solutions according to certain criteria. The common criteria include waveform similarity between the fast and slower shear-waves, or minimum spectral interference of split shear-waves (MacBeth and Crampin 1991). Here we adopt a criterion that maximizes the separation of the fast and slow shear-waves, following the approach of Yuan (2001). Once the split shear-waves are separated, we construct a time-delay spectrum between the fast and slow waves that allows the picking of time delays as a function of the vertical travel time, yielding a time-delay section for interpretation purposes.

Basic equations for rotation scanning

Figure 1 shows a map view of shear wave splitting when an up-going converted shear wave travels in a medium with a preferred distribution of heterogeneities. The principal direction of the medium forms an oblique angle θ with the survey line. The orientation of the three component geophone forms a right-handed coordinate system: radial component R, transverse component T and vertical component V, pointing to the reader. The polarization of the fast split shear wave S_1 is parallel to the principal direction and that of the slow shear wave S_2 perpendicular to it.

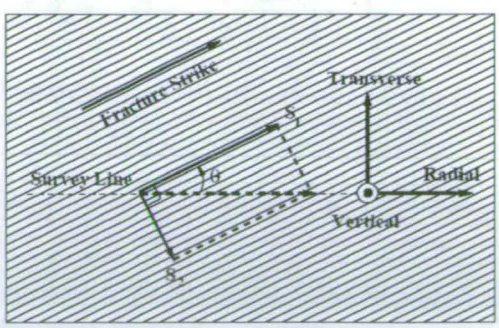

Figure1: Map view of shear wave splitting when an up-going converted shear wave travels in a vertically fracture medium.

To process the split shear waves, it is common to use the convolution model of seismic wave propagation. Thus, in the frequency domain, the wavefield recorded by the radial and transverse components can be written as,

$$\begin{bmatrix} R(\omega) \\ T(\omega) \end{bmatrix} = \begin{bmatrix} \cos\theta & \sin\theta \\ \sin\theta & -\cos\theta \end{bmatrix} \begin{bmatrix} S_1(\omega) \\ S_2(\omega) \end{bmatrix} + \begin{bmatrix} N_R(\omega) \\ N_T(\omega) \end{bmatrix} \quad (1)$$

where $N_R(\omega)$ and $N_T(\omega)$ are the noise components in the radial and transverse directions. To maximize the separation between the fast and slow shear-waves, one may calculate the residual errors between the fast and slow waves as

$$E(\theta, \Delta t, \omega) = S_1(\omega) - S_2(\omega) e^{i\omega\Delta t} \quad (2)$$

where Δt is the time delay between the fast and slow waves. Substituting into equation (1) and changing into the time domain, it becomes,

$$\begin{aligned} E(\theta, \Delta t, t) &= (R(t)\cos\theta + T(t)\sin\theta) - (R(t-\Delta t)\sin\theta - T(t-\Delta t)\cos\theta) \\ &-(N_R(t)\cos\theta + N_T(t)\sin\theta) + (N_R(t-\Delta t)\sin\theta - N_T(t-\Delta t)\cos\theta) \end{aligned} \quad (3)$$

Equation (3) forms the basis for 2C vector rotation analysis. One can perform double scanning over the rotation angle θ and time delay Δt, and the objective function $F(\theta, \Delta t)$ to minimize the summed $E(\theta, \Delta t, t)$:

$$F(\theta, \Delta t) = \left(\sum_{k=0}^{n} E(\theta, \Delta t, t_k)^p\right)^{1/p} \quad (4)$$

for a time window length with n samples.

Time-delay spectra

The time-delay spectra can be constructed by scanning over vertical time using the correlation method. According to the 2C rotation analysis results, we are able to rotate the data into the fast and slow components. First we form a trace pair from traces of the fast and slow components. We then set a time window and use the correlation method to compute the correlation coefficients within the window. The time window slides downwards and therefore a time-delay spectrum is constructed.

Application results

The converted-wave data from the study area reveal a significant amount of splitting over the volcanic formations, indicated by the strong coherent energy in the transverse component (Figure 2). We use the above method and carry out a detailed analysis of the converted-wave splitting. As shown in Figure 2, we select the reservoir target as indicated by the lines for the 2C rotation analysis and Figure 3 shows the scanning results, the objective function calculated from equation (4). The average orientation angle is about 40 degrees from the inline X-direction (anticlockwise) and the average time delay is 25-30 milliseconds, indicating about 2% shear-wave splitting. The data are then rotated into the Fast/Slow components. Figure 4 shows time-delay spectra from selected CDP locations, from which a time-delay section can be obtained. Figure 5 is the interpretation results on the time-delay gradient section. As shown in Figure 5, areas of volcanic rocks with high gas accumulation show a significant amount of splitting (SS202 and SS1), whilst no-gas bearing rocks show little splitting (SS201). The splitting anomalies seem to be good indicators of gas accumulation.

Discussion and conclusions

We have presented a case study using converted-wave splitting to delineate gas reservoirs in volcanic rocks. We find that the degree of shear-wave splitting can be correlated to the known gas reservoirs. Higher values of shear-wave splitting in the presence of gas saturation is

consistent with equivalent medium modelling, as in the case studied by Angerer et al. (2002). We have also presented an efficient and convenient method for analysing converted-wave splitting in single-azimuth converted-wave data. Our approach includes two key steps: rotation scanning to maximize the separation of the split shear-waves and small-window correlation to build time-delay spectra.

Acknowledgements

We thank PetroChina Daqing Oilfield Ltd. for permission to show the data. This work is funded by the Edinburgh Anisotropy Project (EAP) of the British Geological Survey, and is published by the permission of the Executive Director of the British Geological Survey (NERC) and the EAP sponsors.

References

Angerer, E., Crampin, S., Li, X.Y. and Davis, T.L., 2002, Processing, modelling and predicting time-lapse effects of overpressured fluid-injection in a fractured reservoir: Geophysical Journal International, **149**, 267-280.

Crampin, S. and Lovel, J.H., 1991, A decade of shear-wave splitting in the Earth's crust: what does it means? what use can we make of it? and what should we do next? Geophysical Journal International **107**, 387-407.

Gaiser, J. and Van Dok, R., 2001, Green River basin 3D/3C case study for fracture characterization: Analysis of PS-wave birefringence: 71st Ann. Internat. Mtg: Soc. of Expl. Geophys., 764-767.

Granger, P., Bonnot, J., Gresillaud, A. and Rollet, A., 2001, C-wave resolution enhancement through birefringence compensation at the Valhall Field: 71st Ann. Internat. Mtg: Soc. of Expl. Geophys., 772-775.

MacBeth, C. and Crampin, S., 1991, Examination of a spectral method for measuring the effects of anisotropy: Geophysical Prospecting, Eur. Assn. Geosci. Eng., **39,** 667-690.

Vetri, L., Loinger, E., Gaiser, J., Grandi, A. and Lynn, H., 2003, 3D/4C Emilio: Azimuthal processing and anisotropy analysis in a fractured carbonate reservoir: The Leading Edge, **22**, 675-679.

Yuan, J., 2001, Analysis of four-component sea-floor seismic data for seismic anisotropy: PhD Thesis, University of Edinburgh.

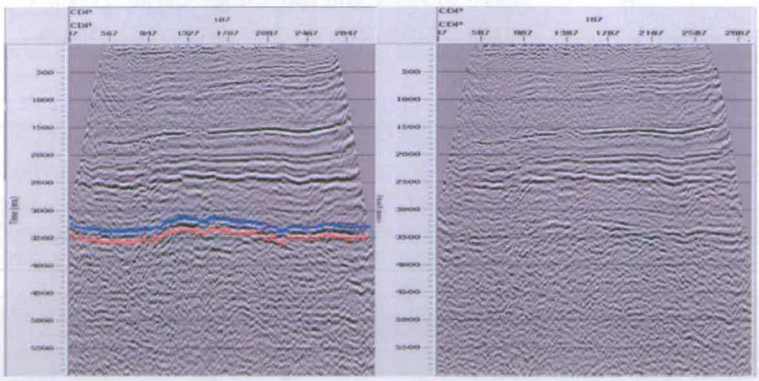

(a) (b)

Figure 2: Input data for 2C rotation analysis. (a) is the radial component and (b) is the transverse component. The blue and red lines show the top and bottom of the target.

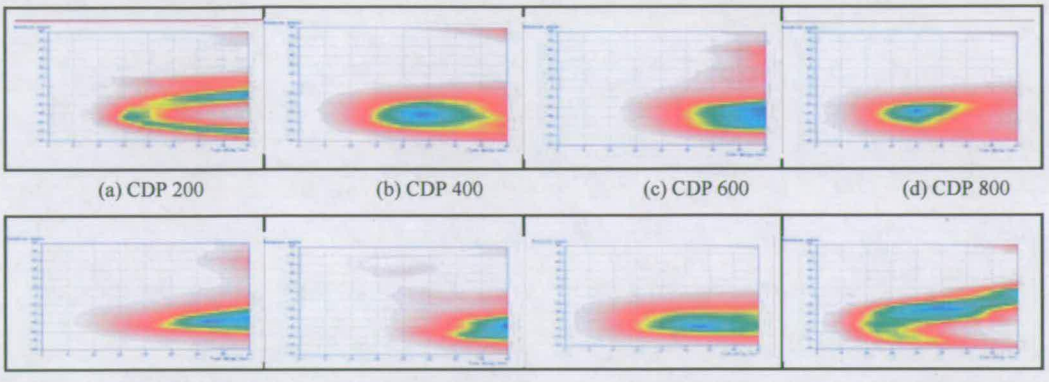

(a) CDP 200 (b) CDP 400 (c) CDP 600 (d) CDP 800

(e) CDP 1000 (f) CDP 1200 (g) CDP 1400 (h) CDP 1600

Figure 3: Rotation analysis for the data in Figure 2. The scanning is looking for a minimum value (in blue). The vertical axis is rotation angle, and the horizontal axis is time-delay.

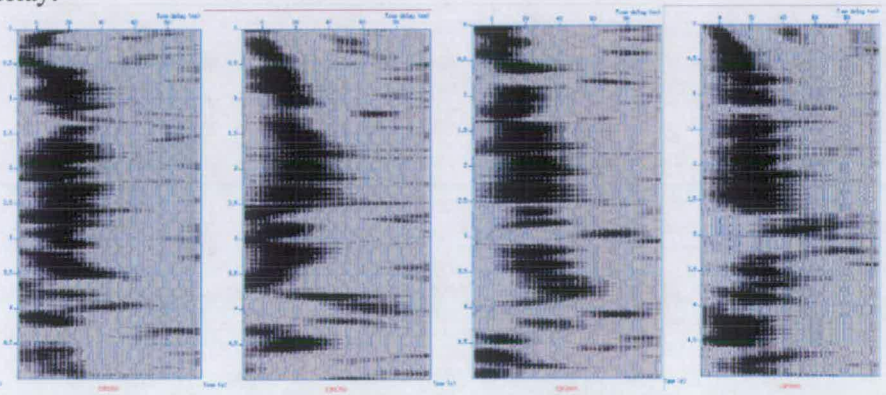

(a) CDP 1500 (b) CDP 1750 (c) CDP 2000 (d) CDP 2500

Figure 4: Time-delay spectra of selected CDPs. The horizontal axis is time-delay, and vertical axis is travel time.

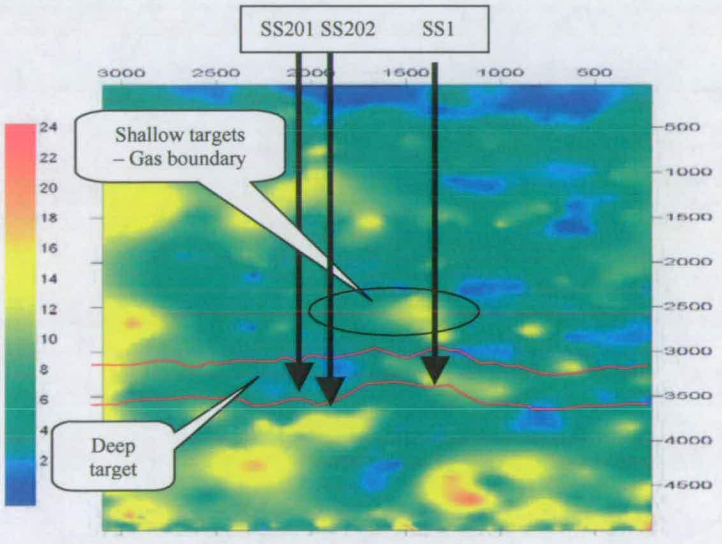

Figure 5: Interpretation results on the time-delay gradient section. SS202 and SS1 are gas-producing wells, and SS201 is a dry hole.

Estimating anisotropic parameters from PS converted-wave data: a case study

Lifeng Wang, Hengchang Dai and Xiang-Yang Li, British Geological Survey, Xianyi Sun, PetroChina Daqing Oilfield*

Summary

Anisotropic parameters are estimated from PS converted-wave (*C*-wave) data. The data were acquired by digital MEMS (micro-electro-mechanical system) sensors over a volcanic gas reservoir in Northeast China with a mixed sand and shale sequence in the overburden. This gives rise to shear-wave splitting as well as anisotropic moveout effects. We find that the amount of splitting determined from the data can be correlated to the known gas reservoirs, revealing a potential for using shear-wave splitting to delineate gas reservoirs in volcanic rocks. Furthermore, we use a four-parameter theory to evaluate the effects of non-hyperbolic moveout due to an asymmetric raypath and transverse isotropy (TI). These four parameters include the PS converted wave stacking velocity (V_{C2}), the vertical velocity ratio (γ_0), the effective velocity ratio (γ_{eff}), and the anisotropy parameter (χ). This four-parameter theory leads to an improvement in imaging quality and correlation between the P-waves and converted-waves.

Introduction

It has become increasingly common knowledge that anisotropy is widely present in the Earth subsurface. Sedimentary layers such as shales and thin bedding sequences in the overburden often give rise to vertical transverse isotropy (VTI, or polar anisotropy), whilst the presence of near-vertical fractures in sand or carbonate hydrocarbon reservoirs may result in horizontal transverse isotropy (HTI, or azimuthal anisotropy). For VTI, a major seismic effect is non-hyperbolic moveout, whilst for HTI, we have shear-wave splitting, both of which are intensively studied in the literature (e.g. Helbig and Thomsen, 2005, Crampin and Lovell, 1991). However, due to data quality issues, it is not very common to find both of these effects present in a land shear-wave dataset that can be clearly identified and used for reservoir characterization.

Recently, the use of digital MEMS (micro-electro-mechanical system) sensors has substantially improved the quality of land converted-wave data (e.g. Calvert et al. 2005). As a result, here we present an example of using MEMS-based converted-wave technology for jointly evaluating shear-wave splitting and the effects of non-hyperbolic moveout in Northeast China. The data were recorded over a volcanic gas reservoir buried at depths ranging from 2800m to 3600m, and the overburden is primarily composed of a mixed sand and shale sequence. As a result, the converted-wave data reveal a significant amount of shear-wave splitting over the volcanic formation; whilst in the shallow overburden, significant non-hyperbolic moveout can also be observed, which cannot be corrected fully by accounting for the asymmetric raypath. This paper studies the effects of non-hyperbolic moveout on imaging quality and event correlation. The paper also evaluates the effects of shear-wave splitting and its application for characterizing gas reservoirs.

Estimating anisotropic parameters for VTI

According to Li and Yuan (2003), four parameters are required for performing converted-wave velocity analysis and moveout correction. These four parameters are the vertical *P*- and *S*-wave velocity ratio γ_0, the effective velocity ratio γ_{eff}, the converted-wave stacking velocity V_{C2} and anisotropic parameter χ_{eff}. The following work flow may be used to determine these four parameters (V_{C2}, γ_0, γ_{eff} and χ_{eff}): 1) obtain γ_0 by a coarse correlation between the *P*- and *C*-wave stacked sections; 2) estimate V_{C2} from the near-offset moveout signature (offset-depth ratio $x/z<1.0$); 3) estimate γ_{eff} from the intermediate-offset moveout ($x/z<1.5$) and χ_{eff} from the far offset moveout ($x/z<2.0$). An interactive velocity tool has been developed by Dai (2003), which can be used to perform the above steps interactively (Figure 1).

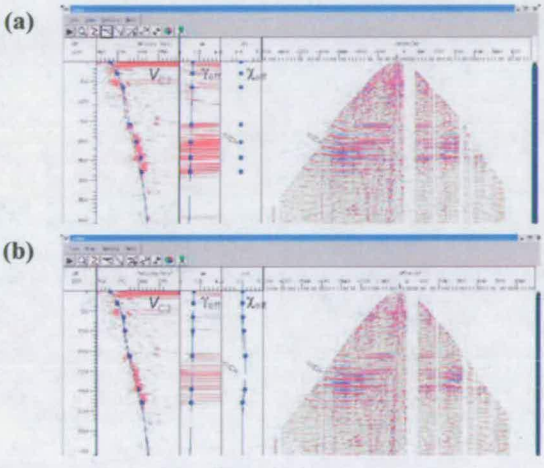

Figure 1: Analysis of the effects of anisotropy on converted-waves: velocity analysis and moveout correction (a) without and (b) with anisotropy. Note that from left to right, the three panels show the semblance analyses for V_{C2}, γ_{eff} and χ_{eff}, respectively.

Non-hyperbolic moveout analysis and results

The analysis is performed on the radial component (PSV-wave). Figure 1 compares *C*-wave velocity analysis with and without consideration of anisotropic effects. In the shallow section, there is still significant residual moveout without considering anisotropy (Figure 1a – setting χ_{eff} to zero), whereas the event is properly aligned after taking account for anisotropy (Figure 1b – non-zero χ_{eff}). Using the interactive tools, we can determine values of V_{C2}, γ_{eff} and χ_{eff} across the whole section, as shown in Figure 2. We can see that the amount of anisotropy is very significant for the events around 2.0 seconds (Figure 2d). In comparison, the other quantities (V_{C2}, γ_0 and γ_{eff}) all vary very smoothly. V_{C2}, γ_0, γ_{eff} and γ_{eff} are referred to as the anisotropic velocity model for stacking and migration.

Figure 3 compares the corresponding stacking results with and without considering anisotropy. The horizons in the zone around 2.0 seconds are only slightly better resolved with anisotropy (Figure 3b) than without anisotropy (Figure 3a). This is because the contribution of the far-offset *C*-waves to the final stack is relatively small compared with the *C*-waves in the intermediate offsets, as in Figure 1.

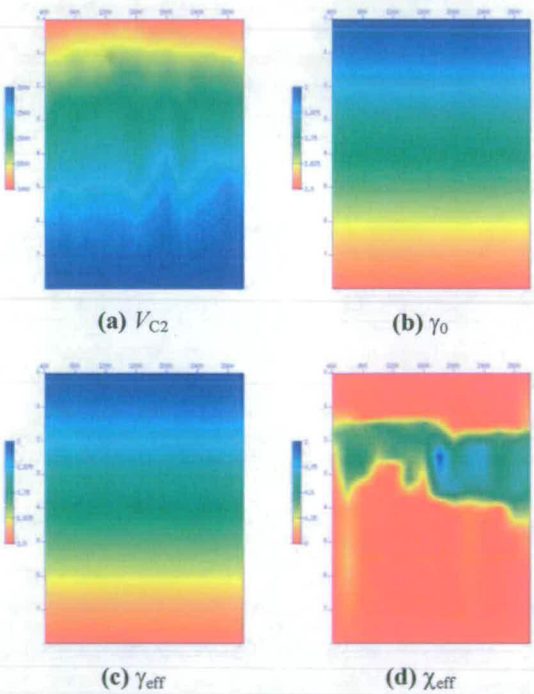

(a) V_{C2} **(b)** γ_0

(c) γ_{eff} **(d)** χ_{eff}

Figure 2. The four parameters (a) V_{C2}, (b) γ_0, (c) γ_{eff} and (d) χ_{eff} estimated from C-wave moveout analysis using the interactive tools as shown in Figure 1 for the radial component (PSV-wave).

The final migrated PP- and PSV-sections are shown in Figure 4, where the regional events (T06, T1 and T2, etc.) can all be mapped from both the PP- and PS-sections, giving rise to a very high degree of correlation.

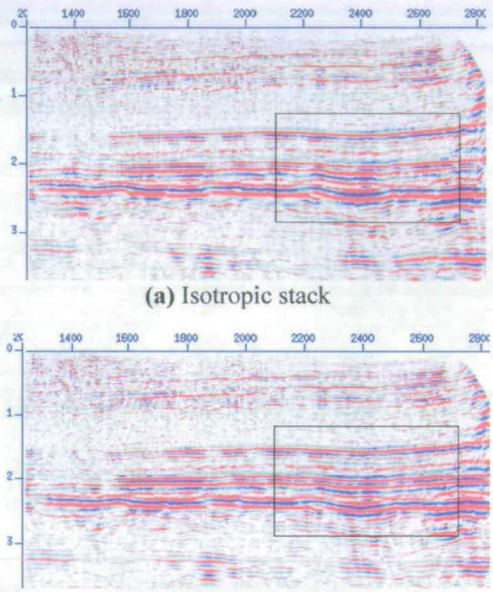

(a) Isotropic stack

(b) Anisotropic stack

Figure 3: Comparison of converted-wave stacked sections: (a) without and (b) with anisotropy for radial component (PSV-wave).

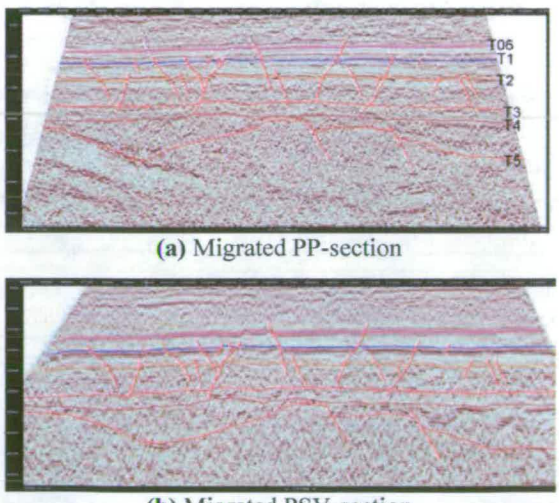

(a) Migrated PP-section

(b) Migrated PSV-section

Figure 4. Comparison of final migrated sections: (a) PP-wave and (b) PSV converted wave (Radial component).

Estimating anisotropic parameters from converted-wave data

Shear-wave splitting analysis

Shear-wave splitting in volcanic rocks has been reported before (e.g. Crampin and Lovell 1991). Volcanic rocks are known to be heterogeneous and can contain a large amount of fractures and vuggy pores, as well as other small heterogeneities. When these small-scale features are gas-charged and stress-aligned, it will introduce azimuthal anisotropy, giving rise to shear-wave splitting. In the previous sections, we have analyzed the vertical component (PP-wave) and the horizontal radial component (PSV-waves) for VTI. Here we focus only on the two horizontal components for shear-wave splitting.

Most of the rotation algorithms for shear-wave splitting, such as Alford rotation, require multi-azimuth distribution. However, the converted-wave data used in this study are acquired with a 2D configuration and single-azimuth source and receiver distribution. For single-azimuth data, a rotation scanning procedure is often needed that searches for optimum solutions according to certain criteria. One of the common criteria is the similarity of waveforms between the fast and slower shear-waves. Here we adopt a criterion that maximizes the separation of the fast and slow shear-waves, following the approach of Yuan (2001).

Time delay spectra

Once the split shear-waves are separated, we construct a time-delay spectrum between the fast and slow waves that allows the picking of time delays as a function of the vertical travel time, yielding a time-delay section for interpretation purposes. The time-delay spectrum can be constructed by scanning over vertical time using the correlation method. For each trace pair of the fast and slow split shear-waves, we use a sliding time-window to compute the correlation coefficients within the window, which produces a time-delay spectrum.

Results of splitting analysis

In order to maintain the characteristics of shear-wave splitting, we have reprocessed the two horizontal components using the same processing flow, and Figure 5 shows the results. The converted-wave data from the study area reveal a significant amount of splitting over the volcanic formations, indicated by the strong coherent energy in the transverse component (Figure 5b). Note that in the absence of splitting, the transverse component should contain mainly noise. We have carried out a detailed analysis of the converted-wave splitting using the rotation-scanning method and time-delay spectrum analysis.

Figure 6 shows the scanning results for some selected CDPs over the target horizon marked by the blue and red lines in Figure 5. The average orientation angle is about 40 degrees from the inline X-direction (anticlockwise) and the average time delay is 25-30 milliseconds, indicating about 2% shear-wave splitting (Figure 7). The data are then rotated into the Fast/Slow components (Figure 8).

Figure 9 shows the time-delay spectra from selected CDP locations, from which a time-delay section can be obtained. Figure 10 is the interpretation results on the time-delay gradient section. As shown in Figure 10, areas of volcanic rocks with high gas accumulation show a significant amount of splitting (SS202 and SS1), whilst non-gas bearing rocks show little splitting (SS201). The splitting anomalies seem to be good indicators of gas accumulation.

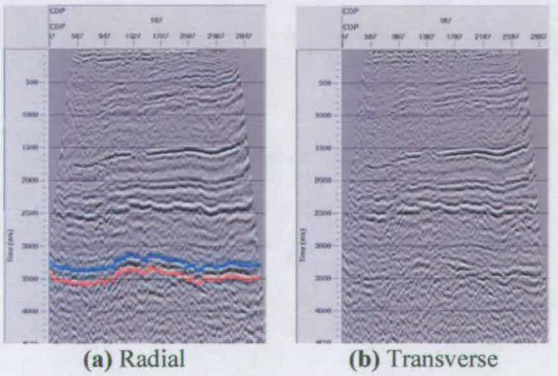

(a) Radial **(b)** Transverse

Figure 5: Input data for rotation-scanning analysis: (a) radial and (b) transverse components. The blue and red lines show the top and bottom of the target.

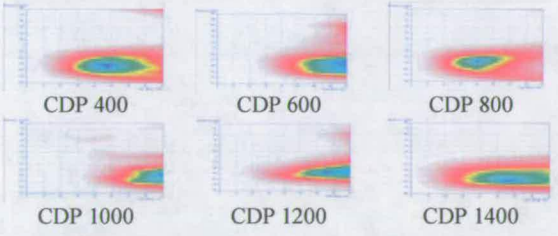

Figure 6. Rotation analysis for the data in Figure 5. The scanning is looking for a minimum value (in blue). The vertical axis is rotation angle, and the horizontal axis is time-delay.

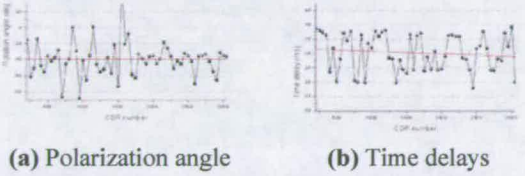

(a) Polarization angle **(b)** Time delays

Figure 7. Picked (a) rotation angle and (b) time delays of the split shear-waves from the scanning results in Figure 6.

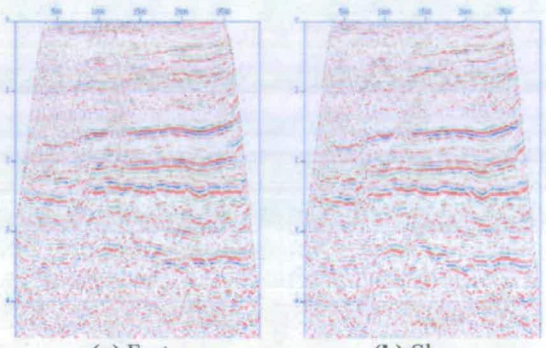

(a) Fast (b) Slow

Figure 8. The separated (a) fast and (b) slow split shear-waves obtained by applying the rotation angle in Figure 7a to the data in Figure 5.

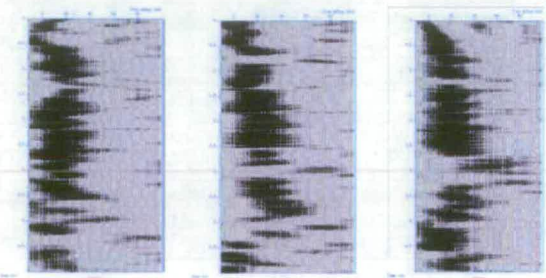

Figure 9. Time-delay spectra of selected CDPs. The horizontal axis is time-delay, and vertical axis is travel time.

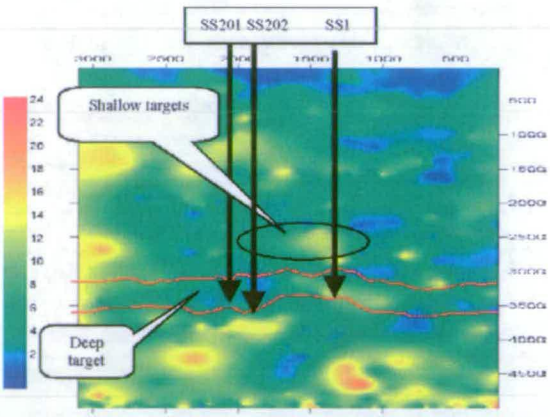

Figure 10. Interpretation results on the time-delay gradient section. SS202 and SS1 are gas-producing wells, and SS201 is a dry hole.

Discussion and conclusions

We have evaluated both shear-wave splitting and non-hyperbolic moveout in converted-wave data. We find that the degree of shear-wave splitting can be correlated to the known gas reservoirs. Higher values of shear-wave splitting are associated with higher degrees of gas saturation. We have also shown that the converted-wave non-hyperbolic moveout in the presence of anisotropy can be fully compensated for using the four-parameter theory of Li and Yuan (2003), which leads to an improvement in both imaging quality and event correlation between PP and PS converted-waves.

Acknowledgements

We thank PetroChina Daqing for permission to show the data. We thank Wang Guishui, Min Chunhua, and Qian Zhongping for processing the data. This work is supported by the CNPC international collaboration programme and PetroChina Daqing Ltd. through the Edinburgh Anisotropy Project (EAP) of the British Geological Survey (BGS), and is published with the approval of all project partners and the Executive Director of BGS.

References

Calvert, A.S., Novak, J.M., Maher, J., Burch, D.N., Bird, D., Larson, R., 2005, A tale of two surveys: experiences processing two similar but different land 3D-3C MEMS surveys, 75th SEG meeting, Houston, USA, Expanded Abstracts, 975-978.

Crampin, S. and Lovel, J.H., 1991, A decade of shear-wave splitting in the Earth's crust: what does it means? what use can we make of it? and what should we do next? Geophysical Journal International **107**, 387-407.

Dai H. 2003. Integrative analysis of anisotropy parameter and velocities for PS converted waves. 73rd SEG meeting, Dallas, USA, Expanded Abstracts, 1577-1580.

Li, X.-Y. and Yuan, J., 2003. Converted-wave moveout and conversion-point equations in layered VTI media: theory and application. Journal of Applied Geophysics, **54**, 297-318.

Helbig, K. and Thomsen, L., 2005, 75-plus years of anisotropy in exploration and reservoir seismics: A historical review of concepts and methods: Geophysics, **70,** 9ND-23ND.

Yuan, J., 2001, Analysis of four-component sea-floor seismic data for seismic anisotropy: PhD Thesis, University of Edinburgh.

Appendix C

Published material

- **Wang, L.,** Li, X.Y. and Sun, X., 2006, Analysis of converted-wave splitting in volcanic rocks: a case study from northeast China, 68th Mtg EAGE Conference, Expanded Abstract

- **Wang, L.,** Dai, H., Li, X.Y. and Sun, X., 2006, Estimating anisotropic parameters from PS-converted wave data: a case study, 76th Mtg.: Soc. Expl. Geophys. Expanded Abstract.